# Development of an energy filtering direct electron detector for diffraction studies in the SEM

**Stefano Vespucci**

A thesis presented for the degree of
Doctor of Philosophy

Department of Physics
University of Strathclyde
Glasgow
16/02/2017

---

This thesis is the result of the authors original research. It has been composed by the author and has not been previously submitted for examination which has led to the award of a degree.

Signed:
Date:

To my grandfather.

# Abstract

This thesis describes the application of an energy filtering digital direct electron detector for diffraction studies of materials in the field emission scanning electron microscope (SEM). The main aim was the development of the digital complementary metal-oxide-semiconductor hybrid pixel detector, "Timepix" for electron backscatter diffraction (EBSD), a technique which allows the acquisition of precise crystallographic information from the surface of a sample, such as crystallographic orientation, phase and strain. EBSD results from nitride semiconductor, silicon and diamond thin films and tungsten-carbide cobalt samples are presented and used to illustrate the advantages of acquiring EBSD patterns with the Timepix detector, in particular to demonstrate the improvement in the contrast and increase in the detail contained in the EBSD patterns as consequence of the energy filtering.

Alongside EBSD, new applications were developed such as reflection high energy electron diffraction (RHEED) in the SEM. RHEED is a very surface sensitive technique which in principle could allow the study of ultrathin samples where conventional SEM based methods are limited.

The combination of RHEED and Kikuchi diffraction, led furthermore to the development of surface wave resonance electron channelling contrast imaging (SWR-ECCI), which allows crystalline defects such as surface steps, grain boundaries, dislocations and stacking faults to be imaged with a high level of surface sensitivity,

extending furthermore the application of ECCI to non-continuous surfaces. This is obtained by selecting experimental geometries which stimulate the surface wave resonance at the specimen surface.

Transmission diffraction in the SEM was also explored, resulting in the acquisition of transmission diffraction patterns and in the generation of images of the sample obtained under experimental conditions analogous to scanning transmission electron microscopy. This allowed for example, bright and dark field images of the specimen to be obtained. The resulting images exhibited crystalline contrast not often observed in the SEM.

The Timepix sensor is constructed from a piece of single crystal silicon. Diffraction effects within this single crystal were found to result in the Timepix detector response exhibiting an underlying diffraction pattern; that is a detector diffraction pattern (DDP). The DDP provides a watermark from which the location of the camera relative to the position of the electron beam on the sample may be precisely and accurately determined. This opens up new opportunities for improved mapping of the strain distribution in materials for example.

The development of all the novel techniques summarized above opens up new horizons which need to be explored.

# Acknowledgements

I consider completing a PhD a singular and very important moment. This would not have been possible without the help of a countless number of people who supported, helped and inspired me.

First of all I must express my gratitude to my supervisor, Dr Carol Trager-Cowan, for the guidance, the support and continuous encouragement provided during my PhD. Her enthusiasm in electron microscopy was definitely fruitful for my research work.

I would like to thank my second supervisor Dr Paul Edwards for sharing with me his great knowledge and experience on the electronic microscope and helping me resolving problems I encountered. In this regard I can't but thank Mr David Clark for his constant and invaluable help in building and repairing any type of mechanical component I needed, and Mr Gerald Drinkwater, who shared with me his great technical knowledge of electronics and for helping me in building various electronic devices.

I consider myself privileged to have been in contact with Dr Aimo Winkelmann, who has influenced, more than anyone else, my attitude and way of approaching the theoretical and practical aspects associated with scattering and diffraction, in particular EBSD; he furthermore provided countless simulations of EBSD patterns and pieces of code; I am particularly grateful to him. I must also thank Dr Ben

Hourahine who always shared his knowledge and advice in countless discussions.

A huge thanks goes to Dr Dima Maneuski and Prof Val O'Shea, for sharing with me their great experience on detector systems, for providing the Medipix2 and Timepix detectors that I used during my research. I am grateful to Dima also for the long discussions in front of pints of beer on Friday nights and the friendship he demonstrated to me.

I am particularly grateful to Dr Ken Mingard, who gave me hospitality several times at NPL, for various experiments, sharing with me his vast experience in the field of electron backscatter diffraction. I must also thank Prof Michael Campbell for inviting me on several occasions to CERN for a number of Medipix meetings, which have been very instructive and important for my research. I would also like to thank Dr Austin Day and Prof Angus Wilkinson for helpful discussions at various conferences.

I would like to thank EPSRC, NPL and the University of Strathclyde for the financial support of my PhD studentship, which allowed me, among other things, to participate in a large number of international conferences, which contributed significantly to enriching my personal wealth of experience.

I am very grateful to the people who provided me the samples which I used in a variety of experiments. These include Prof Peter Parbrook, Tyndall National Institute, University College, Cork, Ireland, for providing us with the GaN sample and Alexandre Tallaire, Laboratoire des Sciences et des Procds des Matriaux LSPM-CNRS, Universit Paris 13, France for providing the diamond sample. I would like to thank Dr Yu Chen, University of Strathclyde, Glasgow, UK for providing me with the gold nanoparticles; Dr Philip Shields, University of Bath, Bath, UK for providing the GaN nanorods; Dr Simon Fleischmann, Ferdinand-Braun-Institut, Berlin, Germany, for prividing the AlGaN layer on patterned sapphire substrate sample, and Prof Michael Kneissl, Technische Universitat, Berlin, Germany for providing the AlGaN/AlN/Sapphire structures; Dr Joseph Roberts, School of Engineering, University of Liverpool, for providing the $HfO_2$ samples.

A special thanks is for my officemate/friends, Gunnar and David, for standing my cumbersome presence in the office, and for their help on a large number of occasions. In this regard, a big thanks goes to Nouf and Elena as well. I would like to furthermore thank Naresh for the long discussions on ECCI, and Martin, Michael, Elaine and Jochen for an always interesting and entertaining time on Level 2 around the coffee table.

A particular thanks goes to Mr Ken Muir and Mr Mark Hutcheon for the entertaining time spent together in the Physics department.

I am also very grateful to the PhD examiners, Prof Ken Durose and Dr Kevin Ronald, for providing useful suggestions and tips to improve this thesis and making it stronger.

Last, but the most important, I would like to thank my wife Chiara for her love and for her continuous support and encouragement, and my daughter Maya, who is my source of joy. The same thanks go to my family, who have always encouraged and supported me in every choice of my life. I love you.

Stefano Vespucci Glasgow, 16/02/2017

# Contents

# List of abbreviations

| | |
|---|---|
| 2D | two-dimensional |
| 3D | three-dimensional |
| ADF | annular dark-field |
| ASIC | application-specific integrated circuit |
| BKD | backscatter Kikuchi diffraction |
| BSE | back scattered electrons |
| CBED | convergent-beam electron diffraction |
| CC | cross correlation coefficient |
| CCD | charge-coupled device |
| CMOS | complementary metal-oxide semiconductor |
| DAC | digital to analog converter |
| DD | detector distance |
| DDP | detector diffraction pattern |
| DP | diffraction pattern |
| DQE | detective quantum efficiency |
| EBSD | electron backscatter diffraction |
| EBSP | electron backscatter diffraction pattern |
| ECCI | electron channelling contrast imaging |

| | |
|---|---|
| ECP | electron channelling pattern |
| EDS | energy dispersive X-ray spectroscopy |
| EELS | electron energy loss spectroscopy |
| EFTEM | energy filtered transmission electron microscopy |
| ELO | epitaxial lateral overgrowth |
| FEG | field emission gun |
| FFT | fast Fourier transform |
| FIB | focused ion beam |
| FOLZ | first-order Laue zone |
| FWHM | full width at half maximum |
| GUI | graphical user interface |
| HAADF | high angle annular dark field |
| HOLZ | high-order Laue zones |
| HPD | hybrid pixel detectors |
| LSF | line spread function |
| LVDS | low-voltage differential signaling |
| MBE | molecular beam epitaxy |
| MOVPE | metalorganic vapour phase epitaxy |
| MTF | modulation transfer function |
| NPS | noise power spectrum |
| PC | pattern centre |
| PCR | pixel configuration register |
| REM | reflection electron microscopy |
| RHEED | reflection high-energy electron diffraction |
| SAD | selected area diffraction |
| SADP | selected area diffraction pattern |

| | |
|---|---|
| SE | secondary electrons |
| SEM | scanning electron microscope |
| SOLZ | second-order Laue zone |
| SREM | scanning reflection electron microscopy |
| STEM | scanning transmission electron microscopy |
| SWR | surface wave resonance |
| t-EBSD | transmission electron backscatter diffraction |
| TED | transmission electron diffraction |
| TEM | transmission electron microscopy |
| THL | threshold |
| TKD | transmission Kikuchi diffraction |
| ToA | time of arrival |
| TOT | time over threshold |
| TSL | Timepix synchronization logic |
| USB | universal serial bus |
| WDS | wavelength-dispersive X-ray spectroscopy |
| ZOLZ | zero-order Laue zone |

# Chapter 1

# Motivation

It is astonishing to think about how materials are part of the development of civilization. Terms like Stone Age, Bronze Age and Iron Age are all great examples of how materials have strongly influenced the history and culture of human beings on the Earth, and defined step changes in the civilization of peoples.

The use of solid state materials can be traced back more than three million years, from when wood and flint were used as tools, for hunting, processing food and making fire [1, 2]. Technology evolved rapidly over the centuries and humans learnt how to use metals, to melt and cast them for the creation of more complex tools and to create alloys. The technological evolution made our lives safer, more convenient and more comfortable.

The rapid technological evolution continued, and today it is moving faster than any time in history, leading to the development of a variety of new materials, such as metals alloys, ceramics, polymers and semiconductors. It is now possible to manipulate matter at the atomic level, allowing the creation of a wide variety of tools and devices having ever stronger impact on all aspects of human life. This is driving technology toward the creation of ever more complex and sophisticated devices. These includes vehicles, computers, phones, medical equipment, electronic devices, and devices for the generation of light.

Device performance is linked to the properties of the materials used for their construction. The strength of a metal, the efficiency of a solar cell and the electrical resistivity of an electrical component, are all good examples of how microscopic properties affect macroscopic devices. Materials scientists, physicists and engineers study the physical, chemical, electrical, magnetic and optical properties of materials and the relationship between the microstructure and the macroscopic properties. They also study the history of a material, e.g., how its properties change as it is processed and how the process affects the performance of the materials. This is used for example to understand the reason for device failure.

The study of the structure of materials is crucial. This involves the use of tools such as diffraction analysis using X-rays, electrons, or neutrons, or spectroscopic and chemical analysis techniques such as Raman spectroscopy, wavelength-dispersive X-ray spectroscopy (WDS), energy dispersive spectroscopy (EDS), cromatography, thermal analysis, cathodoluminescence, etc.

This thesis describes the development of a digital direct electron detector for a series of scanning electron microscope (SEM) based techniques used for the characterization of crystalline materials, ranging from metals, to ceramics and to semiconductors.

In the last few decades, ever more and precise characterization techniques have been developed in the SEM, to address the increasing needs of more detailed information on crystalline materials. Some of these diffraction based technique are e.g. acquisition of electron channelling patterns (ECPs), scanning reflection electron microscopy (SREM), electron channelling contrast imaging (ECCI), reflection high energy electron diffraction (RHEED) and electron backscatter diffraction (EBSD).

The aim of the research reported in this thesis is to show that, by using a digital direct electron detector, ‘Timepix’, it is possible to advance the capabilities of some of the already existing characterization techniques, e.g., EBSD and RHEED, and also to take a step forward by introducing new characterization methods in the SEM, which could allow the characterization of materials where conventional techniques are not applicable.

Originally the goal of the work was the development of a detector for energy filtered EBSD. During the course of the study, a detector for RHEED studies in the SEM was also developed, leading to an higher level of surface sensitivity. This approach revealed its potential when EBSD and RHEED patterns were obtained in transmission mode in the SEM, from an AlGaN nanorod specimen without any sample preparation.

Influenced by the work of colleagues on ECPs, which can be treated using the same theoretical framework used in EBSD, a novel approach for the acquisition of ECCI micrographs was introduced, using the information obtained from the RHEED patterns, introducing what has been called surface-wave-resonance ECCI (SWR-ECCI), which permits the application of ECCI to non-continuous surfaces like nanorods, where the current ECCI technique is not applicable.

A new diffraction effect was observed which results from the Timepix sensor being constructed from a piece of single crystal silicon. Diffraction effects within this single crystal were found to result in the Timepix detector response exhibiting an underlying diffraction pattern; that is a detector diffraction pattern (DDP). The DDP provides a watermark from which the location of the camera relative to the position of the electron beam on the sample may be precisely and accurately determined. This opens up new opportunities for improved mapping of the strain distribution in materials for example.

The techniques developed open up new several new directions for research, and these are in the process being explored.

The structure of the thesis is the following;

In Chapter 2 the basic concepts of crystallography and quantum mechanics, which are of fundamental importance for the understanding and interpretation of the results of the electron diffraction experiments, are introduced.

In Chapter 3 a brief introduction to the most common electron based imaging and scattering modes which are relevant to the context of this thesis is given. The conventional EBSD and RHEED techniques are discussed in detail.

In Chapter 4 the Timepix detector is introduced and the development of a novel method for the energy calibration of the Timepix threshold, the parameter which allows the detector to perform energy filtering at electronic level, is described.

In Chapters 5 and 6 the development of an EBSD and RHEED system in the SEM using the Timepix detector is reported, showing the advantages of the direct electron imaging of energy filtered EBSD and RHEED patterns. Chapter 6 also contains the preliminary results regarding the development of the SWR-ECCI.

In Chapter 7 the development of software which allows the Timepix detector to be used for mapping is discussed. The acquisition of EBSD and TKD maps is demonstrated.

In Chapter 8 the DDPs are described, and a description of the method developed for the determination of the position of a divergent source of energetic radiation (electrons, X-rays, neutrons, etc.) from a two dimensional detector, is discussed.

Finally Chapter 9 provides an overview of the thesis with concluding discussion.

# Chapter 2

# Theoretical framework

In this chapter the theoretical framework required for the understanding of electron diffraction experiments is introduced. The terminology which will be used during the whole thesis is also defined. The contents of this chapter have general validity, and can be applied to the description of electron diffraction techniques applied to crystals, such as EBSD and RHEED. Most of the theoretical framework treated in this chapter will be applied in the later chapters.

## 2.1 Bravais lattice and crystal planes

A crystal can be thought of as a repetition in three-dimensional (3D) space of identical blocks consisting of one or more atoms, called a basis [3, 4]. The structure of a crystal is then obtained by placing a basis at each point of the lattice. The lattice may be defined by three basis vectors, $\mathbf{a}_1$, $\mathbf{a}_2$, $\mathbf{a}_3$, so that each point of the lattice can be written as

$$\mathbf{r} = u_1\mathbf{a}_1 + u_2\mathbf{a}_2 + u_3\mathbf{a}_3 = \sum_{i=1}^{3} u_i\mathbf{a}_i = u_i\mathbf{a}_i \tag{2.1}$$

where $u_1, u_2, u_3$ are arbitrary integers. In the last expression the Einstein summation convention was used, by which, if the subscript occurs twice, then the summation is implicit.

The angles between the basis vectors are usually represented by three Greek symbols $\alpha, \beta, \gamma$.

If the modulus of the basis vectors is defined as $a = |\mathbf{a}_1|, b = |\mathbf{a}_2|, c = |\mathbf{a}_3|$, the seven existing crystal systems can be defined using a set of six numbers, $\{a,\ b,\ c,\ \alpha,\ \beta,\ \gamma\}$, called lattice parameters of the unit cell.

The seven crystal systems are the following:

| | | |
|---|---|---|
| triclinic (a): | $\{a, b, c, \alpha, \beta, \gamma\}$ | $a \neq b \neq c;\ \alpha \neq \beta \neq \gamma$ |
| monoclinic (m): | $\{a, b, c, \frac{\pi}{2}, \beta, \frac{\pi}{2}\}$ | $a \neq b \neq c;\ \beta \neq \frac{\pi}{2}$ |
| hexagonal (h): | $\{a, a, c, \frac{\pi}{2}, \frac{\pi}{2}, \frac{2\pi}{3}\}$ | $a = b \neq c;$ |
| rhombohedral (R): | $\{a, a, a, \alpha, \alpha, \alpha\}$ | $a = b = c;\ \alpha \neq \frac{\pi}{2}$ |
| orthorhombic (o): | $\{a, b, c, \frac{\pi}{2}, \frac{\pi}{2}, \frac{\pi}{2}\}$ | $a \neq b \neq c;$ |
| tetragonal (t): | $\{a, a, c, \frac{\pi}{2}, \frac{\pi}{2}, \frac{\pi}{2}\}$ | $a = b \neq c;$ |
| cubic (c): | $\{a, a, a, \frac{\pi}{2}, \frac{\pi}{2}, \frac{\pi}{2}\}$ | $a = b = c;$ |

It is possible to place additional points in the unit cell, the so-called centering vectors:

$$\mathbf{A} = \left(0, \frac{1}{2}, \frac{1}{2}\right) \tag{2.2}$$

$$\mathbf{B} = \left(\frac{1}{2}, 0, \frac{1}{2}\right) \tag{2.3}$$

$$\mathbf{C} = \left(\frac{1}{2}, \frac{1}{2}, 0\right) \tag{2.4}$$

$$\mathbf{I} = \left(\frac{1}{2}, \frac{1}{2}, \frac{1}{2}\right) \tag{2.5}$$

When the centering vectors are combined with the seven primitive lattices, seven additional lattices are found. Those 14 lattices are the so-called Bravais Lattices [5].

The position of an atom inside the unit cell is expressed by the position vector $\mathbf{r}$:

$$\mathbf{r} = x\mathbf{a}_1 + y\mathbf{a}_2 + z\mathbf{a}_3 = r_i\mathbf{a}_i \tag{2.6}$$

where the numbers $(x, y, z)$, known as fractional coordinates, are real numbers between 0 and 1.

It is common to denote particular crystallographic planes with the so-called Miller indices. Assuming that the crystal plane does not pass through the origin, the Miller indices can be obtained in the following way: let us call $s_1, s_2, s_3$ the intercepts of a particular lattice plane with the basis vector $\mathbf{a}_1$, $\mathbf{a}_2$, $\mathbf{a}_3$, expressed in units of basis vector length. If the plane is parallel to a specific basis vector then the component is taken as $\infty$. The triplet composed of the inverted value of the intercepts, $\frac{1}{s_1}, \frac{1}{s_2}, \frac{1}{s_3}$, reduced to the smallest possible integers, enclosed within square brackets is called the Miller indices of the plane.

Because most of the crystallographic reference frames are non-Cartesian, the distances and angles between vectors are calculated using the dot product operation which does not depend on a particular reference frame. The dot product is defined as the product of the modulus of the vectors times the cosine of the angle between vectors;

$$\mathbf{p} \cdot \mathbf{q} = |\mathbf{p}||\mathbf{q}| \cos\theta \tag{2.7}$$

If the vector $\mathbf{p}$ has component $p_i$ with respect to the crystal basis $\mathbf{a}_i$, that is $\mathbf{p} = p_i\mathbf{a}_i$, the length of the vector may be written as $|\mathbf{p}| = \sqrt{(p_i\mathbf{a}_i \cdot p_j\mathbf{a}_j)} = \sqrt{(p_i(\mathbf{a}_i \cdot \mathbf{a}_j)p_j)}$. If the direct metric tensor is defined as $g_{ij} \equiv \mathbf{a}_i \cdot \mathbf{a}_j$, then the length of a vector and the angle between two vectors can be written as

$$|\mathbf{p}| = \sqrt{p_i g_{ij} p_j} \tag{2.8}$$

$$\theta = \cos^{-1}\left(\frac{\mathbf{p}\cdot\mathbf{q}}{|\mathbf{p}||\mathbf{q}|}\right) = \cos^{-1}\left(\frac{p_i g_{ij} q_j}{\sqrt{p_i g_{ij} p_j}\sqrt{q_i g_{ij} q_j}}\right) \tag{2.9}$$

If the direct metric tensor is explicitly written as,

$$g_{ij} = \begin{bmatrix} \mathbf{a}\cdot\mathbf{a} & \mathbf{a}\cdot\mathbf{b} & \mathbf{a}\cdot\mathbf{c} \\ \mathbf{b}\cdot\mathbf{a} & \mathbf{b}\cdot\mathbf{b} & \mathbf{b}\cdot\mathbf{c} \\ \mathbf{c}\cdot\mathbf{a} & \mathbf{c}\cdot\mathbf{b} & \mathbf{c}\cdot\mathbf{c} \end{bmatrix} = \begin{bmatrix} a^2 & ab\cos\gamma & ac\cos\beta \\ ab\cos\gamma & b^2 & bc\cos\alpha \\ ac\cos\beta & bc\cos\alpha & c^2 \end{bmatrix}$$

it can be seen that it contains the information contained in lattice parameters $\{a,\ b,\ c,\ \alpha,\ \beta,\ \gamma\}$ in a form which allows the computation of length and angles [4].

In diffraction it is useful to work in terms of reciprocal space, which is generated by three reciprocal basis vectors, defined as

$$\mathbf{a}^* = 2\pi\frac{\mathbf{b}\times\mathbf{c}}{\mathbf{a}\cdot(\mathbf{b}\times\mathbf{c})} \tag{2.10}$$

$$\mathbf{b}^* = 2\pi\frac{\mathbf{c}\times\mathbf{a}}{\mathbf{a}\cdot(\mathbf{b}\times\mathbf{c})} \tag{2.11}$$

$$\mathbf{c}^* = 2\pi\frac{\mathbf{a}\times\mathbf{b}}{\mathbf{a}\cdot(\mathbf{b}\times\mathbf{c})} \tag{2.12}$$

from which is clear that

$$\mathbf{a}_i\cdot\mathbf{a}_j^* \equiv 2\pi\delta_{ij}. \tag{2.13}$$

where $\delta_{ij}$ is the Kronecker delta defined as:

$$\delta_{ij} = \begin{cases} 0 & \text{if } i \neq j, \\ 1 & \text{if } i = j. \end{cases} \tag{2.14}$$

Every reciprocal lattice point $\mathbf{g}_{hkl}$ can be written as a combination of reciprocal basis vectors,

$$\mathbf{g}_{hkl} = h\mathbf{a}^* + k\mathbf{b}^* + l\mathbf{c}^* = g_i\mathbf{a}_\mathbf{i}^* \tag{2.15}$$

.

A reciprocal lattice vector $\mathbf{g}_{hkl}$, having components $(h, k, l)$, is perpendicular to the plane having Miller indices $(hkl)$, and its length is proportional to the inverse of the spacing between the corresponding lattice planes

$$|\mathbf{g}_{hkl}| = \frac{2\pi}{d_{hkl}} \tag{2.16}$$

.

As seen in the following sections, reciprocal lattice vectors are very useful for the interpretation of diffraction experiments.

## 2.2 Stereographic projection

Stereographic projection is a very useful tool for representing three dimensional crystalline directions in two dimension [4,6,7]. Geometrically speaking stereographic projection is a mapping function which projects a sphere onto a plane. This is often useful for studying the crystal distribution in textured materials, crystal symmetries, displaying diffraction patterns etc.

The stereographic projection is schematically shown in Fig. 2.1(a). Any direction **OP**, where **P** is a point on the surface of the north hemisphere and **O** the centre of the sphere, can be associated with a point in the equatorial plane of the sphere by stereographic projection. The point **P′**, being the stereographic projection of the direction **OP**, is located at the interception of the equatorial plane with the segment connecting the south pole of the sphere with the point **P**.

Typically the axes of the projection sphere is aligned with a specific sample direction, e.g. sample normal, rolling direction or transverse direction [7]. In this case the equatorial plane observed by the north pole represents a pole figure, which is used to map the crystallographic directions with respect to the sample frame.

When the axes of the projection sphere is aligned with a specific crystallographic direction, the inverse pole figure is instead obtained, showing the crystal orientations of a given sample direction (typically the normal direction) with respect to the crystal axes. The inverse pole figure can help to visualise certain types of textures. A good summary on the methods used for the representation the texture can be found in Ref. [8] and references therein.

The example in Fig. 2.1(b) shows a full inverse pole figure from a crystal having cubic symmetry. Here all symmetrically equivalent directions are shown. For cubic materials there are 48 symmetrically equivalent crystal directions. The inverse pole figure shows only 24 of those, because it shows only the direction on the north hemisphere. The consequence of the crystal symmetry is that only a limited portion of the inverse pole figure is required to display directions in the sample. This minimum portion of the inverse pole figure is called the standard stereographic triangle. This is highlighted in yellow in Fig.2.1(b).

In EBSD, individual orientation measurements are shown as points in the inverse pole figure. The individual point orientation measurements from the whole sample

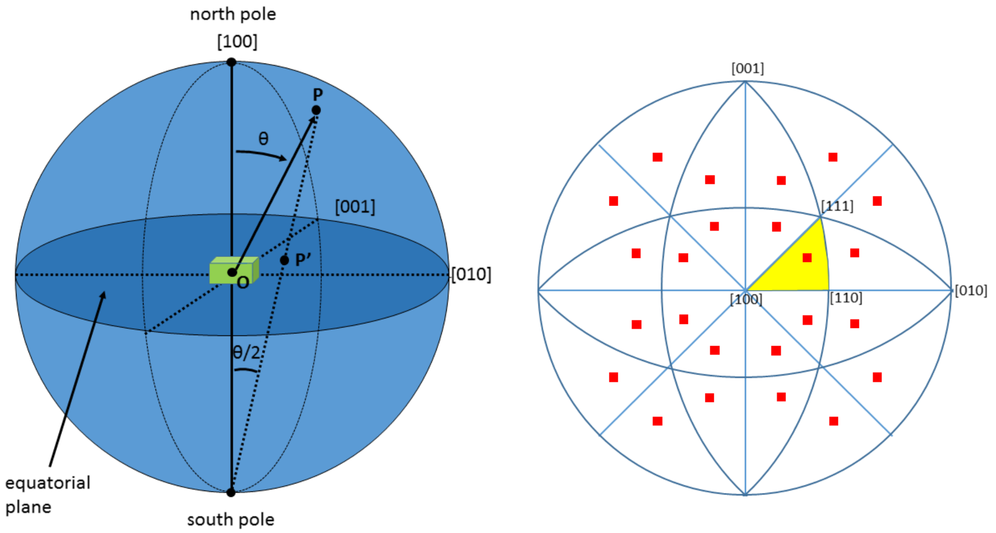

(a) (b)

Figure 2.1: Illustration of the (a) stereographic projection and (b) corresponding complete inverse pole figure for a cubic crystalline system where the the standard stereographic triangle is highlighted in yellow.

plotted together on the inverse pole figure reveal the orientation distribution of the crystal in the specimen [7].

## 2.3 Kinematical theory of diffraction

High energy electrons interact strongly with a solid specimen. When propagating through the specimen, electrons are most likely to undergo multiple scattering events in their path. In a number of situations, for the understanding and interpretation of experimental results, in particular the geometries of diffraction patterns, it is useful to simplify the theoretical treatment by assuming that electrons are scattered only once within the specimen, using the so-called single scattering, or kinematic, approximation [9–11]. Most of the equations used in this section are taken from

Ref. [9].

Although the intensities in the experimental patterns usually deviate significantly from the kinematic prediction, and are better described using a dynamical theory of diffraction, the geometry exhibited by the diffraction patterns, e.g. the position of the diffracted spots or the edges of the Kikuchi lines, are almost identical to those predicted by the dynamical theory. This can be easily understood considering that both of the approaches are subject to the same principle of energy and momentum conservation [9].

The crystal potential $V(\mathbf{r})$ within a specimen is a function of the spatial position $\mathbf{r}$ and may be represented as the sum of two terms

$$V(\mathbf{r}) = V_0(\mathbf{r}) + \Delta V(\mathbf{r}) \tag{2.17}$$

where $V_0(\mathbf{r})$ is the mean potential, and $\Delta V(\mathbf{r})$ is the fluctuation of the potential within the solid specimen respectively. $\Delta V(\mathbf{r})$ is usually small, so that the kinematic approach can be used.

It is possible to have three different cases of scattering depending on the nature of $V_0$. When $V_0 = 0$ the kinematic approach to the scattering is assumed to be applicable.

Another situation is when $V_0$ is constant. It may be large so that the electrons may be scattered by the constant potential many times. Fortunately, since the diffraction effect comes from the spatial variation of the potential ($\Delta V$) the multiple scattering by a constant potential is equivalent to a re-normalization of the wavelength of the high-energy electrons [9].

A third case occurs when $V_0$ has a general form, $V_0 = V_0(\mathbf{r})$. Under specific assumptions this case can be treated kinematically, but its treatment is more complicated than the previous two, and will not be discussed here. Its treatment can be found in Ref. [9]. Due to the quantum nature of the electrons, a quantum-mechanical treatment is necessary. In this regard the electron beam can be described by a plane wave $\psi_0$ defined as:

$$\psi_0 = \exp(i\mathbf{k}_0 \cdot \mathbf{r}); \tag{2.18}$$

where $\mathbf{r}$ is the position vector and $\mathbf{k}_0$ is the wave vector having modulus $|\mathbf{k}_0| = \frac{2\pi}{\lambda}$. The wave vector depends on the energy of the electron through the wavelength, $\lambda$, which is related to the momentum of the electron as described by the de Broglie relation:

$$\lambda = \frac{h}{p} = \sqrt{\frac{h^2}{2mE}}, \tag{2.19}$$

where $h$ is the Planck constant, $p$ the classical momentum, and $m$ and $E$ the mass and the energy of the electron. This relation is valid for energy below $\approx 50$ keV. For higher energies relativistic effects have to be considered. The relativistic electron wavelength is

$$\lambda = \sqrt{\frac{h^2}{2m_0E}(1 + \frac{E}{E_0})}, \tag{2.20}$$

where $m_0$ is the rest mass of electron and $E_0 = m_0c^2 \simeq 511$ keV.

When an incident plane-wave is scattered by a crystal potential of the form of equation (2.17), the constant part of the potential, $V_0$, transforms the incident wave vector into a new wave vector, $\mathbf{k}$, which is in general complex, which is subsequently kinematically scattered due to the fluctuating part, $\Delta V$, of the potential. In this way the treatment is no different from the case when $V_0 = 0$. To distinguish between the two cases, the treatment is called kinematical and quasi-kinematical for $V_0 = 0$ and $V_0 \neq 0$ respectively.

In free space ($V(\mathbf{r}) = 0$) a plane wave of the form (2.18) is a solution of the one-body Schrödinger equation

$$\left[\frac{-\hbar^2}{2m}\nabla^2 + V(\mathbf{r})\right]\psi(\mathbf{r}) = E\psi(\mathbf{r}) \tag{2.21}$$

which can be used for describing the propagation of high energy electrons in a solid. The plane wave has a wave-vector $k_0 = \sqrt{\frac{2mE}{\hbar^2}}$.

In the crystal another possible solution of (2.21) is a spherical wave, generated at a point $\mathbf{r}'$ in the crystal,

$$G(\mathbf{r},\mathbf{r}') = -\frac{m}{2\pi\hbar^2}\frac{\exp(ik_0|\mathbf{r}-\mathbf{r}'|)}{|\mathbf{r}-\mathbf{r}'|} \tag{2.22}$$

usually called the Green's function, which satisfies the Scrödinger equation everywhere but at the point $\mathbf{r} = \mathbf{r}'$. Substituting (2.22) in (2.21), it can be seen that in the free space

$$(E + \frac{\hbar^2}{2m}\nabla^2)G(\mathbf{r},\mathbf{r}') = \delta(\mathbf{r}-\mathbf{r}') \tag{2.23}$$

where $\delta(\mathbf{r}-\mathbf{r}')$ is the Dirac delta function. Combining the previous relations and using the properties of the Dirac delta function it is possible to obtain a relation which leads to a clear and simple physical interpretation of the scattering process,

$$\psi(\mathbf{r}) = \psi_0(\mathbf{r}) + \psi_s(\mathbf{r}) = \psi_0(\mathbf{r}) + \int G(\mathbf{r},\mathbf{r}')V(\mathbf{r}')\psi(\mathbf{r}')d\mathbf{r}'. \tag{2.24}$$

For a incident plane wave (2.18), the total wave field generated is formed by two components, the incident plane wave itself $\psi_0(\mathbf{r})$, and a scattered wave field $\psi_s(\mathbf{r})$, composed of a superposition of spherical waves originating at positions $\mathbf{r}'$, whose strength corresponds to the factor $V(\mathbf{r}')\psi(\mathbf{r}')$. This is shown in Fig. 2.2.

Each Green's function in the scattering component describes the propagation of a wave originating from a point $\mathbf{r}'$ to the point $\mathbf{r}$, which travels without any further scattering event.

When the potential $V(\mathbf{r})$ is weak, i.e. when the amplitude of the scattered field is much smaller than amplitude of the incident wave field, $\psi_s(\mathbf{r}) << \psi_0(\mathbf{r})$, it is possible to replace the unknown $\psi(\mathbf{r}')$ in the second term of Eq. (2.24), with $\psi_0(\mathbf{r}')$, obtaining the so-called first (order) Born approximation, or kinematic approximation:

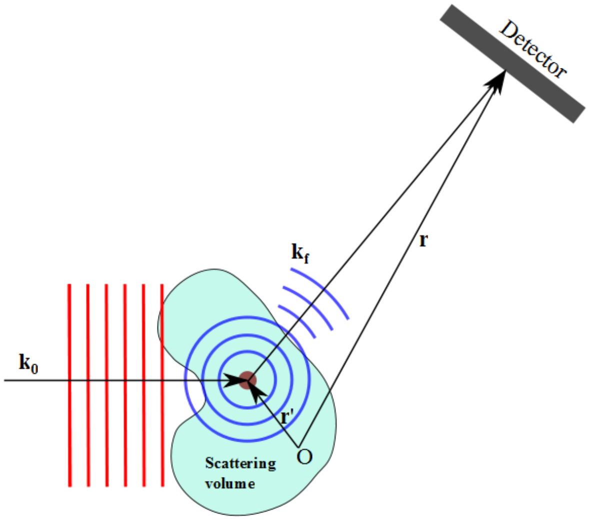

Figure 2.2: Illustration of the scattering process: incident plane wave having wavevector $\mathbf{k}_0$ and the spherical wave generated at the atomic position $\mathbf{r}'$ having wavevector $\mathbf{k}_f$. For convenience the origin of the coordinate system, **O**, is placed within the scattering volume.

$$\psi(\mathbf{r}) \approx \psi_0(\mathbf{r}) + \int G(\mathbf{r},\mathbf{r}')V(\mathbf{r}')\psi_0(\mathbf{r}')d\mathbf{r}'. \tag{2.25}$$

In the situation sketched in Fig 2.2, where the origin of the coordinate system, **O**, is assumed for convenience to be placed within the scattering volume, and where the incident plane wave is at a large distance from the specimen ($r >> r'$), it is very useful to proceed with a further approximation. When $r >> r'$, where the potential can be approximated to zero, then $|\mathbf{r}-\mathbf{r}'| \approx r$ and $k_0|\mathbf{r}-\mathbf{r}'| \approx k(r - r\cos\theta) = k_0 r - \mathbf{k}\cdot\mathbf{r}'$, $\theta$

being the angle between $\mathbf{k}$ and $\mathbf{r}'$, the Green's function can be then be approximated to

$$G(\mathbf{r},\mathbf{r}') \approx -\frac{m}{2\pi\hbar^2}\frac{\exp(ik_0 r)}{r}\exp(-i\mathbf{k}\cdot\mathbf{r}'), \tag{2.26}$$

obtaining the asymptotic form, or far-field limit of the Green's function, leading to an approximation of the total wave field

$$\psi(\mathbf{r}) \approx \psi_0(\mathbf{r}) + \frac{\exp(ik_0 r)}{r} f^{(B)}(\mathbf{k},\mathbf{k}_0), \tag{2.27}$$

where $f^{(B)}(\mathbf{k},\mathbf{k}_0)$ is the Born (or kinematic) scattering amplitude, given by

$$f^{(B)}(\mathbf{k},\mathbf{k}_0) = f^{(B)}(\mathbf{k}-\mathbf{k}_0) = -\frac{m}{2\pi\hbar^2}\int V(\mathbf{r}')\exp[-i(\mathbf{k}-\mathbf{k}_0)\cdot\mathbf{r}']d\mathbf{r}', \tag{2.28}$$

which determines the strength of the scattering and shows that it is proportional to the Fourier transform of the potential $V(\mathbf{r})$. Due to the far-field approximation the scattering amplitude is independent of the distance between target and detector, depending only on the angles to the detector from the target [9].

In the case of quasi-kinematic diffraction, when $V_0$ is constant, the solution of (2.21) can be written as $\psi_0 = \exp(i\mathbf{k}'\cdot\mathbf{r})$, where $k' = \sqrt{\frac{2m(E-V_0)}{\hbar^2}}$. Following a similar procedure used for the kinematic case and remembering that $\Delta V$ is the fluctuation part of the potential within the solid, then

$$\psi(\mathbf{r}) \approx \psi_0(\mathbf{r}) + \int G(\mathbf{r},\mathbf{r}')\Delta V(\mathbf{r}')\psi_0(\mathbf{r}')d\mathbf{r}' \tag{2.29}$$

which leads to the following equation for the total wave field

$$\psi(\mathbf{r}) \approx \psi_0(\mathbf{r}) + \frac{\exp(ik_0 r)}{r} f(\mathbf{k}, \mathbf{k}_0) \tag{2.30}$$

where

$$f(\mathbf{k}, \mathbf{k}_0) = -\frac{m}{2\pi\hbar^2} \int \Delta V(\mathbf{r}') \exp[-i(\mathbf{k} - \mathbf{k}') \cdot \mathbf{r}'] d\mathbf{r}'. \tag{2.31}$$

This last equation is similar to the one obtained for the kinematic case (2.28), but in this case $\mathbf{k}'$ differs from $\mathbf{k}$ in both magnitude and direction. In transmission diffraction experiments to a good approximation $k' \approx k$, and $\Delta V(\mathbf{r}) \approx \Delta V(\mathbf{X})$ where $\mathbf{X}$ is a vector in the two dimensional spatial coordinate of the plane normal to the incident beam direction. If $\mathbf{k}'$ is written as $\mathbf{k}' \approx \mathbf{k}_0 + i\mu\hat{\mathbf{z}}$, where $\mu$ is the mean absorption coefficient and $\hat{\mathbf{z}}$ the unit vector of the z axis perpendicular to the sample surface, an approximated expression for the scattering amplitude is obtained,

$$f(\mathbf{k}, \mathbf{k}_0) = -\frac{m}{2\pi\hbar^2} \int \Delta V(\mathbf{X}') \exp[-i(\mathbf{k} - \mathbf{k}_0) \cdot \mathbf{X}'] d\mathbf{X}' \int \exp(-\mu z) dz \tag{2.32}$$

which differs from the pure kinematic case since the intensity of the incident beam is no longer constant, but it is attenuated due to the effect of the inelastic scattering [9, 12, 13].

### 2.3.1 Scattering by a single infinite crystal and geometrical interpretation

From the previous section it can be seen that at large distances from the specimen, the intensity of the scattered wave is proportional to the amplitude of the scattering $f(\mathbf{k}, \mathbf{k}_0)$. When the kinematic approximation is applied, this amplitude reduces to the Born scattering amplitude, which is simply equal to the Fourier transform of the potential $V(\mathbf{r})$.

In the case of elastic scattering by a single atom, the amplitude of the scattering can be related to the electron atomic scattering factor, tabulated in the International Tables for Crystallography [14]. Additionally, there are a number of parametrizations which allow the calculation of the atomic scattering factor of the form

$$f^{(e)}(s) = \sum_{j=1}^{n} a_j \exp(-b_j s^2), \tag{2.33}$$

where $s = \frac{\sin\theta}{\lambda}$, $2\theta$ is the scattering angle, and $a_j$ and $b_j$ are the fitting parameters [15–18].

The scattering factor is typically largest in the forward scattering direction. Usually the magnitude of the momentum transferred in the direction of the incidence beam is small. The process of propagation of electrons in the specimen is not very sensitive to the variation of the potential in the incident direction. In general the kinematic approximation breaks down when the distance from the centre of the atom is very small [9].

In the case of single crystals, which consist of the repetition in three dimensional space of identical unit cells, the potential of the entire crystal is the sum of the potential of the unit cell $\phi(\mathbf{r})$, summed over all unit cells translated in different directions. This can be written $V(\mathbf{r}) = \phi(\mathbf{r}) * L(\mathbf{r})$, where the symbol $*$ indicates the operation of the convolution product. The convolution product $C(\mathbf{r})$ of two functions $f(\mathbf{r})$ and $g(\mathbf{r})$ is defined by

$$C(\mathbf{r}) \equiv f(\mathbf{r}) * g(\mathbf{r}) = \int f(\mathbf{R}) g(\mathbf{r} - \mathbf{R}) d\mathbf{R}. \tag{2.34}$$

As stated previously, the amplitude of the scattered waves is proportional to the

Fourier transform [19] (indicated with the symbol $\mathscr{F}$) of the crystal potential, so that

$$\begin{aligned} f(\mathbf{q}) &= \mathscr{F}\{\phi(\mathbf{r}) * L(\mathbf{r})\} = \mathscr{F}\{\phi(\mathbf{r})\} \times \mathscr{F}\{L(\mathbf{r})\} && (2.35) \\ &= \frac{1}{\Omega} F(\mathbf{q}) \sum_{g} \delta(\mathbf{q} - \mathbf{g}) && (2.36) \end{aligned}$$

where $\Omega$ is the volume of the unit cell, $F(\mathbf{q})$ is the amplitude of the wave scattered by the unit cell, $\delta$ is the Dirac delta function, and $\mathbf{g}$ a reciprocal lattice vector. The term $F(\mathbf{q})$ is called the structure factor, which can be written as

$$F(\mathbf{q}) = \sum_{j=1}^{N} f_j^{(e)}(s) \exp(-i\mathbf{q} \cdot \mathbf{r}_j). \tag{2.37}$$

It is possible that for a specific set of Miller indices, the exponential part of Eq. (2.37) is zero, independently of the atomic scattering factor, so that the intensity of the diffracted beam is zero. When this happens the reflection is said to be kinematically forbidden.

If the Fourier coefficient of the electrostatic potential is defined as

$$V_{\mathbf{g}} \equiv \frac{1}{\Omega} \sum_{j=1}^{N} f_j^{(e)}(s) \exp(-i\mathbf{q} \cdot \mathbf{r}_j) \tag{2.38}$$

where the summation is extended to all atom positions within the unit cell, the Fourier transform of the potential can be written as

$$V(\mathbf{q}) = \sum_{g} V_{\mathbf{g}} \delta(\mathbf{q} - \mathbf{g}) \tag{2.39}$$

where $q = 4\pi s$, and $f_j^{(e)}(s)$ can be calculated using the relation (2.33).

As shown previously in Eq. (2.16), a diffraction vector $\mathbf{g}_{hkl}$ is perpendicular to the set of lattice planes characterized by the Miller indices $(hkl)$, so Eq. (2.35) can be interpreted by saying that in the kinematic approximation the diffracted amplitude is non-zero only when the change in the momentum $\mathbf{q}$ coincides with one of the reciprocal lattice vector $\mathbf{g}_{hkl} = h\mathbf{a}^* + k\mathbf{b}^* + l\mathbf{c}^*$, which is the so-called Laue condition. It is also possible to interpret the diffraction in an another (equivalent) way, as shown in Fig. 2.3, proposed by Bragg: If $\theta$ is the angle that the incident wave forms with a plane $(hkl)$, then the difference in the path length (highlighted in green in the figure) from waves scattered by two successive planes is $2d_{hkl}\sin\theta$, where $d_{hkl}$ is the lattice spacing between planes.

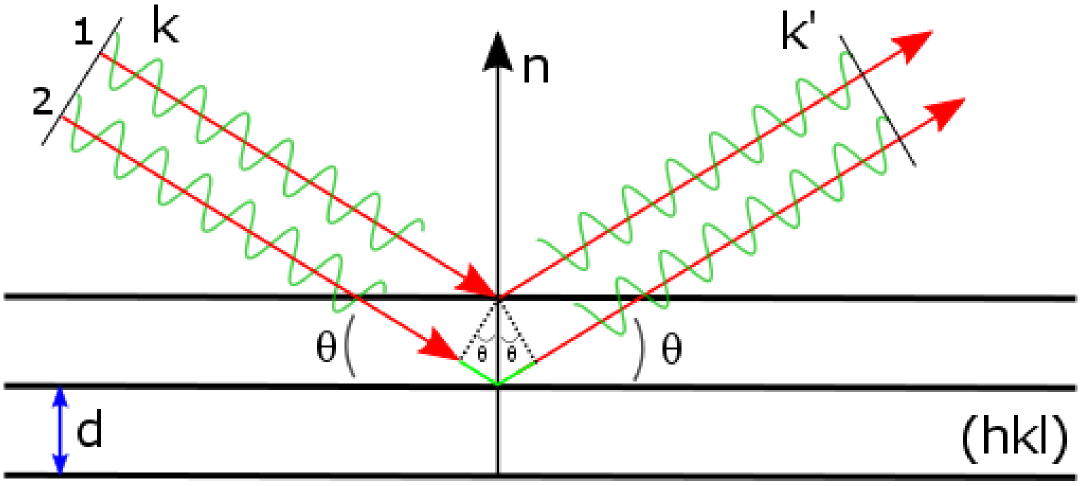

Figure 2.3: Illustration of the Bragg scattering process.

The constructive interference occurs when the difference in the path length is an integer multiple of the wavelength of the incidence wave

$$2d_{hkl}\sin\theta = n\lambda \tag{2.40}$$

which is the so-called Bragg law. The angle which satisfies this relation is called the Bragg angle. An easy geometrical interpretation of the diffraction process can be seen by using the Ewald sphere as shown in Fig. 2.4.

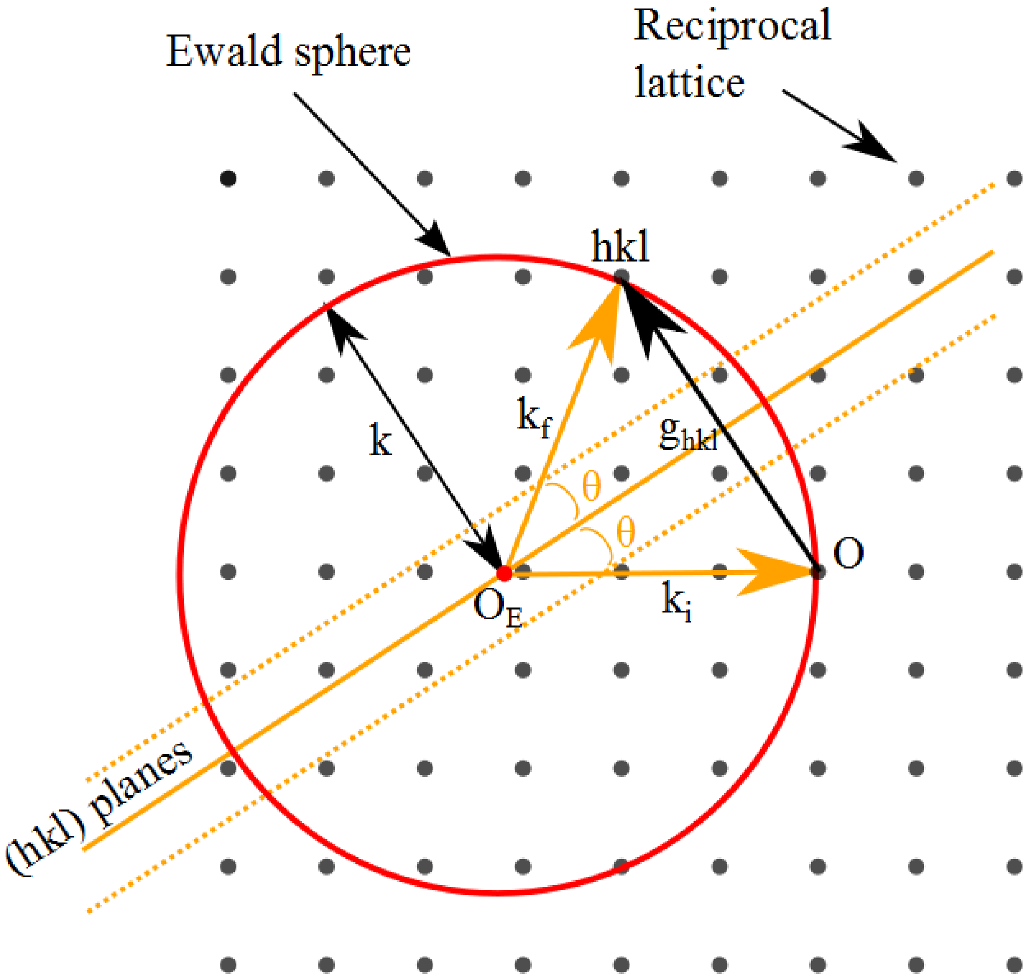

Figure 2.4: Geometrical interpretation of the scattering process using the Ewald sphere construction.

Because of the conservation of energy in elastic scattering, all scattered waves $\mathbf{k}_f$ have to have a length equal to the length of the incident beam $\mathbf{k}_i$, which has its tip pointing to the origin of reciprocal lattice space, indicated with $O$, and a length corresponding to $|\mathbf{k}_i| = \frac{2\pi}{\lambda}$. Geometrically this means that all scattered wave vectors lie on a sphere centred at the origin of the $\mathbf{k}_i$ vector, being the origin of the Ewald sphere, indicated with $O_E$ in Fig. 2.4.

Because of the conservation of momentum, the difference between the incident and scattered wave vectors has to be equal to one of the reciprocal lattice vectors, that is $\mathbf{k}_f - \mathbf{k}_i = \mathbf{g}$. A compact equation of the Ewald sphere can be obtained considering $(\mathbf{g} + \mathbf{k}) \cdot (\mathbf{g} + \mathbf{k}) = \frac{4\pi^2}{\lambda^2}$, so that

$$\mathbf{g} \cdot (2\mathbf{k} + \mathbf{g}) = 0 \tag{2.41}$$

which shows also that the bisector plane of $\mathbf{g}$ contains the vector $\mathbf{k}+\mathbf{k}'$. This relation will appear again when the deviation parameter is discussed.

### 2.3.2 High order Laue zone rings

A feature often observable in diffraction patterns are the high order Laue zone (HOLZ) rings. They can provide precise information on the interplanar distance, and thus provide information about the lattice parameters. The HOLZ rings are determined by the intersection of the Ewald sphere with the reciprocal lattice when the incidence beam direction, $[uvw]$, is parallel to one of the zone axes, as shown in Fig. 2.5.

The equation which satisfies this condition is

$$hu + kv + lw = n \tag{2.42}$$

where $hkl$ are the coordinate of the allowed reflectors, and $n$ is an integer which specifies the order of the Laue zone.

For $n = 0$, $n = 1$, $n = 2$, the rings are called the zero order Laue zone (ZOLZ), the

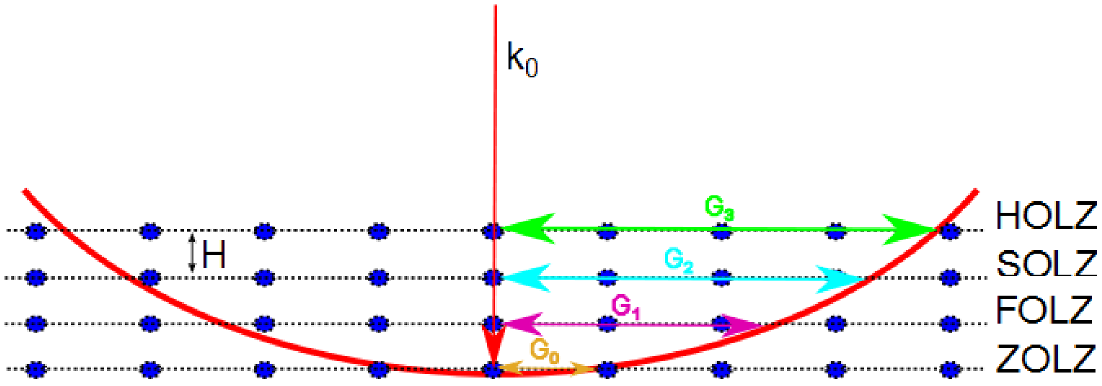

Figure 2.5: Geometrical interpretation of HOLZ rings.

first order Laue zone (FOLZ) and the second order Laue zone (SOLZ) respectively. For larger order they are called high order Laue zone (HOLZ).

The radius of the HOLZ rings, $G_n$, where the subscript $n$ refers to the order of the Laue zone, is related to the interplanar spacing in reciprocal space, $H$, parallel to the beam direction and to the electron wavelength $\lambda$ which defines the radius of the Ewald sphere. This relation is

$$G_n = \left(\frac{4n\pi H}{\lambda}\right)^{\frac{1}{2}}. \tag{2.43}$$

Both $G_n$ and $H$ are in reciprocal-space units ($\mathrm{m}^{-1}$). The radius of the HOLZ ring can be easily measured on the diffraction patterns. Experimentally diffraction patterns are recorded as a gnomonic projection on the detector screen [20]. If the projection parameters such as the camera length (the specimen to the detector distance) and the centre of the projection centre are known, HOLZ rings can be used to measure the lattice parameters [6, 20].

The radius of the HOLZ rings can be linked to the interplanar spacing in real space through:

$$\frac{1}{H} = \left(\frac{4n\pi}{\lambda}\right)\left(\frac{1}{G_n}\right)^2 \tag{2.44}$$

For transmission experiments, if the camera length $L$ is known, then

$$\frac{1}{H} = \left(\frac{4n\pi}{\lambda}\right)\left(\frac{\lambda L}{r_n}\right)^2 = 4n\pi\lambda\left(\frac{L}{r_n}\right)^2 \tag{2.45}$$

where $r_n$ is the measured radius of the HOLZ rings in the diffraction pattern.

### 2.3.3 Scattering from a crystal having a finite size

When the electrons are scattered within a limited region of the crystal (volume/area) both intensities and shapes of the diffraction features, e.g. diffraction spots or streaks in the case of RHEED patterns, may be influenced by the finite size of the region contributing to the diffraction.

It is useful to introduce the so-called shape function [4], $D(\mathbf{r})$, defined as

$$D(\mathbf{r}) = \begin{cases} 1 & \text{inside the crystal} \\ 0 & \text{outside the crystal} \end{cases}$$

The crystal potential $V_f(\mathbf{r})$, generated by the atoms in the solid, becomes the product of the crystal potential times the shape function: $V_f(\mathbf{r}) = V(\mathbf{r})D(\mathbf{r})$.

Using the properties of the Fourier transform and Eq. (2.39) the finite potential can be written as

$$V_f(\mathbf{q}) = \sum_{\mathbf{g}} V_{\mathbf{g}} D(\mathbf{q} - \mathbf{g}). \tag{2.46}$$

Although similar to Eq.(2.39), the effect of the finite size of the crystal introduces a shape in reciprocal space. By calculating for example the shape function, also known as the shape amplitude, in reciprocal space for a planar thin foil having a thickness $z_0$, having its normal parallel to the z-axis, it can be seen that

$$\begin{aligned} D(\mathbf{q}) &= \int_{-\infty}^{+\infty} e^{-2\pi i q_x x} dx \int_{-\infty}^{+\infty} e^{-2\pi i q_y y} dy \int_{-\infty}^{+\infty} e^{-2\pi i q_z z} dz && (2.47) \\ &= -\delta(q_x)\delta(q_y)\left[\frac{e^{-2\pi i q_z z}}{2\pi i q_z}\right]_{-z_0/2}^{z_0/2} && (2.48) \\ &= z_0\delta(q_x)\delta(q_y)\frac{\sin(\pi q_z z_0)}{\pi q_z z_0} && (2.49) \end{aligned}$$

which is shown in Fig. 2.6. The red and blue lines show the trend of the $D(q)$ and $D^2$(q) functions respectively.

The use of a finite crystal size is necessary in many diffraction experiments because the electron beam probes only a limited volume/area of the sample, so that the shape function depends substantially on the shape of the electron probe and its projection on the sample. This has an important consequence in terms of the Bragg condition. As seen from the previous section, with an infinite crystal size the Bragg condition is only satisfied for mathematical points (which make the event highly improbable) of the reciprocal lattice which lie on the Ewald sphere; however for a finite crystal size a scattering event becomes more probable because it extends the size of the reciprocal lattice point, so that the reciprocal lattice point is no longer a mathematical point, but it occupies a finite volume in reciprocal lattice space.

### 2.3.4 The deviation parameter

As already seen in the previous section, even if the Bragg condition is not exactly satisfied, diffraction can still occur, and for this reason it is common to use the so-

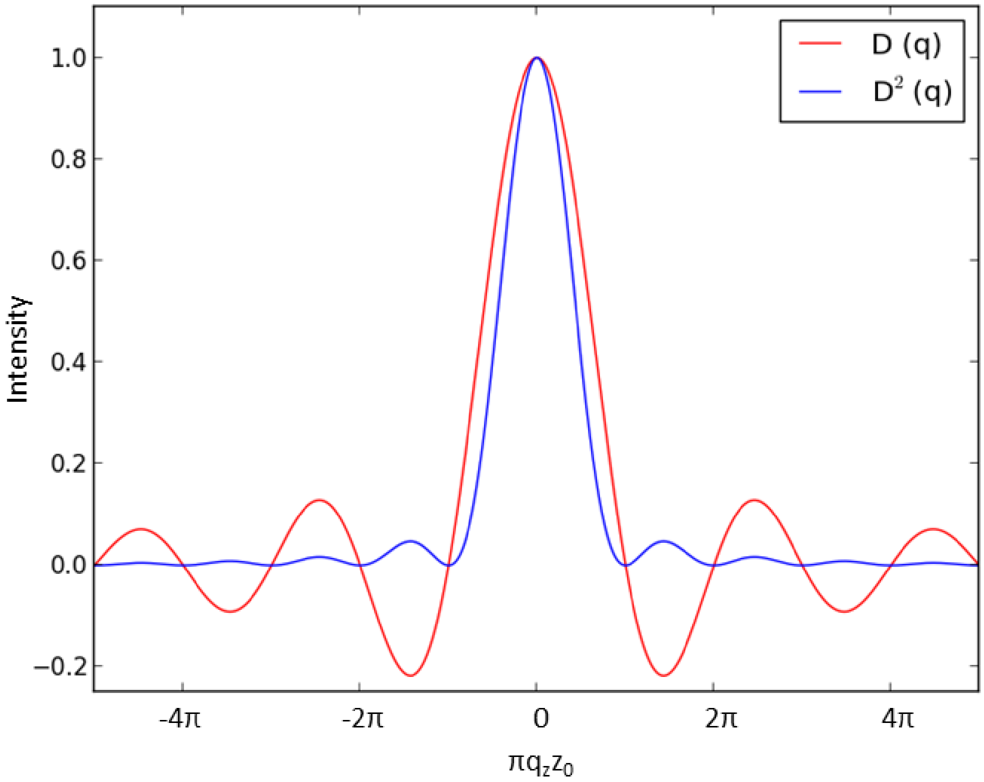

Figure 2.6: Reciprocal shape functions $D$ and $D^2$ for a thin foil having thickness $z_0$.

called the deviation parameter, $\mathbf{s_g}$, also called the excitation error, to quantify this deviation from the exact Bragg condition, as shown in Fig. 2.7.

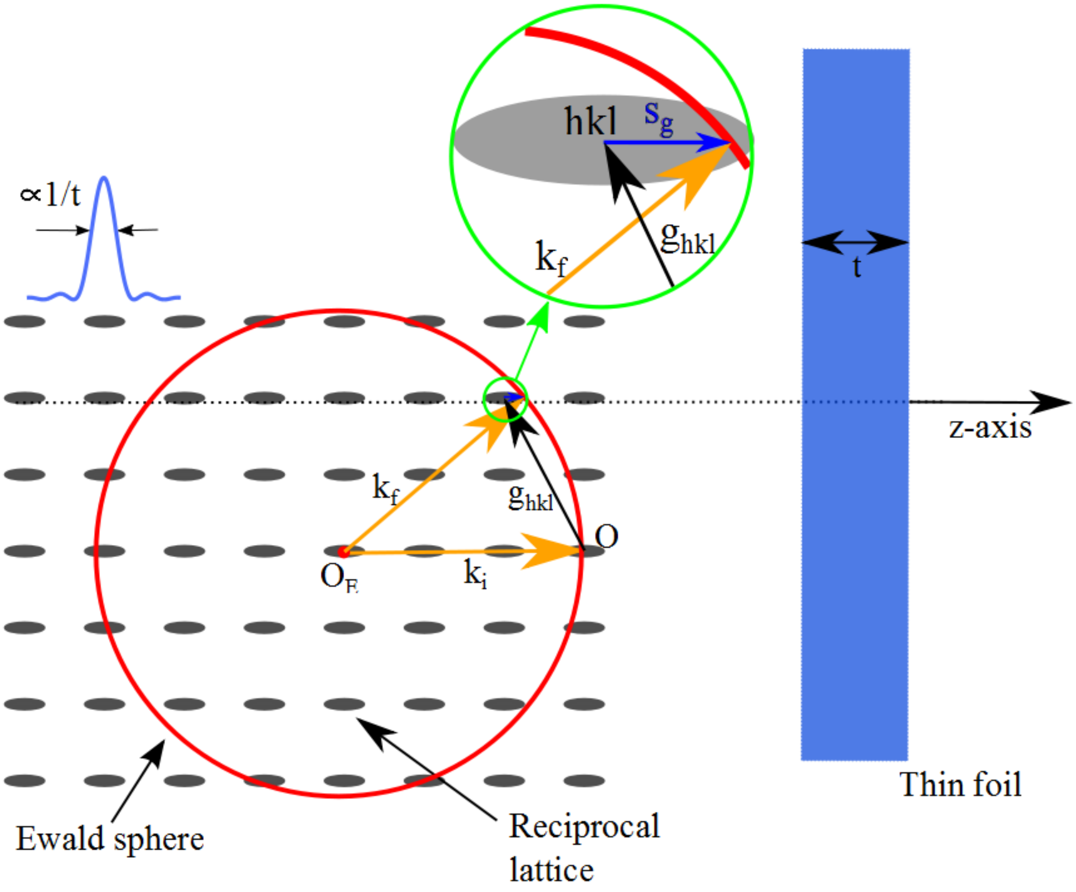

Figure 2.7: Geometrical interpretation of the deviation parameter. The green circular inset is used to show in more detail the geometrical relationship between the Ewald sphere and the vectors $\mathbf{k_f}$, $\mathbf{g}_{hkl}$ and $\mathbf{s_g}$.

In the previous section the equation of the Ewald sphere (Eq. 2.41) was obtained; now a similar expression for the deviation parameter can be obtained. The vector $\mathbf{k} + \mathbf{g}_{hkl} + \mathbf{s}$ must lie on the Ewald sphere, so

$$(\mathbf{g}_{hkl} + \mathbf{s}) \cdot (2\mathbf{k} + \mathbf{g}_{hkl} + \mathbf{s}) = 0, \tag{2.50}$$

which can be rewritten as

$$2(\mathbf{k}+\mathbf{g}_{hkl})\cdot\mathbf{s}+s^2=-\mathbf{g}_{hkl}\cdot(2\mathbf{k}+\mathbf{g}_{hkl}). \tag{2.51}$$

It can be seen the equation of the Ewald sphere (Eq. 2.41) appears on the right-side of this equation. If the angle between the foil normal and the vector $\mathbf{k}+\mathbf{g}_{hkl}$ is denoted with $\alpha$ then

$$s+\frac{s^2}{2|\mathbf{k}+\mathbf{g}_{hkl}|\cos\alpha}=\frac{-\mathbf{g}_{hkl}\cdot(2\mathbf{k}+\mathbf{g}_{hkl})}{2|\mathbf{k}+\mathbf{g}_{hkl}|\cos\alpha}\equiv s_{\mathbf{g}} \tag{2.52}$$

which will be used as the definition of $s_{\mathbf{g}}$, the deviation parameter.

From the previous equation it can be seen that the deviation parameter is positive when a lattice point $\mathbf{g}_{hkl}$ lies inside the Ewald sphere, negative when it is outside the Ewald sphere; considering that $\mathbf{k_f}-\mathbf{k_i}=\mathbf{g}_{hkl}+\mathbf{s_g}$, where $\mathbf{s_g}=s_{\mathbf{g}}\hat{z}$, it is clear that when $\mathbf{s_g}$ is zero the Bragg condition is exactly satisfied.

The deviation parameter is determined by the orientation of the incidence beam with respect to the crystal, and so it is an experimental parameter controlled by the operator. It is of fundamental importance in electron diffraction because most of the diffraction intensities depend on this parameter, in both transmission and backscattering geometries.

### 2.3.5 Kikuchi lines

Kikuchi diffraction is a special type of diffraction [21–25]. The coherent diffraction discussed in the previous sections assumed a parallel incident beam incident on a crystalline material. In this case the Ewald sphere is intercepting the reciprocal lattice at certain points creating a diffraction pattern composed, in the case of monocrystalline materials, of diffraction spots visible in transmission electron diffraction. Often in addition to the coherent diffraction, especially in relatively thick samples, the incoherent scattering of the primary beam with the sample, not necessarily inelastic, occurs, generating a distribution of the electrons, whose direction is randomized [26].

Electrons in this category are usually called diffusely scattered electrons [6, 27], and are the protagonists of the Kikuchi diffraction. The energy lost in this type of incoherent interactions is of the order of few tens of electron volts or less [6, 27]. When this energy is compared to the energy of the primary beam, it is possible to assume that these electrons have the same wavelength as the electrons of the incident beam. This assumption is reasonable when the sample is not very thick. If the specimen is significantly thick the inelastic processes would be predominant, destroying the information contained in both the Kikuchi diffraction and the Bragg diffraction. For relatively thin samples the coherent diffraction is predominant since the electrons would have less probability of being incoherently scattered [6, 28].

The Kikuchi diffraction takes place in the following way. Consider a family of lattice planes, as shown in Fig. 2.8(a); these will be characterized by a specific vector in reciprocal space $\mathbf{g_{hkl}}$. In the figure it is possible to see that any electron incident with a Bragg angle, $\theta_\mathbf{B}$, on the crystal plane, or alternately by an angle of (90°-$\theta_\mathbf{B}$) with respect to the vector $\mathbf{g_{hkl}}$(or $-\mathbf{g_{hkl}}$), is diffracted coherently (Bragg) from the lattice plane. It is possible to immediately notice that the family of directions that satisfy this condition lies on the cones obtained by rotating the yellow and green rays shown in Fig. 2.8(a) around the vector $\mathbf{g_{hkl}}$; the resulting cones are usually called Kossel cones [29] (since these were first observed in the context of X-ray diffraction [30–34]).

Kossel cones are shown in Fig. 2.8(b), which furthermore shows how the Kikuchi lines are formed by the intersection of the Kossel cones with a plane, in this case

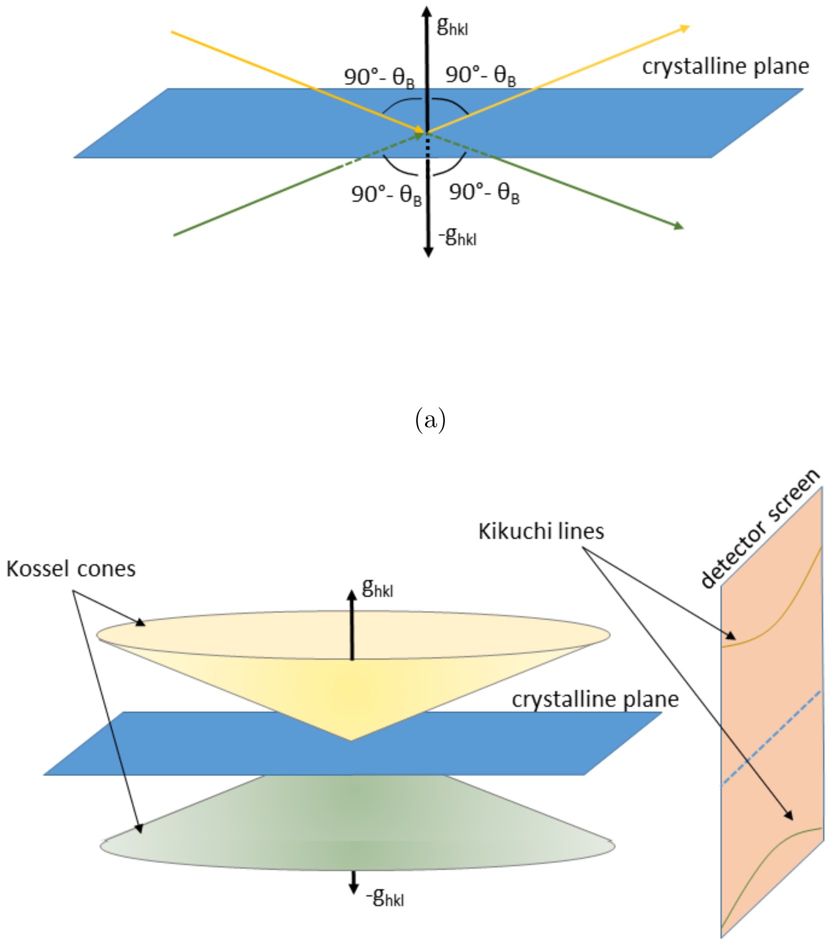

(a)

(b)

Figure 2.8: Illustration showing Kikuchi line formation (not in scale); (a) few single Bragg reflections from the set of crystalline planes characterized by the $\mathbf{g_{hkl}}$ reciprocal vector, and (b) the intersection of Kossel cones with the detector screen forming the Kikuchi lines.

the detector screen. Intersection of a cone with a plane is a hyperbola; however, since the angle involved in the Bragg diffraction are small, typically on the order of a degree or less depending on the energy, the hyperbolas appear effectively as lines on the screen, and are referred to as *Kikuchi lines*.

A particular feature of the Kikuchi lines is that unlike the diffraction spots these Kossel cones are basically fixed to the lattice plane from which they are formed, which means that on rotating the crystal the cones rotate with it; this allows a more precise orientation of the crystal with respect to what can be obtained with the diffraction spots [6].

As already mentioned, the incoherent interaction creates a range of electron directions in the crystal; this implies that there will always be electrons satisfying the Bragg condition for any family of crystal planes in the crystal, i.e. there will be two Kossel cones for each family of crystalline planes. The geometric arrangement of the Kossel cones and thus the Kikuchi lines on the screen, reflect the crystal structure of the specimen and orientation of the crystal.

Kikuchi lines are visible in different experimental geometries that will be discussed in this thesis, for example, in transmission, in reflection and in backscattering geometries.

## 2.4 Indexing parallel beam diffraction patterns

As mentioned in section 2.3.1, when the Ewald sphere intercepts points in the reciprocal lattice diffraction may occur. In a single crystal the diffraction spots visible on the detector screen can be used in a number of ways, depending on what is already known about the specimen, for example to obtain information such as crystal type, crystal orientation with respect to the beam or with respect to other areas of the sample etc. The indexing, that is the identification of the diffraction spots in the diffraction pattern, is relatively easy when the direction of the incident electron beam is parallel to a major zone axis, because in this case the symmetry of the crystal is more evident. If the beam is not directed along a major zone axis, manual indexing can be laborious and is usually done using a computational approach which is described below [4, 6].

In order to explain the indexing procedure in a simple manner a cubic system is used as a reference.

Figure 2.9(a) shows the fundamental relationship between the measure of the distance between the direct beam and a diffracted beam on the screen, $R$, and the lattice spacing of the diffracting planes, $d$.

It is possible to note that the product between $R$ and $d$ is constant and equal to $\lambda L$

$$Rd = \lambda L, \tag{2.53}$$

where $\lambda$ is the wavelength of the incident beam and $L$ is the distance between the specimen and the detector screen. Equation 2.53 is easily obtained considering that (see Fig. 2.9(a))

$$\frac{R}{L} = \tan 2\theta \approx 2\theta \tag{2.54}$$

$$\frac{\lambda}{d} = 2\sin\theta \approx 2\theta \text{ (Bragg's law)} \tag{2.55}$$

$$\frac{R}{L} = \frac{\lambda}{d}. \tag{2.56}$$

Since $\lambda L$ is constant, the different values of $R$ are related to each other by

$$R_1 d_1 = R_2 d_2 = R_3 d_3 = \ldots \tag{2.57}$$

and the ratio of any two values of $R$ is equal to the inverse ratio of the lattice spacings:

$$\frac{R_1}{R_2} = \frac{d_2}{d_1} \tag{2.58}$$

If the lattice parameters and the allowed reflections are known, only certain d-spacings can be associated with the diffraction spots visible in the diffraction patterns, see Fig. 2.9(b).

Once two or more diffraction spots are tentatively identified, it is necessary to cross-check if the angles between the identified diffraction spots match.

Once two non-collinear points are indexed in the diffraction pattern, all the other diffraction spots can be obtained by linear combination of the first two, as long as the diffraction spots belong to the ZOLZ. In this regard the Weiss zone law can be used to check the consistency of the indexing since each reflection $hkl$ must lie on the $[UVW]$ zone, that is $hU + kV + lW = 0$.

Once two reciprocal lattice vectors $\mathbf{g_1}$ and $\mathbf{g_2}$ are identified, the beam direction, $\mathbf{B}$, can be calculated through the cross product of two vectors

$$\mathbf{B} = \mathbf{g_1} \times \mathbf{g_2}. \tag{2.59}$$

## 2.5 Consideration of the dynamical theory of diffraction

There are a number of experimental conditions for which a kinematic treatment of the scattering is not sufficient to describe the rich variety of features observable in diffraction patterns. This is due to the limitation of the assumption that an electron

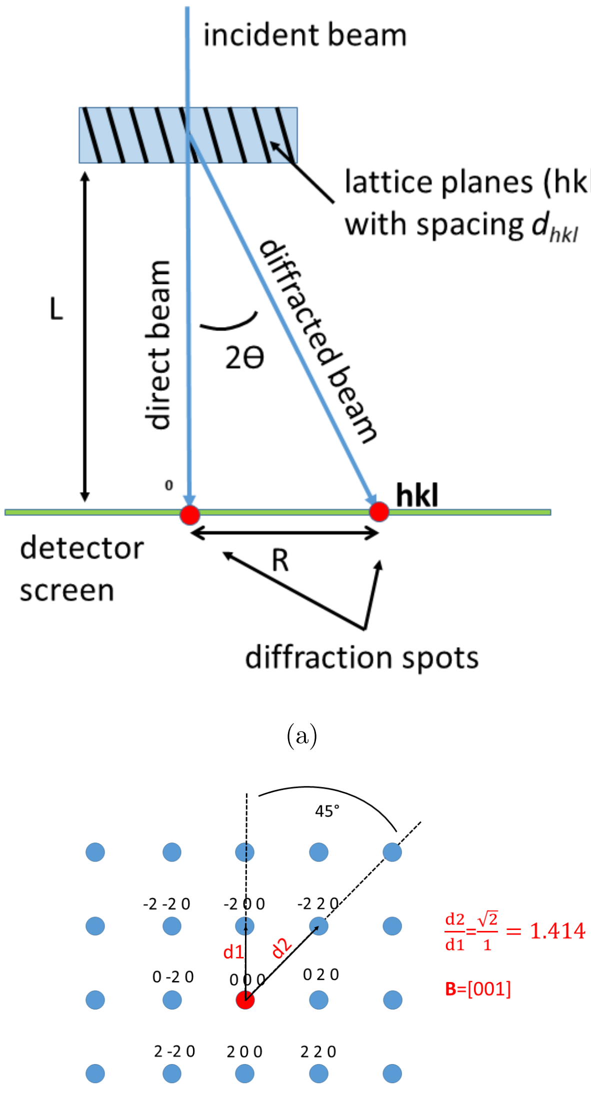

(a)

(b)

Figure 2.9: Indexing of a diffraction pattern, (a) relationship between lattice spacing and its measurement on the detector screen and (b) relationship between the diffraction spots in the diffraction pattern in a cubic crystal when the beam is parallel to the **B**=[001] direction.

is scattered only once, which is not generally true.

The dynamical theory of diffraction takes into account multi-scattering events, i.e., the electron can be scattered more than once along its path [9,35,36]. It allows also the treatment of the inelastic processes by adding an imaginary part to the crystal potential, which results in attenuation of the diffracted intensities due to the inelastic, incoherent interaction of the electrons within the sample. This results in the wave function of the high energy electrons inside the crystal being influenced by the periodic potential energy originating from the periodicity of the atoms in the crystal.

There are several equivalent approaches to the problem of dynamical electron scattering. Usually the choice of one method rather than another depends on how well a specific method suits a specific problem. Mathematically speaking this choice differs in the use of different orthogonal basis functions. There are two commonly used approaches.

The Howie-Whelan equation [11, 37–39] uses a "beam representation", $\{\phi(\mathbf{g})\}$, which are plane wave states for the electron, and is often used for the simulation of the contrast generated by crystalline defects, or by general strain fields in the crystal, where the variation in the amplitude of a diffracted beam is studied as function of depth in the crystal. This is particularly suitable for those who are interested in the directions of the beams when the electrons leave the crystal, giving less consideration to how the electrons propagate inside the crystal.

The Bloch wave approach [35,40–42], which uses Bloch functions, $\{\psi(\mathbf{r})\}$, gives a better description of how the electrons travel inside the crystal, which wave vectors are allowed inside the crystal, and the relation between the wave vector and the energy (dispersion relation), which is closely related to the problem of determining the band-structure of a crystal. This last approach is typically used for the simulation of EBSD and ECP patterns and is the one that will be described in more detail in section 3.4.3.

In both cases what is important is that the amplitude of a scattered high energy electron beam will be transferred back and forth, and so ”dynamically”, between the diffracted and forward-scattered directions. When the Bragg condition is precisely satisfied, i.e. when the deviation parameter is zero, the physical length over which this periodic transfer of amplitude occurs is called the “extinction distance”,

$$\xi_{\mathbf{g}} = \frac{\pi V_c \cos\theta_B}{\lambda F_{\mathbf{g}}} \tag{2.60}$$

which depends on the lattice parameters, through the volume of the unit cell $V_c$, on the energy of the electrons, through $\lambda$, on the structure factor $F_{\mathbf{g}}$ of the specific reflection, and on the Bragg angle $\theta_B$. This parameter is very important and may be used to explain the source of different types of contrast in both diffraction patterns and micrographs. One of the effects related to this parameter can be seen in section 3.4.2, when a discuss about the range of wavelengths contributing to the formation of EBSD patterns will be given.

The origin of the extinction distance arises from the slightly different balance of the kinetic and potential energy of the wave vectors travelling through the crystal, depending on how they overlap the atomic position. This asymmetry will result in some cases in the interference of waves with each other, or a different absorption depending on their path. As shown later, this is the origin of the contrast reversal effect in EBSD patterns discussed in section 5.1.3.

A more detailed discussion of the dynamical theory of diffraction can be found in Ref. [4, 6, 9, 43] where the computational methods are also described.

# Chapter 3

# Experimental methods

This chapter provides a brief introduction to the most common electron-based imaging and scattering modes which are relevant in the context of this thesis. This chapter will be also useful for clarifying the terminology that will be used in the following chapters and for placing the present work in a wider context.

## 3.1 Introduction

Electron microscopy [44] is based on the use of an electron beam to create some sort of image from a specimen. Depending on a number of specifications such as the sample geometry, the type of electron beam illumination, the type of signal collected, etc., various imaging modes can be exploited [45].

There are many types of electron microscopes through which several techniques are exploited. The two main types of microscope in which most of the techniques can be used are the transmission electron microscope (TEM) [4, 6, 28] and the scanning electron microscope (SEM) [27, 45, 46].

Although the experimental results described in this thesis are all obtained in the

SEM this chapter gives also an overview of a few important imaging modes of TEM, which are in some way relevant in the context of this thesis.

TEM and SEM are complementary to each other, and, over time, techniques originally implemented in one type of microscope have been implemented for the other type and vice versa. Examples are the use of transmitted electrons in the SEM for bright and dark field imaging, or the use of backscattered electrons and secondary electrons in the TEM [6, 27, 45].

Typically the spatial resolution of a TEM is one order of magnitude higher than a SEM; it is in the sub-nanometer range for a TEM and in the nanometer range for the SEM, depending on the imaging mode. A TEM operates at much higher accelerating voltages, typically in the range of 40-400 keV (or higher), while a SEM usually operates in the range of 0-30 keV. In a TEM the energy has to be high because the image is typically formed by collecting the electrons transmitted through the specimen; the specimen has to be very thin, electron-transparent (typically less than 100 nm in order to be electron transparent). Specimens used in the SEM are often bulk materials.

The electron column is conceptually the same for both microscopes, even if differences exist [45]. The electron beam is generated by a source that is located at the head of a column. High quality electron guns produce electrons with a small spatial volume and small angular spread [27, 46]. Thermionic emitters such as tungsten filament and $LaB_6$ are common. Field emission guns (FEGs) with higher resolution are slowly replacing the thermionic emitters due to their high brightness, long-term stability and lifetime [27, 46]. Both microscopes operate under ultra high vacuum conditions [6, 45].

A series of electromagnetic lenses is used to reduce the diameter of the electron beam and to focus it on the sample. The SEM column contains scanning coils which allow the beam to be scanned over the surface of the sample. This system can be also found in TEMs designated for scanning transmission electron microscopy (STEM).

TEM has an important imaging system placed between the specimen and the detector system. This is composed of lenses and apertures which are used to both deflect and select the electrons from the specimen to a detector of some sort (typically a phosphor screen for traditional imaging modes). This is also used to select specific imaging modes. One of these lenses, the objective lens, is often considered the heart of a TEM. A SEM is not provided with such a system, and no lenses are used after the specimen.

## 3.2 Important TEM imaging and diffraction modes

When a parallel electron beam hits a specimen, assumed for convenience to be crystalline, a fraction of the electrons proceed without suffering any deflection from the original direction, another fraction is instead diffracted, as illustrated in Fig. 3.1.

The transmitted beam goes through the objective lens; it passes through the point A in the back focal plane of the objective lens, and it ends in the image plane where the image is formed. In a similar way any other diffracted beam forms a diffraction spot B in the back focal plane and then reaches the image plane, where it overlaps with the image formed by the direct beam.

The system of lenses in the TEM allows the viewing screen to display either the diffraction pattern on the back focal plane of the objective lens or the image of the sample in the image plane of the objective lens. These are called the *diffraction mode* and *imaging mode* respectively.

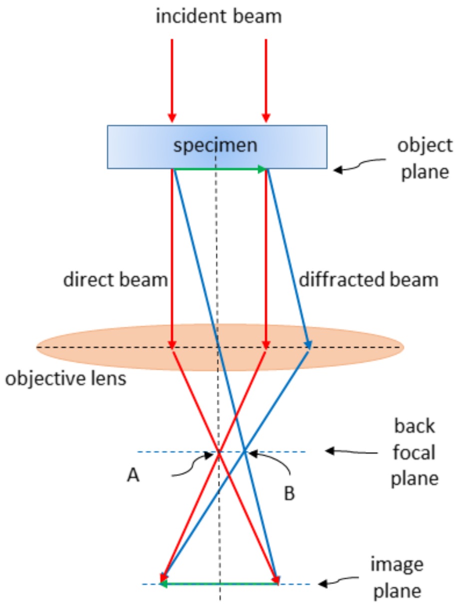

Figure 3.1: TEM image formation. Reproduced from [6].

### 3.2.1 Bright and dark field imaging

A TEM image can be obtained by either using the direct beam and the diffracted beams together, or by selecting only specific beams and blocking all the others. This allows the definition of two important modes in TEM: *bright field* and *dark field* imaging. In bright field imaging only the direct beam is used to form the image. In dark field imaging any of the diffracted beams is used to form the image. To accomplish this task an aperture, called an *objective aperture*, is placed on the back focal plane of the objective lens, and it is adjusted to select the specific beam (or beams) to form the image; this is shown in Fig. 3.2.

### 3.2.2 Contrast mechanisms

TEM images, in both bright or dark field mode, can show a variety of contrast mechanisms [6].

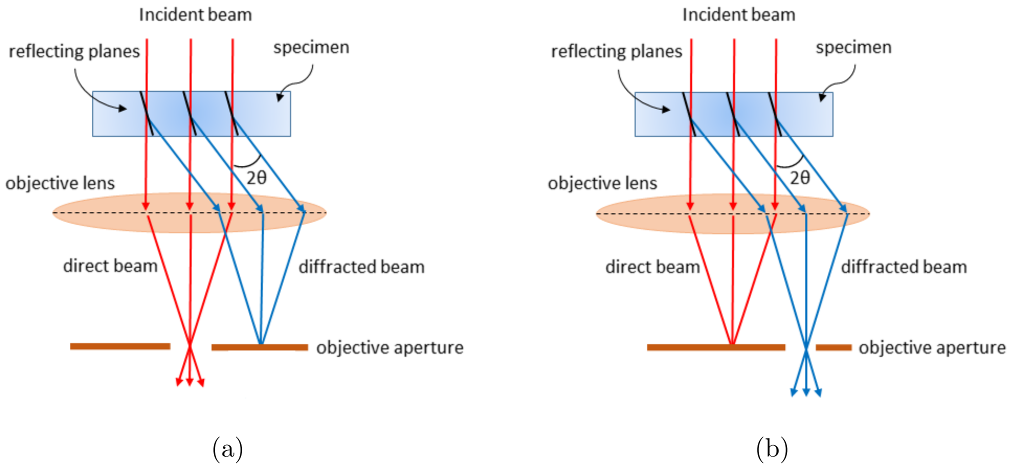

Figure 3.2: Illustration of (a) bright field and (b) dark field imaging modes. Reproduced from [6].

*Amplitude contrast* may result from the variation of mass and/or thickness in the specimen. The contrast mechanism is based on the absorption of electrons by the specimen; in bright field imaging for example thicker regions of the specimen will appear darker, whilst regions with voids or less material will appear brighter, due to the different absorption of electrons in the two regions.

*Atomic number contrast*, or *Z contrast* may arise from the incoherent elastic scattering, i.e. Rutherford scattering [47–49], of electrons. The Rutherford scattering cross section is a strong function of the atomic number, $Z$; this allows the differentiation of regions of different composition in the specimen.

An important form of amplitude contrast, especially for crystalline materials, is the *diffraction contrast* which allows variation in the crystal orientation in a crystalline specimen to be revealed [6, 28, 38]. In crystalline materials the intensity of the direct beam is reduced in areas where the direction of the incident beam satisfies (or approaches) the Bragg condition for a particular family of crystal planes; thus areas of the specimen with different crystal orientations can be revealed. Since this contrast depends on the angle at which the beam is incident on the sample, it is possible to orient the sample to select suitable diffraction conditions to highlight the desired details of a microstructure. This is very useful for example in the identification of lattice defects in crystals. By selecting the orientation of the sample, it is possible not just to determine the position of defects but also to determine their type. By orienting the sample so that one particular plane is only slightly tilted away from the strongest diffracting angle, any distortion of the crystal plane will produce particularly strong contrast variations [6, 50].

*Phase contrast* may also be observed whenever two or more beams contribute to the image, interfering with each other. The interference due to a difference in the phase of the electron waves is manifested as an intensity variation in the image. This type of contrast can be difficult to interpret and it is very sensitive to many factors such as the thickness, the orientation of the sample, focus, astigmatism etc. Its sensitivity is also the reason why the phase contrast can be used to reveal the atomic structures of thin samples; examples of phase contrast effects are stacking fault fringes or thickness fringes, characteristic Moiré fringes produces by lattice defects, etc. [4, 6, 28].

The same types of contrast mechanism are also observed in STEM mode, which is an important mode of transmission electron microscopy.

### 3.2.3 STEM

In STEM, as with TEM, the electrons pass through a sufficiently thin specimen. However image formation in the scanning mode is substantially different from static-beam image formation. STEM differs from conventional transmission electron microscopes because the electron beam is focused to a narrow spot which is scanned over the sample in a raster pattern and the electrons are converged on the specimen with a specified convergent angle. This process is exactly the same principle used in an SEM. The recorded signal varies in intensity depending on the specific point on the specimen illuminated by the probe.

In STEM mode electron detectors are used in exactly the same way as the aperture is used in conventional TEM as shown in Fig. 3.3(a). Direct or diffracted beams are selected by using different detectors at different positions. The bright field (BF) detector intercepts the direct-beam electrons, while detectors such as annular dark-field (ADF) and high angle ADF (HAADF) detectors are used to collect scattered electrons.

STEM mode is a very powerful tool because it allows additional information to be obtained from the specimen, by exploiting the variety of signals produced by the electron-specimen interaction. These include secondary electrons (SEs), back scattered electrons (BSEs), Auger electrons, X-rays, cathodoluminescence, etc., see Fig. 3.3(b) [6,45].

### 3.2.4 Diffraction modes

It has been already mentioned that TEM allows the display of diffraction patterns (DPs) using the diffraction mode. Depending on the type of illumination, parallel or convergent, it is possible to have two types of diffraction modes.

When the illumination is parallel the DP is usually called *selected area diffraction pattern* (SADP). The term “selected” is used because in this mode it is possible to choose from which part of the specimen the diffraction pattern is obtained. This can be done by using an aperture placed after the objective lens. SADPs are very useful because they give direct crystallographic information about small areas of the specimen [4,6]. They can be used to identify the type of the specimen (monocrystalline, polycrystalline or amorphous), identify crystal structures and orientation, and to select particular dark-field imaging conditions. This capability is one of the most

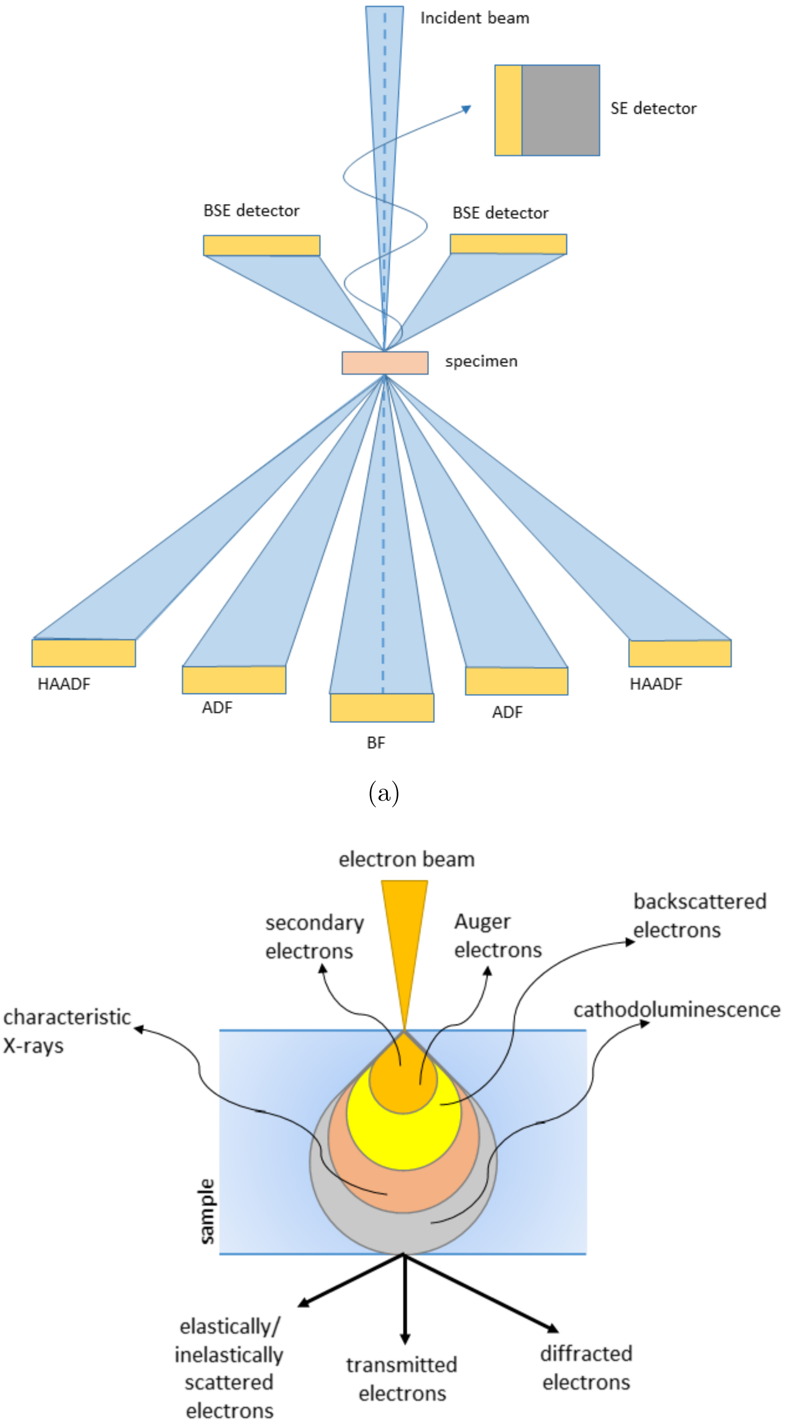

(a)

(b)

Figure 3.3: Illustration showing how the (a) different types of detector are used for collecting the signal and (b) the electron-specimen interaction volume produced by the electron probe. Reproduced from [6].

important features of the TEM. A disadvantage of this mode is that the smallest diameter of the illuminated area that can be selected in SAD is relatively large, of the order of 100 nm [6]. This is a great disadvantage when in some cases the features to be observed are smaller than this value, as in many nano-structured materials. Moreover, in the presence of very thin specimen thicknesses the Bragg condition is relaxed providing inaccurate information. This limitation can be overcome using convergent beam diffraction.

When the illumination is convergent the diffraction mode is called *convergent beam electron diffraction* (CBED) [6, 28, 51]. The region sampled by the converging beam is a function of the probe size and the electron-specimen interaction volume. This is generally much smaller than the spatial limitation of the SAD [6]. Figure 3.4 compares SAD and CBED. A DP produced by a monocrystalline specimen, for example, would consist of diffraction spots in the SADPs; it would consist of diffraction disks in the CBED patterns. The disks have an angular radius equal to the convergence angle of the incident electron beam.

CBED not only overcomes the limitations of SADPs, but contains furthermore a variety of additional diffraction features such as HOLZ spots and lines, Kikuchi lines and a number of features arising from dynamical effects. The convergence angle in practice opens up a much larger angular view of the reciprocal space to look into, so it gives a complete three dimensional crystallographic analysis of the specimens with a very high spatial resolution. This enables the determination of specimen thicknesses, lattice parameters, crystal symmetries (point group and space group) and lattice defects, Debye-Waller factors and other important information [6, 52, 53].

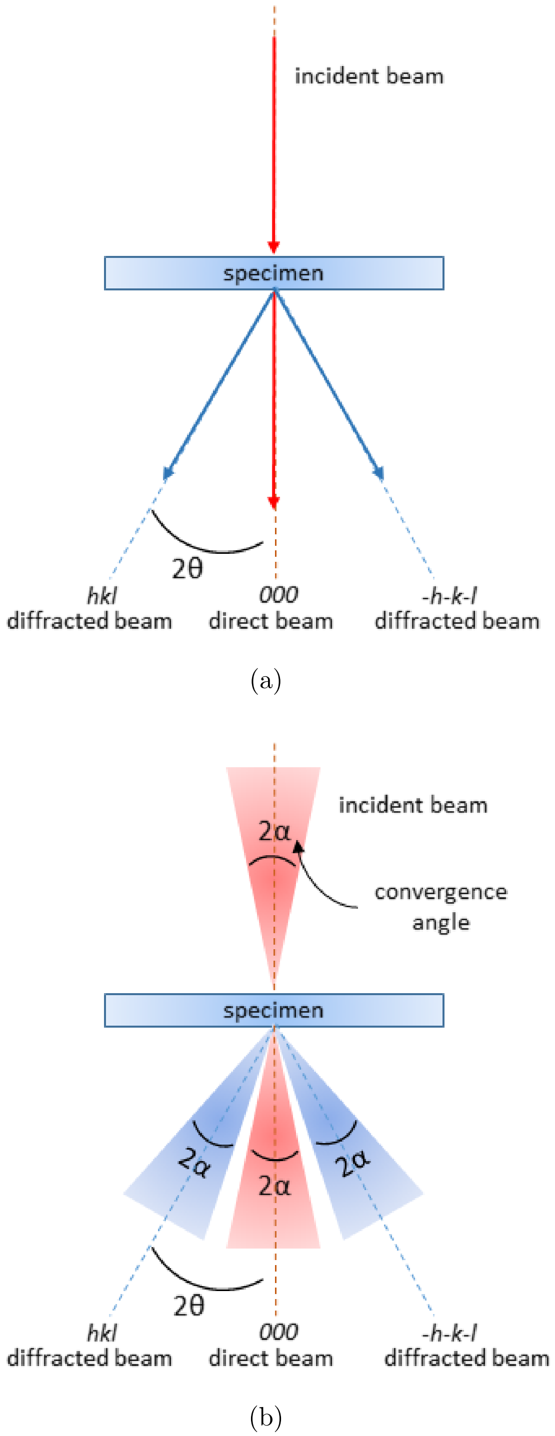

Figure 3.4: TEM diffraction modes obtained using (a) parallel beam electron illumination and (b) convergent electron beam illumination. Reproduced from [6].

### 3.2.5 Energy filtering

Energy filtered transmission electron microscopy (EFTEM) is also a very important TEM mode. In EFTEM only electrons of particular kinetic energies are used to form the image or diffraction pattern. This is possible by using a spectrometer, placed either in-column or post-column, which allows the selection of electrons having a specific energy [6, 54]. This technique can be used for chemical analysis of the specimen. When a very thin sample is illuminated with a beam of high-energy electrons some of the electrons interact with the sample and are scattered elastically or inelastically (e.g. phonon scattering, inner shell ionisation, plasmon scattering etc. [4, 6, 54]). Inelastic scattering results in both a loss of energy and a change in momentum, which in the case of inner shell ionisation for example is characteristic of the types of elements contained in the sample [6, 55, 56]. When the electron beam emerging from the sample is passed through a magnetic prism, then the flight path of the electrons is deflected depending on their energy. It is possible to place an adjustable slit to allow only electrons with a certain range of energies to form an energy filtered image on a detector. The slit can be adjusted to only allow electrons which have lost a specific amount of energy to be used, producing elementally sensitive images. The energy slit can also be adjusted so as to only allow electrons which have not lost energy to pass through and form the image. This prevents inelastic scattering from contributing to the image enhancing the contrast in the image. It is particularly useful to perform *energy filtered electron diffraction* and remove the diffuse background and enhance the contrast in the diffraction features [54, 57].

In a similar way, using convergent illumination, *electron energy loss spectrometry* (EELS) is used to analyse transmitted electrons to determine the amount of energy they have lost in the interactions with the specimen. It provides local EELS spectra containing information about the interacting atoms, elemental identity, chemical bonding, valence and conduction band electronic properties, surface properties, and element-specific pair distance distribution functions [6, 58–60]. Also energy-filtered CBED is common [61].

### 3.2.6 Reflection electron microscopy

Reflection electron microscopy (REM) is another imaging technique which can be performed in the TEM. In contrast with the previously mentioned TEM/STEM based techniques, REM is substantially different from the others because it is based on the use of electrons reflected by the specimen's surface, and is used for studying surfaces [62–66]. The sample is not even required to be thin. Fig. 3.5 illustrates the imaging geometry in REM. A bulk crystal specimen is illuminated by a parallel beam with a glancing-angle condition. In the back focal plane of the objective lens the diffraction pattern is called the *reflection high-energy electron diffraction* (RHEED) pattern [67–70], and is generated by the surface layers of the specimen; RHEED patterns are described in a more detailed way in section 3.3 since they are often used as a standalone application, for example in molecular beam epitaxy (MBE) crystal growth chambers [70].

By changing imaging conditions it is possible to select the desired reflection, generally a specular reflection satisfying a Bragg condition, to be parallel to the optical axis of the objective lens. All the other directions are blocked by the objective aperture. On the image plane of the objective lens an image of the surface structure is formed; the image contrast is determined by the local reflected intensity passing through the aperture [62, 64, 65].

Because of the tilt, the REM images are foreshortened by an amount which depends on the reflection used. The consequence is that parts of the specimen will be focused at different positions behind the lens. This makes the interpretation of REM images difficult [62, 64, 65].

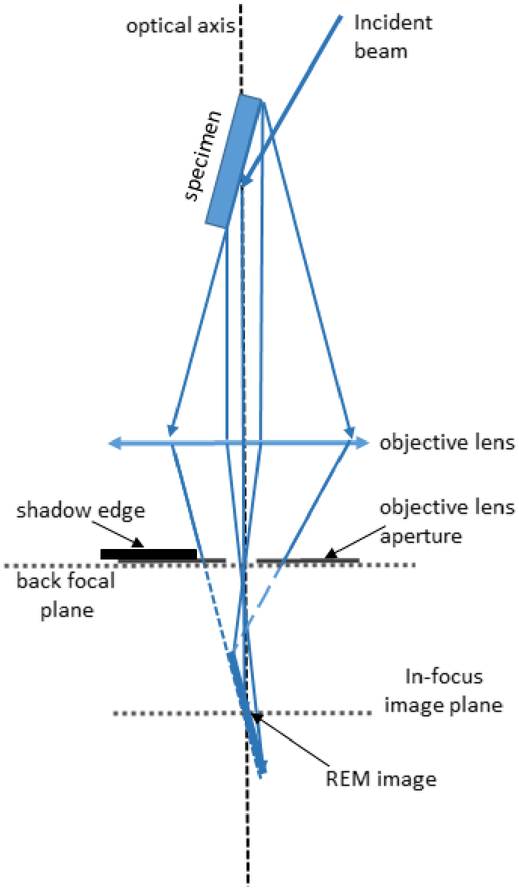

Figure 3.5: Image formation in REM. A RHEED pattern from the surface structure is formed on a back focal plane of the objective lens. Diffracted beams pass through the objective lens aperture and form a REM image. In-focus plane and shadow edge are indicated for clarity. Reproduced from [64].

REM is a powerful method to study surface effects such as surface reconstructions, atomic steps and crystalline defects [67–70]. The diffraction contrast mechanism used to explain conventional TEM images may also be used to explain REM images. In a similar way as TEM is related by reciprocity to STEM, REM is related to *scanning reflection electron microscopy* (SREM) [71–73]. In SREM the electron beam is focused into a narrow spot which is scanned over the specimen in a raster pattern. Typically the intensity of one Bragg-reflected beam is used to generate the image.

One of the advantages of using SREM over REM is that SREM allows the foreshortening factor to be reduced by signal processing and the use of a dynamic focus of the electron beam to reduce the out-of-focus effect [64].

## 3.3 Reflection high energy electron diffraction

Reflection high energy electron diffraction (RHEED), as already mentioned in section 3.2, is a type of diffraction obtained when electrons are diffracted by a surface when the primary beam is incident at a glancing angle. RHEED is often used as a standalone application, to monitor the growth of crystalline materials in a dedicated growth reactor equipped with an in-situ RHEED system, such as molecular beam epitaxy chambers [74]. Due to its high surface sensitivity, RHEED is particularly advantageous for the characterization of epitaxially grown thin film materials. It can reveal changes in the coverage of the surface as the growth process evolves, to determine lattice parameters, the surface structure and the eventual surface reconstruction, crystallographic orientation, the morphology of the surface, and other useful information [62, 69, 70, 75].

RHEED is generally performed in high vacuum ($\approx 10^{-9}$ Torr ). A focused beam of electrons streaks the specimen surface at near-grazing angle incidence, typically of the order of few degrees, and it is then reflected directly onto a phosphor screen, without the use of lenses between the sample and the phosphor.

The primary electron beam energies used in RHEED are typically 10-20 keV, so the electrons have a short mean free path [62, 69, 70, 76–79]. This, together with the glancing-angle incident geometry, makes the interaction volume limited to the near-surface region. The surface can be then thought as a planar diffracting grid, a reason why RHEED is considered to be a 2-dimensional type of diffraction [80–82, 82].

This reduced dimensionality results in the degeneration of the reciprocal lattice points to rods vertical to the specimen surface. The intersection of these rods with the Ewald sphere results in the formation of diffraction spots and/or streaks in the RHEED patterns.

As described in section 2.3.1, the Ewald sphere combines momentum and energy conservation. In the case of a surface lattice

$$|\mathbf{k}_i| = |\mathbf{k}_f| \tag{3.1}$$

$$\mathbf{k}_f - \mathbf{k}_i = \mathbf{G}_m \tag{3.2}$$

where $\mathbf{k}_i$ and $\mathbf{k}_f$ are the incident and final wave vectors, and $\mathbf{G}_m$ is a point of the three-dimensional reciprocal space [62, 69, 70]. The intersection of the Ewald sphere with the reciprocal lattice determines from which family of crystallographic planes diffraction is allowed. Because the lattice is two-dimensional, this simply means that the parallel component of the three-dimensional vector $\mathbf{G}_m$ (the projection on the two dimensional lattice) has to be equal to one of the two-dimensional reciprocal lattice vectors. This can be written as:

$$\mathbf{k}_{f,t} - \mathbf{k}_{i,t} = \mathbf{S}_m \tag{3.3}$$

where $\mathbf{S}_m$ is one of the vectors of the two-dimensional reciprocal lattice. In reflection geometry, the reciprocal lattice is no longer composed of points, but they degenerate into a cigar-like structures perpendicular to the surface, as shown in Fig. 3.6.

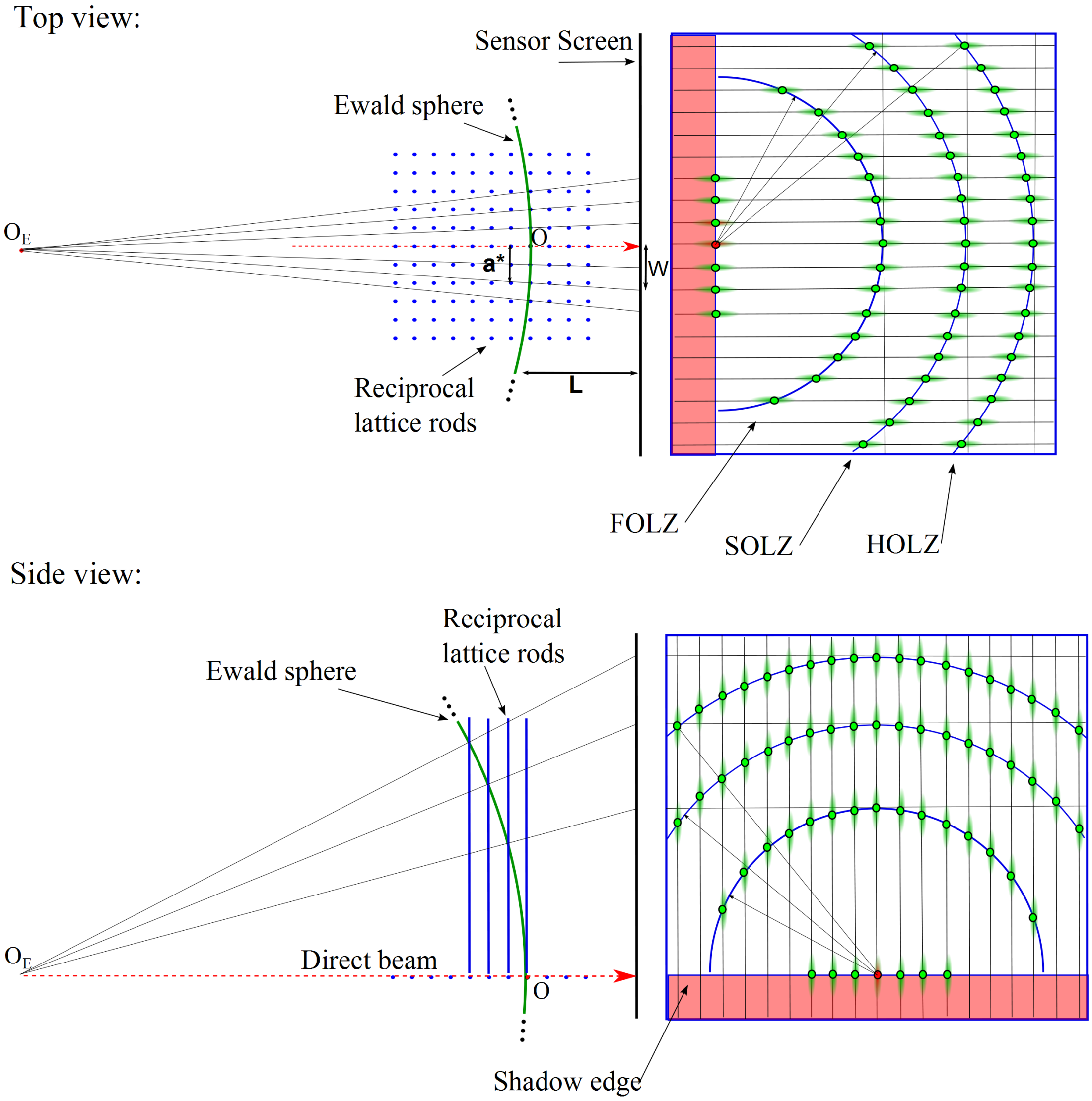

Figure 3.6: Geometrical interpretation of RHEED pattern formation. The centre of the Ewald sphere is the point $O_E$. The origin of the reciprocal lattice is the point O. The right side of the figure shows the position of the diffraction spots on the screen. The direct beam is highlighted in red. Reproduced from [70].

These rods originate at the corresponding two-dimensional reciprocal lattice points on the surface $\mathbf{S}_m$ and extend infinitely in the perpendicular direction. Because of energy conservation, the allowed diffracted points are determined by the intersection of the Ewald sphere with the rods. The diffraction pattern is composed of the projection on the screen of those intersections. It is important to understand that, because of this elongation of the rods in the direction perpendicular to the surface, diffraction is not only allowed for the reciprocal lattice points placed at the intercept of the surface of the Ewald sphere with the two dimensional reciprocal lattice, but also for reciprocal lattice points contained in the volume of the Ewald sphere, e.g. far from the origin, $O$, of the reciprocal lattice space, as shown in Fig. 3.6.

As with other diffraction techniques, the geometrical interpretation of RHEED patterns requires the knowledge of parameters such as specimen to detector distance, incidence angle and beam direction of the primary electron beam [69, 74].

The specimen to detector distance, $L$, can be easily determined by measuring the spacing between diffraction spots, $W$. This spacing is proportional to the spacing between the reciprocal lattice points, as it is possible to observe in Fig. 3.6. If the reciprocal lattice spacing, $a^*$, is known, the specimen to detector distance can be calculated through:

$$L = \frac{2\pi}{\lambda}\frac{W}{a^*}. \tag{3.4}$$

The incidence beam angle can be measured by using the specular beam, i.e. the reflection of the primary beam on the specimen surface. This is done by measuring the distance $d$ between the specular spot and the shadow edge (the intersection of the specimen surface plane with the detector screen, see Fig 3.7). The incidence

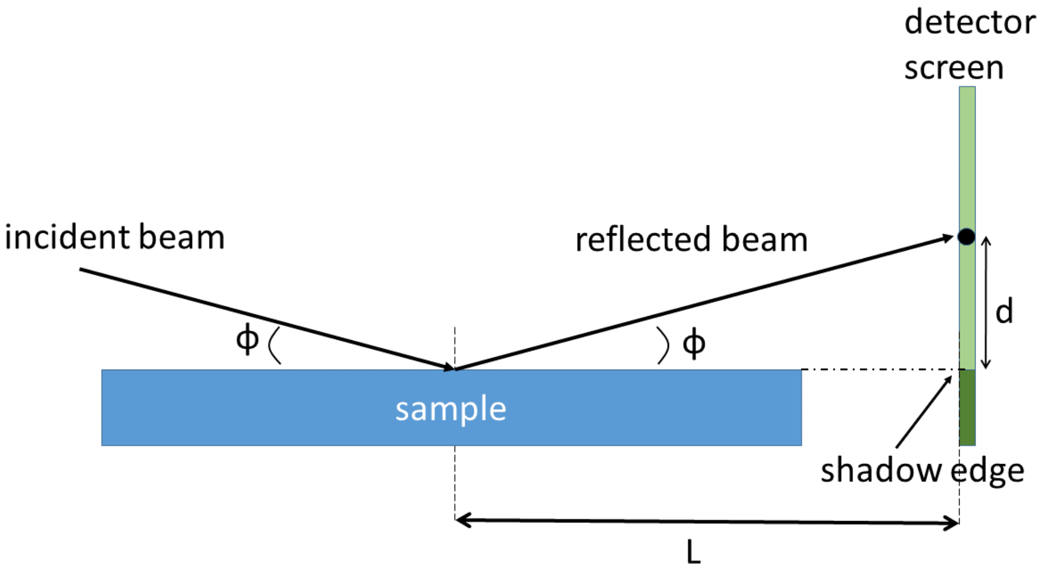

Figure 3.7: Specular reflection of the primary beam in RHEED.

angle, $\phi$ can be easily determined by:

$$\phi = \tan^{-1}\frac{d}{L}. \tag{3.5}$$

In a similar way the same parameters may be determined using the HOLZ ring, using equation 2.45.

If the specimen to detector distance is known, an important measurement in RHEED is the determination of the lattice parameters [62, 69, 70] which can be measured through:

$$a^* = \frac{2\pi}{\lambda}\frac{W}{L}. \tag{3.6}$$

This method is often used to monitor the change in lattice parameters and or lattice relaxation during the growth process, with a very high precision, of the order of a few thousandths of an Angstrom [83–86].

For a perfect surface, i.e. infinitely smooth surface with long range order, and an ideal instrument response, sharp diffraction spots are expected [64] since rods in the reciprocal space produced by a perfect crystal are very sharp, so that the intersection of the Ewald sphere with the rods defines very sharp RHEED spots on the screen.

Often imperfections such as limited long range order parallel to the surface, e.g. stepped surfaces, islands, or domains [69], result in an increase in the thickness (the diameter) of the reciprocal lattice rods. When this happens the intersection between the Ewald sphere and the rods no longer consists of sharp spots, but streaks, as shown in Fig. 3.8.

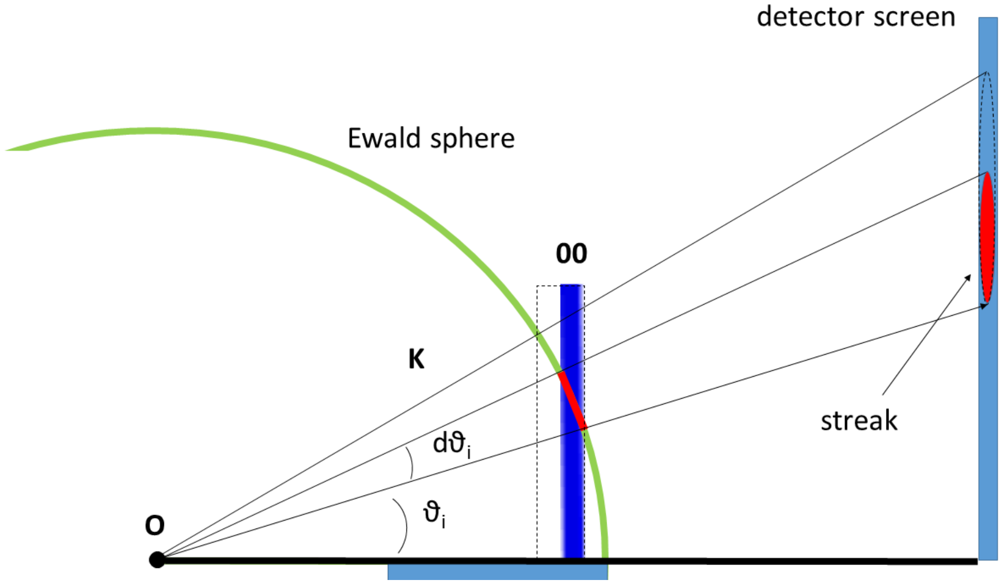

Figure 3.8: Streaks formation in RHEED.

To understand more quantitatively how streaks are formed consider for simplicity a square lattice with lattice constant $a$ [69]. It is possible to see that when electrons are scattered from atoms at positions $\rho = na\mathbf{x} + ma\mathbf{y}$, with $n = 1, 2, \ldots, N-1$ and $m = 1, 2, \ldots, M-1$, the amplitude of the scattered waves can be written as a geometric series

$$A(\mathbf{S}) = \sum_{n,m}^{N-1,M-1} \exp(iS_x na + iS_y ma) \tag{3.7}$$

which results in

$$A(\mathbf{S}) = \frac{1 - e^{iS_x Na}}{1 - e^{iS_x a}} \frac{1 - e^{iS_y Ma}}{1 - e^{iS_y a}}. \tag{3.8}$$

This leads to the so-called Laue function:

$$I(\mathbf{S}) \propto |A(\mathbf{S})|^2 = \frac{\sin^2(NS_x a/2)}{\sin^2(S_x a/2)} \frac{\sin^2(MS_y a/2)}{\sin^2(S_y a/2)} \tag{3.9}$$

which has its maximum values for the points when $\mathbf{S}$ is a vector of the 2-dimensional reciprocal lattice, i.e., $(S_x, S_y) = (2\pi n/a, 2\pi m/a)$; the maximum intensity is proportional to the number of scatterers. If one considers only the $S_x$ component, it can be see that the peak has an intensity of $N^2$ and the width of the peak is $\approx \frac{2\pi}{Na}$, where $Na$ is the length of the region. In terms of the Ewald construction this means that the rods are not sharp, but have a thickness $\Delta S_x = \frac{2\pi}{L}$. The intersection of the Ewald sphere with the rod will result in streaks perpendicular to the surface having a angular length of $d\vartheta_i = 2\pi/KL \sin\vartheta_i$. Measuring the length of the RHEED streaks, in the direction perpendicular to the surface, gives information about the dimension of the region of the surface over which the coherent scattering occurred.

## 3.4 SEM imaging and diffraction modes

As previously mentioned in section 3.2 the mechanism of image formation in the SEM is substantially different from TEM.

In SEM a focused electron beam is scanned, in a raster fashion, over the surface of the sample using scan coils, which are used to deflect the electron beam on a rectangular area on the sample surface. The magnification mechanism in the SEM is thus different from TEM [87, 88].

In the SEM the magnification is not a function of the objective lens power, but it is determined by the ratio between the dimensions of the area scanned on the sample and the dimensions of the image displayed on the screen. For a fixed screen size, high magnification results in a reduction in the area scanned on the sample, and consequently the magnification is simply controlled by the scanning coils.

Electrons of the primary beam interact with the sample through elastic and inelastic scattering mechanisms, losing energy and producing different types of signal within the interaction volume. Typically the volume of interaction extends from 100 nm to several microns, depending on the energy of the primary beam, the composition and density of the sample, etc [27, 45, 46].

One of the most basic SEM modes is based on the detection of secondary electrons, consisting of electrons leaving the sample from a volume close to the surface, typically having energies less than $\approx 50$ eV [27, 46]. The number of secondary electrons depends, among other things, on specimen topography; steep surfaces and edges appear brighter than flat surfaces, resulting in images with a clear three-dimensional appearance. The resolution of secondary electron images can be less than 1 nm using field emission guns.

Backscattered electrons (BSEs) have energies ranging between $\approx 50$ eV and the energy of the incident electron beam. They come from deeper regions of the sample, and consequently the resolution of images produced by the backscattered electrons is generally poorer than those produced by SE. On the other hand backscattered electrons contain important information about the atomic number, density of the material and structural properties. This allows identification of regions with different densities or having a different chemical composition.

In crystalline materials BSEs provide important crystalline information; sections 3.4.1 and 3.4.2 show how BSEs can be used to generate electron channelling patterns (ECPs), electron channelling contrast images (ECCIs) and electron backscatter diffraction patterns (EBSPs), which are of particular relevance for this thesis.

There are also other types of signals that can be used in SEM imaging, these include: characteristic X-rays, visible light emitted by samples, currents generated within the sample, transmitted electrons, etc. [27, 46, 89–107].

### 3.4.1 ECP and ECCI

Electron channelling patterns (ECPs) were reported for the first time in 1967 by Coates [108–110] who showed a strong crystalline orientation dependence of the backscatter electron intensity with respect to the crystallographic orientation of the sample. Booker in 1967 [111] confirmed Coates observations and provided a theoretical interpretation of the phenomenon. The theoretical explanation was based on the use of Bloch waves and the dynamic theory of diffraction, very similar to the one used by Howie and Whelan [37, 38] for transmission electron diffraction. Since the variation of the backscattered electron intensity rapidly changes in the proximity of the Bragg condition, Booker predicted that this phenomenon could be used to reveal crystallographic defects on the surface of appropriately oriented crystalline samples [109, 112, 113].

Experimentally, ECPs are acquired by scanning the electron beam at low magnification across a crystalline sample. As the beam is scanned over the surface, the angle between the incident beam and the crystal planes changes. When the beam changes its angle around the Bragg condition for a particular family of crystallographic planes for example, the resulting backscatter intensity results in the formation of Kikuchi bands, as shown in Fig. 3.9(a).

When scanning the SEM electron beam at high magnification on the sample instead, the beam trajectories are essentially parallel to each other, leading to a constant yield of backscattered electrons as the beam is scanned across the area (in a perfect single crystal). Localized lattice distortion (bending) occurring in proximity of imperfections of the crystal, (e.g. crystalline defects or steps on the surface) generate BSE image contrast, as sketched in Fig. 3.9(b). This approach is known as electron channelling contrast imaging (ECCI).

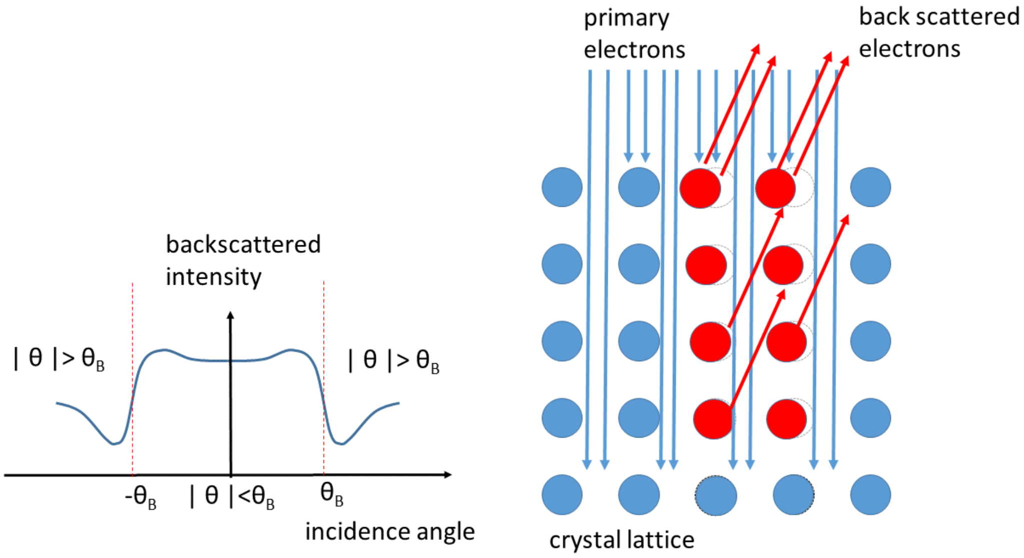

(a) (b)

Figure 3.9: Intuitive illustration showing the channelling mechanism. Reproduced from [114].

Crystal distortions such as low angle tilt and rotation boundaries, atomic steps and extended defects, change the local orientation of the crystal lattice producing a change in the backscattered intensity [113]. This variation is particularly strong when the electron beam direction is near the Bragg condition for a set of diffracting planes, in the so-called two beam condition, where only two Bloch waves are predominately excited. The desired diffraction condition is set by the ECP.

Extremely small changes in orientation and strain are detectable using ECCI, allowing, for example, extended defects such as dislocations and stacking faults to be imaged [109,112,115–124].

Since an ECP reflects the symmetry of the crystal, it can furthermore be used to measure crystal orientations and identify crystal types. Because of the limited field of view of ECPs, typically of the order of few degrees, electron backscatter diffraction has supplanted this particular application.

### 3.4.2 EBSD

Electron backscatter diffraction (EBSD), also known as backscatter Kikuchi diffraction (BKD), is a powerful SEM based characterization technique which enables the non-destructive analysis of crystalline materials, like metals, ceramics, geological and semiconductor materials, with high resolution [125,126].

EBSD can be used for orientation mapping, defect studies, phase identification (identification of the crystal type, e.g. cubic, hexagonal, etc.), grain boundary identification, and strain mapping [29,127–134].

When used in combination with complementary techniques, e.g., energy dispersive spectroscopy (EDS), it also allows the extraction of both physical and chemical information, particularly useful for phase identification; used in combination with focused ion beam (FIB) milling it allows the 3D reconstruction and analysis of the microstructure by serial sectioning of the sample [135–137].

Recently there has been growing interest in the acquisition of Kikuchi patterns acquired in transmission mode, i.e. by collecting Kikuchi patterns produced by the electrons transmitted through the specimen. The technique is called transmission EBSD (t-EBSD), or, transmission Kikuchi diffraction (TKD), in the SEM [138,139]. TKD has a significantly higher spatial resolution than EBSD. It has to be acknowledged that the term transmission EBSD contains an unfortunate contradiction ("oxymoron") which has nevertheless grown into use in the SEM community.

EBSD patterns were first observed by Nishikawa and Kikuchi in 1928, in both backscattering and transmission modes, using electron-sensitive film [22]. The technique was developed further by Alam et al. in 1954 [140], and later by Venables and Harland (1973) [141] and by Venables and Bin-Jaya (1977) [142]. In 1984 the first commercial system was produced by Moon and Harris exploiting the work of Dingley at the University of Bristol [143]. In the 1990s fully automated EBSD systems in the SEM had been developed by Adams et al. [144] and Krieger Lassen et al. [145,146].

The capability to automatically index EBSPs and map the spatial distribution of crystal orientation led to EBSD becoming a good alternative to X-ray pole figure analysis of texture, and so opened up new horizons in quantitative orientation mapping and grain boundary studies.

Due to the availability of SEMs and the relative ease of sample preparation, EBSD has experienced an increasing acceptance in laboratories for routine analysis in the last few decades [147].

### Generation and interpretation of EBSD patterns

Experimentally EBSD is conducted in a SEM equipped with an EBSD detector, composed of a phosphor screen, compact lens (and/or optical fiber) and low light CCD camera chip. A typical set up is shown in Fig. 3.10.

An EBSD pattern (EBSP) is visible on a phosphor screen when a stationary beam of electrons is focused on a point of the specimen surface. The sample consists of a flat/polished crystalline specimen which is usually tilted by approximately 70° from the horizontal, to enhance the contrast in the resulting EBSD pattern. The detector is placed in front of the specimen to intercept electrons backscattered from

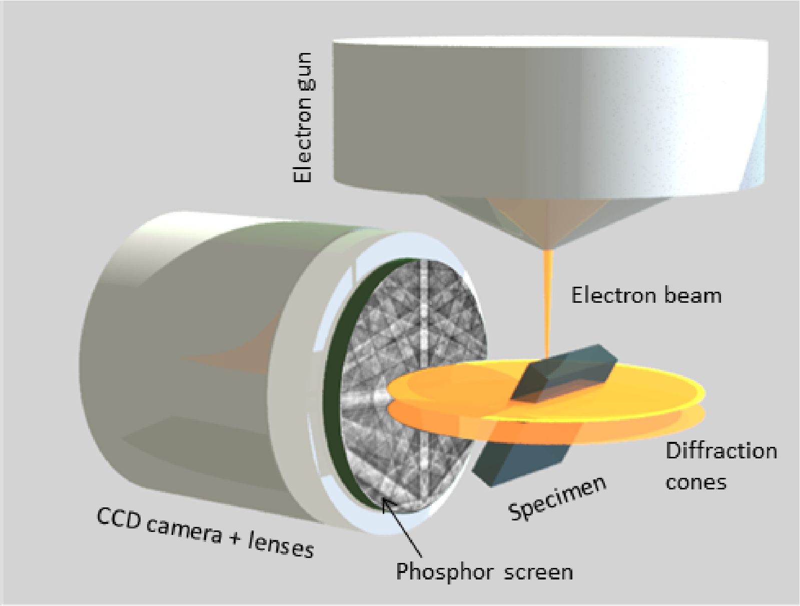

Figure 3.10: Illustration of a conventional EBSD system.

the sample, which cause the fluorescence of the phosphor, revealing the diffraction pattern. A digital camera and lenses are then used to record the image of the diffraction pattern formed on the phosphor screen.

On penetrating the specimen, the electrons of the impinging beam are both elastically and inelastically scattered within the specimen. Some of the electrons may experience one or more subsequent deflections from the original trajectory and return back to the surface, leaving the sample. This creates a diverging source of electrons with a broad range of energies and directions [27,109,112,148,149] within the interaction volume. Some of the electrons generated within the interaction volume travel in such a way that their energy and direction satisfy the Bragg condition, Eq. 2.40, for a set of planes and undergo diffraction.

Due to the cylindrical symmetry of the Bragg reflection condition with respect to the lattice plane normal, diffraction cones (Kossel cones) are formed. When these cones intersect the phosphor screen (see Fig.3.11), Kikuchi lines are observed in a gnomonic projection on the screen. The Kikuchi lines appear as almost straight lines because the cones are very shallow, as the Bragg angle $\theta$ is of order $1^\circ$. Each pair of parallel Kikuchi lines form a Kikuchi band (see Fig 3.12 for example). The angular width of the Kikuchi band is twice the Bragg angle for the considered reflection, and so is related to the interplanar spacing through Eq. 2.40. The angle between Kikuchi bands corresponds to the interplanar angle between the corresponding atomic planes.

The centre of the projection is called the pattern centre (PC), which geometrically corresponds to the projection of the source point (from which the EBSD is generated within the specimen) on the screen. The determination of the PC is extremely important for several applications, and the uncertainty in this parameter usually limits the precision of several EBSD based measurements. This is discussed in Chapter 8.

The electrons contributing to the actual diffraction pattern come from a reduced volume of the entire electron-specimen interaction volume, of the order of $\approx 20$ nm in depth times the projected area of the incident beam (usually having a spot size of a few nanometres); the majority of the electrons contribute to a diffuse, featureless background, which is superimposed on the EBSD pattern. A raw (as acquired) EBSP then consists of a series of bright bands, on a continuous background, as shown in Fig. 3.12(a).

Using image processing techniques it is possible to remove the featureless background (and also artefacts due to irregularities on the screen, such as scratches, blind or bright pixels etc.) from the recorded image, and, as shown in Fig. 3.12, extract an EBSD pattern which shows an increased quality and contrast.

A background (see Fig. 3.12(b)) can be obtained in several ways. The beam can be scanned across a large area containing grains with different orientation so that the diffraction features are averaged out, resulting in a featureless background.

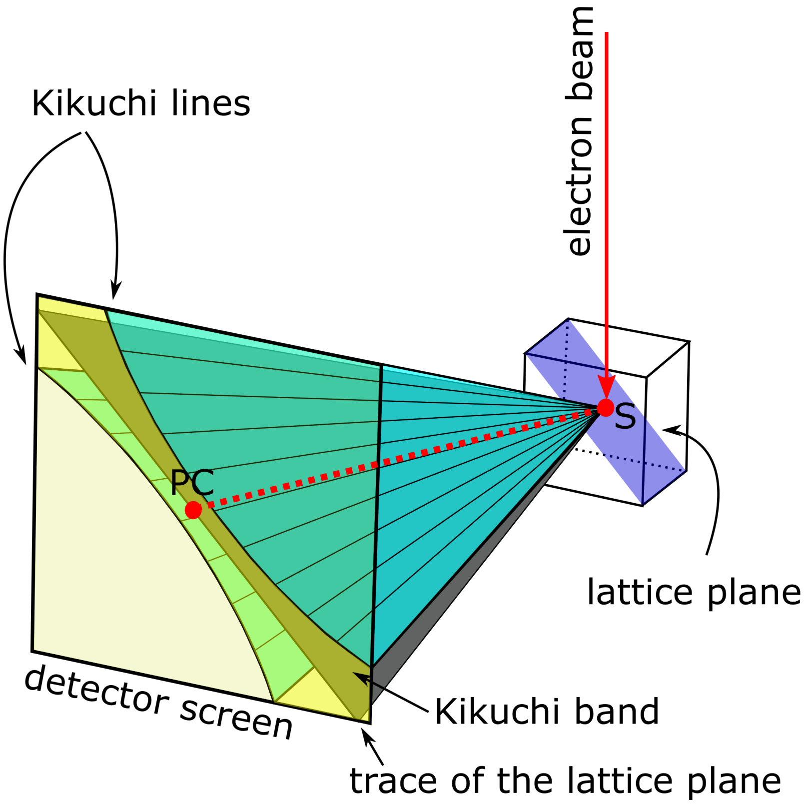

Figure 3.11: Schematic of the diffracting cones with respect to the reflecting plane, the specimen, and the phosphor screen. Reproduced from [147].

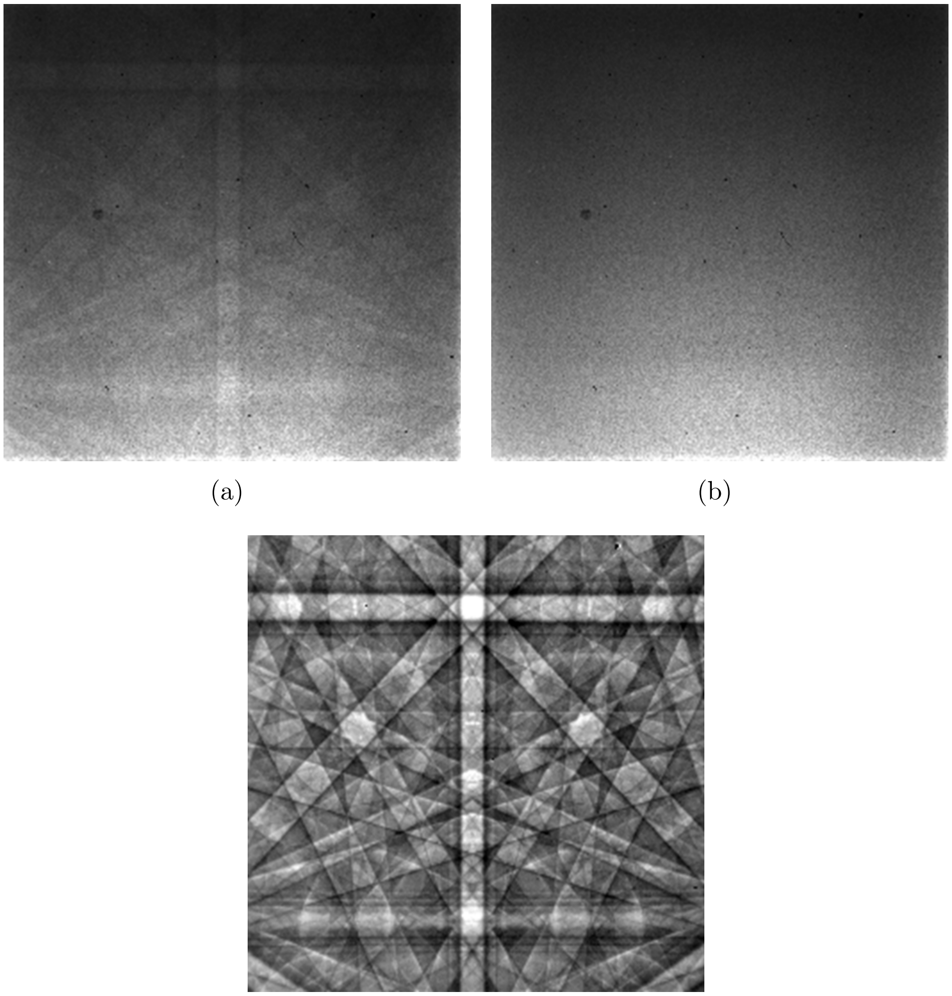

(a) (b)

(c)

Figure 3.12: Example of EBSD pattern from silicon at 20 keV: (a) raw EBSD pattern, (b) background, (c) flat fielded EBSD pattern.

Alternatively it is possible to defocus the beam in spot mode until the Kikuchi pattern fades away. Using image processing filtering techniques it is also possible to create an artificial background. Each of these techniques has advantages and limitations and their use has to be determined depending on the specific application.

As can be seen in section 3.4.3 a detailed description of the intensity distribution in the EBSPs involves the use of the dynamical theory of electron diffraction [150]. On the other hand the geometry of the EBSP features can be understood, to a first approximation, using a kinematical approach, as explained in Chapter 2, by considering the angular direction of electrons which have been Bragg reflected from the lattice planes of the crystal specimen.

Considering that each Kikuchi band (pair of Kikuchi lines) is effectively fixed to the plane from which it is formed, an EBSD pattern provides a direct measurement of a sample's orientation. This is illustrated in Fig. 3.13: rotation of a crystal will produce a rotation of the EBSP; a tilt of a crystal will produce a shift in the EBSP.

Presently, in commercial systems, Kikuchi bands are the only features used to extract information from EBSPs, and only the kinematic intensity of the Kikuchi bands is considered. Each particular crystal structure has a unique corresponding geometry in terms of EBSD patterns. Commercial software allows the automated indexing of the EBSD patterns. This task is not so straightforward to implement using pattern recognition methods. In order to index an EBSP, software has to accomplish several tasks, including band recognition, the choice of suitable bands for the calculations, and the association of them with a particular Kikuchi band. The presence of a background makes this task more difficult, because the edges of the bands are not usually well defined, but rather a diffuse broad band, so conventional methods such as line filtering, gradient or contour tracing methods are not very suitable [147].

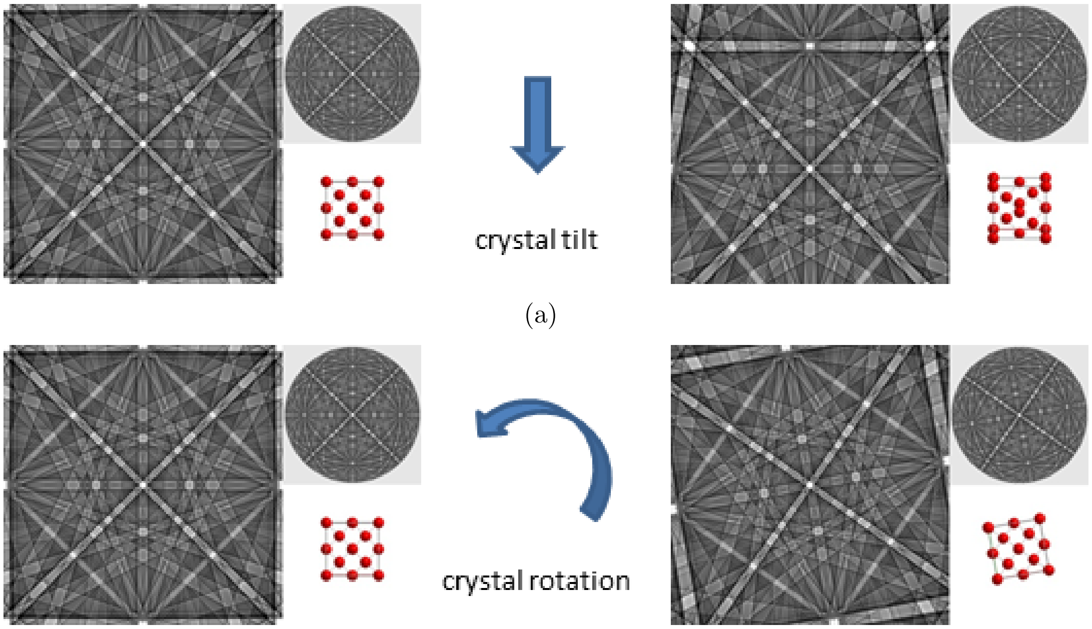

(a)

(b)

Figure 3.13: Effect of rotation and tilt of a silicon crystal structure and corresponding EBSD pattern: (a) Si (100) crystal tilted by 10°, (b) Si (100) crystal rotated by 10°. The inset placed on the right side of each picture shows the 3D spherical Kikuchi pattern and the corresponding real view of the crystal structure. Images were produced using the ESPRIT DynamicS software [151].

Band recognition is usually performed by using the Hough transform [152]. The extracted bands are then used to calculate the angles between the different crystal planes, which are then compared with theoretical interplanar angles tabulated in databases to identify the crystal structure. It is clear that by using this geometrical approach not all the information contained in the EBSP is extracted.

A real EBSP contains much more information, such as non-obvious intensity distributions which cannot be predicted with a geometrical/kinematic approach. These include excess/deficiency intensity distributions in the EBSP which can give information on the direction of the incidence electron beam with respect to the specimen, diffraction features of higher order such as HOLZ rings, and fine EBSP structure, which is very sensitive to the energies from which the actual EBSP is formed and to the lattice constant parameters. Sometimes RHEED-like spots may also appear in the EBSP.

Very recently (2015) the analysis of the intensity distribution in EBSD using dynamical theory of diffraction has been used by Winkelmann and Nolze [153] to determine the polarity of non-centrosymetric crystals such as GaP, not possible with conventional EBSD, and also to determine the chirality in quartz crystals [154], showing the importance of a dynamical approach and also opening up new horizons for the use of EBSD. In this case the band recognition is not performed using the standard Hough base algorithm, but using a normalized cross correlation based method, where the intensity distributions in the simulated EBSP, using dynamical simulations, are compared with the intensities of the experimental EBSP.

The following section shows the approach used to calculate those intensities.

### Energy filtering

There is ongoing research to produce a detailed understanding of the physical mechanisms involved in the formation of EBSPs. As discussed in the previous section, by using the dynamical theory of diffraction approach, it is possible to obtain EBSP simulations showing very good agreement with the experimental EBSD patterns. However the range of energies of the electrons contributing to the EBSP and the depth from which they emerge from the sample are still not completely understood [155–157].

Since the diffraction features appearing in the EBSPs are very energy-sensitive, it is clear from experimental evidence that the range of energies contributing to the predominant diffraction pattern is narrow and close to the primary beam energy. Since the width of the Kikuchi bands is a function of the wavelength, and hence the energy of the electron, if a large range of energies contribute significantly to the pattern, then an overlapping of Kikuchi bands of different energies would result in a poorly defined Kikuchi band, which is in contrast to the observed patterns.

An estimation of the energy spread can be obtained by observing the fine detail of the EBSP, like HOLZ rings and triangle-like features formed by the intersection of Kikuchi bands, and comparing these with simulated patterns obtained by summing simulated EBSPs obtained for different energies. This has been illustrated in Ref. [156], using GaN patterns obtained using a 20 keV beam. The predominant contribution has been attributed to a range of energies within $\approx$ 0.5 keV of the primary beam.

To experimentally investigate the influence of the energy spectrum of the electrons contributing to the EBSP, energy-resolved EBSPs have been recorded using an electrostatic energy filter [157, 158].

The energy filter used in the experiments was based on the use of electrostatic retarding grids, having a energy resolution better than 10 eV, placed between the sample and the phosphor screen, to reject electrons having an energy below specific values, set by applying an electrostatic potential to the grids. The system was used to investigate the effect of the energy filtering on the Kikuchi band contrast, defined as

$$C = \frac{\text{Maximum intensity} - \text{Minimum intensity}}{\text{Maximum intensity} + \text{Minimum intensity}}, \tag{3.10}$$

where the maximum and minimum values refer to the intensity of the mean band profile of a specific Kikuchi band in the pattern. The definition of the contrast is not unique [159]; the one given above has been chosen to facilitate the comparison with the experimental results presented here with the experimental results presented in Ref. [148].

The authors of Ref. [157, 158] found that the Kikuchi contrast increases significantly when energy filtering is applied, explaining the effect in terms of reduction of high energy loss electrons contributing to the EBSP.

The experimental evidence implies that we can roughly differentiate three groups of scattered electrons:

1. elastically scattered electrons which are either:
    - (a) coherently elastically scattered (e.g. RHEED spots) or
    - (b) incoherently quasi-elastically scattered (through phonon scattering energy loss typically less than an electron volt)
2. inelastically scattered electrons which have lost only a relatively small amount of energy of the order of typically a few plasmon energies (tens of eV)
3. inelastically scattered electrons which have lost significant energy (several 100

eV).

The number of electrons belonging to group (1a) is usually much smaller than the number of electrons belonging to group (1b) for a typical EBSD experiment.

Diffraction effects are exhibited by groups (1) and (2), comprising the low-loss electrons plus elastically scattered electrons. The diffraction effects are gradually diminished for electrons with increasing energy loss in group (2).

High loss electrons predominantly contribute to a diffuse background not containing diffraction information, which obscures the diffraction features, reducing the observed contrast.

The general increase in the band contrast when energy filtering is applied has been shown for materials covering a range of atomic numbers and densities [157,158]. The contrast was found to reach a maximum value when the energy of the filter was set to within $\approx 3\%$ of the energy of the primary beam [157,158]. When the energy of the filter was set at an energy very close to the energy (within $\approx 200$ eV) of the primary beam (15 keV), the contrast and the sharpness of the Kikuchi bands was found to be reduced. The effect was explained by considering that for energies very close to the energy of the beam, the actual depth from which the electrons originated may be smaller than a quarter of the extinction distance.

A well established result from the (two-beam) dynamical theory developed for TEM [6] shows that the width of the rocking curve (a rocking curve is a plot of the intensity diffracted by a particular crystalline plane as function of the angle of incidence of the incident radiation), and so the range of angles contributing to the diffraction for a specific reflection, is independent of the thickness for thicker samples, and is given by

$$\Delta\theta = \frac{4}{g\xi_g} \tag{3.11}$$

while for thinner samples the width of the rocking curve becomes

$$\Delta\theta = \frac{1}{gt} \tag{3.12}$$

where $g$ is the magnitude of the diffracting vector $\mathbf{g}$, $\xi_g$ is the extinction distance relative to the diffracted beam $\mathbf{g}$, and $t$ is the thickness of the specimen.

When the thickness of the specimen is above a quarter of the extinction distance (based on a premise that energy filtration selects the depth range for thick samples), the range of angles contributing to the diffraction is constant, but as the specimen becomes thinner than this, the range of angles contributing to the diffraction increases as the thickness is decreased, i.e., there is more overlapping of Kikuchi bands having slightly different positions.

When the energy of the filter is set very close to the energy of the primary beam, the depth from which the electrons originate may be shallower than a quarter of the extinction distance, so that a larger number of angles is added to the diffraction causing an overlapping of Kikuchi bands which results in an increase in the blurring of the band itself.

An important aspect of energy filtering is that it reduces the depth and lateral extent of the regions contributing to the pattern, thus improving the spatial resolution of the technique, opening up new possibilities for the characterization of material with reduced grain sizes [157, 158].

The performance obtainable using the energy filter presented by [157, 158] is limited by the hardware used for the experiments, which introduces strong chromatic aberration arising from the use of electrostatic components, a reduced capture angle, and strong reduction in the signal intensity. The size of the filter requires an SEM chamber to be large enough to contain the hardware. To date the use of energy filtering in EBSD has not yet been implemented at the commercial level.

Further investigations were reported [148, 160], using an experimental set up designed originally for high-resolution electron momentum spectroscopy, with an energy resolution better than 0.5 eV. The authors investigated the variation of the Kikuchi contrast as a function of energy loss and as function of the diffraction geometry, i.e, incidence angle of the primary beam.

At a steep incidence angle, the contrast in the Kikuchi band decreased as function of the energy loss, which is expected since the larger the energy loss, the larger the number of inelastic scattering events experienced by the outgoing electrons.

At shallow incidence angles this was no longer the case since the electrons penetrate much less deeply. Because the source of electrons inside the crystal can be generated at a depth from the surface shallower than a quarter of the extinction distance, where the diffraction effects are not completely developed, the maximum contrast is found for energy losses larger than zero. In the latter case the electrons experience a few inelastic scattering events after their generation, corresponding to the electrons travelling to a depth where the outgoing inelastic scattering is still negligible, but where the depth allows the complete development of the dynamical diffraction effects. This increases the contrast in the observed Kikuchi band, in agreement with Ref. [157, 158].

In the following chapters we will see how, by using novel direct electron detectors, such as Timepix [161], the combination of compact size, high electron detection efficiency and direct energy filtering can be used together to improve significantly the performance of the EBSD systems.

### 3.4.3 Dynamical simulation of EBSPs

The simulation of a realistic EBSD pattern, which includes a description of the Kikuchi band intensities, HOLZ rings and other details of the EBSPs, involves the use of the dynamical theory of diffraction, which takes into account the fact that electrons are scattered multiple times by atomic planes within the solid, and includes the inelastic scattering experienced by the electrons travelling through the solid.

The physical model used for the dynamical simulation of EBSD patterns assumes that the incident electron beam, having a certain divergence and energy spread depending on the characteristics of the electron optics, penetrates the crystal, undergoing a series of elastic and inelastic scattering with the atoms which modify the distribution (energy and direction) of the incident electrons inside the crystal.

An efficient way of computing the scattered intensities consists of using the reciprocity principle [150], according to which the outgoing beam can be thought of as being sourced from the nucleus site with a broad angular distribution and the energy of the primary electrons. [150]. After their generation, the outgoing electrons, whose strength will depend on the inelastic (quasi-elastic) cross section of the considered process, are subsequently subjected to inelastic scattering events from the surrounding atoms of the crystal. The coherence of the incoming beam is assumed to be lost after the inelastic scattering event, so that, with this assumption, interference between the incoming and outgoing beams does not occur [150].

The predominant contribution to EBSD formation comes from the quasi-elastically scattered electrons, but there is a partial contribution from electrons which have lost some energy. Since the majority of electrons have an energy close to the primary beam (because the energy distribution is strongly peaked toward higher energies) the main features of the Kikuchi bands can be simulated assuming that the electrons of the outgoing beam have the energy of the primary beam. This argument is also reinforced by the fact that electrons which have lost a significant amount of energy contribute a diffuse background to the EBSD.

For the moment, the effect of the incidence angle and the outgoing angle of the electron trajectories (with respect to the surface's normal) is omitted. As we will see later, this may influence the Kikuchi contrast in the experimental EBSPs.

The wave function of the electrons inside the crystal [35] can be described as a superposition of Bloch waves with wave vector $\mathbf{k}^{(j)}$:

$$\Psi(\mathbf{r}) = \sum_j c_j \exp(2\pi i \mathbf{k}^{(j)} \cdot \mathbf{r}) \sum_g C_g^j \exp(2\pi i \mathbf{g} \cdot \mathbf{r}), \tag{3.13}$$

where $c_j$ are the excitation amplitudes of the Bloch waves and $C_g^j$ are the amplitudes of the partial Bloch waves with wavevector $\mathbf{k}_\mathbf{g}^{(j)}$.

The resulting wave function is the solution of the Schrödinger equation for an incident wave $\exp(2\pi i \mathbf{K}_0 \cdot \mathbf{r})$ having an energy $E = \dfrac{h^2 K_0^2}{2m}$:

$$\frac{-h^2}{8\pi^2 m} \nabla^2 \Psi(\mathbf{r}) - |e| V(\mathbf{r}) \Psi(\mathbf{r}) = \frac{h^2 K_0^2}{2m} \Psi(\mathbf{r}). \tag{3.14}$$

Using the translational invariance of the crystal potential it is possible to write the crystal potential as a Fourier series, and so write the scaled crystal potential $U(\mathbf{r})$ in the form

$$U(\mathbf{r}) = U^c(\mathbf{r}) + iU'(\mathbf{r}) = \sum_\mathbf{g} U_\mathbf{g} \exp(i 2\pi \mathbf{g} \cdot \mathbf{r}), \tag{3.15}$$

where the term $U^c(\mathbf{r})$ is the scaled crystal potential, and $U'(\mathbf{r})$ an additional imaginary potential which includes the absorption [41].

The Fourier coefficient of the scaled crystal potential $U_\mathbf{g} = U_\mathbf{g}^c + iU'_\mathbf{g}$, is composed of a real term, $U^c_{\mathbf{g}}$, and an imaginary term, $U'_{\mathbf{g}}$. Here $U^c = \frac{2m|e|V_{\mathbf{g}}}{\hbar^2}$, where $V_{\mathbf{g}}$ the Fourier component of the crystal potential (in volts), $m$ the relativistic electron mass, and $U'_{\mathbf{g}}$ is a term which includes the loss of electrons from the initial population as a consequence of the inelastic scattering [12, 41].

The Fourier component of the crystal potential $V_{\mathbf{g}}$ can be calculated from the contribution of the atoms in the unit cell through

$$V_g = \frac{1}{\Omega}\sum_i f_i^e(s)\exp(-i\mathbf{g}\cdot\mathbf{r}_i), \tag{3.16}$$

where $\mathbf{r}_i$ are the atomic positions inside the unit cell, $\Omega$ the unit cell volume, and $f_i^e(s)$ (see Eq. 2.33 for details) is the atomic scattering factor.

By substituting these expressions for the wave function and potential into the Schrödinger equation we obtain the dispersion relation:

$$[\mathbf{K}^2 - (\mathbf{k}^{(j)} + \mathbf{g})^2]C^{(j)}_{\mathbf{g}} + \sum_h U_{\mathbf{g}-\mathbf{h}}C^{(j)}_{\mathbf{h}} = 0 \tag{3.17}$$

where $\mathbf{K}$ is the electron wave vector inside the crystal with $K^2 = k_0^2 + U_0$. Equation (3.17) is the heart of the dynamical theory of diffraction.

The wave vectors $\mathbf{k}^{(j)}$ can be written in the form

$$\mathbf{k}^{(j)} = \mathbf{K} + \lambda^{(j)}\mathbf{n} \tag{3.18}$$

where $\mathbf{n}$ is a unit vector perpendicular to the surface, and equation (3.17) can be treated as an eigenvalue problem, from which the eigenvalues $\lambda^{(j)}$ and the eigenvectors with elements $C^{(j)}_{\mathbf{g}}$ can be determined. From the boundary condition the elements $c_j$ are obtained, so that the wave function (3.13) can be finally determined.

To overcome the long computational time necessary for the calculations using the previous method when a large number of reflectors are used, the Bethe perturbation scheme may be applied, which includes the effect of the weak reflectors by the use of strong beams $U_g^{\text{eff}}$ without increasing the matrix dimensions

$$U_{\mathbf{g}}^{\text{eff}} = U_{\mathbf{g}} - \sum_{h} \frac{U_{\mathbf{h}} U_{\mathbf{g}-\mathbf{h}}}{2KS_h} \tag{3.19}$$

where $2KS_h = K^2 - (\mathbf{K} + \mathbf{h})^2$ and $S_h$ is the excitation error.

The choice of strong and weak beams is decided by considering the structure factor and excitation error associated with the particular beams.

Once the wave function (3.13) is determined, the backscattered intensity can be easily calculated for any point $\mathbf{r}$ inside the crystal. Backscattered electrons are generated predominantly at atomic sites, so it is necessary to calculate the probability density $\Psi\Psi^*$ at atomic positions. In the backscattering case, a generalized potential can be used to determine the interaction of diffracted electrons with the lattice, where the potentials have the form of the Dirac delta function, that is point sources, which are broadened by thermal vibrations [162]. The resulting dynamically backscattered intensity can be written as

$$I_{\text{dynamical}} \propto \sum_{n,i,j} Z_n^2 B^{ij}(t_1, t_2) \sum_{\mathbf{g},\mathbf{h}} C_{\mathbf{g}}^{(i)} C_{\mathbf{h}}^{(j)*} \exp(-B_n s^2) \exp[2\pi i(\mathbf{g} - \mathbf{h}) \cdot \mathbf{r}_n] \tag{3.20}$$

where $\mathbf{r}_n$ are the atom positions, $\exp(-B_n s^2)$ the Debye-Waller factors, and $B^{ij}$ the depth integrated interference term of the Bloch waves $i$ and $j$

$$B^{ij} = c_i c_j^* \frac{\exp[2\pi i(\lambda^i - \lambda^{j*})t_2] - \exp[2\pi i(\lambda^i - \lambda^{j*})t_1])}{2\pi i(\lambda^i - \lambda^{j*})} \tag{3.21}$$

The physical meaning of the previous relations is that there will be directions for which the probability density overlaps with the atomic sites, giving rise to a strong backscattered intensity, as a consequence of the phonon scattering occurring at those positions. The region of enhanced backscattered intensities corresponds to the range of directions within the Kikuchi bands and zone axes, where the probability density is focused at atomic planes.

A decreased backscattered intensity occurs at the border of the Kikuchi bands where the probability density is focused mainly between atomic planes. However, under particular experimental situations, the intensity distribution can be altered, giving rise to contrast reversal effects [140,156]. This happens for example when the incidence angle of the primary beam with respect to the specimen surface is steep. In this condition the depth from the surface from which the backscattered electrons are generated is larger [46]. The reason for this behaviour has been attributed to the stronger absorption of Bloch waves which travel along atomic planes, when compared with those travelling between atomic planes [156].

When the backscattering is generated well away from the surface, the distance travelled by the Bloch waves may become so large as to cause their strong absorption, so that the contribution of the Bloch waves travelling between atomic planes becomes predominant. In this situation, the strong intensity in the middle of the Kikuchi bands is strongly attenuated, and the predominant backscattering comes from the residual overlapping of Bloch waves travelling between atomic planes, which is responsible for the backscattered intensity at the edge of the Kikuchi band, with the consequent observation of a reversed Kikuchi contrast [156].

The direction of the primary beam may also affect to some extent the distribution of intensities in the EBSPs [163]. The backscattering of the highly energetic electrons is different for the different scattered directions in the crystal.

In EBSD geometries, where usually the primary beam has a shallow incidence angle, there is a significant anisotropy of the initial distribution of inelastically scattered electrons, which causes the appearance of selective enhancement and suppression of intensity in specific edges of the Kikuchi bands, depending on their orientation with respect to the primary beam direction [163].

Figure 3.14 summarizes qualitatively the important aspects of the process responsible for the creation of excess and deficiency lines in EBSPs.

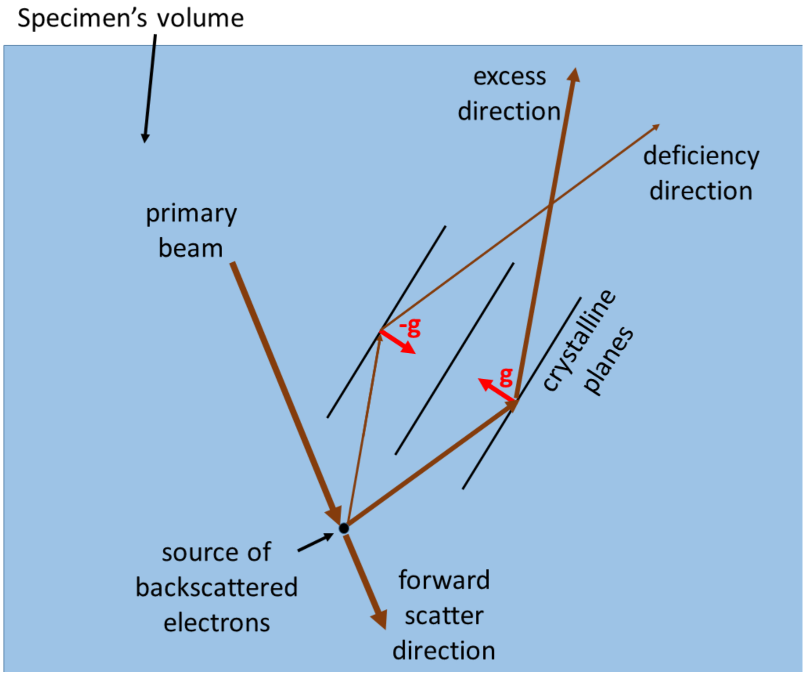

Figure 3.14: Mechanism of the formation of excess and deficiency lines in EBSD patterns. Reproduced from [156].

It turns out that electrons generated from a point source inside the crystal have a different probability of being scattered from a particular set of crystal planes, depending on their direction with respect to the reflecting planes. The electrons having a forward scattered direction will have a higher probability of being scattered than electrons whose direction deviates more from the forward scattered direction. These electrons are subsequently dynamically scattered by the surrounding crystal lattice.

If one considers the formation of the Kikuchi band characterized by the plane **g** in the figure, it can be noticed that the number of electrons diffracted by the plane **g** is larger than the number of electron diffracted by the plane −**g**, giving rising to the creation of the observed excess/deficiency lines.

This effect can be modelled [163], assuming that the beam **g** is excited to different degrees according to a function $\chi$, which describes the deviation from the isotropic scattering distribution and which is assumed for simplicity to be Gaussian, depending on **g**, the incidence direction and the detected direction:

$$f_n(\mathbf{q}+\mathbf{g}) \propto Z_n \cdot \chi_{\mathbf{g}}(\mathbf{k}_{in}, \mathbf{k}^{\alpha}_{out}) \tag{3.22}$$

where

$$\chi_{\mathbf{g}} = 1 + a\ \exp\left(\frac{-(\mathbf{k}^{\alpha}_{out} - \mathbf{k}^{eff}_{in} + \mathbf{g})^2}{b^2}\right). \tag{3.23}$$

The dynamical backscattering intensity can be then rewritten by taking into account the deviation from the isotropic scattering, in the form

$$I^{ED}_{\text{dynamical}}(\mathbf{k}^{eff}_{in}, \mathbf{k}^{eff}_{out}) \propto A \sum_{n,i,j} Z_n^2 B^{ij}(t) \sum_{\mathbf{g},\mathbf{h}} \chi_{\mathbf{g}}\chi_{\mathbf{h}} C^{(i)}_{\mathbf{g}} C^{(j)*}_{\mathbf{h}} \exp(-B_n s^2) \exp[2\pi i(\mathbf{g}-\mathbf{h})\cdot\mathbf{r}_n]. \tag{3.24}$$

This model does not describe exactly the details of the process, but provides a very good qualitative description of the excess-deficiency features appearing in experimental patterns without increasing the computational load.

## 3.5 Experimental details

### 3.5.1 Hardware and software

All the experiments reported in this work were performed in a Sirion 200 Schottky FEG scanning electron microscope, as purchased without any additional modifications, from FEI instruments [164].

Additional hardware includes an ADLINK PCI-9221 [165], a 16-bit high-resolution and low-cost multi-function DAQ card, which has been used for the external control of the SEM's scanning coils, necessary for mapping purposes and a FTDI chip [166] used for implementing serial communication between hardware.

The readout system used for the Timepix detector consists of a FitPix interface [167]. The Timepix detector is described in more detail in section 4.3.

The commercial software used for the dynamical simulation of EBSD patterns is ESPRIT DynamicS [168]. It is a powerful dynamical EBSD pattern simulation software which allows the use of both kinematic models and dynamical theory of electron diffraction to simulate the EBSD patterns. The software supports the import of crystallographic phase definitions of various formats, CIF (Crystallographic Information File) and CEL (PowderCell), etc. ESPRIT DynamicS is particularly useful for the simulation of HOLZ rings and EBSPs from non-centrosymmetric crystals [153, 154, 168].

Microsoft Visual Studio C# [169, 170] was used for the creation of graphical user interfaces which have been used to interface hardware, including the Timepix detector, the ADLINK PCI-9221 card and the FTDI chip etc.

Pixelman [171, 172], a multi-platform data acquisition and processing software package for Medipix2, Timepix and Medipix3 detectors has been used for the data acquisition.

Anaconda [173], a high performance distribution of Python [174, 175] and the R [176, 177] scripting languages, have been used for generating scripts for data analysis and computing purposes.

ImageJ [178–180], an open source image processing program, has been extensively used for general image processing purposes.

### 3.5.2 Sample details

A number of specimens were used in this work, in order to illustrate the different aspects of each presented technique. These samples include:

- monocrystalline silicon, provided by Austin Day, grown with the standard Czochralski process [181]. This sample has been used for the acquisition of EBSD and RHEED patterns and to demonstrate the effect of energy filtering;

- monocrystalline GaN (gallium nitride) grown by metal organic vapour phase epitaxy (MOVPE) by Peter Parbrook, Tyndall National Institute, University College, Cork, Ireland. This sample has been used for the acquisition of EBSD and RHEED patterns and to demonstrate the effect of energy filtering;

- monocrystalline diamond, grown by chemical vapour deposition (CVD), provided by Alexandre Tallaire, Laboratoire des Sciences et des Procds des Matriaux LSP-MCNRS, Universit Paris 13, France [182, 183]. This sample has been used for the acquisition of EBSD patterns and to demonstrate the effect of energy filtering;

- polycrystalline WC (tungsten carbide) hardmetal with a cobalt binder phase, provided by Ken Mingard, National Physical Laboratory, London, UK. This sample has been used for the acquisition of EBSD maps;

- GaN nanorods, provided by Dr Philip Shields, University of Bath, Bath, UK [184]. This sample has been used for the acquisition of transmission diffraction patterns in the SEM;

- a cross section of a monocrystalline AlGaN (aluminium gallium nitride) layer structure grown on laterally overgrown AlN/$Al_2O_3$ provided by Professor Michael Kneissl, Technische Universitat, Berlin, Germany [185]. This sample has been used for the acquisition of TKD maps and to demonstrate the imaging with virtual detectors, discussed in Chapter 7;

- a monocrystalline AlGaN layer on a patterned sapphire substrate, grown by hydride vapour-phase epitaxy (HVPE), provided by Dr Simon Fleischmann, Ferdinand-Braun-Institut, Berlin, Germany [186]. This sample has been used for the acquisition of EBSD maps and to demonstrate the imaging with virtual detectors;

- thin films of amorphous $HfO_2$ (hafnium dioxide) grown on bulk silicon, grown by atomic layer deposition (ALD), provided by Dr Joseph Roberts, School of Engineering, University of Liverpool, UK. This sample has been used for the acquisition of detector diffraction patterns, discussed in Chapter 8.

# Chapter 4

# Description of the Timepix detector and its applications

## 4.1 Direct electron detectors

In the last few decades considerable progress has been made in the field of complementary metal-oxide semiconductor (CMOS) technology. It is now possible to pack a very large number of components into a very small area, allowing the creation of an application-specific integrated circuit (ASIC), consisting of integrated circuits customized and optimized for a specific rather than general purpose use. This makes possible the creation of detectors having increased functionalities [187, 188].

Commercial indirect detectors, based on phosphor screen/fibre optics-coupled CCDs still provide good performance for several applications, including electron diffraction [189, 190]. However the problem with indirect detectors is that their resolution is often limited by the intrinsic light scattering within the phosphor and by the number of inefficient steps (lenses and camera) necessary to convert the image on the phosphor into an electronic signal. Consequently, there is an increasing interest in the use of novel direct electron detectors, where the electrons are converted into an electronic signal without the intermediate light conversion step required for CCDs. This is achieved by the use of semiconductor material to convert the energy of a detected particle into an electronic signal, i.e electron-hole pairs.

There are two main reasons why the efficiency of direct detectors is higher than indirect detectors. Firstly, the energy necessary to create an electron-hole pair in a semiconductor is almost an order of magnitude lower than the energy necessary to create an optical photon in a scintillator, i.e higher signal to noise ratio. Secondly, in phosphors, the photons created within the scintillator are emitted in all directions, reducing the collection efficiency; in contrast, in direct detectors, a bias voltage is often applied to the sensor to minimize the charge losses in the lateral directions increasing the collection efficiency [188].

There are two main types of direct electron detectors used in microscopy: monolithic active pixel sensors (MAPSs) and hybrid pixel detectors (HPDs). The former are easier to construct; the sensor and readout electronics are located in the same layer, the manufacturing process is cheaper than for HPDs. In HPDs sensor and electronics are separated. This allows the implementation of detectors with more complex functionalities such as energy filtering and the use of different semiconducting materials as the sensor for example.

Although this work exploited the use of HPDs, specifically the Timepix detector, a basic description of MAPSs is given for completeness.

## 4.2 Monolithic active pixel sensors

A simplified schematic of a MAPS pixel is shown in Fig. 4.1. The pixel consists of three layers: a relatively thick substrate ($\approx 500$ $\mu$m thick), a thin epilayer (5-20 $\mu$m thick) and a thin electronics and passivation layer (2-4 $\mu$m thick).

The substrate is used as support and as a growth substrate for the detector and it does not play any part in the detection process.

When the incident particle interacts with the semiconductor material, electron-hole pairs are generated by impact ionisation within the epilayer and the substrate material. The electrons are collected by the electrode located in the epilayer. The holes are lost by recombination and do not contribute to the signal.

As an alternative to biasing of electrodes immersed in the detector, different doping levels in the electrode, epilayer and substrate are used to generate an inherent electron concentration gradient which leads the electrons to diffuse toward the electrode. In this case the bias voltage is not applied and the charge reaches the electrode by diffusion.

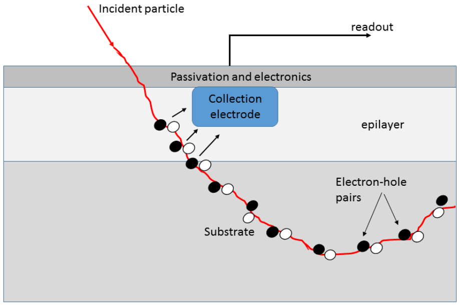

Figure 4.1: Sketch of a MAPS detector. The collected signal is the one contained in the epilayer, in the proximity of the collecting electrode. The signal produced in the substrate is lost or collected by other collection electrodes (not shown) far from the original incident location. Reproduced from Ref. [187].

The readout amplifier and electronics are located above the epilayer, which is covered with a passivation layer. Every pixel is read out sequentially and the signal from each pixel is amplified, sequentially, by a single electronic circuit.

An advantage of MAPSs is that their simple construction allows the production of a detector with a relatively small pixel size, of the order of 25×25 $\mu$m$^2$. However, a fraction of the incident electrons is backscattered from the substrate, creating a signal in regions far from the initial entry point. These electrons lose their energy as they travel along the substrate. When they are scattered back to the epilayer, their lower energy makes them contribute with a larger magnitude to the produced signal (electron energy loss being inversely proportional to the energy of the electron). This effect worsens the resolution. Also, only the portion of energy generated within the epilayer contributes to the signal. There is a fraction of signal which is lost in the substrate.

Another problem with MAPSs is related to the radiation hardness. Because the electronics is placed on the top surface, the incident particles, especially at higher energies and fluxes, may damage the electronic circuits reducing the lifetime of the detector.

## 4.3 Hybrid pixel detectors - Timepix

Timepix is a pixellated photon and particle detector and is one of the outcomes of an international collaboration (Medipix2) hosted at CERN, established to provide a solution for a range of problems in X-ray and gamma-ray imaging in hostile conditions [191]. The Timepix detector belongs to the CMOS hybrid pixel detectors family [161, 192].

Hybrid pixel detectors like Timepix or Medipix2 can be regarded as digital direct

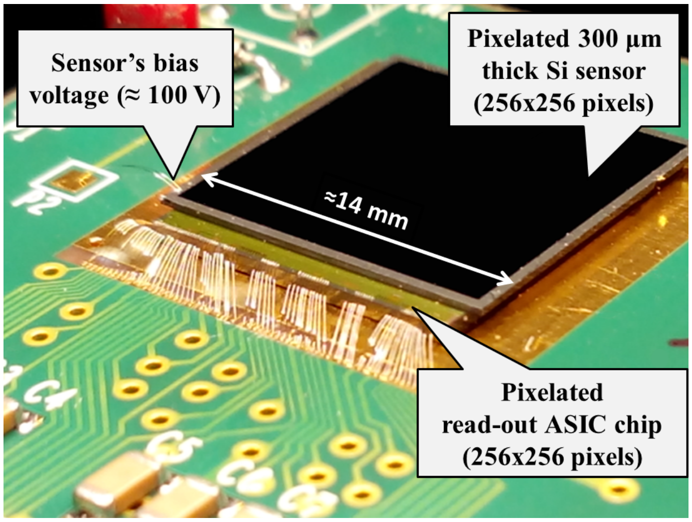

Figure 4.2: The Timepix detector

electron detectors. They provide a digital output rather than give an analogue output, as is the case for the widely used analogue detectors such as CCDs or MAPSs [187]. As already mentioned in the previous section, in the case of MAPSs the detector gives an analogue output proportional to only a fraction of the total energy deposited by the incident photon/particle on the sensor material [187, 193–199].

In the case of hybrid pixel detectors, the sensor and the electronics chip are independent, offering the possibility of a choice in the sensor material and sensor thickness depending on the specific application.

The detector consists of an array of individual independent counters, each having its own amplification circuit in the electronics chip. In the case of the Timepix chip the sensor and electronics are composed of 256 × 256 square pixels, each 55 $\mu m \times$ 55 $\mu m$ in size, covering a global surface of around 1.4 cm × 1.4 cm. An image of the Timepix chip is shown in Fig. 4.2.

It is also possible to combine chips to obtain a bigger sensor area. Each pixel of the sensor is electrically and mechanically connected to the corresponding pixel of the CMOS ASIC electronics chip [161, 187, 200, 201].

Each pixel of the electronics is basically composed of two blocks: an analogue and a digital part (see Fig. 4.3), together containing ≈ 550 transistors. The analogue part, which is the first stage of the amplification process, consists basically of an octagonal input, a shaping amplifier and a discriminator, with a polarity control pin and 4-bit threshold adjustment. The digital part consists of the Timepix synchronization logic (TSL), 14-bit shift register, reference clock, and an 8-bit pixel configuration register (PCR) [161], shown schematically in Fig. 4.3 as a counter. The digital part is responsible for the read-out and the interpretation of the signal depending on its acquisition mode.

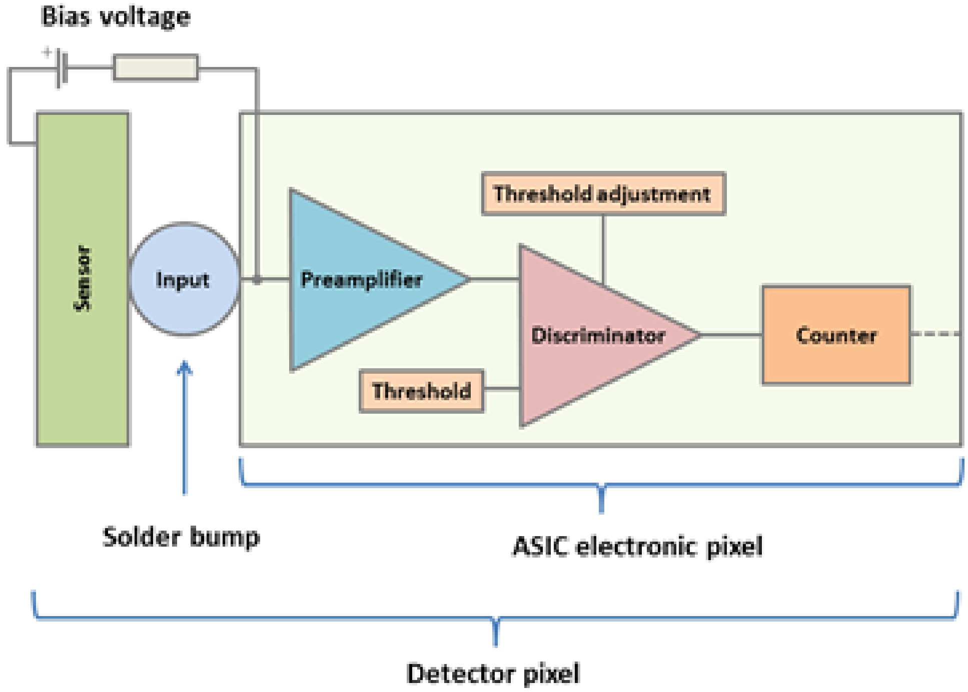

Figure 4.3: Schematic of the Timepix detector electronics.

The basic operating principle is as follows: when a particle hits a sensor pixel, a cloud of charge (electron-hole pairs) is generated within the material of the sensor. In contrast with the previously discussed analogue detectors, the quantity of generated charge is proportional to the total energy deposited within the sensor by the particle. The charge, drifting under the influence of the electric field applied to the sensor, is collected by the solder bump and transferred to the ASIC electronic chip [161, 192].

The signal from the sensor is amplified by the shaping preamplifier and then compared, by the discriminator, with a threshold value. If the signal is greater than the specified threshold value, the discriminator generates a logic signal whose width is proportional to the time for which the voltage at the output of the preamplifier is above the threshold. This output is interpreted by the digital part depending on the operation mode of the particular pixel.

A global threshold is set for all the pixels in the chip, but it can be adjusted individually for each pixel using the 4-bit adjustment placed on each discriminator, to compensate for small differences between pixels.

The optimum adjustment for each pixel is determined by performing an equalization of the matrix: this operation is referred to as a threshold equalization. This operation introduces a more uniform response between pixels within the global detector area. If the threshold level is set above the intrinsic noise of the device, it is possible to operate in noise-free conditions [161].

Each pixel of the detector can be individually programmed in order to work in one of the three possible configurations: Medipix, Time Over Threshold (TOT), and Time of Arrival (ToA) mode [161].

In Medipix mode the device is used as a counter. For each pixel, the internal counter increments one unit every time an electron has energy above the threshold value.

In TOT mode the internal counter registers the period of time in which the particle is above the threshold, thus giving energy information about the particle.

In ToA mode the internal counter registers the period of time, from the when the signal is above the threshold, to the end of the measurement.

This work reports the use of the detector in Medipix mode.

Images are recorded using an exposure which does not overflow the maximum pixel counter range (around 11800 counts per frame), but acquisition in integral mode, performed by continuously summing up frames, allows acquisition with a virtually infinite dynamic range (as long as the exposure time for each frame is short enough not to overflow the counter range).

The whole chip can be read out serially, in less then 10 ms using the low voltage differential signaling (LVDS) driver on the chip, or in parallel in less then 300 $\mu$s using the 32-bit CMOS port, using a 100 MHz readout clock [161, 187]. In this work, a serial readout was used and the read out operation and data acquisition were managed by a FitPix readout interface [167] and Pixelman software [172, 202].

In a hybrid pixel technology the sensor is separate from the electronics, and there is negligible radiation damage from the incident particle if the energy of the particle is below a specific value. This value depends on the sensor thickness and detector composition. For 300 $\mu$m thick silicon this threshold is well above 100 keV [193].

The sensor used in our experiments was 300 $\mu$m thick silicon. In the range of energies available in a SEM, typically from 0 to 30 keV, the problem of radiation damage can be neglected.

## 4.4 Imaging properties of the detector

The spatial resolution of an imaging system can be quantified using the modulation transfer function (MTF), which describes the response of the detector to a sinusoidal input image having a given spatial frequency.

Another important quantity is the noise power spectrum (NPS), which describes the spectral component of the noise added to the image by the detection system. These two quantities may be combined to obtain the detective quantum efficiency (DQE), which describes the global system performance, that is the degree of degradation introduced by the detector to the input signal. A characteristic value of the DQE for a detector is the one referring to the zero spatial frequency, which is considered as the effective quantum efficiency of the system.

In electron microscopy the MTF is usually obtained by using a shadow on the detector obtained by illuminating a straight edge. The intensity profile in the direction perpendicular to the edge will have a s-shape form, which is called the edge spread curve. Bright, $b$, and dark, $d$, field values are obtained by averaging the pixel value at the two sides of the edge. The values are then used to obtain the normalized edge spread function $n(x)$:

$$n(x) = \frac{e(x) - d}{b - d} \tag{4.1}$$

where $e(x)$ is the average pixel value at distance x from the edge. Differentiating $n(x)$ with respect to $x$, the line spread function (LSF(x)) is obtained. The MTF is the Fourier transform of the LSF. Usually both LSF and MTF show a Gaussian trend; a more detailed description can be found in [203].

In a digital image the noise contained in the image can be measured as the variance of the pixel to pixel fluctuation in the image. A spectral decomposition of this noise is expressed by the NPS which is the Fourier transform of the noise auto-covariance function. The normalized NPS can be expressed as

$$NPS_{norm} = |\mathscr{F}(\frac{X_{ij} - \mu}{\mu})| \tag{4.2}$$

where $\mathscr{F}$ indicates the Fourier transform, $X_{ij}$ the measured counts over the matrix after the flat field correction, and $\mu$ the mean count in the matrix.

The DQE can be defined as

$$DQE = \frac{(S/N)^2_{out}}{(S/N)^2_{in}} = \frac{MTF^2(f)}{\Phi \times NPS_{norm}(f)} \leq 1 \tag{4.3}$$

where $S$ and $N$ are referred to signal and noise respectively, $\Phi$ the number of incident particles and $f$ the spatial frequencies. For a detector like Timepix, the MTF, NPS and DQE vary as a function of the applied threshold level [193, 204].

When a particle hits the border of a pixel, it can share part of its energy between pixels. In this case, if the threshold level is high enough, the total amount of energy deposited in the main pixel is not high enough to trigger the pixel count. There is therefore a reduction in the effective active area, which leads the periphery of the pixel to be effectively not active. For this reason, as the threshold is increased the reduced charge sharing effect results in a consequent increase in the MTF, which can reach a value larger than the theoretical value of MTF obtainable using the Nyquist sampling theory for a specific pixel pitch [193, 204]. On the other hand, an increase in the threshold level causes an increase in the NPS, with a consequent reduction in the $DQE \propto MTF^2/NPS$, which depends on both MTF and NPS. In general DQE and MTF depend on the sensor material.

The properties of the Medipix2 chip have been characterized by Tlustos el al. [204]; the MTF and DQE were measured using the spectrum from a 25 keV W-tube, and a 300 $\mu m$ thick silicon sensor. Using a threshold energy of 9.1 keV the DQE was found to reach a value as high as 25-26%, which approaches the maximum theoretical value of 27% for the detector. Using a threshold energy of 18.5 keV, the DQE was found to reduce to 5%.

Spatial resolution has been found to vary between 8.2 line-pairs/mm at 9.1 keV and 11 line-pairs/mm at 18.5 keV, when the MTF is at the 70% of its maximum [204].

All the characteristics of hybrid pixel detectors as presented above make this family of detectors unique compared to other currently existing technologies. A more detailed description of the detectors and a comparison between the technologies of different detectors and their performance are described in Refs. [187, 193].

## 4.5 Development of a novel calibration method for Timepix

As discussed in section 4.3, energy discrimination is an intrinsic feature of the Timepix detector, which allows the use of the detector as a high-pass filter: that is, counting only particles having an energy above a specific threshold value. The filtering process is something that happens at the electronic level. The user can set the Timepix energy threshold by choosing from among a discrete number of digital values. Once a specific digital value is selected, it is converted through an internal digital-to-analogue converter (DAC) into a voltage (the internal value is not accessible).

Practically speaking the digital values used for setting the Timepix threshold are only unit-less numbers. In order to be able to select a specific energy of the threshold, expressed in volts, a calibration procedure which relates the digital threshold values to a particular energy is necessary.

This section describes and shows the experimental results obtained by using the calibration method developed (by the author) to calibrate the digital threshold in the Timepix detector. This method is used to quantify the energy filtering in all experiments in this thesis.

The conventional methods to calibrate the Medipix family of detectors uses monochromatic radiation sources, which could be either sharp peaks from radioactive nuclides [205], or monochromatic electron beams from other sources [193].

The calibration method consists of monitoring the particle count as a function of the applied threshold. This is referred to as a threshold scan, when the area of the sensor is illuminated with a particle source having a known energy distribution. When counting the number of detected photons emitted from a monochromatic source as a function of the threshold value, the particle count increases abruptly when the threshold is decreased from energies above the energy of the specific source to lower values. When plotting the particle count as function of the applied threshold, the function ideally should appear as a step curve. In reality due to the energy resolution of the detector, this step is more likely to be a s-shape function.

Figure 4.4(a) shows the experimental result obtained from a Timepix detector when a threshold scan is acquired from a $^{65}$Zn nuclide, which has an X-ray emission peak at 8.03 keV [206]. By differentiating the threshold scan a Gaussian-like function is obtained, having a maximum at the threshold value corresponding to the energy of the source, as show in Fig. 4.4(b).

By repeating this operation for different sources, and plotting the threshold value corresponding to the maximum of each peak as function of the emission energy of the corresponding nuclide, it is possible to obtain a calibration line by linear fitting.

From a Gaussian fit of the peak shown in Fig. 4.4(b), it was possible, using the resulting calibration line, to determine the full width at half maximum (FWHM) of

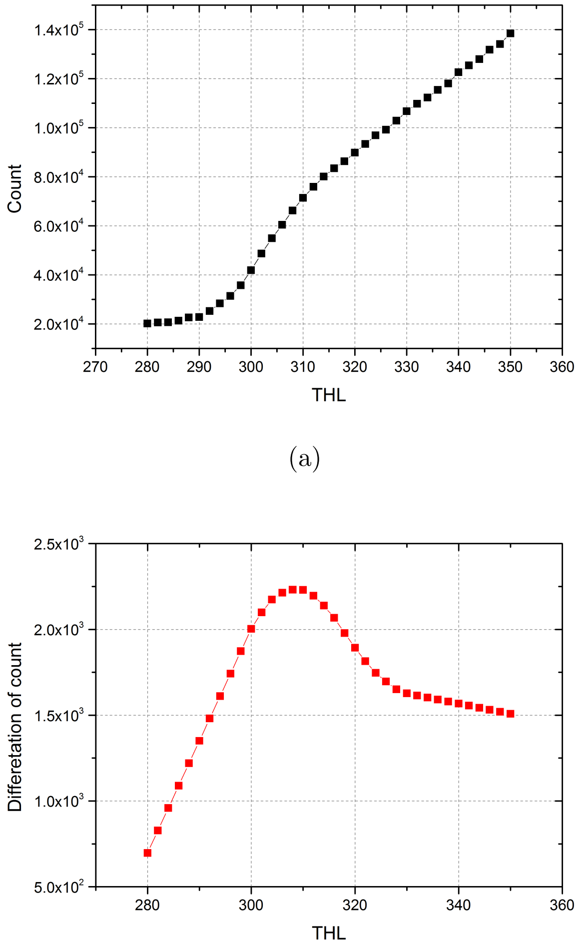

(a)

(b)

Figure 4.4: Result of a threshold (THL) scan using $^{65}$Zn: (a) threshold scan and (b) differentiation of the threshold scan.

the peak to be ≈1.9 keV. This corresponds to ≈ 23.8% at 8.06 keV [206]. This value is consistent with the measurement performed by other authors in Ref. [207], where they reported an energy resolution of 23% at FWHM at 8.64 keV [207].

In our facility, the only means available for the calibration were the radioactive nuclides, and the monochromatic source of electrons generated by the electron beam of the SEM.

The calibration of the detector using radioactive sources is a very time consuming operation, and it requires many hours for the calibrations, even days, depending on the activity of the nuclides. For this reason the electrons generated by the SEM electron gun has been used as the source for the calibration.

This method does have disadvantages. Usually the electron beam available in the SEM consists of a well focused beam, which even if defocused is no larger than a pixel of the detector, so it is hard to illuminate the whole chip.

Another problem arises from the fact that the beam current available in the SEM is usually too large for this task and, when focused in one or a few pixels of the detector, the number of incident particles is larger than the maximum count per frame which the detector is able to handle. To overcome this problem, the threshold calibration used for the EBSD experiments was performed by using the backscattered electrons from the sample as a source.

After the interaction with the specimen, the electron beam is spread out with a wide angular distribution, so that it illuminates the whole chip. The energy distribution of backscattered electrons is broad as well, but with a maximum energy defined by the energy of the primary beam. A threshold scan performed using the latter method is shown in Fig. 4.5(a).

In contrast with the threshold scan obtained using a monochromatic source of X-rays, the threshold scan performed using the backscattered electrons does not show

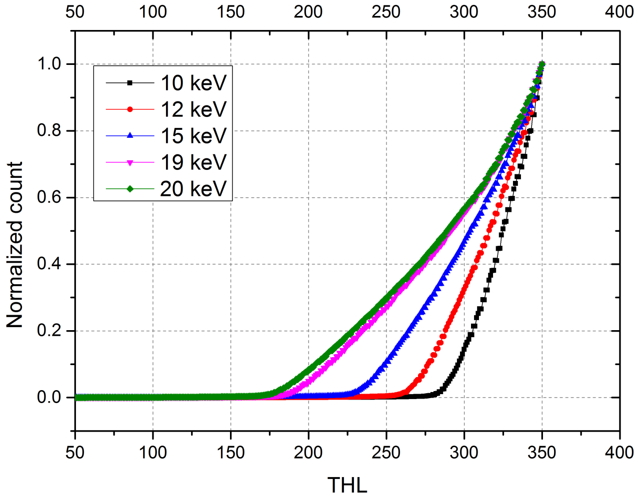

(a)

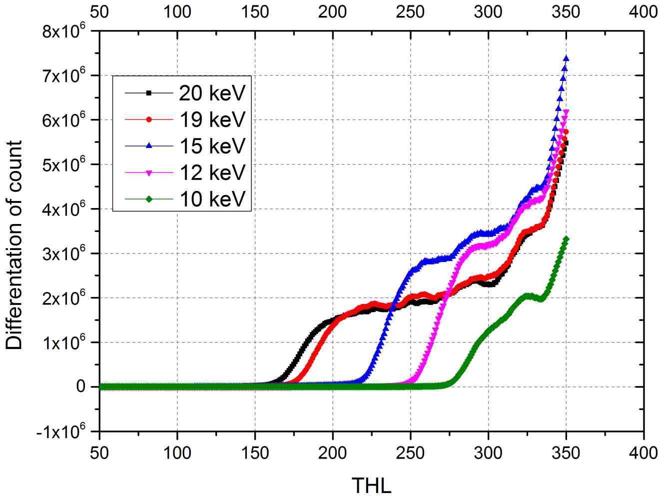

(b)

Figure 4.5: Result of a threshold (THL) scan using backscattered electrons from GaN: (a) threshold scan and (b) differentiation of the threshold scan.

a s-shape trend, but it is characterized by a well defined offset, corresponding to the energy of the primary beam, below which the count is negligible, and above which the count begins to rise monotonically until the minimum threshold is reached.

The advantage of this method is that it is possible to obtain a calibration line using the SEM electron beam as the source, whose energy can be varied continuously from zero to 30 keV, with a very high precision.

The dataset for the calibration is obtained by extrapolating to zero the threshold scan for each energy of the electron beam used. As in the case of nuclides, the threshold scans is differentiated to find the zero intercept of the resulting curves, shown in Fig. 4.5(b).

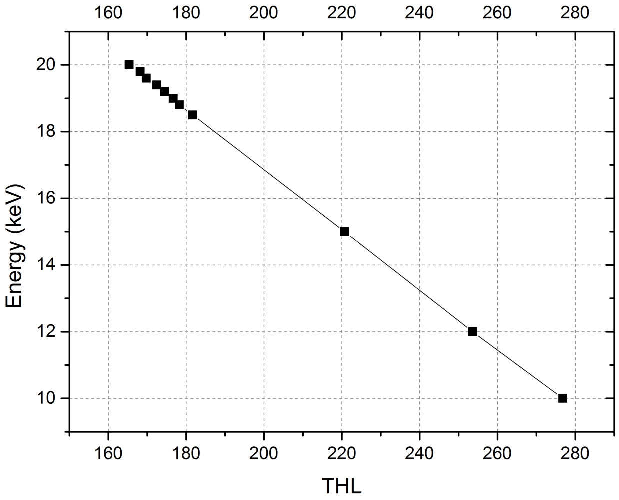

Figure 4.6: Threshold (THL) calibration line using backscattered electrons as the source.

The resulting calibration line shows excellent linearity, as shown in the plot in Fig. 4.6. The result of the linear fit is the following:

$$\begin{aligned}\text{Energy (keV)} &= -902.6\times10^{-4}\ (\pm2.9\times10^{-4})\text{keV}\times THL + 3493.6\times10^{-2}\ (\pm5.8\times10^{-2})\text{keV},\\ R^2 &= 0.99989.\end{aligned}$$

From the slope of the calibration line it can be seen that the minimum increment of the threshold value, i.e. the increment of the threshold energy when the digital value of the threshold is incremented by one unit, corresponds to approximately 90 eV.

The fitting parameters obtained using the threshold value may vary when a threshold equalization is performed. This can be avoided by using an effective threshold, which is obtained by subtracting the DC voltage at the output of the Timepix pre-amplifier from the threshold value. The effective threshold is independent of the threshold equalization. There is a linear relation between threshold and the effective threshold.

The calibration with the backscattered electrons has been compared with the calibration obtained using the radioactive nuclides. This is shown in Table 4.1. The fitting parameters refer to the calibration of the effective threshold, since the measurements were performed with different threshold equalizations.

## 4.6 Discussion

A comparison between the two calibration lines shows that the two slopes are the same, within the uncertainty of the measurement, but there is a difference between the value of the two intercepts, which falls outside the experimental uncertainty. There is also a small difference in the $R^2$ coefficient between the two linear fits. The discrepancy between the values of the two intercepts may probably be attributed to

| Source type | Slope <br> [keV $V^{-1}$] | Uncertainty on the slope [keV $V^{-1}$] | Intercept <br> [keV] | Uncertainty on the intercept [keV] | $R^2$ |
|---|---|---|---|---|---|
| Nuclides | -220 | 7 | 6.8 | 0.3 | 0.99475 |
| Backscattered electrons | -220 | 2 | 7.3 | 0.1 | 0.99947 |

Table 4.1: Comparison of the fitting parameters obtained for the effective threshold energy calibration, using radioactive sources and backscattered electrons as the source respectively.

two major contributions.

The first is the effect of the temperature. Preliminary measurements have shown that there is a significant increase in the temperature of the Timepix chip, which may be higher than 30 °C, when it is operating under vacuum conditions. In this case the dissipation of the heat produced by the chip itself is strongly reduced when compared to the dissipation of the heat occurring when the chip is operating in air at atmospheric pressure.

In our case the two calibration lines were obtained using two different experimental conditions; the measurements performed using radioactive sources were obtained at atmospheric pressure at room temperature, and the measurement performed in the SEM were obtained under vacuum. Because the energy calibration is sensitive to variations of the temperature, it is reasonable to expect an offset between the two calibration lines.

Temperature compensation in the calibration line would be beneficial and could significantly improve the energy response of the detector. Also, the use of an on-chip cooling system would be beneficial for improving the energy resolution of the detector and for selecting and maintaining a stable and appropriate operating temperature.

A second possible contribution to the observed variation in the offset of the two calibration lines may be attributed to the presence of an inert layer deposited on top of the detector chip, usually called the entry window. This layer typically consists of a thin film of aluminium or p-doped silicon which is used as a contact for the bias voltage of the sensor. The energy deposited in this volume by the incoming particles is lost, and the charge generated by the incident particle in this region is not amplified, i.e. does not contribute to the detection process. Electrons, especially at low energies, interact more strongly with matter when compared to X-rays. It may be possible that an offset in the energy calibration may be introduced by the difference in energy loss by the electrons compared to X-rays in the entry window. This offset should then depend on the thickness and composition of the entry window. Unfortunately this information is not accessible to us. This could be the topic of a future project where the energy offset in the calibration line could be measured for detectors having different thin window thickness and compositions, under the same experimental conditions.

The difference between the $R^2$ coefficient of the two linear fits is probably due to the quality of the Gaussian fit used to determine the position of the emission peaks in the nuclide spectrum, especially in a noisy dataset acquired from elements with low activity.

From the measurements reported in this section and the issues discussed above, it can be concluded that it is more appropriate to calibrate the detector using electron sources. The method implemented offers a series of advantages, such as the time necessary to perform the calibration, precise control of the beam energy and the availability of a continuous range of energies. Furthermore there is no need for radioactive materials, which are not always available in laboratories.

Additionally the use of the electron beam as the source for the calibration of the detector might allow a pixel by pixel calibration, which is an operation which generally requires a very long time using radioactive sources. This may be possible if the electron beam can be operated with a very low current and focused on individual pixels, one by one, in an automated manner. This might be an intriguing proposal for future work.

# Chapter 5

# Digital direct electron imaging of energy filtered EBSPs and TKD patterns

This chapter describes the system implemented for the digital direct acquisition of energy filtered EBSPs and TKD patterns using the Timepix detector, demonstrating the advantages of direct electron imaging detection and energy filtering.

## 5.1 Direct electron imaging of EBSD patterns

### 5.1.1 Advantages of direct electron imaging

The use of the Timepix detector for electron imaging avoids the use of the phosphor screen and CCD camera combination, and allows energy filtering to be accomplished without any additional hardware. As shown later in this chapter, the advantages of this system are a reduction in the beam current and acquisition time compared to conventional systems, noiseless acquisition (if the threshold level is set above the electronic noise of the device, it is possible to operate in noise-free conditions), and most importantly, energy discrimination [208]. In addition EBSPs can be acquired over a wide range of energies compared to conventional detectors.

These detector features make possible the acquisition of EBSP containing small-scale details which are not in practice obtainable with existing commercial EBSD systems [208]. This will provide new routes to, for example, the determination of lattice constants, crystal phase identification and the mapping of strain with greater sensitivity.

Wilkinson et al. [209] have demonstrated the advantages of using direct electron imaging for the acquisition of EBSPs. They used a directly exposed (CMOS) monolithic active pixel sensor detector and demonstrated that higher quality patterns may be acquired compared to those recorded using conventional indirect detectors, particularly at low voltages. Here the use of a substantially different detector, the Timepix, is demonstrated which has the additional advantage of applying energy filtering [208].

In our experiments EBSPs were acquired in an FEI Sirion Schottky field emission scanning electron microscope operating in spot mode. Our detector was positioned in a conventional EBSD geometry, in front of a flat/polished specimen which was tilted so that the sample normal was 70° away from the direction of the incident electron beam. For all the EBSPs shown in this chapter, the detector-to-specimen distances and capture angles were determined subsequent to measurement by comparison of the acquired EBSPs with dynamical simulations of the EBSPs produced using Bruker's ESPRIT DynamicS software [168].

Except for when explicitly stated, all the EBSPs shown have been flat fielded by dividing the as acquired EBSP by an image acquired on scanning the beam over a large area of the sample. Scanning the beam effectively averages out the diffraction information so no diffraction pattern is observed, thus providing a background which can be used to flat field the raw EBSPs.

Acquisition times were set depending on beam energy, beam current, the mass and density of the material under study and the required quality (signal to noise ratio) of the EBSP.

To date EBSPs have been acquired with the Timepix detector, which were of sufficient quality to allow identification of the Kikuchi bands, with acquisition times down to 0.5 ms. Fig. 5.1 shows examples of as acquired (i.e., not flat fielded) energy filtered EBSPs from a single crystal GaN thin film recorded with acquisition times of 0.5, 1 and 5 ms respectively.

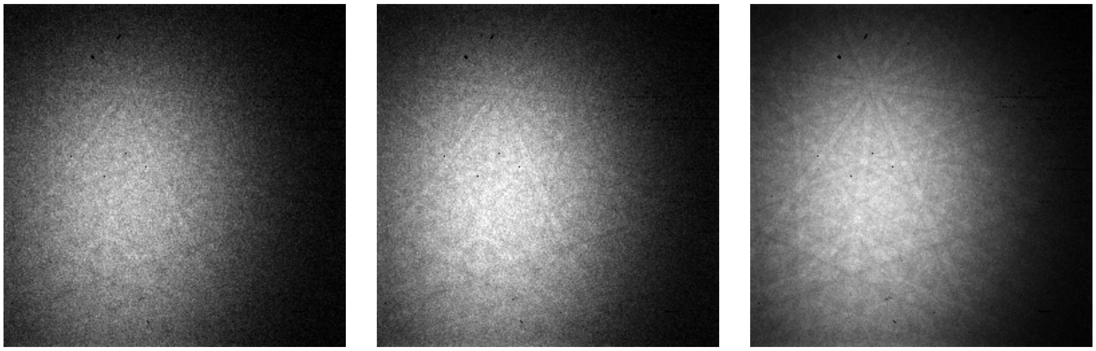
(a) (b) (c)

Figure 5.1: Fast acquisition of energy filtered EBSPs from a single crystal GaN, obtained using a 20 keV electron beam, ≈ 20 nA beam current, 19.4 keV threshold energy, ≈ 5 mm specimen-to-detector distance: (a) 0.5 ms, (b) 1 ms, (c) 5 ms. Reproduced from [208].

These were obtained at an incident beam energy of 20 keV with a threshold energy of 19.4 keV, a beam current of order 20 nA, and a detector-to-specimen distance of ≈ 5 mm providing a capture angle of ≈ 100°. With this measurement we want to stress the fact that the detector allows fast acquisition of EBSPs even using strong energy filtering. On the other hand the EBSP acquired with an acquisition time of

0.5 ms (Fig. 5.1 (a)), shows that the mean count per pixel is very small, close to the limit at which the pattern does not contain enough signal to produce a complete EBSP; in fact a mean count per pixel of the order of 30 ± 22 electrons over the chip was measured.

The intensity of the electrons has an angular dependence and at the edges of the EBSP the number of counted electrons is extremely small, even zero. This shows that the acquisition time is not limited by the detector but by the available electrons, which is determined by the beam current, angular distribution and energy distribution of backscattered electrons.

As mentioned before, the detector allows the acquisition of EBSPs over a large range of energies. To date EBSPs have been acquired at incident electron beam energies down to 3 keV. An example of low energy imaging of EBSPs is shown in Fig. 5.2.

Patterns were acquired from silicon and GaN using a beam energy of 5 keV, using a beam current of $\approx$ 1.5 nA and an acquisition time of 4 and 100 s for silicon and GaN respectively. Even at low beam energies the pattern shows a lot of detail.

At the bottom of the EBSP from GaN (Fig. 5.2 (b)), it is interesting to see the presence of RHEED spots appearing in the pattern. The observation of RHEED spots led to a change in the detection geometry in order to acquire RHEED patterns. This novel technology was subsequently used to investigate the topic of coherent scattering from a surface. This topic is also discussed in Chapter 6.

### 5.1.2 Effect of the energy filtering on the Kikuchi contrast

To demonstrate the effect of energy filtering, EBSPs were acquired from diamond, Si and GaN single crystal films with an incident electron beam energy of 20 keV, a probe current of $\approx$ 10 nA and detector-to-specimen distances of between $\approx$ 8 and

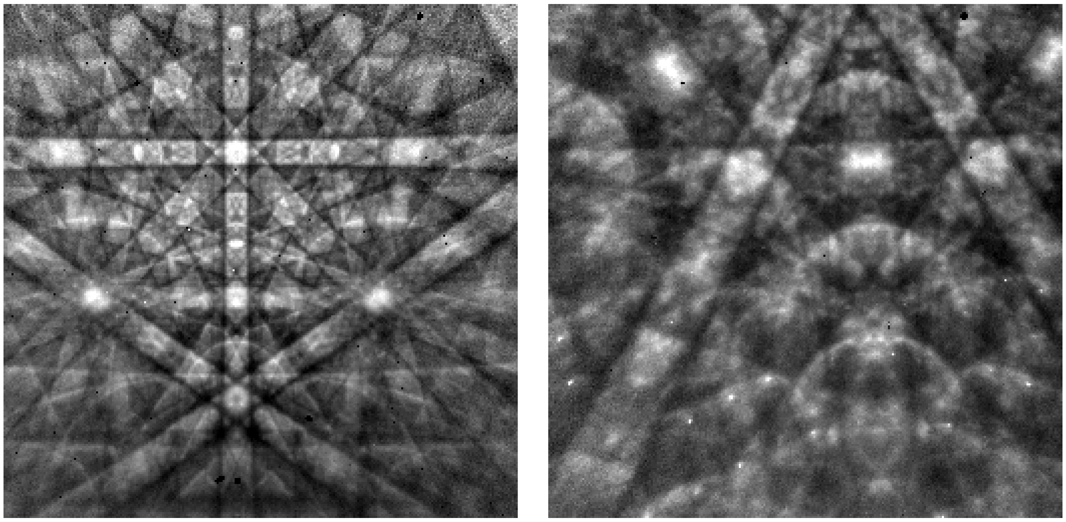

(a) (b)

Figure 5.2: Low energy acquisition of EBSPs: (a) Si (diamond-structure), (b) GaN (wurtzite) acquired using 5 keV electron beam. No energy filtering is applied.

15 mm, which provided capture angles of between ≈ 80° and 50°; these are shown in Fig. 5.3.

These materials were selected to demonstrate the capabilities of the Timepix detector for materials with a range of masses and densities. Flat fielded EBSPs were acquired with the Timepix threshold energy set low (5.5 keV for diamond and GaN and 4.6 keV for Si) and set high and close to the incident beam energy (19.4 keV for all three samples). The low threshold was chosen to be sufficiently above the electronic device noise, in order to work in noise-free conditions.

The threshold energies were determined using the energy calibration procedure discussed in Chapter 4.5. The acquisition times were set so that for each sample, approximately the same total number of electrons was collected at both low and high threshold energies. The number of electrons, acquisition times and the ratio of acquisition times are given in Table 5.1.

To maintain the same number of collected electrons required an increase of the acquisition time by a factor of ≈ 125 for diamond, ≈ 30 for Si and ≈ 6 for GaN re-

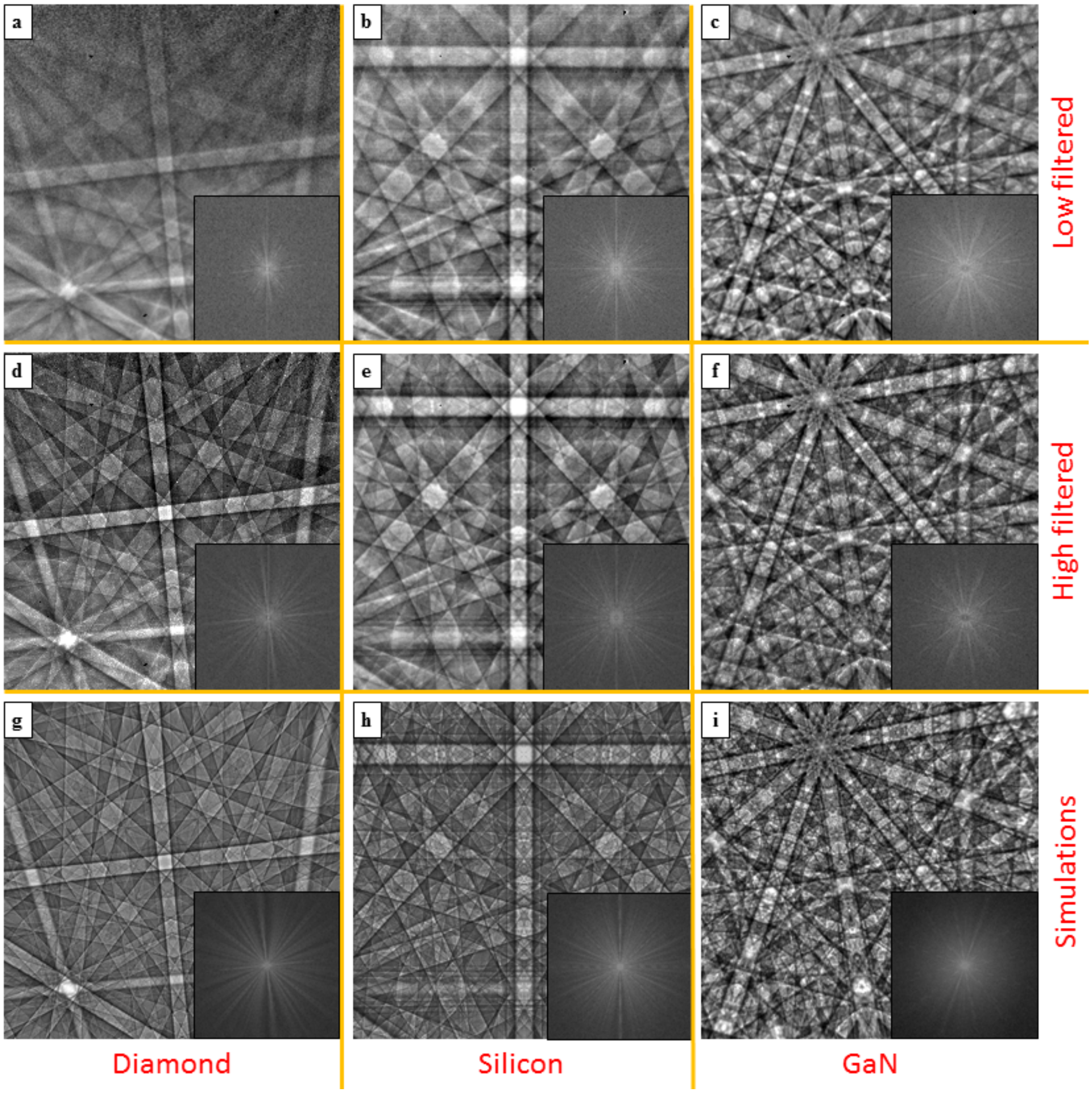

Figure 5.3: Comparison between EBSPs acquired from different specimens using different threshold levels. Reproduced from [208].

| Specimen | Threshold energy [keV] | Count | Acq. time [s] | Ratio |
|---|---|---|---|---|
| Diamond | 5.5<br>19.4 | $7.00\ 10^8$<br>$7.00\ 10^8$ | 0.8<br>100 | ≈125 |
| Silicon | 4.6<br>19.4 | $4.00\ 10^{10}$<br>$4.00\ 10^{10}$ | 50<br>1482 | ≈30 |
| GaN | 5.5<br>19.4 | $6.00\ 10^9$<br>$6.00\ 10^9$ | 10<br>60 | ≈6 |

Table 5.1: Comparison of acquisition times for diamond, silicon and GaN samples with change in threshold energy. Reproduced from [208].

spectively. The differences in this ratio of acquisition times may be attributed to the differences in the energy distribution of backscattered electrons for these materials.

The differences between the energy distributions of electrons backscattered from light, low density materials and heavy, dense materials are illustrated in Fig. 5.4 which shows the Monte Carlo simulations of the backscattered electron energy spectra for Si (atomic weight 28, density 2330 kg $m^{-3}$) and Au (atomic weight 197, density 19300 kg $m^{-3}$).

The simulations shown in Fig. 5.4 (provided by Dr Aimo Winkelmann) use a differential inverse inelastic mean free path approach, which has been found to predict correctly both the elastic peak at the energy of the primary beam, as well as the plasmon loss peaks observed in experiment [210]. The intensities have been normalized so that the integrated backscattered intensity from 20 keV to 10 keV is equal to 1. Au has a relative elastic peak intensity of 0.055 while for Si it is 0.0045.

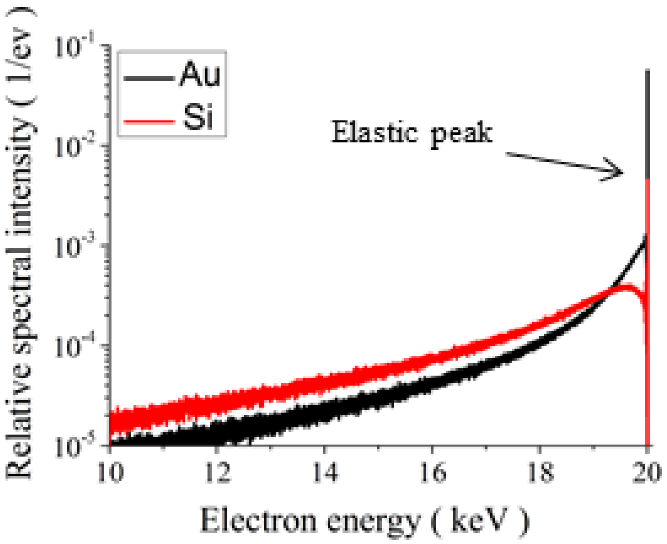

Figure 5.4: Monte Carlo simulations of the backscattered electron energy spectra for Si and Au respectively. The intensities have been normalized so that the integrated backscattered intensity from 20 keV to 10 keV is equal to 1. Reproduced from [208].

This means that for Au, 5.5% of the total (10-20 keV) number of electrons is in the elastic peak alone, while for Si it is only around 0.5%. In addition, for Au there is a greater intensity of electrons near the elastic peak than for Si.

Simulations of EBSPs for diamond, Si and GaN using the dynamical diffraction theory approach (see Chapter 3.4.3) were carried out for a range of single energies from 18 keV to 20 keV at intervals of 500 eV. As the energy changes, subtle changes are observed in the EBSPs. By comparing the experimental patterns with the simulations, the simulation at an energy of 19.5 keV provided the best match to the EBSPs acquired with high threshold energy, based on the normalized cross correlation coefficient. These are shown in Fig. 5.3 for diamond, Si and GaN respectively.

The insets placed at the bottom-right of each EBSP in Fig. 5.3 show the power spectrum of the EBSP obtained by performing a 2-dimensional Fast Fourier Transform (FFT) on the pattern. These power spectra provide an indication of the global EBSP quality; that is a measure of the detail, contrast and sharpness of the diffraction pattern.

A 2-dimensional power spectrum is a 2 dimensional histogram showing the intensity of each spatial frequency contained in the image. The lower frequencies are located close to the centre of the power spectrum; the frequencies increase with increasing distance from the centre.

To illustrate the effect of filtering on the observation of higher order Kikuchi bands more clearly, Figs. 5.5 (a) and (b) show zoomed-in images (from Fig. 5.3) of a region around the (220) band for both high and low energy filtered EBSPs from Si. Figs. 5.5 (c) and (d) shows this band isolated from the rest of the pattern through selecting the FFT wave-vector directions associated with this band in the FFT spectrum and taking the inverse FFT [211].

To obtain a measure of the improvement in contrast in the EBSPs of energy filtering, the average contrast was calculated for a Kikuchi band profile for both as acquired (i.e., not flat fielded) low and high energy filtered EBSPs. The contrast is defined as:

$$C = \frac{\text{Maximum intensity} - \text{Minimum intensity}}{\text{Maximum intensity} + \text{Minimum intensity}} \tag{5.1}$$

The improvement in the Kikuchi contrast has been calculated from the raw data, and not from the flat-fielded images, in order to avoid the calculation of any enhancement arising from the flat field operation itself. Table 5.2 summarises the results obtained for all samples.

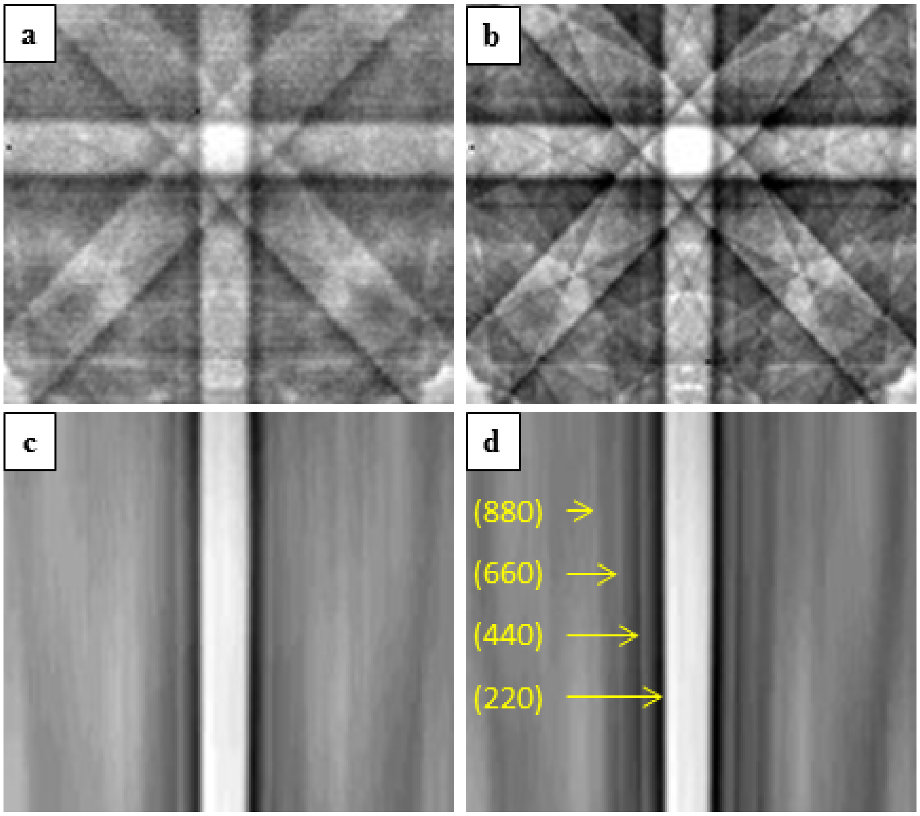

Figure 5.5: "Zoomed in" regions from EBSPs from a diamond-structure single crystal Si acquired with (a) low threshold, (b) high threshold energies, (c) and (d) show the extracted (220) and higher order Kikuchi bands from the EBSPs shown in (a) and (b) respectively. Reproduced from [208].

### 5.1.3 Suppression of excess-deficiency lines in EBSPs

Finally, to further investigate the subtle changes in the diffraction features on energy filtering, the detector was placed further away from the sample and EBSPs acquired with a smaller capture angle of $\approx 30°$. Fig. 5.6 shows EBSPs (flat fielded) acquired from silicon with an incident electron beam energy of 30 keV, a probe current of $\approx 2.5$ nA, and an acquisition time of 100 s. Fig. 5.6 (a) shows an EBSP acquired with a low threshold energy, Fig. 5.6 (b) shows an EBSP acquired at high threshold energy and Fig. 5.6 (c) shows the difference between (a) and (b) obtained

| Specimen | Threshold energy [keV] | Band | Contrast | Contrast enhancement |
|---|---|---|---|---|
| Diamond | 5.5<br>19.4 | {220}<br>{220} | 0.037<br>0.149 | $\approx 4.0$ |
| Silicon | 4.6<br>19.4 | {220}<br>{220} | 0.0304<br>0.0744 | $\approx 2.5$ |
| GaN | 5.5<br>19.4 | $\{11\bar{2}0\}$<br>$\{11\bar{2}0\}$ | 0.074<br>0.159 | $\approx 2.1$ |

Table 5.2: Comparison of contrast for low and high energy filtered EBSPs. Reproduced from [208].

by first flat fielding the raw EBSPs, normalising the resultant images and subtracting (b) from (a).

Note that the difference in the patterns result in asymmetric intensity features on the upper and lower sides of the non-vertical Kikuchi bands. This may be the result of differences in the contribution of inelastically scattered electrons to each of the different-energy-filtered EBSPs. Close examination of Fig. 5.6 (a), the EBSP acquired with the low threshold energy, reveals that the intensity profile of the Kikuchi bands is asymmetric, that is one side of a band is brighter and the other darker than would be case for a symmetric intensity profile. This is highlighted by the line profile of band A as shown in Fig. 5.6 (d).

This excess-deficiency effect may be attributed to anisotropic inelasting scattering of electrons resulting from the geometry of the measurement and the differential cross section for inelastic scattering [163].

This excess-deficiency effect is unexpectedly reduced in the high energy threshold filtered EBSP shown in Fig. 5.6 (b) (also see corresponding line profile of band A in Fig. 5.6 (d)).

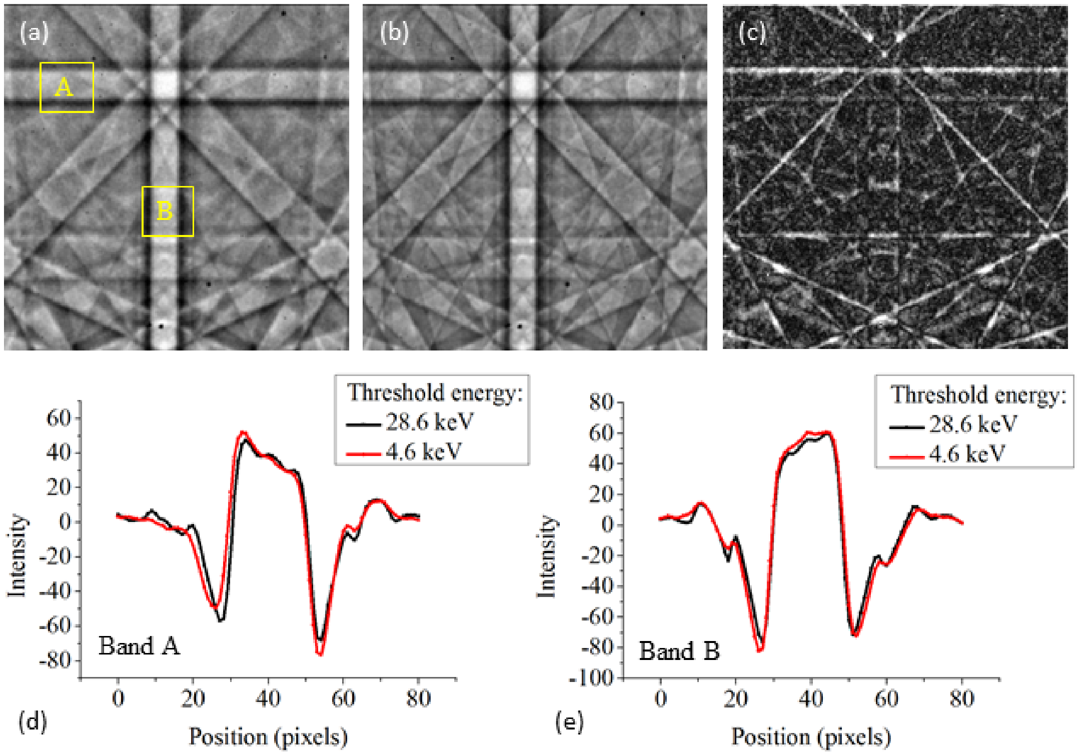

Figure 5.6: EBSPs from a diamond-structure single crystal silicon for an incident beam energy of 30 keV, a probe current of ≈ 2.5 nA, an acquisition time of ≈100 s, a detector-to-specimen distance of ≈ 30 mm providing a capture angle of ≈ 30°, (a) a threshold energy of 4.6 keV (b) threshold energy of 28.6 keV (c) difference between (a) and (b) (d) mean Kikuchi band profile for band A in (a). Reproduced from [208].

### 5.1.4 Discussion

For the EBSD geometry, the first significant result is illustrated in Fig. 5.1. EBSD patterns were obtained using a very high frame rate, up to 2000 frames per second, using a relatively small beam currents, ≈20 nA. EBSPs acquired with acquisition times of 0.5, 1 and 5 ms, using an electron beam energy of 20 keV and a threshold energy of 19.4 keV still contain visible diffraction patterns. It is interesting to note the high signal to noise ratio in the EBSP acquired in 0.5 ms, Fig. 5.1(a), where a diffraction pattern is discernible in the image even though the count is of the order of 30 ± 22 counts per pixel and in the outer part is sometimes zero. This result is promising because it proves the capability of the detector to handle high frame rates, even when energy filtering is applied. On the other hand it shows that in certain circumstances the beam current might be an issue. Sometimes a high beam current can be detrimental in mapping, since it may cause damage to some specimens, it can induce a drift of the electron beam due to local charging of the surface and can induce carbon deposition on the surface due to presence of contaminants in the SEM chamber, etc. In these cases, the current has to be kept low and there is a limitation to the maximum frame rate obtainable with EBSD, since there would not be enough electrons to form a usable EBSD pattern.

The other advantage of direct electron detection is the ability to perform low energy imaging, as shown in Fig. 5.2. Typically commercial EBSD phosphors used in indirect detectors are not optimized to work at low energies. In contrast, the Timepix detector allows a wide range of energies to be used, from kilo electron volts to mega electron volts (Timepix having been primary designed for particle physics [161, 212]).

Low energy imaging is important for many applications. In particular low energies lead to reduced electron-specimen interaction volumes. This allows a drastic increase in the spatial resolution of EBSD, which can be used to study truly nanostructured materials having reduced grain size, or allows changes of the texture to be revealed over a smaller length scale. It could also allow EBSD to be applied to more sensitive materials where the use of low energy electrons is a requirement. EBSD patterns acquired at low beam energies show also a strong Kikuchi contrast, without any energy filtering applied. This should lead to easier indexing of the EBSD patterns.

One of the most important possibilities in using the Timepix detector is the ability to perform energy filtering. In general as illustrated in Fig. 5.4, for lighter, less dense materials the backscattered electrons have a much broader energy spectrum; that is there are more electrons with higher energy loss, so fewer with energy close to that of the incident electron beam. Therefore for a light and low density material, a longer acquisition time is required to acquire a high energy filtered EBSP pattern with a given number of electrons compared to that required for a heavy, dense material.

In the power spectra of the EBSP, an increase of the higher frequency components is observed for the EBSPs acquired at higher threshold energy, indicating that these EBSPs are of higher quality and thus contain more information. For example HOLZ rings are observed in the high energy filtered EBSP from diamond (see Fig. 5.3 (e)) which are not observed in the low energy filtered EBSP. Higher order Kikuchi bands can also be discerned. For GaN fine detail is observable in the HOLZ rings for the high energy filtered EBSP (see Fig. 5.3 (f)).

In the image derived from the high energy filtered EBSP (Fig. 5.5 (c)), the (220), (440), (660) and (880) Kikuchi lines can be discerned. The increase in the detail observed in the EBSPs is attributed to the removal of lower energy, i.e., high-loss electrons which, as discussed previously, give rise to a featureless background. This background obscures the higher order features; its removal results in EBSPs in which more detail is discernible.

Table 5.2 summarises the improvement in the contrast obtainable for all samples.

Note that the greatest change in contrast, on acquiring a high energy filtered EBSP, is obtained for diamond. The absolute change in contrast depends on a number of factors including the quality of the sample surface and the position of the detector relative to the sample. The detector's performance will also vary with threshold energy: for example for a low threshold energy an electron may be counted by more than one pixel, as discussed previously, while this effect will be eliminated at higher threshold energy. The largest change in contrast however, was always obtained for the diamond sample, while the smallest change in contrast was always obtained for the GaN. This may be attributed to the difference in the energy distribution of backscattered electrons for these materials as discussed previously. For lighter, less dense materials the backscattered electrons have a much broader energy spectrum; that is there are more electrons with higher energy loss. These electrons contribute predominantly to the diffuse background; thus removing these electrons from the EBSP significantly improves the contrast in the pattern.

Initially for a given material, care was taken to acquire the same number of electrons for EBSPs recorded at both high and low threshold energies. However subsequent measurements revealed that, as long as the number of electrons was high enough to obtain an EBSP, the contrast improvement on energy filtering was independent of acquisition time. This is expected since the intrinsic contrast and sharpness of the diffraction pattern should not depend on the counting statistics. High threshold images were acquired for acquisition times of 0.5 s which showed the same improvement in contrast.

Fig. 5.6 shows the subtle changes observed in energy filtered EBSPs. In particular excess-deficiency effects are unexpectedly reduced in the high energy threshold filtered EBSP. As explained previously, bands running parallel to the incident beam direction should not show this effect as illustrated by the much smaller asymmetry observed for band B (see Fig. 5.6 (e)). The difference between the patterns acquired at high and low threshold energies as shown in Fig. 5.6 (c) reveals the energy dependence of the excess-deficiency effect across the EBSP. This effect is also visible in other features of the patterns, such as the edge of the HOLZ ring and the intersection of the Kikuchi bands, as indicated by the bright features (indicating large differences between the two patterns) in Fig. 5.6 (c). To explain this unexpected observation requires a quantitative model describing the development of diffraction effects with energy loss. This involves the simultaneous treatment of the multiple inelastic scattering in the sample and dynamical diffraction effects as has been outlined by Dudarev et al. [43] using the density matrix formalism. Our observations indicate that the details of the interrelated multiple inelastic scattering and dynamical diffraction are not completely understood and should thus provide a stimulus for an improved theoretical treatment which, while beyond our current capabilities, will be the focus of future work.

## 5.2 Direct electron imaging of TKD patterns

### 5.2.1 Transmission Kikuchi diffraction and transmission electron diffraction

The spatial resolution in conventional EBSD geometry is limited to the size of the interaction volume, which is, depending on the material, of the order of 20-100 nm [147]. This is a limiting factor for truly nanostructured materials, such as those having very small grain size.

In the last few years interest has increased in the use of TKD, that is Kikuchi patterns obtained from electron transparent materials, like those prepared for transmission electron microscopy. This approach has proven to increase the spatial resolution to better then 10 nm [138, 139].

The increase in the spatial resolution due to the reduced interaction volume obtainable in transmission geometry is shown qualitatively in Fig. 5.7 (a-b), where a Monte Carlo simulation is used to show the extension of the interaction volume produced by 30 keV electrons penetrating in a GaN sample.

In contrast with the conventional EBSD technique, the sample preparation in TKD is a bit more laborious. The sample has to be thinned, an operation which is usually done by electro-polishing, ion beam thinning or use of a focused ion beam (FIB). The determination of an optimum thickness is crucial, which is typically in the range of 50-200 nm.

The detector used for TKD is the same as that used for conventional EBSD geometry. The only difference resides in the specimen geometry. The specimen is placed horizontally, with its normal parallel (or tilted a few degrees) with respect to the direction of the primary electron beam. In this configuration the diffraction pattern is formed from those electrons exiting from the lower part of the sample and reaching the detector.

Recently, detectors have been developed to allow the phosphor screen to be placed horizontally [213], underneath the specimen, to decrease the distortions due to the gnomonic projection in the Kikuchi diffraction patterns and increasing the number of collected electrons. This system uses the same hardware used for conventional EBSD; the position of the CCD camera is unchanged, and the difference resides in the horizontal position of the phosphor screen. The light generated on the phosphor is collected by the camera through an additional mirror, tilted 45°, placed between

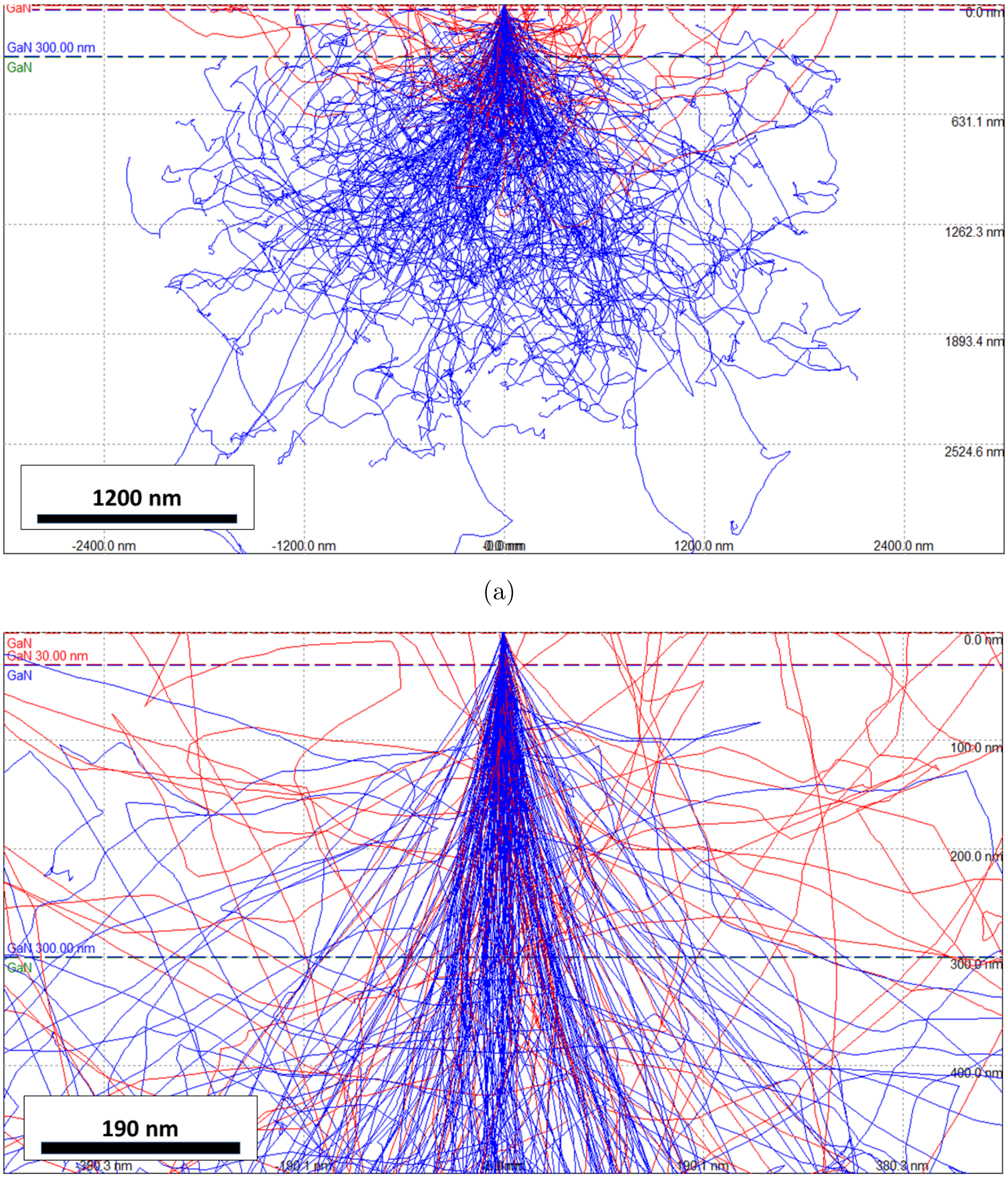

(a)

(b)

Figure 5.7: Monte Carlo simulation of 30 keV electrons interacting with a GaN specimen(a), showing the trajectories of the electrons within the specimen (the red trajectories correspond to the backscattered electrons). A detailed view of the first 30nm (red line) and 300nm (blue line) from the top surface is shown in (b).

the two.

The use of the Timepix detector and its characteristics, especially its very compact size, makes the acquisition of TKD patterns very straightforward. The experimental set up is illustrated in Fig. 5.8.

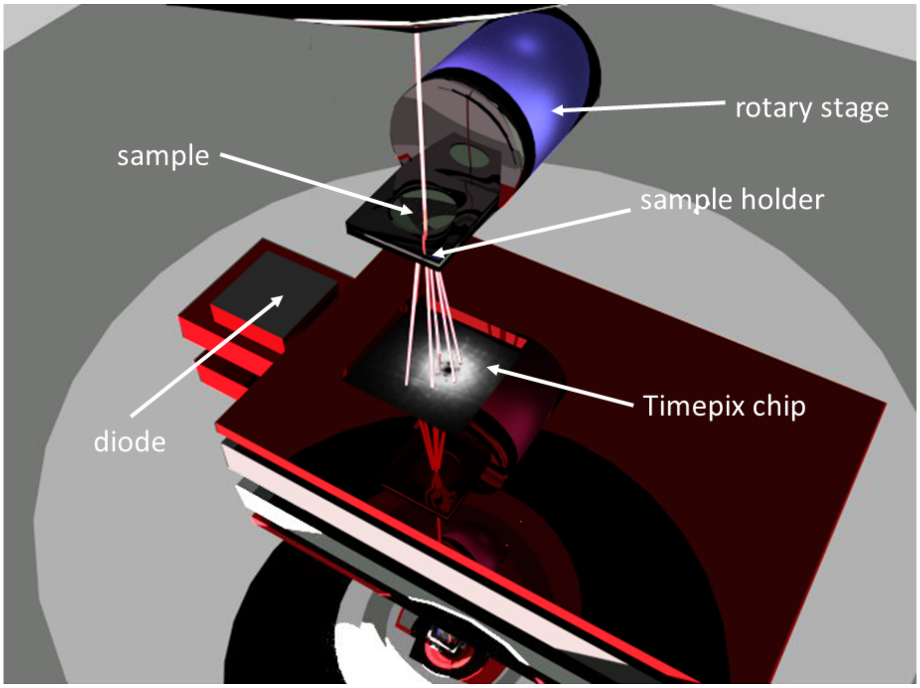

Figure 5.8: TKD geometry using the Timepix detector.

The Timepix chip is fixed on the SEM stage. This allows the control of both the tilt of the detector with respect to the primary electron beam direction, and the control of its position. The electron transparent specimen is held by a TEM grid, which is typically placed horizontally, parallel to the detector, as shown in Fig. 5.8.

To demonstrate TKD, patterns were acquired from a TEM specimen, consisting of a cross section of an epitaxially lateral overgrown (ELO) AlGaN/AlN structure (detail of the growth can be found in Ref. [214]). The specimen was FIB thinned to ≈ 100 nm. In order to avoid contamination from the FIB ion gun, a thin layer of Pt/Au is deposited on the top of the material. A bright field TEM image of the sample is shown in Fig. 5.9.

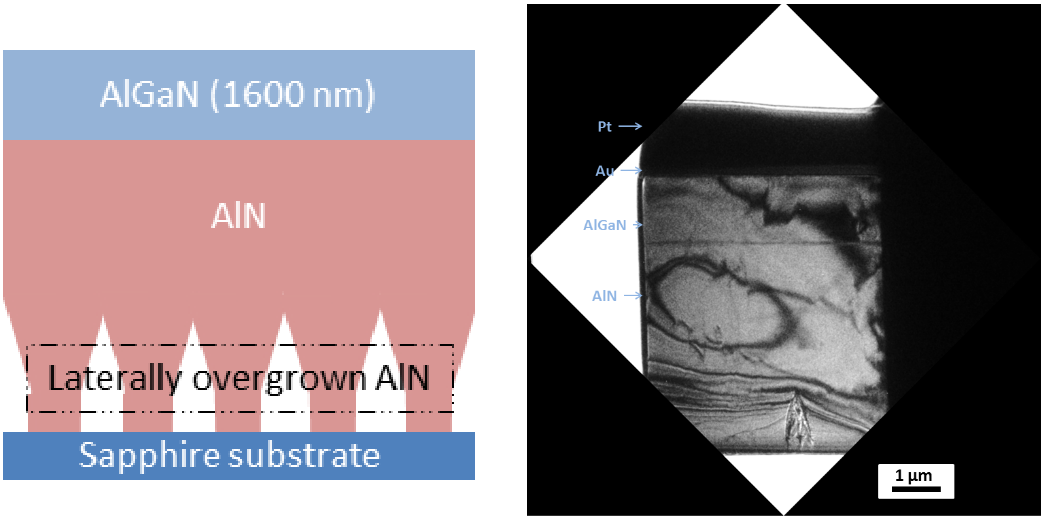

(a) (b)

Figure 5.9: Cross-section of an ELO AlGaN/AlN/Sapphire structure.
(a) simplified structure diagram, (b) bright field TEM image. Courtesy of David Thomson.

The effect of the energy filtering on TKD patterns is shown in Fig. 5.10; TKD patterns were acquired using a beam energy of 30 keV, a beam current of ≈ 2 nA and an acquisition time of 30 ms. The patterns shown in Fig. 5.10 (a) and (b) were acquired using a threshold energy of ≈ 5 keV and ≈ 29 keV respectively. The comparison between the two TKD patterns reveals an increase in the contrast and sharpness in the diffraction features of the TKD patterns when a high threshold energy is used. This was expected since the diffraction effects are produced predominantly from electrons having the energy of the primary electrons, as already discussed in section 5.1.2.

From Fig. 5.10 it can be seen how TKD patterns differ from EBSPs patterns. In transmission experiments there is a significant contribution from the coherent scattering of the primary beam, which results in diffraction spots as observed in TEM.

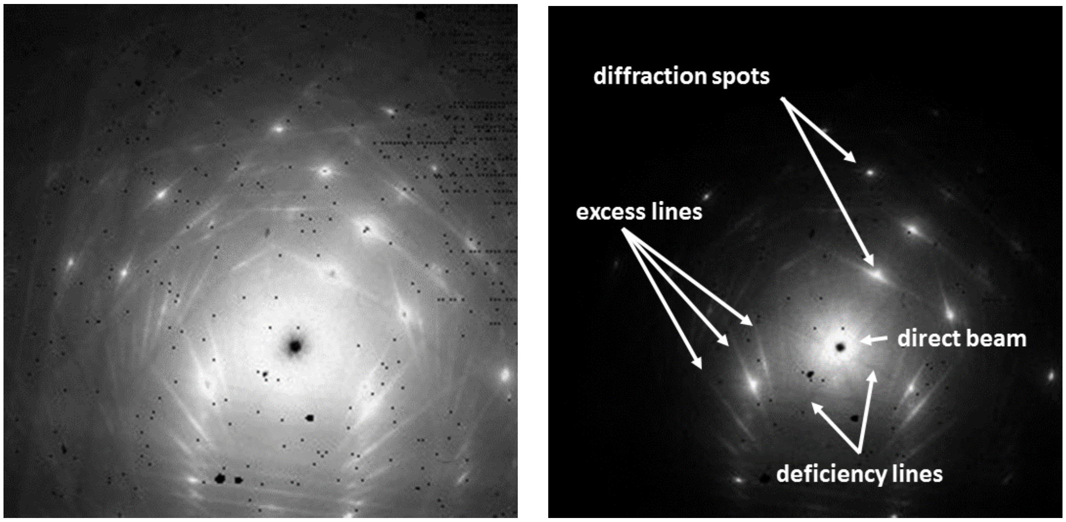

(a) (b)

Figure 5.10: Effect of the energy filtering on TKD patterns from a wurtzite single crystal AlN $\approx$ 100 nm thick. Beam energy 30 keV, beam current $\approx$ 2 nA, 30 ms acquisition time and (a) threshold $\approx$ 5 keV, (b) threshold $\approx$ 29 keV.

When the detector to specimen distance is reduced, to increase the field of view of the pattern, it is possible to image series of Laue zones, as shown in Fig. 5.11.

As shown in section 7.3, the use of the diffraction spots might be also used for imaging purposes, to perform dark field imaging in the SEM.

Preliminary experimental results obtained by performing TKD on GaN nanorods (see Fig. 5.12 (a)) have shown that the contribution of the coherent scattering in the transmission Kikuchi pattern depends on the thickness of the specimen. The diffraction pattern shown in Fig. 5.12 (a) has been indexed by using the method described in section 2.4. The resulting beam direction was found to be $\mathbf{B} = [2\bar{1}2\bar{3}]$.

The GaN nanorods used for this experiment have a base diameter of $\approx$ 700 nm, and the thickness decreases at the tip of the nanorods, where it is less than 50 nm. TKD patterns acquired from the positions 1, 2 and 3, highlighted in red in Fig. 5.12(a), are shown in Fig. 5.12(b-d) respectively.

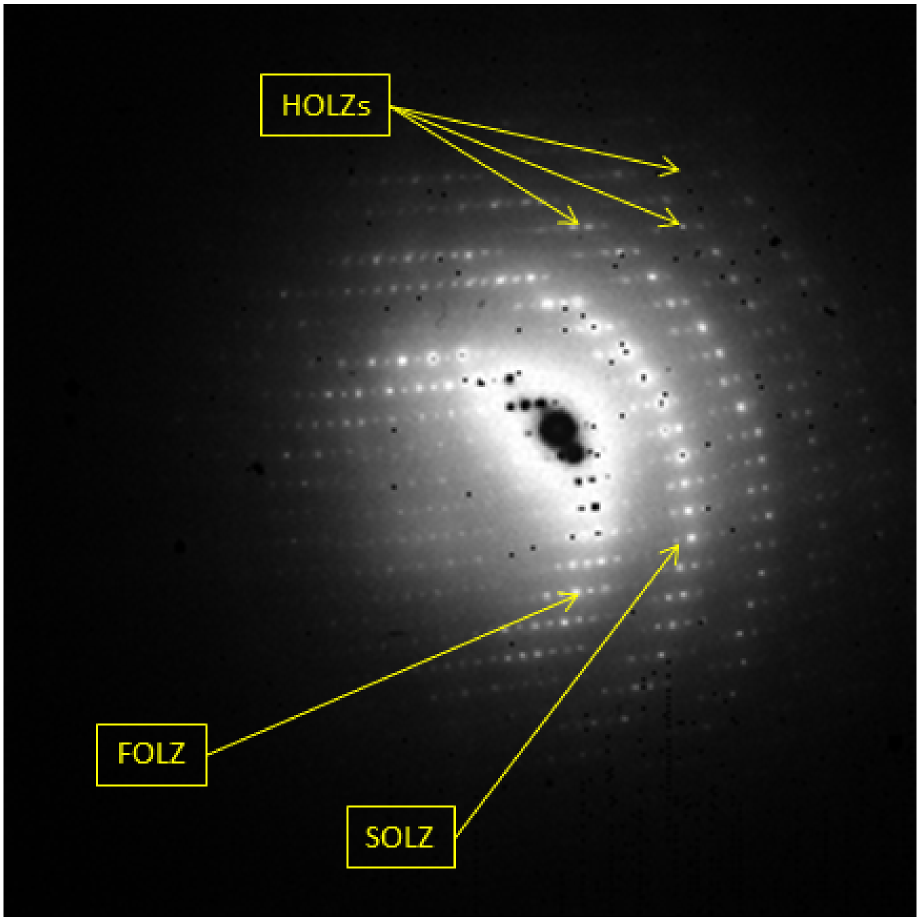

Figure 5.11: Raw TKD pattern from a wurtzite single crystal AlGaN cross-section 100 nm thick aquired using an electron beam energy of 30 keV. The TKD pattern shows high order Laue zones and the angular electron intensity distribution.

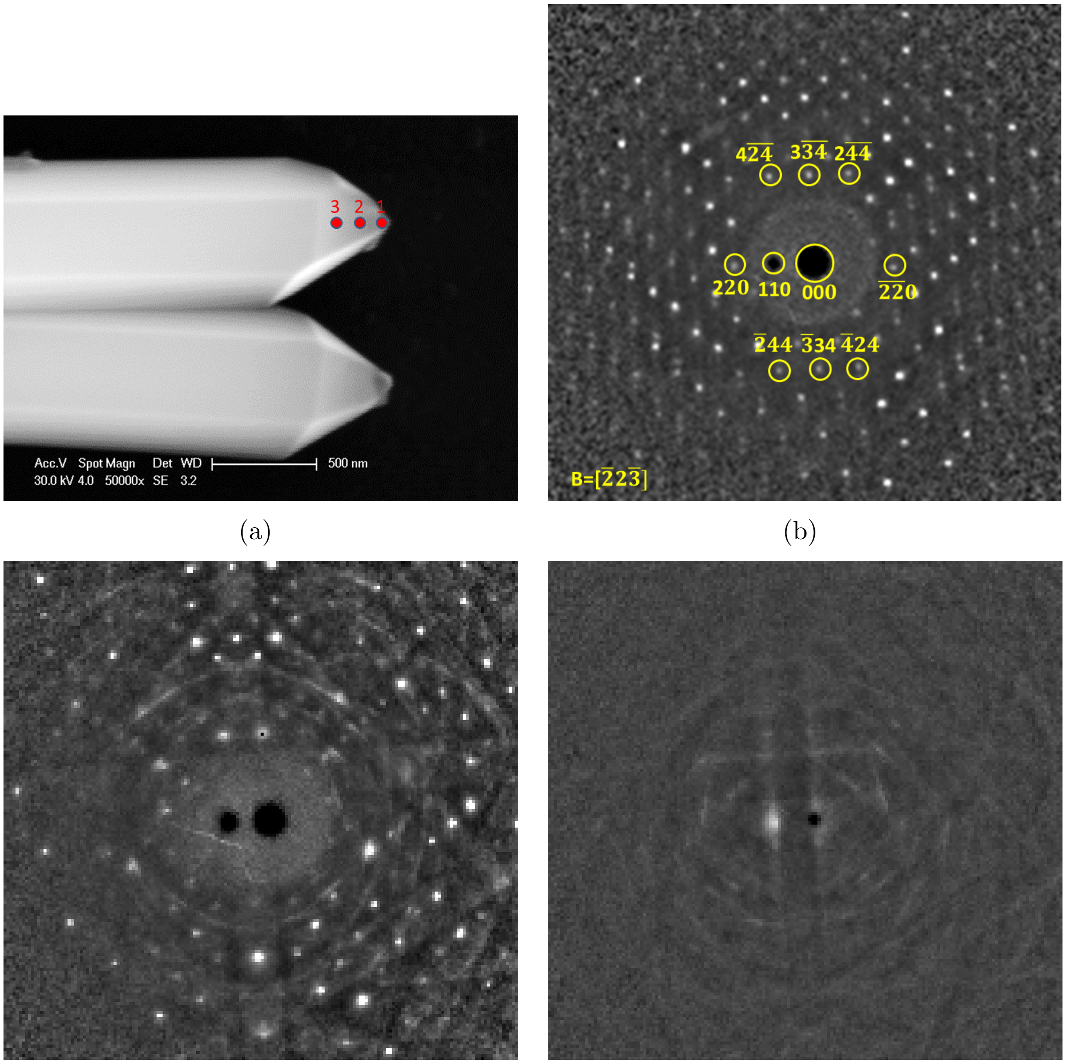

(a) (b)

(c) (d)

Figure 5.12: Effect of the specimen's thickness on (flat field corrected) TKD patterns acquired from a wurtzite single crystal GaN nanorods using an electron beam energy of 30 keV. (a) SEM image of the nanorods. TKD patterns acquired from the positions 1, 2 and 3 (highlighted in red in (a)) are shown in (b), (c) and (d) respectively. Beam direction is $\mathbf{B} = [\bar{2}2\bar{3}]$.

### 5.2.2 Discussion

As observed for the backscattering geometry, the use of energy filtering in TKD patterns increases the contrast and sharpness of the diffraction features like Kikuchi lines and diffraction spots, as shown in Fig. 5.10. Here for example the deficiency lines close to the direct beam appear more visible in the filtered TKD pattern, and in general the pattern is less covered by the diffuse background. Also the diffraction spots are sharper.

Although the application of energy filtering is beneficial in TKD, it is expected that the improvement in the patterns is less effective when compared to the backscattering geometry. This is easily understood considering that the transmitted energy distribution is more peaked to the higher energies when compared to the backscattered energy distribution, so there are fewer low energy electrons contributing to the image, especially for thin samples, where the coherent Bragg diffraction is predominant.

In this regard is it possible to note that all the TKD patterns acquired using the detector perpendicular to the SEM axis, see Fig. 5.8, can be considered effectively as transmission electron diffraction. In this geometry, the contribution of the Bragg scattering, i.e. diffraction spots, is significant. This is visible also in Fig. 5.11, showing how, by decreasing the detector to specimen distance, that is by increasing the field of view of the pattern, it is possible to access a series of Laue zones. This is reminiscent of convergent beam electron diffraction (CBED) (see section 3.2). In our experimental set up the convergence is relatively small when compared to CBED. The convergence angle in CBED is of the order of tens of milliradians (a few degrees). In our experiments the convergence angle is of the order of a few milliradians (a fraction of a degree). The resulting angular width of the diffraction discs is very small.

There are a number of factors in common between EBSD/TKD and CBED. In EBSD/TKD the electrons, after being scattered by the atoms in the crystal, lose all memory of direction and may also lose energy. This creates the diverging source of electrons. When the direction satisfies a Bragg condition for some family of lattice planes, electrons can be scattered again producing the Kikuchi pattern. In CBED the convergent beam illumination makes the electrons incident on the crystal cover a range of different incidence angles, creating the CBED pattern. In both cases the patterns contain more information if the specimen is relatively thick; in the case of Kikuchi patterns it has to be thick enough for the creation of diverging electrons to occur and then for them to be Bragg scattered. In CBED the thickness has to be thick enough for dynamical scattering to be reinforced.

As explained in section 2.3.2 and 3.2, the analysis of these types of features could allow the measurement of the lattice parameter with high precision [6, 28].

Generally TKD patterns acquired using the conventional TKD set up [138, 139], i.e. with the detector screen parallel to the incident electron beam, do not contain diffraction spots. In this configuration the detector collects predominantly electrons scattered over a range of angles deviating significantly from the direct beam direction (where the Bragg diffraction is predominant).

The indexing of TKD patterns acquired with an on-axis detector can be problematic using conventional EBSD software, especially when the diffraction spots significantly reduce the visibility of the Kikuchi lines. Image processing methods used to identify the Kikuchi edge and/or intensities often fail when the intensity from the diffraction spots is predominant. Probably, in the latter case, an automatic transmission electron diffraction (TED) indexing method would be more appropriate.

Alternatively the strong intensities arising from the diffraction spots should be eliminated, choosing for example an appropriate thickness for the materials. This is shown qualitatively in Fig. 5.12.

When TKD patterns are acquired from the thinnest part of the nanorods, TKD patterns are strongly dominated by the diffraction spots, with the Kikuchi bands barely visible, see Fig. 5.12 (b). If TKD patterns are acquired from regions where the thickness is large, $\approx 300$ nm or more, the contribution of the diffraction spots almost disappears, with the exception of the direct beam, as shown in Fig. 5.12 (d). In this case the effect of the thickness is also visible in the form of contrast reversal in the Kikuchi bands, as already discussed in section 3.4.3. For intermediate thicknesses, Fig. 5.12 (c), a contribution of both diffraction spots and regular (bright) Kikuchi bands can be observed. As one moves from the tip to the base of the nanorod, there is a continuous transition between the two extreme cases.

This can be explained considering two main physical mechanisms occurring at the same time. One is the elastic coherent Bragg diffraction, responsible for the generation of the diffraction spots. The other is the two step process responsible for the production of the Kikuchi lines, that is the quasi-elastic production of a distribution of electrons having a range of directions and their subsequent coherent diffraction. The probability of the first mechanism is higher that the second. In other words a larger interaction volume is necessary to produce the source of electrons which contributes to Kikuchi bands, compared to the one necessary for generating coherent diffraction. This means that for thinner specimens the diffraction spots are predominant, while for thicker specimens the Kikuchi bands are predominant. Of course there is an upper limit to the maximum thickness which can be used, after which electrons produced by both mechanisms will undergo inelastic scattering, which consequently destroys the coherence of both processes. The latter effect starts to be visible in the pattern shown in Fig. 5.12 (d). Here the coherence of the diffraction spots and Kikuchi bands is almost completely destroyed. It is quite clear that in order to use TKD, a suitable thickness should be chosen for each material.

In general, the clear advantage in the use of transmission geometry is the reduction in the acquisition times and beam currents due to the position of the detector, which allows the collection of many more electrons per unit time when compared to other geometries. Furthermore, as already demonstrated by other authors [132, 138, 139], there is an increased spatial resolution due to the reduced interaction volume. This is qualitatively shown in Fig. 5.7 (a), where a Monte Carlo simulation is used to show the extension of the interaction volume produced by 30 keV electrons penetrating into a bulk GaN sample. The top 100 nm is highlighted in red, and shown more clearly in 5.7 (b). It is clearly visible that the lateral extension of the interaction volume within the first 100 nm is much smaller than the remaining volume of the specimen.

In this experimental geometry the detector shows a dysfunctional behaviour. The area of the detector close to the intersection of the incident beam and the detector chip, where a large number of electrons are detected, shows a saturation effect [215]. In a conventional detector system, i.e. photographic films or phosphor film, this results in very bright spots in the diffraction pattern, or even entire areas of the detector, where the number of incident electrons is larger than the dynamic range of the detector. This usually strongly reduces the visibility of the other diffraction features in the pattern. In all TKD patterns shown in this section, instead, the pixels which in principle should reach their maximum particle count and became thus bright, show instead a very limited count. This is due to a pile up effect in the detector. In transmission experiments this drawback could be seen as an advantage, because it enhances the visibility of the diffraction features, which would be affected if the detector were strongly exposed by the primary beam. This simplifies the determination of the diffraction condition.

# Chapter 6

# Development of a RHEED system in the SEM

This chapter demonstrates the acquisition of RHEED patterns in the SEM using the Timepix detector.

## 6.1 RHEED in the SEM

In the experiments RHEED patterns were acquired in an FEI Sirion Schottky field emission scanning electron microscope operating in spot mode. The Timepix detector was positioned on the SEM stage, with its normal parallel to the direction of the electron gun axis, and the specimen kept vertical or slightly tilted, and moved horizontally to intercept the electron beam, as shown in Fig. 6.1. A small sample holder was built to allow the sample to be rotated around the specimen normal axis, to obtain RHEED patterns at different azimuthal angles.

A RHEED pattern acquired from silicon, using a 30 keV electron beam, is shown in Fig. 6.2. As in the case of EBSD patterns previously discussed, a flat field

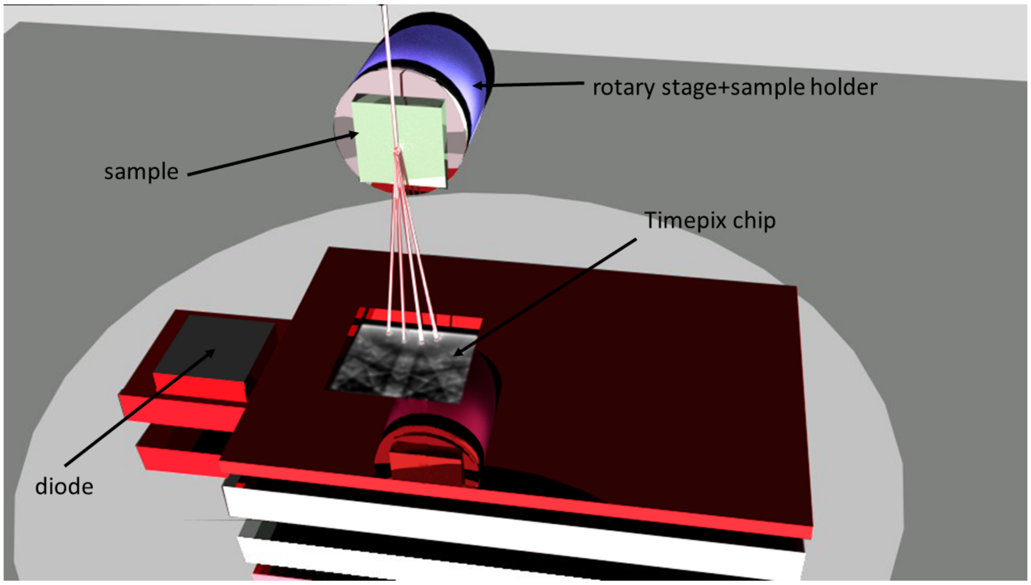

Figure 6.1: Timepix detector in RHEED geometry.

correction is also shown.

The diffraction patterns in this geometry show a number of features which are usually not visible in the conventional EBSD geometry. The geometrical arrangement makes more visible the features generated by the reflected electrons which predominantly experience coherent scattering from the sample surface. These features include the spots appearing in the pattern forming the RHEED pattern, parabolic Kikuchi lines and sharp HOLZ rings. Also the Kikuchi lines show strong excess-deficiency lines, as in the TKD patterns, as a consequence of the fact that the diffraction patterns are generated by the forward scattered electrons, as already discussed in section 3.4. Furthermore the Kikuchi bands close to the shadow edge experience (see section 3.3) the effect of the mean inner potential in the direction normal to the surface. This mean inner potential causes a characteristic bending of the Kikuchi lines close to the shadow edge.

These details are clearly visible in Fig. 6.3 which shows a flat fielded RHEED pattern from a GaN sample, obtained using a 20 keV electron beam. The strong

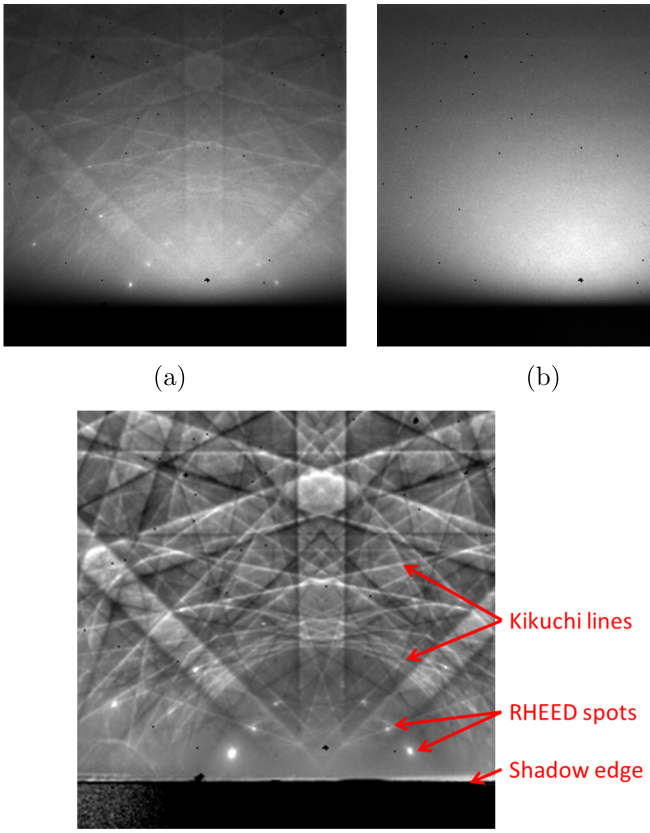

(a) (b)

(c)

Figure 6.2: Direct electron imaging of RHEED pattern from a diamond-structure single crystal silicon, obtained using 30 keV electron beam: (a) raw data, (b) background, (c) flat fielded.

excess of intensity visible in RHEED spots, HOLZ rings and Kikuchi lines are related to an effect called the surface-wave resonance which is describe later in the chapter.

Depending on the degree of disorder of the surface or its morphology, it is possible to have different types of RHEED patterns. If the surface of the sample consists of a flat, smooth monocrystalline surface, electrons are reflected from the surface, so reflection patterns are observed, whose features consist of spot/streaks appearing on the pattern. In addition, depending on the state of the surface, e.g. order of the texture, presence of steps on the surface, etc., the RHEED patterns can show particular features which are characteristic of each particular state of the surface. A variety of examples and models are treated in Ref. [69]. If the surface is rough or has protusions, a transmission pattern may be also visible, and this will be described in the following section.

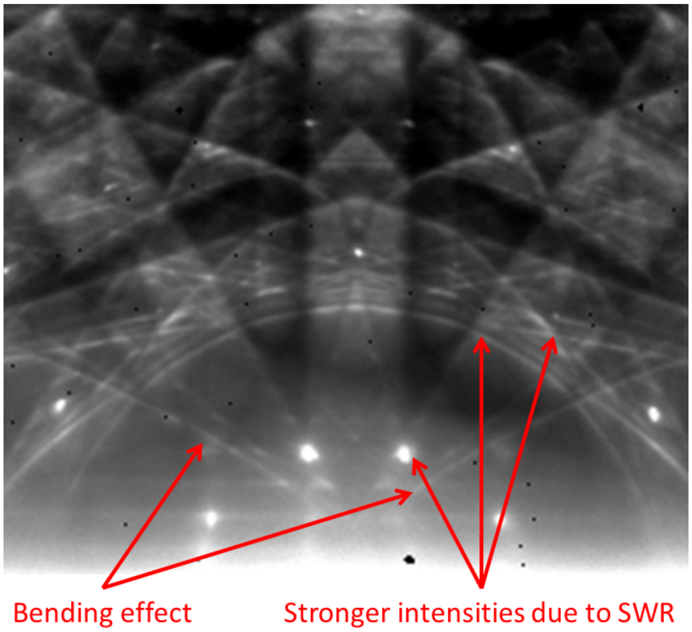

Figure 6.3: RHEED pattern from a wurtzite single crystal GaN, obtained using 20keV electron beam.

## 6.2 RHEED in transmission mode

There are situations in which the RHEED pattern is formed in transmission mode. Again, this is an oxymoron which has nevertheless grown into use in the RHEED community.

When the surface is sufficiently rough, or has protrusions, or when the specimen is composed of nanostructures, the electrons can penetrate through the sample (see Fig. 6.4) and give rise to transmission patterns which can be quite different from reflection RHEED patterns; they are, effectively, the same as diffraction patterns in the TEM [6]. Often, transmission patterns are visible during the initial growth of crystalline material films, during the nucleation of the buffer layer or after sublimation, e.g. when a flat surface is not yet achieved. As the crystal growth evolves one observes a transition between transmission patterns and reflection patterns; often both transmission and reflection RHEED patterns are visible at the same time.

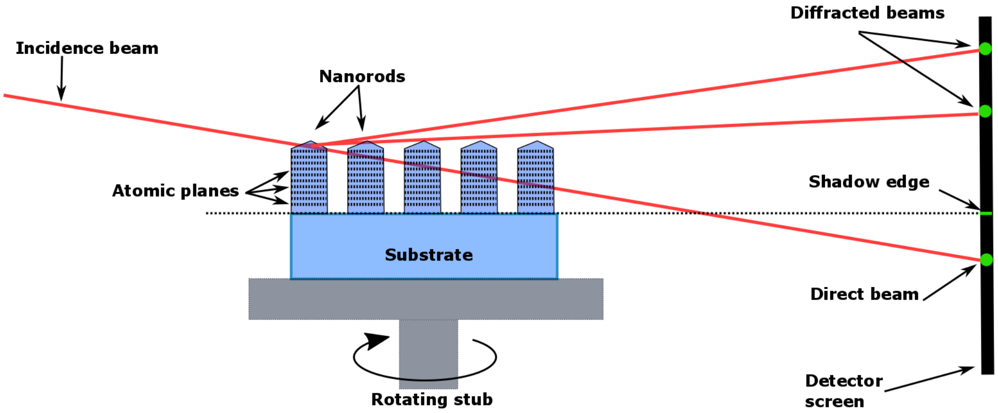

Figure 6.4: RHEED pattern formation in transmission mode

The diffraction pattern is generated from a volume which is limited by the mean free path of the electron. Typically, the interaction volume is contained within a few tens of nanometres of the surface. The main difference with respect to reflection mode is that the reciprocal lattice space is no longer composed of rods, but is composed of points in 3D space, as for bulk diffraction. This has been discussed previously in section 2.3.1.

Usually streaks do not appear in transmission mode, and the diffraction pattern is composed of diffraction spots. The limited extension of the interaction volume relaxes the Bragg condition for the family of crystal planes, causing a broadening of the diffraction spots.

Examples of transmitted RHEED patterns from an AlGaN nanorod sample, using a 30 keV beam electrons, are shown in Fig. 6.5. The two patterns, obtained using different diffraction conditions, were indexed using the method described in section 2.4. The beam direction is $[2\bar{1}\bar{1}0]$ and $[01\bar{1}0]$ for the diffraction patterns shown in Fig. 6.5 (a) and (b) respectively.

The transmitted RHEED patterns look similar to the TKD pattern shown in Fig. 5.11 (a). In this case the specimen has not been thinned, but the diffraction pattern is generated from a small volume from the tip of the nanorods.

As for reflection RHEED patterns, after an appropriate calibration, lattice parameters can be determined [216].

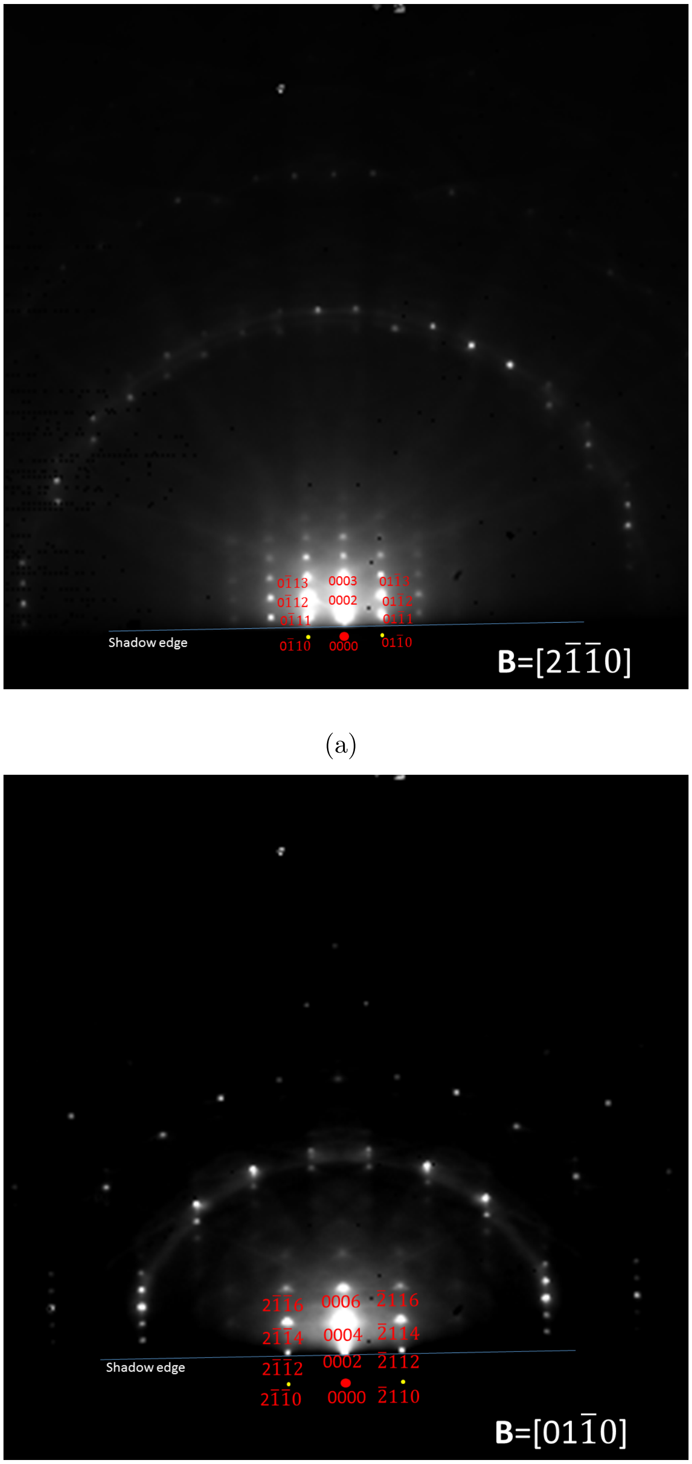

(a)

(b)

Figure 6.5: Transmission RHEED from a wurtzite single crystal GaN acquired using a 30 keV electron energy and two electron beam directions **B**: (a) **B**=[$2\bar{1}\bar{1}0$] and (b) **B**=[$01\bar{1}0$].

## 6.3 Surface-wave resonance effect

One of the most interesting effects visible in the RHEED geometry is the so-called surface-wave resonance (SWR) [69], usually particularly visible when the specular beam (i.e. the reflection of the primary beam on the specimen surface, see section 3.3) intercepts the edge of one of the Kikuchi lines. (SWR is also visible in other circumstances as shown later in this section).

The effect gives rise to a strong enhancement in the diffracted intensity. This is shown in Fig. 6.6, where three flat fielded patterns from a thin GaN film were acquired at slightly different azimuthal angles, using a 25 keV electron beam. It shows the change in the intensity when the pattern is rotated from (a) to (c), and in one of the intermediate positions (b), the surface-wave resonance occurs.

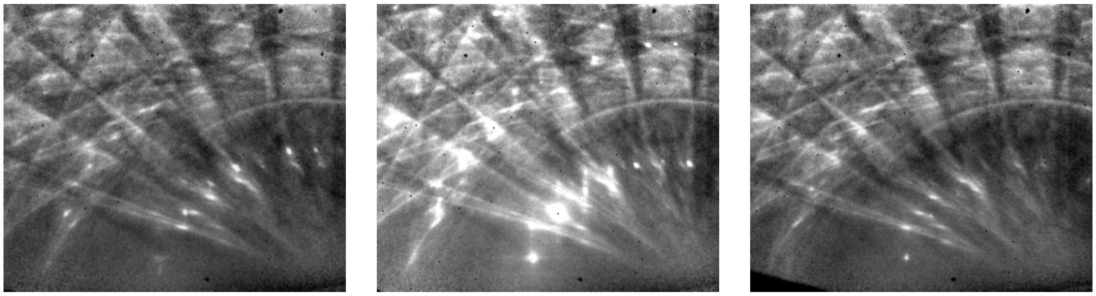
(a) (b) (c)

Figure 6.6: Surface-wave resonance effect in a RHEED pattern from a wurtzite single crystal GaN, obtained using a 20 keV electron beam: (a) off-resonance condition before the specular beam crosses the Kikuchi line, (b) resonance condition, (c) off-resonance condition after the beam crosses the Kikuchi line.

This effect was first observed by Kikuchi and Nakagawa in 1933 [217]. It is observed when for a particular incidence angle, the normal component of the momentum of the electron is not sufficient to cross the potential barrier at the surface, and is then totally internally reflected, creating an evanescent excited state confined at the surface, which transfers energy to the diffracted beams, enhancing the entire pattern [69, 218–223].

In general the resonance condition is expected to occur when a diffracted beam, $\mathbf{k}_m$, propagates through the crystal but is evanescent outside it. These conditions are determined by considering the change in the components of the incident wave vector perpendicular to the sample normal $\mathbf{n}$, as the electrons enter and leave the crystal. If one considers the components of the incident and diffracted beams, where the capital $\mathbf{K}$ indicates the unrefracted wave vector in the vacuum, and $\mathbf{k}$ the same vector corrected for refraction in the crystal, the components of the incident and diffracted beams can be written as

$$\begin{aligned}\mathbf{K}_0 &= \mathbf{K}_{0t} - \Gamma_0\mathbf{n} \\ \mathbf{k}_m &= \mathbf{k}_{mt} + \gamma_m\mathbf{n} \\ \mathbf{K}_m &= \mathbf{K}_{mt} + \Gamma_m\mathbf{n} \qquad (6.1)\end{aligned}$$

where the subscript $t$ indicates the component of the vector parallel to the sample surface, and $\Gamma_0$, $\gamma_m$ and $\Gamma_m$ the magnitude of the normal component of $\mathbf{K}_0$, $\mathbf{k}_m$ and $\mathbf{K}_m$ respectively. The vector $\mathbf{K}_0$ is the incident beam and the vector $\mathbf{K}_m$ is regarded as the continuation of the vector $\mathbf{k}_m$ if it could leave the sample.

Because of the two dimensional elastic scattering condition $K_m^2 = K_0^2$, $\mathbf{K}_m$ can be written as

$$\mathbf{K}_{mt} = \mathbf{K}_{0t} + \mathbf{B}_m \qquad (6.2)$$

where $\mathbf{B}_m$ is one of the two dimensional reciprocal lattice vectors.

Because the energy of the beams inside the crystal is affected by the mean inner potential of the crystal, the relation between the components of the diffracted beam inside and outside the crystal is

$$k_m^2 = K_m^2 + U \tag{6.3}$$

and because the parallel component of the beams are conserved

$$\gamma_m^2 = \Gamma_m^2 + U \tag{6.4}$$

which simply shows the change in the perpendicular momentum due to the refraction.

The condition under which a diffracted beam can propagate through a crystal but cannot escape from it requires the coefficients $\gamma_m$ and $\Gamma_m$ in Eq. 6.1, to be real and imaginary respectively [69].

Considering Eq. 6.1 and 6.2, this turns out to be satisfied when

$$\begin{aligned} \Gamma_m^2 &= K_0^2 - |\mathbf{K}_{0t} + \mathbf{B}_m|^2 < 0 \\ \gamma_m^2 &= K_0^2 - |\mathbf{K}_{0t} + \mathbf{B}_m|^2 + U > 0 \end{aligned} \tag{6.5}$$

In this condition $\mathbf{k}_m$ is totally internally reflected. The physical meaning of the first equation in Eq. 6.5 is that the vector $\mathbf{K}_m$ (associated with the particle in the vacuum) does not reach the reciprocal lattice rod $\mathbf{B}_m$, which is usually said to be below emergence, or alternatively that the Ewald sphere does not reach the rod $\mathbf{B}_m$, that is $K < |\mathbf{K}_t + \mathbf{B}_m|$, as shown in Fig. 6.7 (a). The meaning of the second equation is that, in order to propagate, the refraction corrected $\mathbf{k}_m$ wave vector has to reach the reciprocal rod $\mathbf{B}_m$, so that $k > |\mathbf{K}_t + \mathbf{B}_m|$, as shown in Fig. 6.7 (b).

The limit of the condition of Eq. 6.5 defines two parabola,

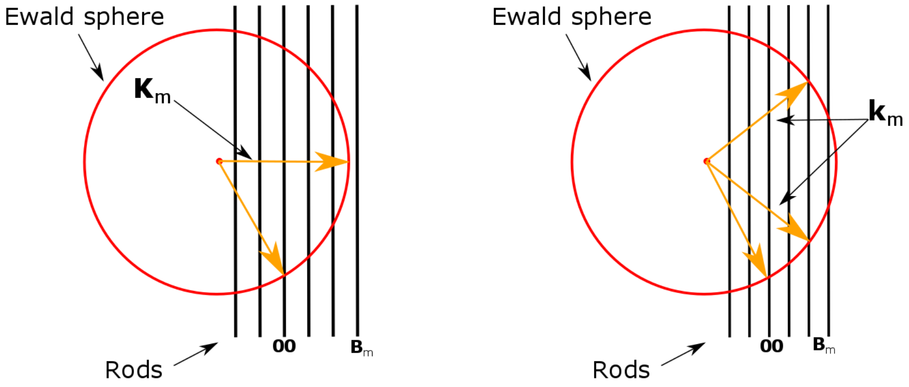

(a)

(b)

Figure 6.7: Geometrical interpretation of the surface-wave resonance, (a) unrefracted Ewald construction for a non-allowed diffracted beam, (b) and Ewald construction for the refracted beams. Reproduced from Ref. [69].

$$\begin{aligned} \Gamma_0^2 &= 2\mathbf{K}_{0t} \cdot \mathbf{B}_m + B_m^2 - U \\ \Gamma_0^2 &= 2\mathbf{K}_{0t} \cdot \mathbf{B}_m + B_m^2 \end{aligned} \tag{6.6}$$

which consist of an envelope within which the bright enhanced Kikuchi lines are contained. By dividing both equations by $K^2$, and considering that $\frac{U_0}{K^2} = \frac{V_0}{E}$, equations for these curves in screen coordinates can be obtained. Here $U_0 = \frac{2me}{\hbar^2} V_0$ is the scaled crystal potential, $V_0$ is the Fourier component of the crystal potential and $E$ the beam energy in the vacuum. For a vector $\mathbf{B}_m$ parallel to the detector plane one obtains

$$\begin{aligned} 2\phi \frac{B_m}{K} + \frac{B_m^2}{K^2} &= \theta^2 + \frac{V_0}{E} \\ 2\phi \frac{B_m}{K} + \frac{B_m^2}{K^2} &= \theta^2 \end{aligned} \tag{6.7}$$

where $\phi$ is the projection of $\mathbf{K}_t$ on $\mathbf{B}_m$ divided by $K$, and $\theta$ is $\frac{\Gamma_0}{K}$ [69].

As the sample is rotated around its normal the interception of the Ewald sphere with the reciprocal lattice rod moves along the rods, and at the same time the Kikuchi envelopes move as well, so when the Kikuchi envelopes cross the interception of the Ewald sphere on the (00) or non-(00) rods, there is often an enhancement in the intensities, which in most cases can dominate the diffraction pattern.

One would expect that each kind of step-like feature or crystal defect could destroy this SWR condition, since the intensity could potentially leak from those irregularities on the surface. Inspired by this idea, this specific diffraction condition has been applied for the development of what has been called SWR-ECCI, which will be discussed in Section 6.4.

## 6.4 Development of a surface-wave resonance ECCI system in the SEM

In this section the development of a novel characterization method which could potentially enable a step change in the application of electron diffraction in the SEM is described.

The innovation resides in the use the information obtainable from both the RHEED and Kikuchi patterns which will allow the selection of specific diffraction conditions, used subsequently for the acquisition and identification of crystalline defects in ECCIs.

This can be done using a combination of a silicon diode and the Timepix detector. This will allow the acquisition of ECCI like maps under specific diffraction conditions, in particular under the condition of surface-wave resonance. The experimental arrangement is shown in Fig. 6.8.

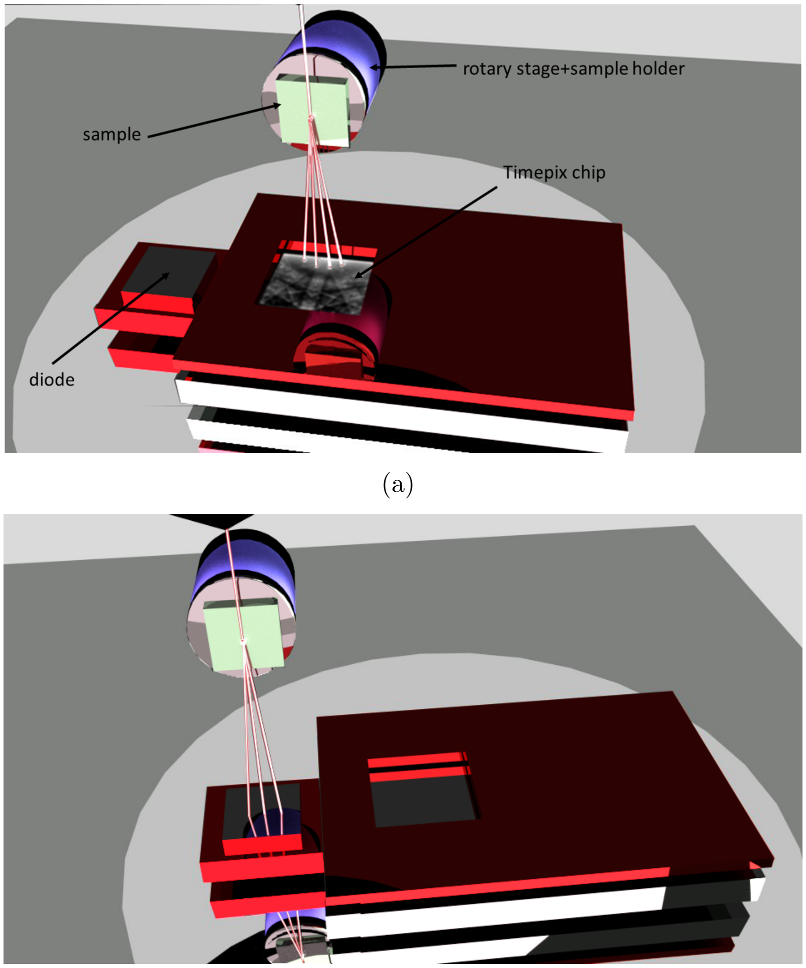

(a)

(b)

Figure 6.8: Experimental set-up for SWR-ECCI, (a) setting the diffraction condition and (b) acquisition of a SWR-ECCI.

An electron beam is incident at near grazing angle (typically 1-3°), in a conventional RHEED geometry, on the specimen's surface, which (in the simplest configuration) is placed on a rotary stage. The two detectors are placed on a 3-axis stage in such a way as to collect the forward scattered electrons.

In this configuration both RHEED and EBSD patterns can be recorded. A similar geometrical configuration was previously used by Baba-Kishi to record RHEED and EBSD patterns on photographic film in the SEM [224].

This experimental geometry is very difficult to achieve with conventional EBSD detectors comprising a phosphor screen coupled to a CCD camera, as there is simply not room in a typical SEM chamber. In addition to its compact form the use of the Timepix detector provides considerable benefits to the acquisition of diffraction patterns, namely reduced exposure of samples to high electron beam currents, and an unprecedented increase in the quality and detail (and therefore information) in the recorded diffraction patterns.

The use of the rotating sample stage allows the specimen to be rotated around the surface-normal direction and RHEED and EBSD patterns to be recorded at different azimuthal angles. As described in section 6.4, on rotating the specimen, strongly enhanced intensity of the RHEED spots is observed as they cross Kikuchi lines (edge of the bands) of the EBSD pattern [69].

The author proposes to acquire electron channelling contrast images under the condition of surface-wave resonance. This method is referred to as surface-wave resonance ECCI (SWR-ECCI) in the following sections.

This approach shares several features of the known scanning reflection electron microscopy (SREM) and ECCI techniques. An SREM image is acquired by monitoring the reflected intensity of a RHEED spot as the electron beam is scanned over the surface of the sample [72]. In ECCI an image is acquired by scanning the electron beam over the specimen and monitoring the intensity of scattered electrons from the sample when it is placed in a specific diffraction condition [122, 124]. This reveals variation in the scattered intensity caused by local variations in the crystal orientation. Both techniques allow grain structure and defects to be imaged.

By using SWR-ECCI a high level of surface sensitivity should be obtained, as discussed previously in this chapter, due to both the surface character of the RHEED and of the localized character of the SWR effect.

SWR-ECCI has furthermore an additional important advantage, which allows a big limitation of the ECCI technique to be overcome: the knowledge of the diffraction condition.

In ECCI the diffraction condition is usually determined by acquiring an ECP from larger area of the surface, which is then used, by rotating and tilting the sample, to set a specific diffraction condition. This is the bottleneck for a series of applications and limits the applicability of the ECCI technique, since there are many cases where the topography of the surface or the limited size of the surface prevent the acquisition of usable ECPs.

The use of SWR-ECCI allows the determination of the diffraction condition without using ECPs, in fact, as already discussed, this information is contained in the RHEED/EBSD pattern in a intrinsic way. This could allow the extension of the ECCI to non-flat surfaces such as nanorods.

The method used to acquire SWR-ECCI images is as follows:

1. Setting a SWR condition. This can be done using eq. 6.1, and/or obtaining an experimental azimuthal plot (total intensity as function of the azimuthal angle) using the Timepix chip from which it is possible to select a particular resonance condition.

2. Using the silicon diode to obtain an SWR-ECCI from a region of interest of the surface, using the set diffraction condition.

The silicon diode is mostly used to speed up the acquisition time. In principle it could be also done using the Timepix detector.

Once the diffraction condition is set, the position of the silicon diode can be optimised to maximize the recorded signal intensity, without changing the diffraction condition.

Examples of our first (non-optimised) SWR-ECC images from a sample of AlGaN are shown in Fig. 6.9. Strong contrast is observed for both sub-grains (areas showing different grey scale) and dislocations (the dots with black-white contrast) in the image. For comparison an image obtained in an off-resonance condition, from a different region of the sample is shown in Fig. 6.10.

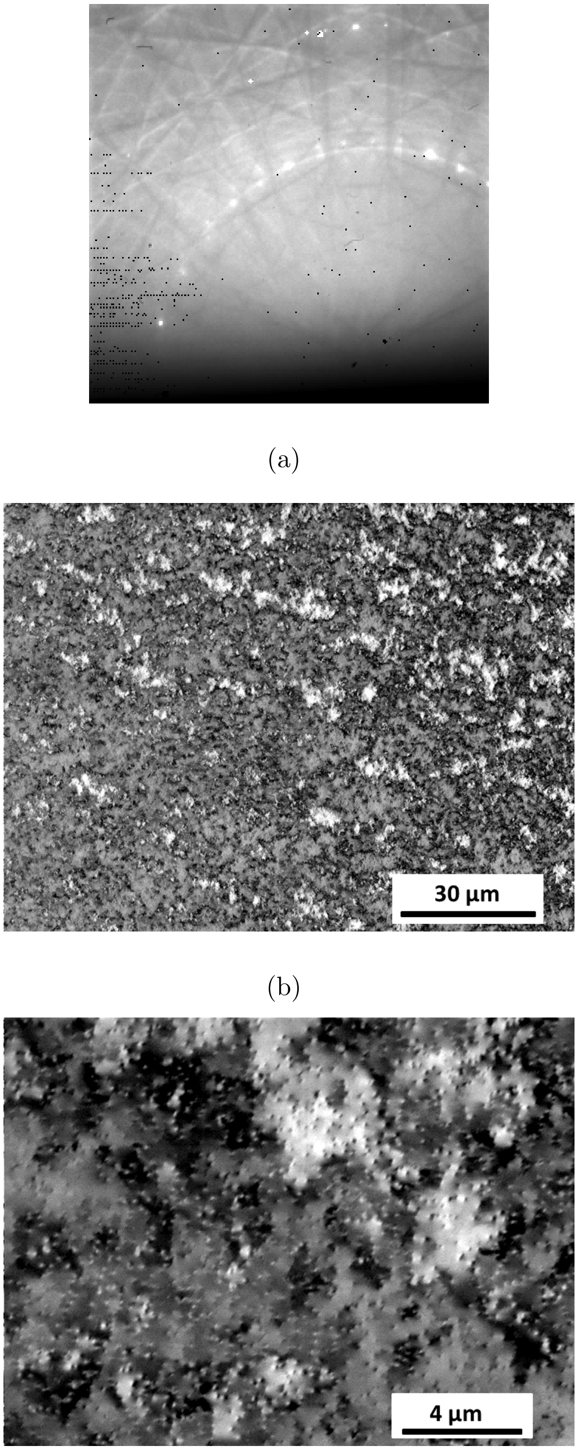

(a)

(b)

(c)

Figure 6.9: Example of SWR-ECCI from a wurtzite single crystal AlGaN using a 30 keV electron beam,

(a) RHEED/Kikuchi pattern and (b-c) SWR-ECCI images of the same area obtained using different magnifications.

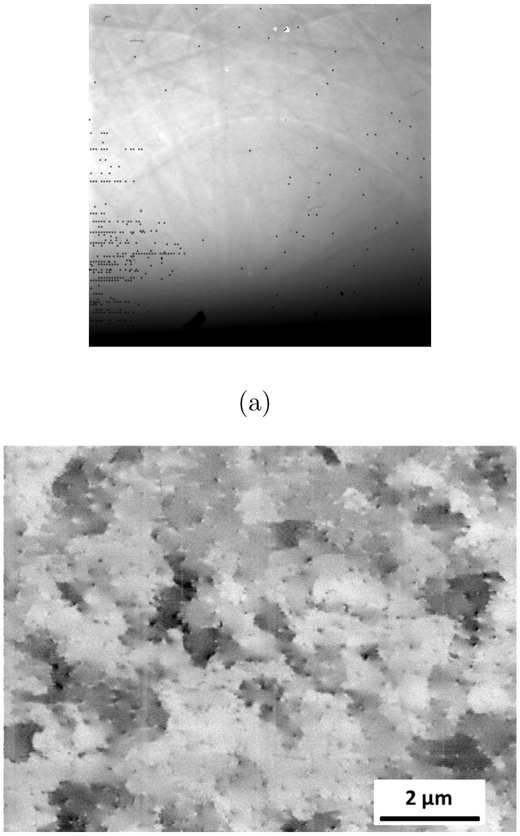

(a)

(b)

Figure 6.10: Example of a SWR-ECCI from a wurtzite single crystal AlGaN using a 30 keV electron beam, (a) RHEED/Kikuchi pattern and (b) SWR-ECCI in off-SWR condition.

## 6.5 Discussion

This chapter demonstrates the acquisition of RHEED patterns in a scanning electron microscope. The use of a strong tilt of the sample allows access to a type of diffraction that is substantially two-dimensional and is predominantly generated from the topmost surface region of the sample. The discussion related to this topic is mostly qualitative; the primary objective of the experiments was to demonstrate that the reflection geometry is accessible in the SEM by using the Timepix detector. There were significant experimental limitations in the hardware used to fit the detector and the specimen into the SEM. This allowed the exploration of a very limited range of the possible measurements available for this geometry. However the attempt was undoubtedly useful to understand the limitations of our current set up, and most importantly to understand what is necessary for improving it.

RHEED patterns show a number of features which are not usually visible in EBSD geometry, such as: the shadow edge; strong excess and deficiency lines in the Kikuchi bands; strong intensities in pattern manifested in the form of bright semicircles; and the characteristic bending effect of the Kikuchi lines close to the shadow edge, as shown in Fig. 6.2. These are basically caused by two effects: the first is the condition of SWR that contributes with an increase in the intensities of certain diffraction features in the pattern; and the second is the effect of the mean inner potential which bends those Kikuchi bands which are close to the surface.

It is also interesting to note the high level of detail within each Kikuchi band, especially close to the shadow edge, where a number of intersecting deficiency lines are visible. The contrast in the latter features is particularly strong; they are similar to Kikuchi patterns obtained in transmission mode rather than backscattering. This is not surprising considering that the diffraction is predominantly produced in the forward scattered directions, where excess-deficiency effects are more predominant, as already discussed in section 3.4.3, (see equations 3.22 and 3.23 and Fig. 3.14).

These fine details, especially the large number of higher order Kikuchi lines, could be beneficial for obtaining precise information about the crystal structure. This is similar to what is done in CBED, where the higher order Kikuchi lines can be used to determine subtle variation in lattice parameters, since subtle changes in the crystal structure results in larger changes in the higher order diffraction features [6].

One important piece of information obtainable from the RHEED patterns is the diffraction condition. Chapter 3 showed that, in contrast to Kikuchi lines, the RHEED pattern changes as the beam direction is changed with respect to the crystal. If precise control of the sample position had been possible, it would have been possible to orient the specimen in such a manner so as to establish precise diffraction conditions, e.g. a two beam condition for a particular set of crystalline planes. The combination of the diffraction spots and the Kikuchi lines would allow the precise setting of a particular diffraction condition and the precise deviation parameters from the two beam condition to be determined. This is something which is not usually achievable using only the Kikuchi pattern.

As already discussed the determination of the diffraction condition in the SEM is crucial for the interpretation of the diffraction contrast visible in ECCI micrographs. Contrast mechanisms in fact, depend on the local deviations from the Bragg condition caused by local distortion of the crystal. Usually the diffraction condition is set through the use of ECPs. In the latter the beam is rocked over the sample so as to cover a certain range of angles and the backscatter intensity is measured as a function of the incidence angle, which is in general modulated by the crystal symmetry. Sometimes this operation is not possible; this occurs for example when the surface of the sample is too rough and the resulting ECP is dominated by shadows of the surface, which obscure the contrast arising from the crystal itself. The same effect happens when there are three dimensional features on the surface, for example in three dimensional nano structures. Another limitation occurs when the size of the specimen is relatively small; in this case the range of angles accessible is much reduced, and is not sufficient for extracting the desired information from the ECP. In these cases a diffraction condition is hard or even impossible to set.

This problem can be solved by using the RHEED patterns. The same information is accessible without the need to rock the beam over the surface, but only by acquiring the information from a single point on the surface.

This also has another advantage. It makes it possible to obtain local diffraction conditions from limited areas of the sample, for example from within grains in polycrystalline materials. This would allow the local interpretation of the contrast in ECCI images.

Other information accessible from the use of RHEED is the lattice parameter. As shown in section 6.1, the spacing between RHEED spots is related to the inter planar spacing. This information is routinely used to measure lattice parameters in the MBE growth chamber during the growth of crystals. The precision obtainable using this approach is relatively high, down to a few thousandths of an Angstrom [83–86].

The same measurement could be transferred to the SEM platform, and lattice parameter measurements could be extended to monitor the spatial variation of the lattice parameters on crystal surfaces. This would be possible, in principle, by developing a mapping RHEED system, that is the acquisition of RHEED patterns from a mesh of points from the specimen surface. By indexing the RHEED patterns point by point it would be possible to locally measure the lattice parameter and its variation, i.e strain, by monitoring the change in the position of the diffraction spots and/or the radius of the HOLZ rings.

One of the limitations in the precision achievable in the measurement of lattice parameters in conventional RHEED systems resides in the instrument response, for example in the spot size which is relatively large, of the order of a millimetre. An SEM electron gun allows much more control of the electron beam when compared to conventional RHEED systems. This could allow, in principle, more precise measurements in the SEM. Our present experimental set up did not allow this aspect to be explored, but this is an interesting area for future work.

Another interesting possibility accessible with RHEED is the ability to study polycrystalline materials. In this case RHEED would be a useful tool for evaluating crystal orientation distributions, presence of preferential growth direction etc. In the SEM this information is already accessible by EBSD. On the other hand, if the size of the grains, or their depth, is very small, causing the electron specimen interaction volume to probe different grains, EBSD is limited. In this case RHEED could be a good alternative, considering that the depth resolution is much higher than EBSD. The main advantage of using RHEED would be then the much higher surface sensitivity.

In the example shown in Fig. 6.5 the patterns consist, effectively, of transmission patterns very similar to those obtained in TEM. It has been shown in section 6.2 that when there are three-dimensional features on the surface, for example when the surface is sufficiently rough, e.g. has protrusions or when the specimen is composed of nanostructures, the electrons can penetrate through the sample forming transmission diffraction patterns.

Although it is not shown in this work, it is also possible, in general, to observe diffraction patterns that have characteristics intermediate between reflection diffraction patterns and transmission patterns. Similar to the case of conventional RHEED, RHEED in transmission mode is a powerful means to study materials having a certain preferential texture. In contrast with the transmission diffraction patterns obtained in a TEM, the transmission patterns obtained in RHEED geometry show a shadow edge. The direct beam lies below the shadow edge, as illustrated in Fig. 6.4. The transmission diffraction patterns shown in Fig. 6.5 have been indexed, hence the diffraction condition found, by using the method described in section 2.4, using the relationship between the distances and angles between diffraction spots.

Transmission RHEED in the SEM might also be useful for the study of textured materials, polycrystalline materials, or in general for the study of preferential growth direction, as in the case of fiber texture, biaxial texture etc. Many polycrystalline materials do not have a random distribution of orientations, and show preferential orientations. This can be revealed by RHEED patterns, from which it is possible to calculate the out-of-plane orientation and its dispersion. Methods used to extract this type of information and a range of examples are discussed in Ref. [216].

In the case of polycrystalline materials having random orientation, the RHEED pattern is no longer composed of spots, but semi-circles. When the crystal orientation is not random, e.g. in the case where there is a preferential orientation, the semi-circles becomes arcs of circles. From the geometrical arrangement of those features it is possible to quantify the preferential crystal direction, and also the out-of-plane directions.

Since each RHEED pattern is effectively a slice of the pole figure for a specific azimuthal angle, by acquiring RHEED patterns from different azimuthal angles (to note that in transmission RHEED geometry the full 360° rotation can be accessed) it is possible to reconstruct the entire pole-figure, and obtain the orientation distributions [216].

Definitely, one of the most interesting results obtained in reflection geometry is the SWR-ECCI, shown in section 6.4. Also in this case the results were rather qualitative due to the lack of precise control of the specimen position. Section 6.4 showed that the excitation of surface states by resonance creates a confined state under the sample surface, which releases energy and intensify the intensity of the whole diffraction pattern. This condition has been used for the acquisition of ECCI micrographs under a resonance condition. Examples of the first (non-optimised) SWR-ECC images from a sample of AlGaN are shown in Fig. 6.9. Here a strong contrast is observed for both sub-grains (areas showing different grey scale) and dislocations (the dots with black-white contrast) in the image. For comparison an image obtained in an out of resonance condition, from a different region of the sample is shown in Fig. 6.10.

As already described in sections 6.4 and 3.4.1, in both cases very small changes in orientation and strain are detectable, revealing, for example, low angle tilt and rotation boundaries and atomic steps and enabling extended defects such as dislocations to be imaged. The black-white spots appearing in both Fig. 6.9 and 6.10 can be associated with threading dislocations [122]. Variations in grey scale indicate variations in tilt or twist.

In particular the micrograph obtained under a SWR condition shows higher contrast and detail than the one obtained without a strong resonance condition. Attempts were made to obtain micrographs from the same area but in a different resonance condition but unfortunately none of them were successful. A number of instabilities in the mechanical stage and the motors made it, practically speaking, impossible to obtain images from the same area.

For the same reason it has not been possible to investigate the behaviour of the resonance condition when, at the same time, a two beam diffraction condition is met. It would have been interesting to observe the coupling effect of the two mechanisms, and to determine to what degree the enhancement in the micrograph contrast can be attributed to one or the other mechanism.

A suitable mechanical stage, capable of controlling, with very good precision, the position, the tilt and the rotation of the specimen with respect to the primary beam, would be essential for such investigations. Initial efforts to develop such a system have been made.

Another potential of the technique, arising from the higher surface sensitivity [69, 70], is that this technique is particularly suitable for the characterization of the first topmost few atomic layers of specimens. This opens up the application of the imaging techniques to the study of defects in ultrathin films such as graphene for example.

In general using SWR-ECCI, a new improved level of surface sensitivity, spatial and depth resolution is expected to be obtained. Further work is of course necessary to explore all these possibilities.

# Chapter 7

# Mapping with Timepix

This chapter describes the development of software designed for the implementation of EBSD mapping using the Timepix detector.

## 7.1 Mapping software

Section 4.3 shows that the Timepix detector has imaging capabilities, that is it allows the acquisition of single images. This chapter describes the implementation of software which allows the Timepix detector to be used for mapping. The software was originally created for the implementation of EBSD mapping, but it has more general applications.

As discussed in chapter 3, the acquisition of EBSD maps consists of the acquisition of EBSPs from a regular array of points on the specimen surface. Each EBSP in the array is then processed, depending on the specific analysis, and the resulting information arising from each EBSP will be displayed as a single point in the EBSD map.

In order to obtain an EBSD map the software accomplishes the following steps:

1. Set the detector parameters and acquisition parameters.
2. Position the SEM electron beam on a specific point on the specimen surface.
3. Acquire an EBSP.
4. Wait for the time necessary to readout and save the data.
5. Repeat the previous three steps for each point of the map.

The Timepix parameters and acquisition modes are set by the dedicated Pixelman software [171]. It can be optionally controlled by "remote" from an external application.

The SEM beam position is controlled by external hardware. This consists of an ADLINK PCI-9221, a 16-bit high-resolution and low-cost multi-function DAQ card, which has two analogue channels from which it is possible to generate voltages used to set the two position coordinates of the SEM beam.

The start and the end of the acquisition is controlled by hardware which consists of a USB FTDI chip [166], which is basically an USB to TTL serial universal asynchronous receiver/transmitter (UART) converter, used to trigger in and trigger out the start and the end of the acquisition using the functionality provided by the FitPix interface [167].

The software has been written in Microsoft Visual C# (by the author of the thesis), and it has a user friendly graphical user interface (GUI), see Fig. (7.1).

The remote connection to the Pixelman software and the initialization of the hardware is made by a GUI which also allows the testing of the single components; these are shown in Fig. 7.1.

The mapping parameters, e.g. number of points in the map, the region of interest (the portion of the sample from where the map is acquired) etc., can be set by the

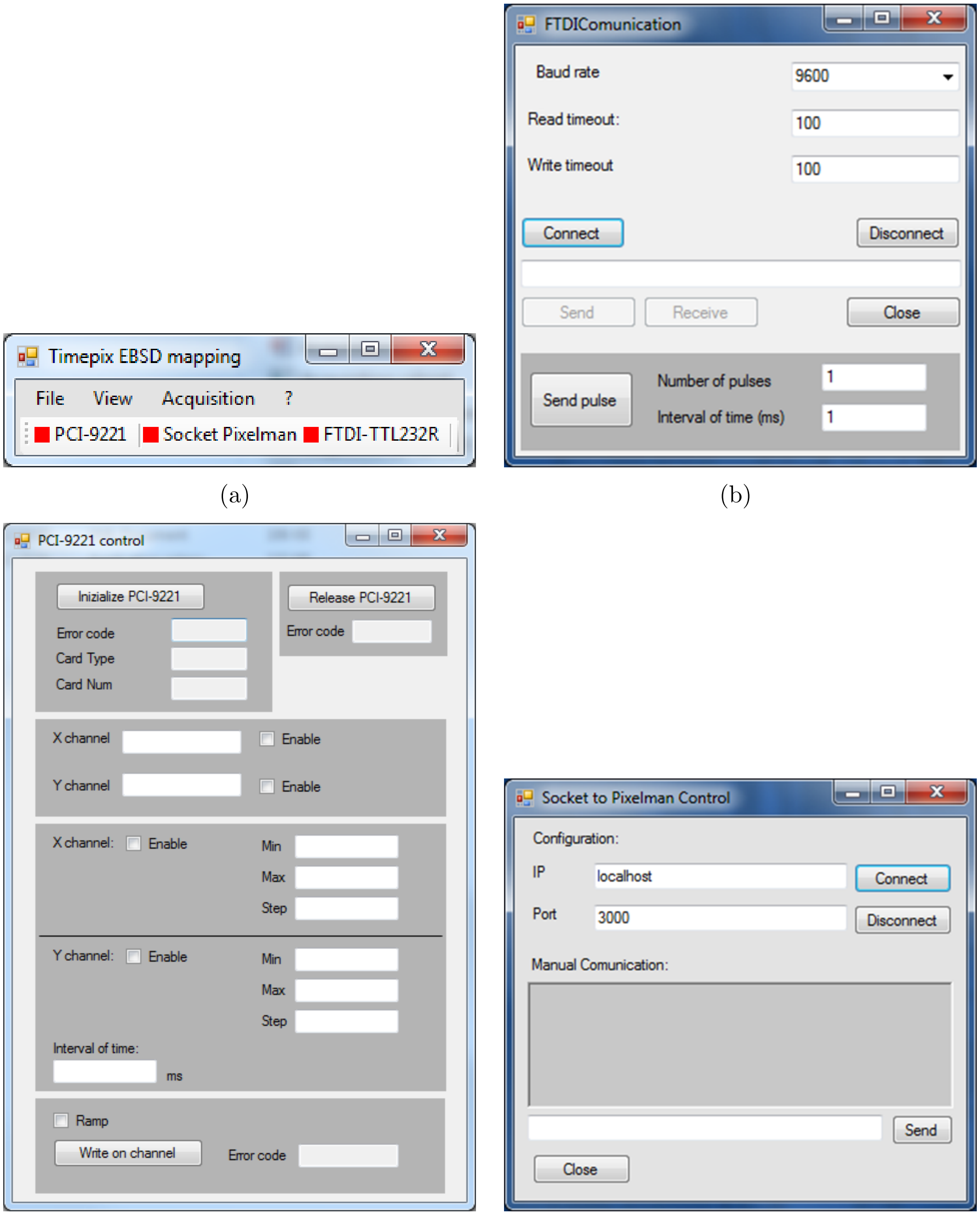

Baud rate: 9600

Read timeout: 100

Write timeout: 100

Number of pulses: 1

Interval of time (ms): 1

IP: localhost

Port: 3000

(a)

(b)

(c)

(d)

Figure 7.1: EBSD mapping software and few of its GUIs: (a) main interface, (b) FTDI Chip inizialization, (c) PCI-9221 inizialization and (d) inizialization of the remote control of the Pixelman software.

“Set scan” GUI, see Fig. (7.2) (a), which is the subroutine which performs the acquisition and synchronizes the series of operations needed for mapping.

A useful function has been implemented to allow the selection of only a selected area of the whole Timepix chip (the red square displayed on the top right of the EBSD pattern in Fig. (7.2) (b) is an example) for the generation of the intensity map. The chip in fact can be thought as an array of 256 × 256 independent single diodes. It is thus possible to obtain intensity maps using a smaller number of selected pixels. This technique has been discussed in Ref. [225]. This is equivalent to moving a virtual diode to different positions with respect to the specimen. As shown later, this reveals contrast in the image arising from different scattering geometries.

The raw data are saved in a folder so that they can be processed after the map is finished.

The raw data can be loaded from the main interface, shown in Fig. (7.2) (a), and all EBSPs can be visualized and checked, Fig. (7.2) (b).

The software allows the visualization of the intensity map, which gives an image showing topographic contrast, Z-contrast, and orientation contrast from the region of interest. This is usually sufficient to show the morphology of the surface. The resulting image should be comparable with the image which would be obtained with a silicon diode if it were used instead of the Timepix detector.

The software also allows the interactive display of the EBSPs at the position of the mouse on the intensity map (Fig. 7.2 (b)). This is useful to show the correspondence between the point of a map and the pattern from which it was derived.

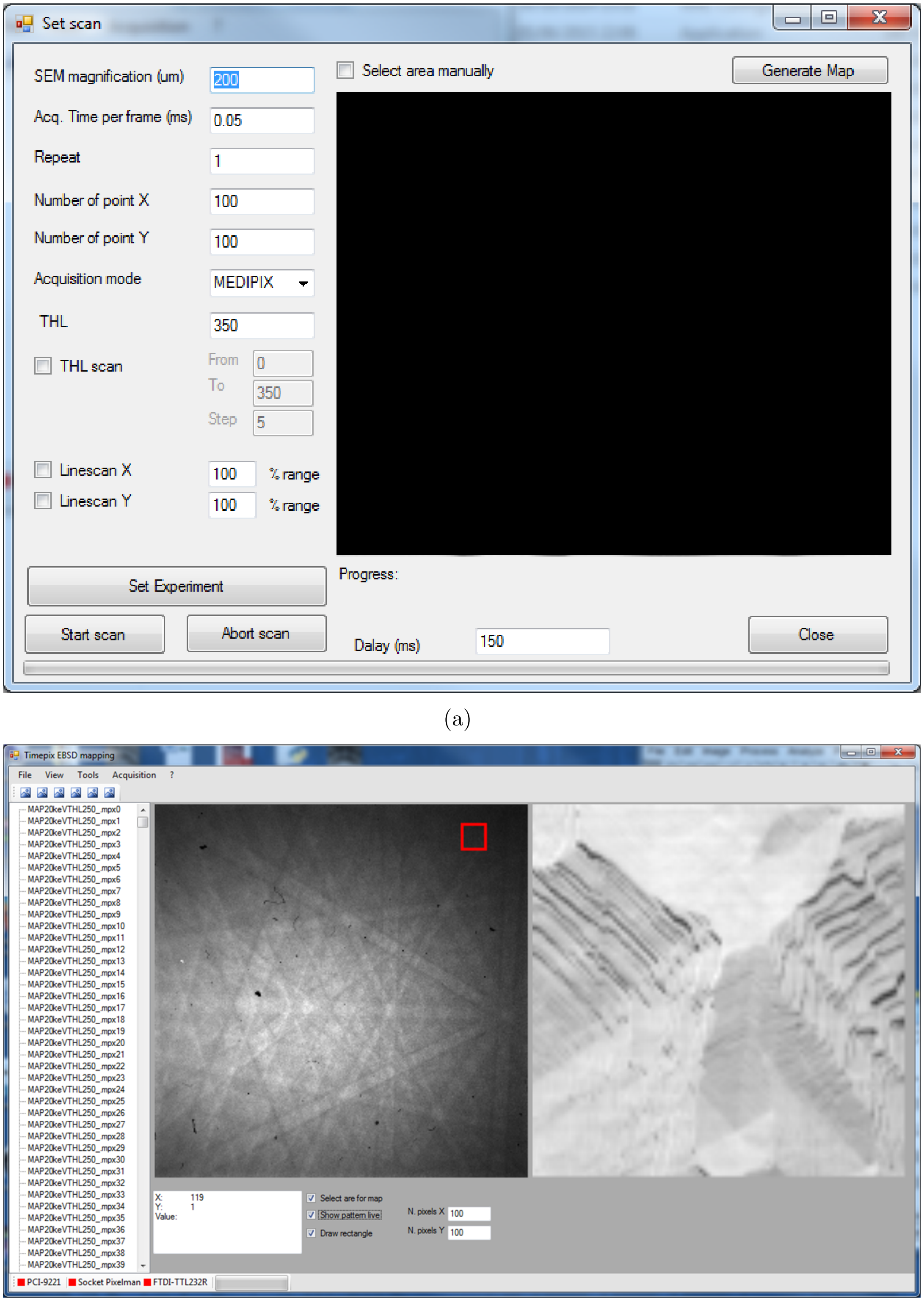

SEM magnification (um) 200

Acq. Time per frame (ms) 0.05

Repeat 1

Number of point X 100

Number of point Y 100

Acquisition mode MEDIPIX

THL 350

☐ THL scan From 0 To 350 Step 5

☐ Linescan X 100 % range

☐ Linescan Y 100 % range

☐ Select area manually

Progress:

Dalay (ms) 150

(a)

MAP20keVTHL250_.mpx0
MAP20keVTHL250_.mpx1
MAP20keVTHL250_.mpx2
MAP20keVTHL250_.mpx3
MAP20keVTHL250_.mpx4
MAP20keVTHL250_.mpx5
MAP20keVTHL250_.mpx6
MAP20keVTHL250_.mpx7
MAP20keVTHL250_.mpx8
MAP20keVTHL250_.mpx9
MAP20keVTHL250_.mpx10
MAP20keVTHL250_.mpx11
MAP20keVTHL250_.mpx12
MAP20keVTHL250_.mpx13
MAP20keVTHL250_.mpx14
MAP20keVTHL250_.mpx15
MAP20keVTHL250_.mpx16
MAP20keVTHL250_.mpx17
MAP20keVTHL250_.mpx18
MAP20keVTHL250_.mpx19
MAP20keVTHL250_.mpx20
MAP20keVTHL250_.mpx21
MAP20keVTHL250_.mpx22
MAP20keVTHL250_.mpx23
MAP20keVTHL250_.mpx24
MAP20keVTHL250_.mpx25
MAP20keVTHL250_.mpx26
MAP20keVTHL250_.mpx27
MAP20keVTHL250_.mpx28
MAP20keVTHL250_.mpx29
MAP20keVTHL250_.mpx30
MAP20keVTHL250_.mpx31
MAP20keVTHL250_.mpx32
MAP20keVTHL250_.mpx33
MAP20keVTHL250_.mpx34
MAP20keVTHL250_.mpx35
MAP20keVTHL250_.mpx36
MAP20keVTHL250_.mpx37
MAP20keVTHL250_.mpx38
MAP20keVTHL250_.mpx39

X: 119
Y: 1
Value:

☑ Select are for map
☑ Show pattern live
☑ Draw rectangle

N. pixels X 100
N. pixels Y 100

(b)

Figure 7.2: EBSD mapping software and further GUI interfaces: (a) Set scan and (b) Intensity map.

## 7.2 EBSD mapping

The software described in the previous section has been tested on a polycrystalline WC/Co hard metal sample. The area of the surface selected for the EBSD map is shown in Fig. 7.3(a). The corresponding intensity map, obtained using the integrated response of the EBSD detector as function of the electron beam position, is shown in Fig 7.3(b).

The intensity map was obtained using a beam energy of 20 keV and a beam current of ≈ 0.25 nA and an acquisition time of 50 ms per point; no energy filtration was applied. The result shows a very good correspondence between the SEM image (Fig. 7.3(a)) obtained from the same (larger) area.

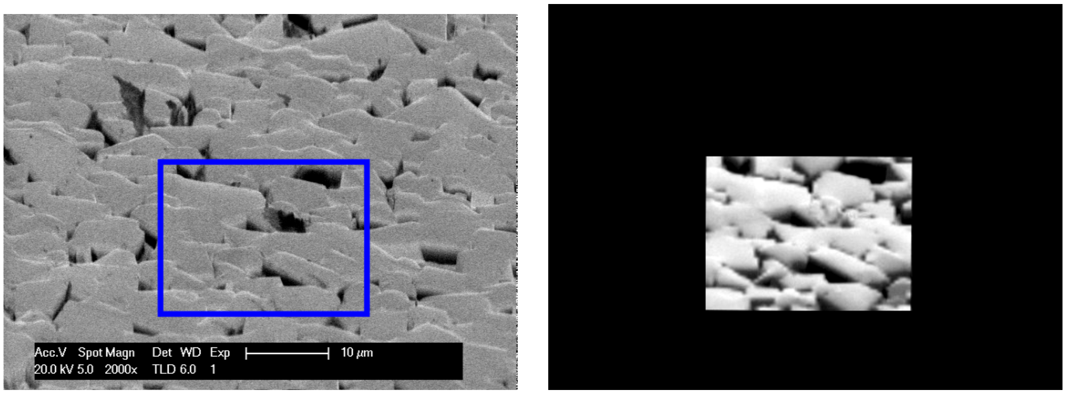

(a) (b)

Figure 7.3: SEM image (a) of an hexagonal polycrystalline WC/Co hard metal surface showing the area of the surface selected for the EBSD map and corresponding (b) intensity map obtained using the integrated response of the EBSD detector as function of the electron beam position. No energy filtration was applied.

An EBSD orientation map from a region of the WC/Co sample was also obtained, using a 30 keV electron beam and a beam current of ≈ 0.25 nA. Two EBSPs from the EBSD orientation map are shown in Fig. 7.4. The EBSD patterns were indexed using an hexagonal phase using a conventional Hough-based indexing method, that is, only considering the geometrical arrangement of the Kikuchi bands.

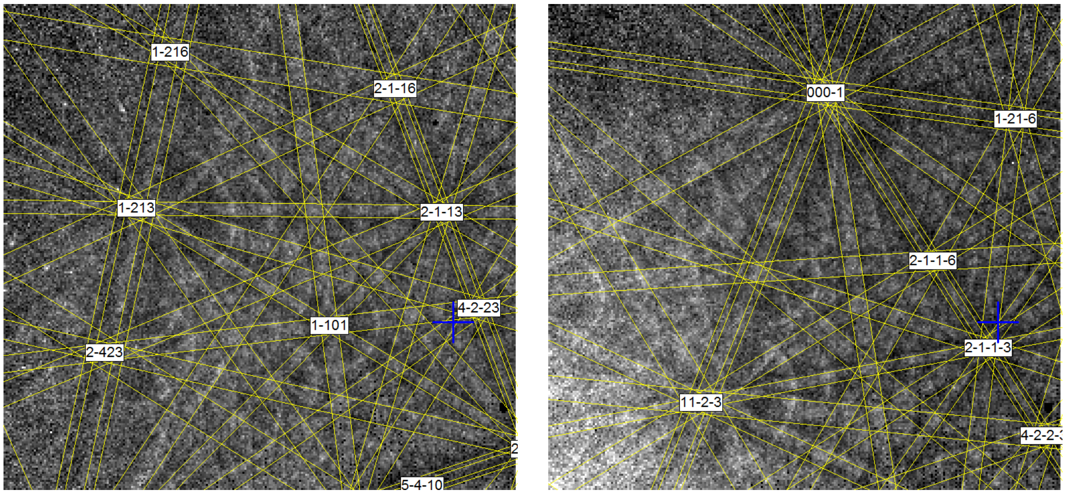

(a) (b)

Figure 7.4: Examples of indexed EBSPs from an hexagonal polycrystalline WC/Co.

The resulting EBSD map is shown in Fig. 7.5, where the resulting intensity map (a), the orientation map (b), the legend showing the standard stereographic triangle where each colour is associated with the crystal orientations (c), and an image obtained on overlapping the intensity map with the orientation map (d) are shown. It is possible to see clearly the different grains showing different crystallographic orientations.

There are points in the EBSD map which are not indexed. Failure in the EBSD indexing can be mainly attributed to three effects. One is the shadow casting of grains on the detector screen; this is generated when the neighbour grains have more elevation with respect to the point of the surface under examination, so they do not allow a good portion of the electrons to reach the detector screen. Failure in the indexing happens also when the EBSD pattern is obtained from a point of the surface placed at the edge between grains; in this case the recorded EBSD pattern consists of the overlapping of two or more patterns. Finally indexing failure can be the result of a non-optimal choice of the image processing routine, e.g. number of Kikuchi bands to be examined, filtering etc.

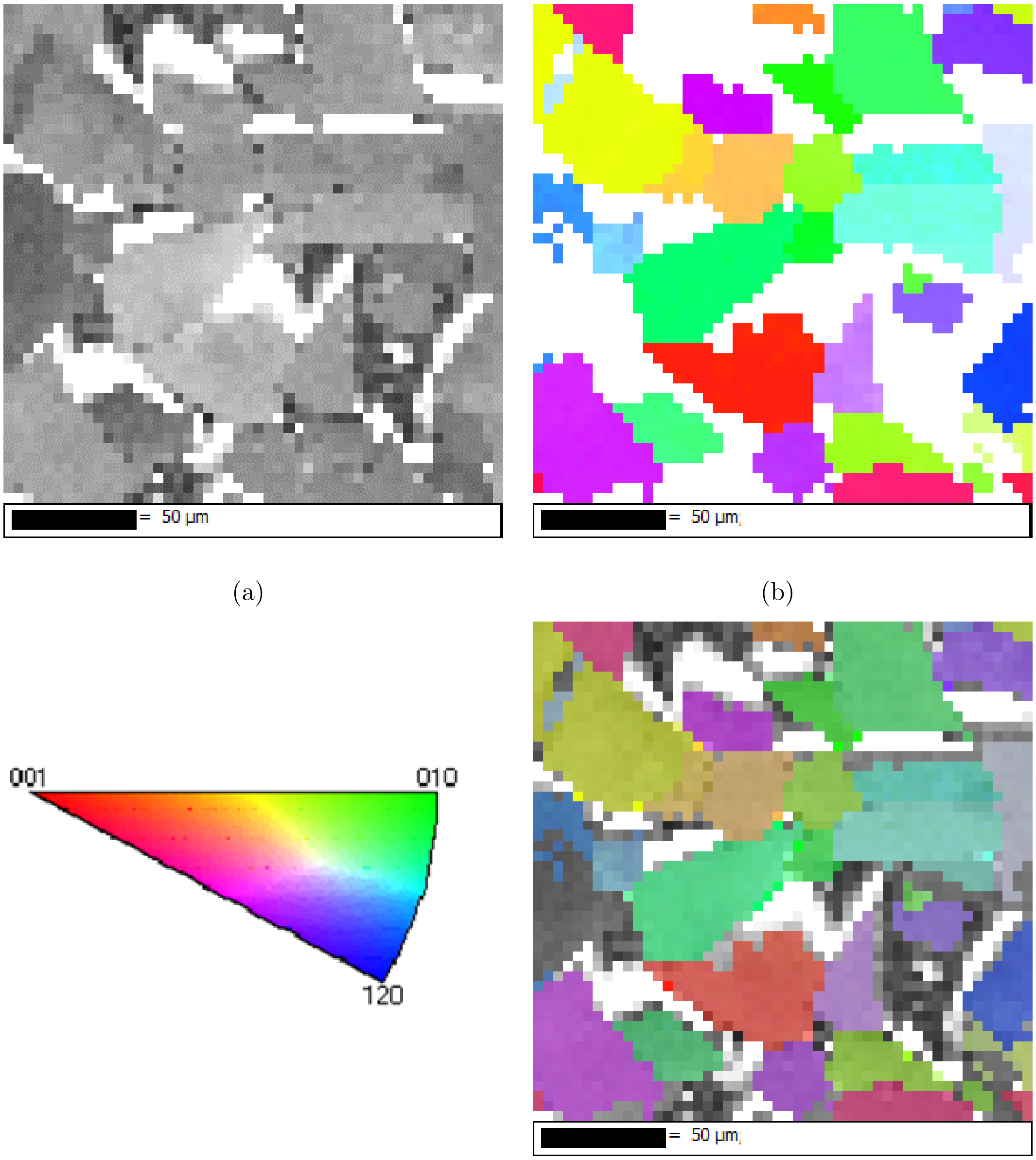

(a) (b)

(c) (d)

Figure 7.5: EBSD map from an hexagonal polycrystalline WC/Co: (a) intensity map, (b) orientation map, (c) the legend showing the standard stereographic triangle of the inverse pole figure where each colour is associated with the crystal orientations, (d) overlap of the intensity map and orientation map.

An intensity map was also obtained from a *c*-plane ([001]) oriented single crystal

AlGaN sample (details of which can be found in Ref. [186]). This sample has been grown on a honeycomb-patterned sapphire substrate, which promotes the formation of parasitic (pyramidal shaped) crystallites. A SEM image of the specimen is shown in Fig. 7.6; here also the area of the surface selected for the EBSD map is indicated. The resulting intensity maps are shown in Fig. 7.7. If images are obtained by using different areas of the detector, the resulting intensity maps may show different contrast.

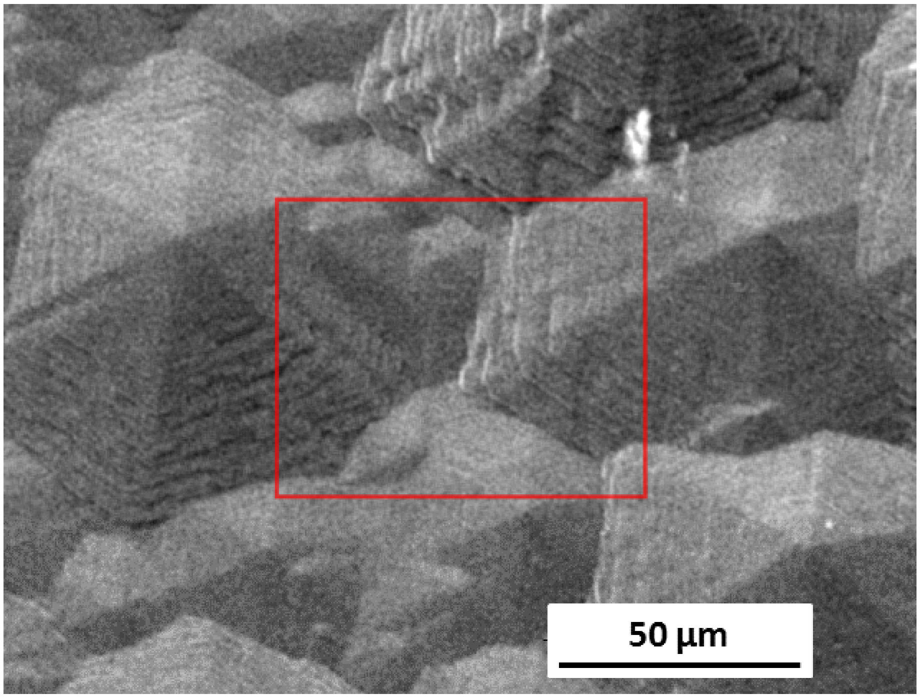

Figure 7.6: SEM image of a wurtzite monocrystalline AlGaN surface.

Fig. 7.7 shows two intensity maps obtained from the same dataset, i.e., EBSPs, but obtained collecting the signal from a different area of the same EBSP. These are highlighted with “A” and “B” in Fig. 7.7. The resulting intensity maps obtained from the two selected areas are shown in Fig. 7.7 (b) and (c) for the areas A and B respectively. In this particular case there is an almost complete contrast reversal.

This can be understood considering that electrons scattered predominately in the direction of one particular virtual detector, due to the tilt of the surface, are mutually excluded by the other.

Obtaining intensity maps from different areas has another advantage. It is possible to combine data obtained from different areas of the detector, and perform mathematical operations between them. This will be discussed in more detail in Section 7.4.

An example of this is shown in Fig. 7.7 (d) where the intensity map from the area B is subtracted from the intensity map obtained from the area A.

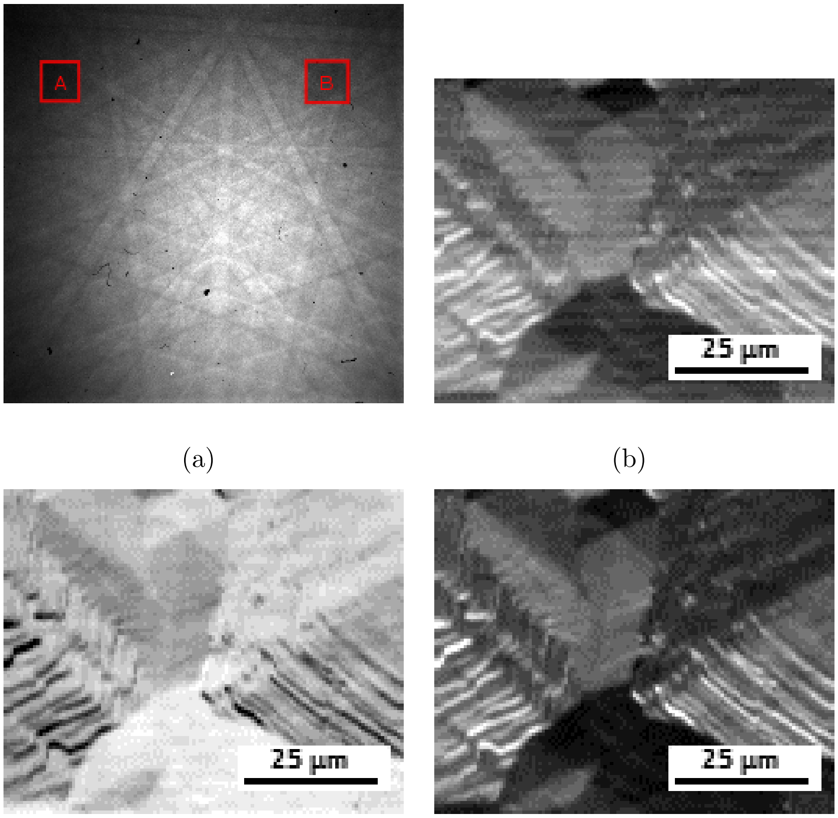

(a) (b)

(c) (d)

Figure 7.7: EBSD map from a wurtzite monocrystalline AlGaN: (a) areas A and B selected for the intensity map, (b) intensity map from area A, (c) intensity map from area B, (d) intensity map obtained subtracting B from A.

An advantage of using virtual diodes is the possibility to perform colour orientation contrast imaging [226] using virtual diodes [225]. This can be obtained by using three virtual diodes, and associating a colour to each of them. In this case these were associated to them the red, green and blue colours.

An example of a colour image is shown in Fig. 7.8, where the position of the virtual diodes, their colours and the corresponding colour image is displayed. The applications of such colour images will be discussed in Section 7.4.

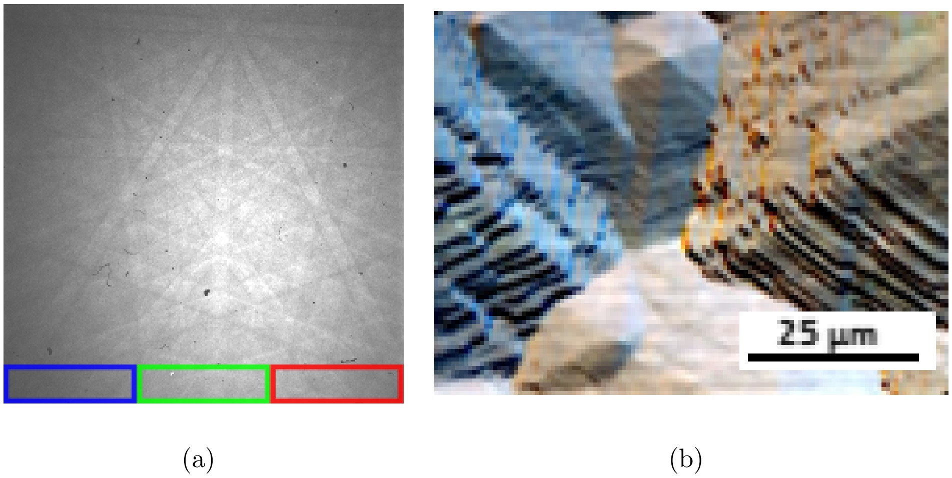

(a) (b)

Figure 7.8: Example of colour imaging using the Timepix detector, (a) position of the three virtual detectors and colour associated to them, (b) resulting colour image.

## 7.3 TKD mapping and STEM

TKD mapping has been also tested in transmission mode. The sample used in this experiment was a cross section of an ELO AlGaN/AlN/sapphire structure described previously in section 5.2.1 and shown in Fig. 5.9. A thin layer of Au/Pt is usually deposited on the sample (on top of the AlGaN in this case) to avoid contamination from the FIB ions during the sample preparation.

TEM images show a variety of features, such as thickness fringes, defect contrast, compositional contrast and so on, as mentioned in section 3.2.

In order to understand the contrast formation mechanisms, the knowledge of the diffraction condition and deviation parameter is fundamental. Also important is the position of the aperture which allows the collection of the electrons scattered only in particular directions, excluding all the others [6].

In our configuration, a real physical aperture was not used, but, as shown in the previous sections, a number of pixels in the chip was selected for the analysis. This is equivalent to performing STEM in the SEM.

Another advantage of using a pixellated detector is that it can act simultaneously as an high-angle annular dark-field (HAADF) or an annular dark-field (ADF) detector in the TEM.

An intensity map obtained from the top of the specimen shown in Fig. 5.9, using the Timepix detector, is shown in Fig. 7.9. It was obtained by acquiring TKDs from $100 \times 68$ points at a beam energy of 30 keV and a beam current of $\approx 2.25$ nA. In this case the lack of control on the sample holder adjustment has prevented the sample to be oriented with the beam parallel to a major crystallographic axis.

The figure shows how different areas of the detector reveal different contrast in the resulting intensity maps. The bright field intensity map, i.e. the one obtained by monitoring the variation in the intensity of the direct beam (Fig. 7.9 (c)) does not reveal a strong difference in contrast from the thin layer of Au/Pl layer, the AlGaN and AlN layer respectively, as in Fig. 5.9. This difference is more visible for example in the dark field maps in Fig. 7.9 (b) and (d), where the metal deposition, the AlGaN and the AlN layer show a different contrast. Note furthermore the reversed contrast between the AlGaN and the AlN layers on comparing Fig. 7.9 (b) and (d).

Intensity maps from the bottom of the specimen are shown in Fig. 7.10. It is interesting to see changes in the contrast as the selected area is varied across the Timepix chip. The linear features appearing in Fig. 7.10 may be attributed to crystalline defects, but at the moment, this cannot be quantified.

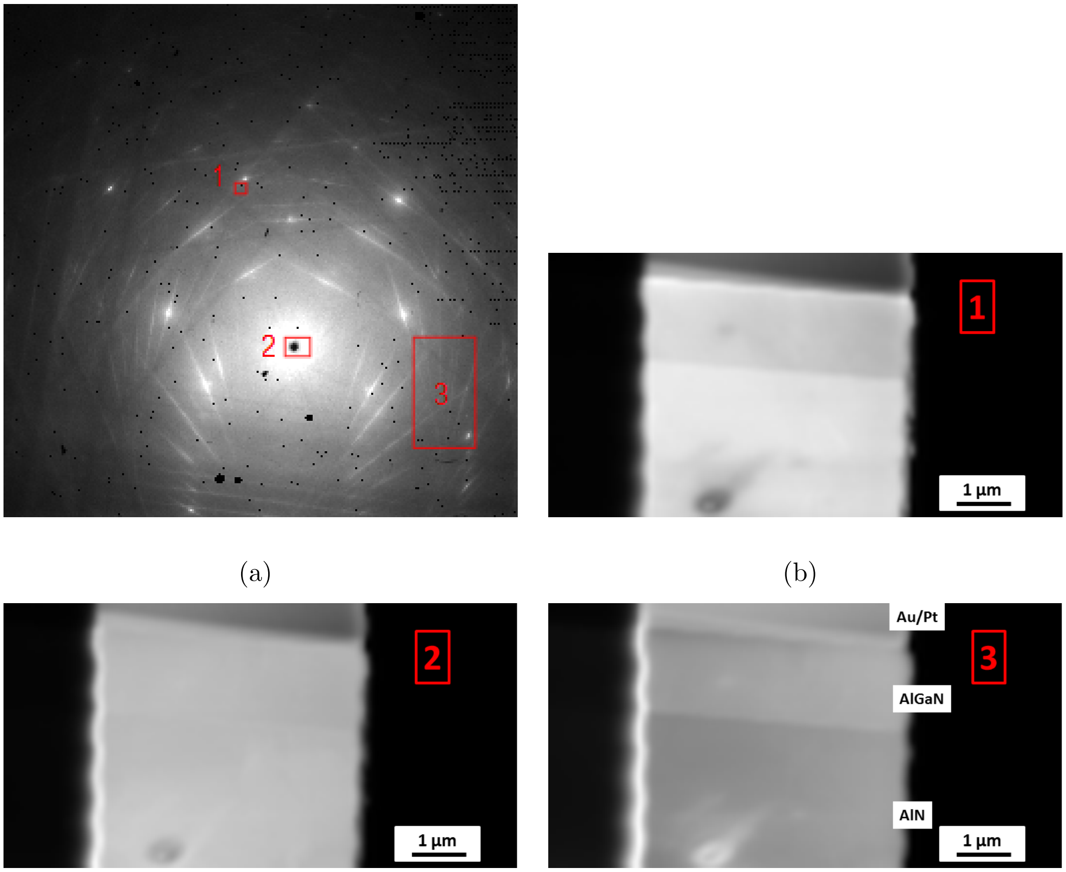

(a) (b)

(c) (d)

Figure 7.9: STEM image from a monocrystalline ELO AlGaN/AlN/sapphire structure (the thin layer of Au/Pt is usually deposited on the sample to avoid contamination from the FIB ions during the sample preparation) obtained using different sub-areas of the Timepix chip: (a) image of the diffraction pattern from the Timepix chip showing the areas selected for the intensity maps, (b) intensity map from area 1, (c) intensity map from area 2, (d) intensity map from area 3.

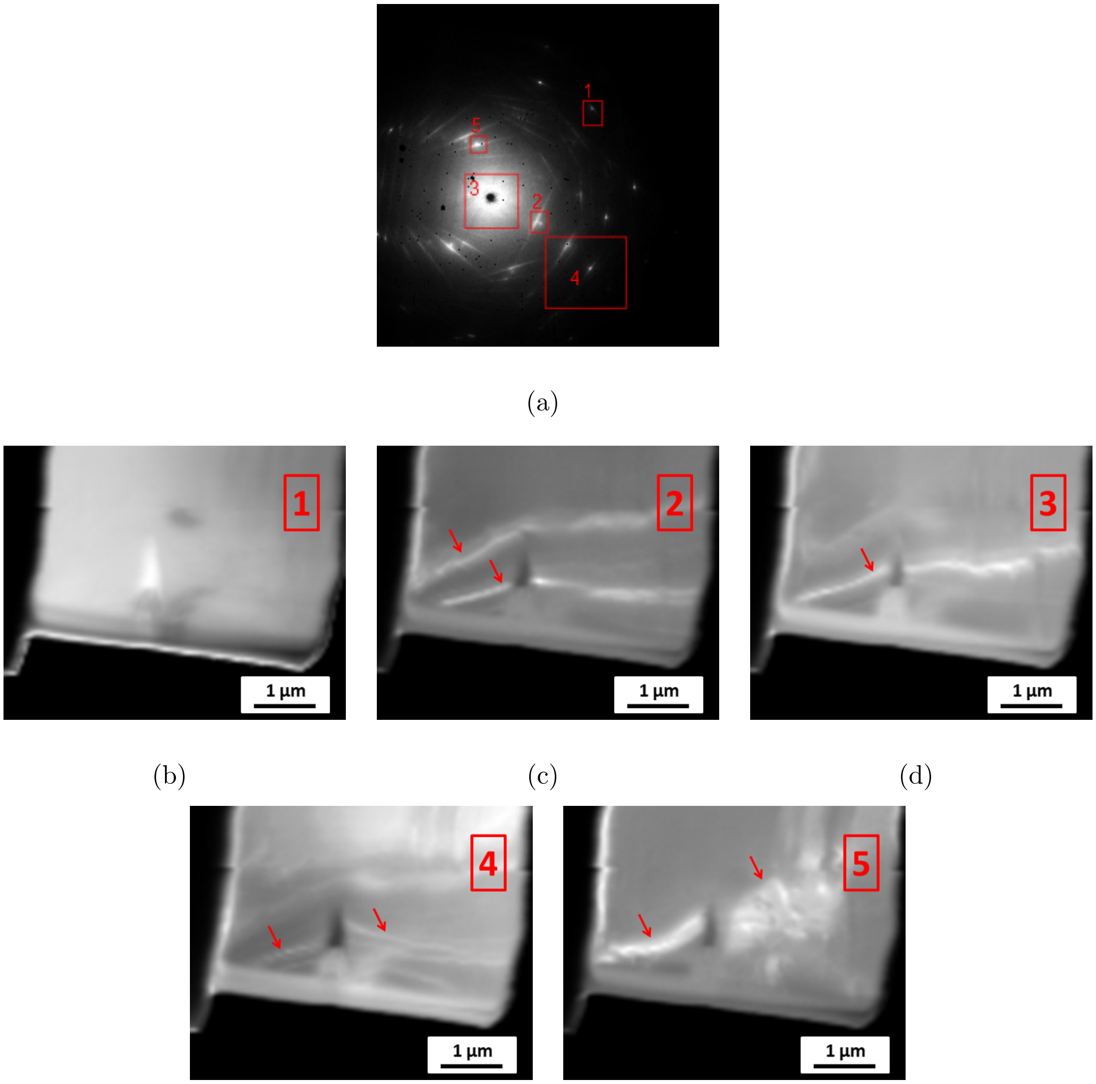

(a)

(b) (c) (d)

(e) (f)

Figure 7.10: STEM image from the wurtzite monocrystalline AlN region of the ELOG AlGaN/AlN/sapphire structure, obtained using different sub-area of the Timepix chip: (a) image of the diffraction pattern from the Timepix chip showing the areas selected for the intensity map, (b) intensity map from area 1 (c) intensity map from area 2,

(d) intensity map from area 3, (e) intensity map from area 4, (f) intensity map from area 5. The bright lines highlighted with the red arrows can be attributed to crystalline defects.

## 7.4 Discussion

This chapter describes the development of software that allows the Timepix detector to be used for obtaining maps displaying different information from the samples. This was shown for both the backscattering and transmission geometry.

In backscattering geometry a first example of mapping is shown in Fig. 7.3. The map shows the result from an EBSD map from polycrystalline WC/Co. The area highlighted in the SEM image shown in Fig. 7.3(a) was used for the map. Figure 7.3(b) shows the intensity map obtained using the integrated response of the EBSD detector as a function of the electron beam position. It provides different types of information on the specimen. First it gives compositional information, due to the Z contrast mechanism. The dark areas in the map correspond to the areas with lower backscattering, which can be associated with the cobalt matrix in the sample. The bright areas are associated with the more dense WC phase. Typically the interpretation of backscattered images is not quantitative, but qualitative. As already explained in Chapter 3, different mechanisms contribute to the contrast formation. These include local tilt, local crystal orientations etc. Shadow casting of the grains on the surface may also lead to a incorrect interpretation of the results. In our case, the dark areas of Fig. 7.3(b) could be also associated with shadow casting of the grains. The grey level variation between different grains can be associated with the different orientations of the grains and/or different morphology of the grains. To obtain quantitative information about the grain orientation EBSD analysis is necessary.

By analysing the EBSD patterns, as shown in Fig. 7.4, the EBSD map shown in Fig. 7.5 is obtained. Here the grains having different crystal orientation are shown with different colours. Each colour is associated with a particular crystal orientation as shown in Figure 7.5(c). The colours have been displayed in the reverse pole figures.

The EBSD patterns were analysed using conventional methods, based on the Hough transform. The few patterns shown in Fig 7.4 were used to show that even using a relatively low current, $\approx 0.25$ nA, and a relatively low acquisition time, 50 ms, the quality of the EBSP patterns is sufficient to perform the indexing, and extract information from them.

EBSD is an established technique and the innovation introduced so far was the use of a novel detector to improve the quality of the EBSD patterns.

The evolution of the technology and the advent of increasingly sensitive and reliable detectors makes possible the use of EBSD detectors for imaging purposes. Two dimensional detectors are, as may seem trivial, arrays of independent detectors. Each detector (i.e. pixel) can be used to monitor the intensity scattered over a particular solid angle. In our case, using the Timepix detector, for the same EBSD map dataset one could obtain $256\times256$ independent images, plus an almost limitless number of images obtained by combining the independent ones. This offers a variety of possibilities in using the detector which can be accessed from a particular experimental dataset [227]. An application of this concept is shown in Fig. 7.7.

The area highlighted with “A” and “B” in the diffraction pattern shown in Fig. 7.7(a) have been used to obtain the intensity maps, shown in Fig. 7.7 (b) and (c) for the area A and B respectively.

Figure 7.7 (d) shows the difference between the signal obtained from A and B. This operation is equivalent to using two silicon diodes placed in different positions with respect to the specimen and performing a differential amplification.

The effect is a strong reduction in the noise, and elimination of artefacts such as the parallel vertical intensity variation across the image due to the scanning beam, as visible in the intensity maps obtained using only one selected area, Fig. 7.7 (b) and (c).

An example of colour imaging was shown in Fig. 7.8. This concept has been discussed extensively in Ref. [226], where the authors showed that it is possible to perform colour orientation contrast imaging to reveal changes in the crystallographic orientation and in the morphology in crystalline materials.

In the case of Fig. 7.8, the different colours highlight predominantly the local tilt of the surface. The three dimensional growth of the specimen resulted in a number of hexagonal pyramid-like features on the surface, as shown in Fig. 7.6. Each side wall of the pyramid has a particular tilt. The latter affects the direction of the backscattered distribution of the electrons which is revealed in different colours in the image. This approach helps to visualize the morphology of the surface.

If the same approach had been used for a polycrystalline material, not having a strong three dimensional topography, e.g. in polished surfaces, the colour image would have been composed of grains having different colours. Each colour would have been associated with a particular crystallographic orientation. In terms of EBSD this can be used as an advantage in the case where there is a poor signal to noise ratio in the EBSP or when for example there is an ambiguity in the assignation of a particular crystallographic orientation to a particular EBSP. In this case the assignment of a particular crystallographic structure could be based on the colour imaging outcome.

The same argument is valid for the case when two materials have the same crystallographic structure but different chemical composition. In the latter the backscatter intensity could be used to discriminate the two materials.

Another general advantage of using colour images is also related to the fact that the human eye is much more sensitive to variations in colour than variations in the grey scale [228, 229]. Colour imaging thus allows subtle detail in the images to be revealed, which might not be distinguished in a grey scale image.

Another powerful application has been shown in 7.3. The exploitation of mapping in transmission mode, in a manner analogous to that performed in the STEM, was shown from an AlGaN cross section. This is shown in Fig. 7.9 and Fig. 7.10, where TKD maps from a cross section of an AlGaN/sapphire structure were acquired.

In our case, instead of having real ADF and HAADF detectors, virtual detectors were used, as before, by integrating the detector count only in specific areas of the detector.

Here the technique allows different types of information to be revealed. For example, the different layer structures: the gold and platinum deposition, the AlGaN or the AlN can be all differentiated. These two latter regions in fact show different intensities transmitted through the crystal. The discrimination between the different layers is particularly visible in the images obtained by processing the data using virtual detectors relatively distant from the central spot, in a manner similar to a HAADF detector, where the Z contrast is the main mechanism of contrast generation. This is seen, for example, in the areas labelled “1” and “3” in Fig. 7.9.

Figure 7.10 is another significant example showing one of the potential applications of this approach. In this case it is possible to see how different types of contrast arise from the several virtual detectors shown in Fig. 7.10(a). At the moment it is not possible to quantify the contrast observed in the micrographs. On the other hand is it very interesting to note how, depending on the position of the virtual detector, different distortions of the lattice can be highlighted. By direct comparison with the TEM image, Fig. 5.9(b), obtained from the same specimen, the lines seen in the AlN region seem to be associated with crystalline defects in the layer. Since, by selecting different virtual detectors, different contrast mechanisms can be revealed, this approach could be used in principle for the identification of crystalline defects. In general this approach can be used to allow a number of TEM based techniques to be performed in the SEM. The disadvantage when compared with an actual TEM is that the spatial resolution is strongly reduced, because it is limited by the probe size of the SEM. On the other hand the use of the SEM makes possible the imaging of large samples, e.g. of the order of square centimetres, with high resolution. This is particularly suitable for those fields of material science where there is more interest in the microstructure rather than the nano/picostructure.

When compared with conventional EBSD, TKD mapping has higher spatial resolution, so that it opens up the characterization to those materials having smaller grain size, making possible the study of misorientation and strain with increased resolution.

It is possible to note that the bright field images shown in Fig. 7.9 (c) and Fig. 7.10 (d) show a black background (i.e. the area where the electron beam is not focused on the sample), where a bright background is in principle expected. As explained already in section 5.2.1 this is due to the fact that when the electron beam is directed directly on the Timepix chip, there is a saturation effect which makes the count very low [215].

As mentioned several times during the thesis, the limitations in the hardware used for the experiments have limited the exploration of the technique. Future developments of the hardware should include some sort of control of the sample stage. This would be essential for setting particular diffraction conditions, orienting the sample and positioning it with respect to the SEM column axis.

The approach in general was worthwhile, since it allowed the access to imaging modes which are not common in the SEM. If a good control over the specimen orientation and over the detector-to-specimen distance is established, the technique should allow significant quantifiable results to be obtained. This should allow the transfer into the SEM platform of a number of imaging and diffraction techniques which are presently only used in the TEM.

# Chapter 8

# Detector diffraction patterns

## 8.1 Detector diffraction patterns

This chapter describes the development of a novel method for the determination of the spatial coordinates of a source of waves using a two-dimensional detector having a crystalline sensor [230]. This method is based on the acquisition of what was called detector diffraction patterns (DDPs), never observed previously. The effect is produced by electrons, X rays, neutrons, ions, and in general by every particle which undergoes Bragg diffraction. The following description regards the formation of DDPs using the electrons as the source. In this particular case DDPs consist of contrast-inverted electron channelling patterns (ECPs) generated on a sensor material when an isotropic source of electrons is placed somewhere in front of the detector.

An ECP may be obtained by scanning a focused beam of electrons over the surface of a monocrystalline specimen and monitoring the backscattered electron intensity as function of the incident angle, as shown in Fig. 8.1 and as also discussed in section

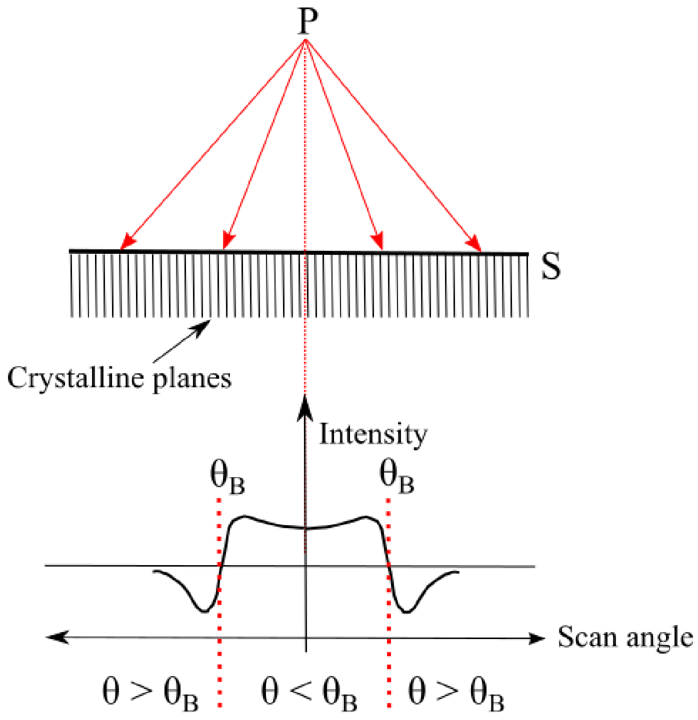

Figure 8.1: ECP/DDP formation.

3.4.1.

During the scanning, the beam originating at a point P impinges on the specimen surface (indicated with an S in Fig. 8.1) with different incidence angles, resulting in different backscattered intensities.

At low magnification the angle between the sample surface and the incident electron beam varies significantly over the field of view. When the angle between the incident beam and a set of parallel crystal planes corresponds to the Bragg angle, (that is, the condition for diffraction is met), a strong modulation in the backscattered intensity occurs, giving rise to the formation of the typical profile of a Kikuchi band as shown in Fig. 8.1.

DDPs have essentially the same origin as ECPs. The process can be illustrated using the same Fig. 8.1 used to explain the ECP formation. If the point P is considered as an isotropic source of electrons, that is electrons simultaneously generated from the point P and propagating in different directions, and consider the surface S as the sensor surface, it is clear that the electrons approach each pixel of the sensor with different incidence angles, so that an electron will be backscattered differently from the sensor material depending on its incidence angle with respect to the crystalline sensor.

The difference between ECPs and DDPs is that in the case of the ECPs the beam has one direction at a time (neglecting the beam divergence) and it is deflected over the sample to cover a range of angles; in the case of DDPs the source of electrons is a static point in space, and emits simultaneously electrons covering a range of directions moving to the sensor.

As with ECPs, DDPs reflect the fact that the sensor material is monocrystalline and that electrons impinging on the detector with different directions will be in general backscattered with different strengths. The intensities observable in the recorded pattern will then show the crystal symmetry of the sensor material as in an ECP pattern.

Because for a detector pixel the greater the backscattering the lower the production of electron-hole pairs within the pixel, the recorded pattern will look like an ECP from the sensor material, but with inverted contrast.

Figure 8.2 illustrates how to reveal the DDP from the raw data. In this case the raw DDP was acquired using the Timepix detector, whose sensor consists of silicon [111], in a conventional EBSD geometry, by focusing a 12 keV electron beam on a 10 nm thick layer of a nanocrystalline $HfO_2$ specimen grown on a silicon substrate. No energy filtering was used. The layer may be considered for this experiment as an amorphous material since it does not produce any EBSD pattern, as shown in Fig. 8.2 (a), and it is only used to produce the divergent source of electrons.

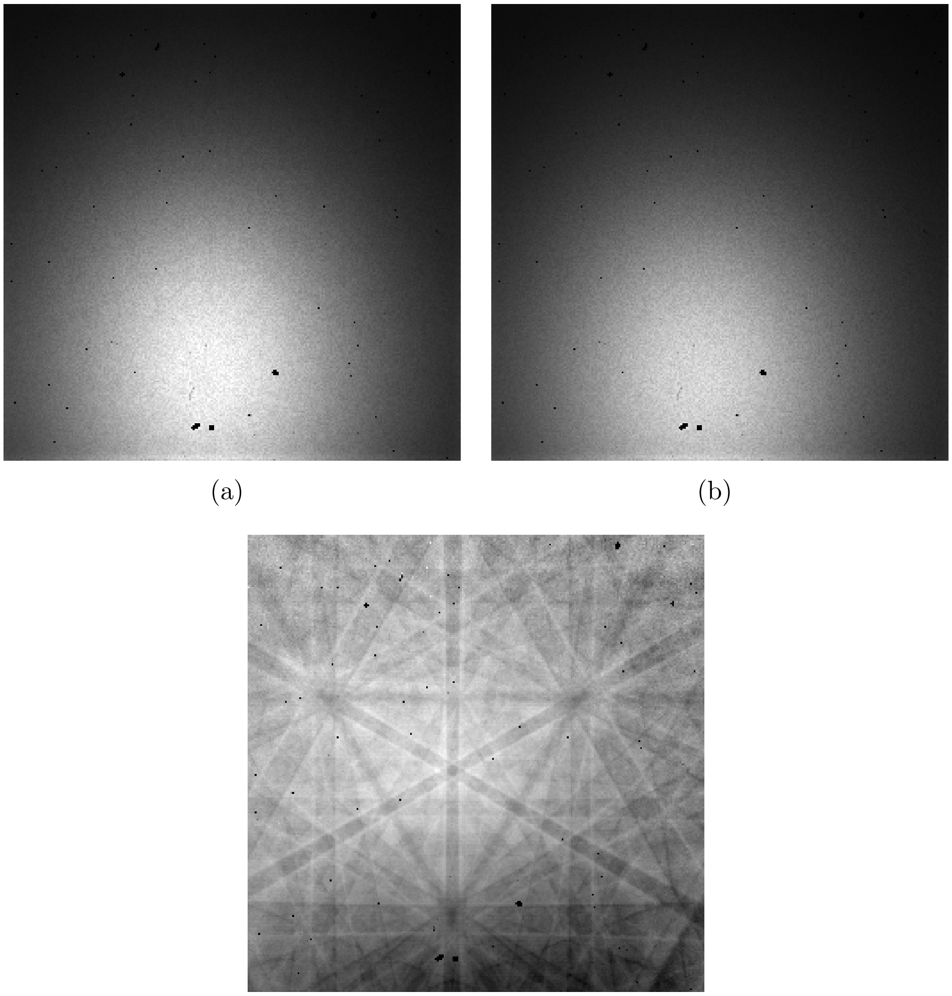

(a)

(b)

(c)

Figure 8.2: Illustration of how to obtain a detector diffraction pattern (DDP): (a) raw DDP, (b) background, (c) flat fielded DDP. No energy filtration was used.

From Fig. 8.2 (a) it is also possible to see that the effect is subtle, and it is hard to see without a flat field correction. By flat fielding Fig. 8.2 (a) with a background, 8.2 (b), obtained by integrating a number of frames from the surrounding area, the DDP is enhanced as shown in 8.2 (c).

Examples of flat fielded DDPs acquired using a range of electron beam energies (5, 12 and 25 keV) are shown in Fig. 8.3 (a-c). Monte-Carlo simulations [231,232] are also displayed in Fig. 8.3(d-f) to show the electron trajectories within the specimen

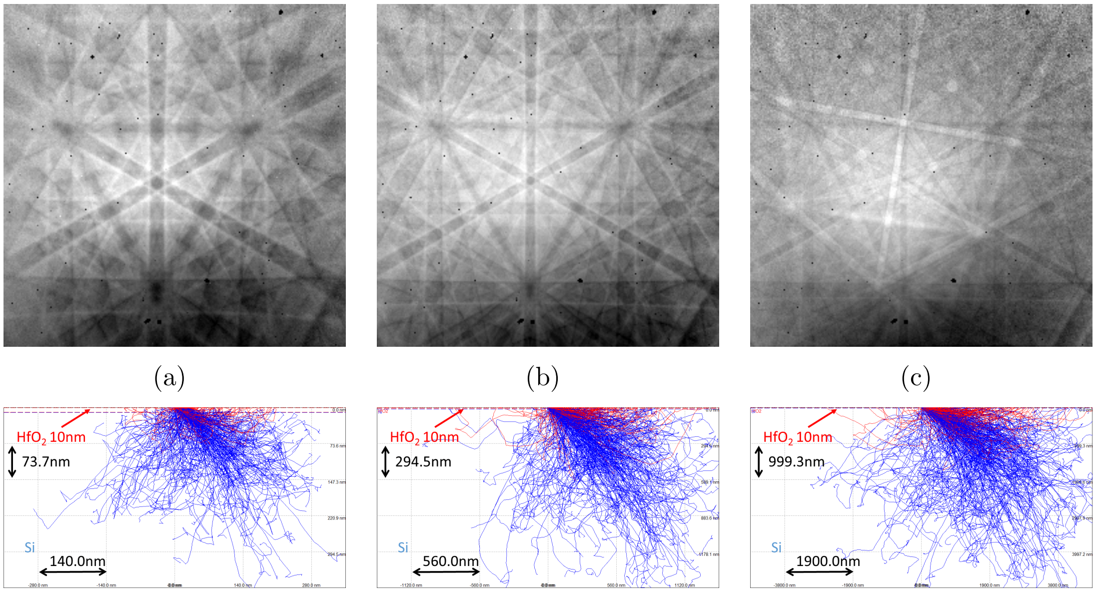

(a) (b) (c)

(d) (e) (f)

Figure 8.3: Example of detector diffraction patterns acquired using different electron beam energies: (a) 5 keV, (b) 12 keV, (c) 25 keV, from a 10 nm thin layer of amorphous HfO$_2$ specimen grown on a silicon substrate. Monte-Carlo simulations (d-f) are used to show the electron trajectories (the red trajectories correspond to backscattered electrons) for the three cases (a-c) respectively. No energy filtration was used.

for the energies used in the experiment. In the pattern shown in Fig. 8.3(c), obtained using 25 keV electron beam, it is interesting to note the overlap between the DDP (showing dark features) and the EBSD pattern from the silicon substrate.

This detector effect has important implications. By calibrating the DDP, that is indexing it using conventional software used to index EBSPs/ECPs, is it possible to determine the position of the point source P with respect to the detector (i.e. the pattern centre, PC), and so the projection parameters, from the detector itself.

The calibration procedure, i.e. the indexing of the diffraction patterns, consists of a quantitative comparison of theoretical Kikuchi pattern simulations with the experimental DDP. The parameters used for the simulations include the electron energy, the source point position with respect to the detector and the orientation of the sensor crystal structure with respect to the detector surface plane [150, 230].

The orientation of the sensor material's crystal structure relative to the edges of the detector can be described by Euler angles $(\phi_1, \Phi, \phi_2)$ which parametrize a rotation sequence around the ZXZ-axes in the Bunge convention [230, 233].

Figure 8.4, shows an example of the indexing of a DDP obtained from a 20 nm thin layer of amorphous $HfO_2$ grown on a silicon substrate using a 12 keV electron beam, obtained using the ESPRIT Dynamics software [168]. For practical purposes the intensity in the image has been artificially inverted, so that the dark Kikuchi bands become bright.

The indexing results in crystal orientation $(\phi_1 = 179.95°, \Phi = 54.53°, \phi_2 = 45.15°)$, $DD = 0.45564$, $PC_x = 0.44680$, $PC_Y = 0.59198$, $CC = 0.701$, where DD, $PC_x$, $PC_y$ and $CC$ are the detector to specimen distance, pattern centre position in the x direction, pattern centre position in the y direction, expressed in screen units (the detector side equals one), and $CC$ the normalized cross correlation coefficient respectively. The $CC$ between two sets of two-dimensional data $t(x, y)$ and $f(x, y)$ (e.g. two images) is defined as [234–236]

$$CC = \frac{1}{n} \sum_{x,y} \frac{(f(x,y) - \overline{f})(t(x,y) - \overline{t})}{\sigma_f \sigma_t}, \tag{8.1}$$

where $n$ is the number of pixels in $t(x, y)$ and $f(x, y)$ ($x$ and $y$ are the pixel coordinates), $\overline{t}$ and $\overline{f}$ are the average of $t$ and $f$ respectively and $\sigma_t$ and $\sigma_f$ are the standard deviations of $t$ and $f$ respectively. CC gives a measure of the similarity between two series of data, and its value varies between 0, indicating no correlation between data, and 1 indicating the perfect match. The value 0.701 indicates a very good match between the simulated and experimental patterns.

To prove the applicability of the concept, that is being able to determine the

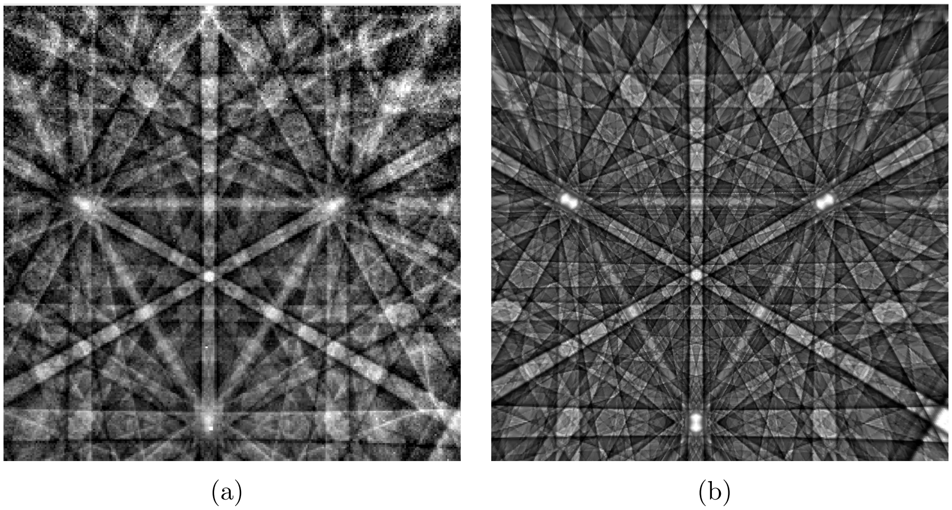
(a) (b)

Figure 8.4: Example of indexing of a DDP: (a) experimental DDP , (b) dynamical simulation of the experimental pattern. Crystal orientation ($\phi_1 = 179.95°, \Phi = 54.53°, \phi_2 = 45.15°$), $DD = 0.45564$, $PC_x = 0.44680$, $PC_Y = 0.59198$, $CC = 0.701$, see text.

position of a point source of particles using DDPs, the simplest experiment would consist of the acquisition of a series of DDPs, each acquired using a different position of the particle source. In practical terms a shift of the point source would result in a shift of the DDP with respect to the detector screen.

This can be easily performed in an SEM, by focusing the electron beam on a surface, and scanning the beam in regular steps along a line.

Such experiments have been performed as follows. In a conventional EBSD geometry the Timepix detector was placed roughly in front of a specimen tilted $\approx 20°$ from the incident beam direction. Using a relatively low magnification, × 500, a 30 keV electron beam has been stepped in a linear scan along the $x$ direction, in the SEM coordinate system, see Fig. 8.5, and ten DDPs have been acquired at regular intervals of space, $\approx 23.8$ $\mu$m (referred to as step size in the following). To increase the signal to noise ratio, for each of the ten positions in the linescan 200 DDPs have been acquired and averaged; this last operation is not affected by the read-out noise of the detector since, as explained in section 4.3, the Timepix detector works in a noise-free condition.

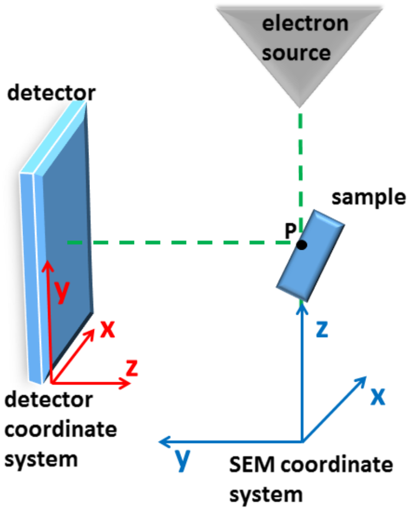

Figure 8.5: Illustration showing the relationship between the SEM coordinate system and the detector coordinate system.

As mentioned previously the role of the specimen is only to generate a diverging point source of electrons in front of the detector.

Each of the DDPs has been processed and indexed using the ESPRIT Dynamics [168] software. The resulting projection parameters were used to measure the effective step size along the $x$ direction in the detector coordinate system. In our experiment the $x$ direction in the detector coordinates was almost coincident with the $x$ SEM scan direction.

By plotting the $\mathrm{PC}_x$ component as function of the number of steps in the linescan a linear trend, as expected, was obtained, as shown in Fig. 8.6. From the slope of the fitted line, which corresponds to $2.17 \times 10^{-3} \pm 3 \times 10^{-5}$ screen units per step, the mean step size in the $x$ direction of the screen (detector) coordinate system can be determined. To obtain its value expressed in standard units it is necessary to multiply

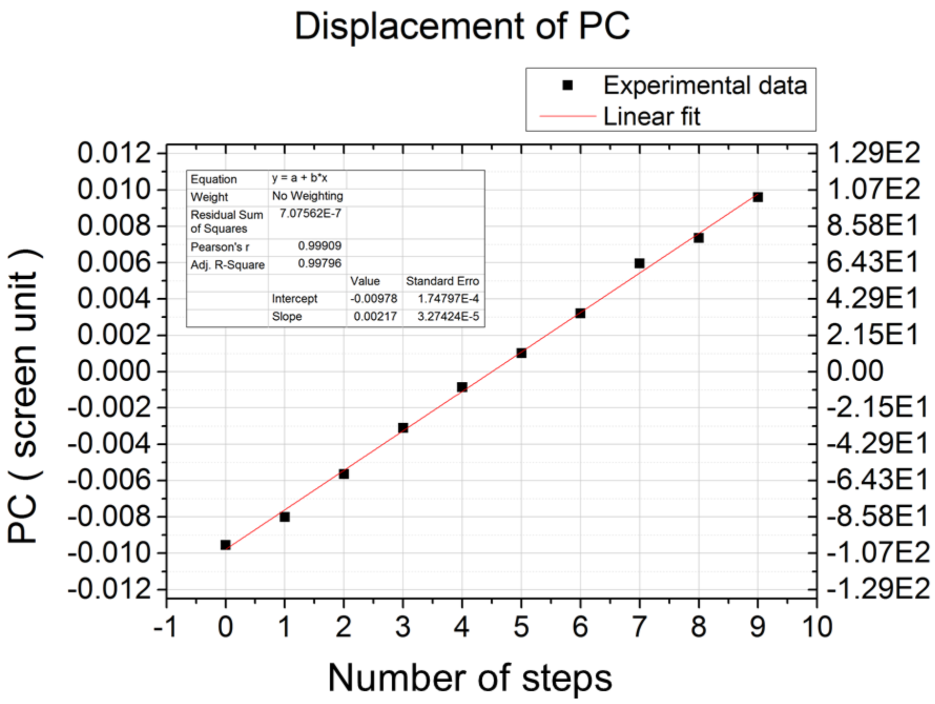

Figure 8.6: Displacement of the pattern centre (PC) measured through detector diffraction patterns as an electron beam is scanned at regular steps on the surface of the $HfO_2$ specimen.

the last value by the width of the screen used in the experiment. The full width of the Timepix detector is ≈ 14080 $\mu$m, but since in the indexed pattern only 195 of the 256 pixels were used, the effective width of the detector was $\frac{195}{256} \times 14080$ $\mu$m= 10725 $\mu$m. The slope of the fitted line (which corresponds to the projection on the detector screen of the step size measured in the SEM coordinate system), expressed in standard units is then $\approx 23.3 \pm 0.3$ $\mu$m.

One of the possible applications of DDPs is the determination of the pattern centre in EBSD/RHEED experiments. As explained in the previous chapters, in EBSD experiments an electron beam is focused on a point on the sample. Due to the elastic and inelastic scattering the direction of the incoming beams are randomized so that the outgoing electrons will have a broad range of directions. When the detector is placed in front of the specimen, the electrons will impinge on the detector with different directions giving rise to the formation of DDP. In this case the DDP is superimposed on the EBSP.

In EBSD experiments the determination of the position of the point source with respect to the detector coordinate system, i.e. the pattern centre, is not trivial, and has crucial importance for a range of EBSD applications, where it is the limiting factor, in particular in strain analysis [237–239].

It is clear that the acquired EBSPs using a 2D single crystal detector will always be superimposed on a DDP, even if it is not visible, providing an "auto-calibrated" EBSD system, where the information about the projection parameters is intrinsically contained in the acquired pattern.

## 8.2 Discussion

This chapter shows a novel method for determining the position of localized sources of radiation. The method is based on the intrinsic angular sensitivity encoded by the internal crystalline structure of the Timepix sensor, which reacts to the incident radiation field, resulting in diffraction effects inside each pixel.

As shown in Fig. 8.1, the detector displays, for each pixel, an intensity related to the direction of the incident particle with respect to the pixel. Each possible three-dimensional position of the source P relative to the detector defines a characteristic two-dimensional intensity pattern of the detector area elements. As an accurate knowledge of the projection center is necessary to calibrate the angular coordinates of the Kikuchi pattern on the detector screen, a key problem in EBSD is the determination of the position of the electron beam spot relative to the detector.

By comparison to simulations, these patterns can be interpreted as electron channeling patterns which are formed not by the sample but in the Timepix detector crystal instead. It is possible to index the detector diffraction pattern using commercial software used for indexing ECP/EBSD patterns.

This electron channeling effect thus provides a one-to-one relationship between pixel position on the detector and the direction towards the source point.

It has been shown in Fig. 8.2 that the effect is very subtle; it is in fact hard to identify it by eye. That is also probably the reason why it has not been seen before.

In our experiments, the relative mixture of sample and detector diffraction patterns was tuned by adjusting the energy of the electron beam, as shown in Fig. 8.3. The same result can be obtaining by varying the thickness of the covering $HfO_2$ film.

Figure 8.3 (a-c) shows the effect of the electron beam energy. The width of the Kikuchi bands in the pattern is inversely proportional to the energy of the primary beam. Diffraction from the crystalline silicon underneath the $HfO_2$ layer is only visible for the 25 keV electron beam. As shown from Fig. 8.3(d-f) the penetration depth of the electron beam is quite limited for the 5 keV and the 12keV electron beams, and the majority of the energy is deposited within the $HfO_2$ layer. For the 25 keV electron beam a larger fraction of energy is deposited into the silicon substrate. When the penetration depth is low the diffraction effect is not fully developed. Once the source of backscattered electrons is produced from the silicon, the electrons have to undergo Kikuchi diffraction in the outgoing path, for the EBSD pattern to be produced. If the few electrons diffracted are re-scattered on passing through the $HfO_2$ layer, this may reintroduce a randomization of the electrons' direction, so that the eventual weak EBSD pattern is almost completely covered by the resultant diffuse background. The result is that only when a high enough energy is used, is the EBSD pattern visible, as in Fig. 8.3(c). The latter has been useful to demonstrate that the DDP is actually a detector effect. By rotating the sample with respect to the detector, the EBSD pattern rotates accordingly and the DDP remains fixed to the detector. The DDP is only modified (shifted) if the relative position of the electron source with respect to the detector is changed, as shown in Fig. 8.6.

In the latter application, a demonstration of a method for determining the position of a localized source of radiation was provided. This made it possible to measure of the electron beam position with respect to the sample, by measuring the shift in the DDP pattern.

In a conventional experiment involving high-quality crystalline surfaces, the DDP contribution is of the order of parts of a percent. However, as the detector diffraction contribution is in principle known, the extraction of the DDP "watermark" pattern from the measured Kikuchi pattern should be possible by image processing techniques like template matching or similar approaches. It should also be possible to produce regular arrays of amorphous reference marks on the sample surface for calibration measurements.

Most importantly, the mode of measurement presented here should also be applicable to other wave sources, where the source size is sufficiently small compared to the solid angle covered by the detector. For an EBSD measurement in the SEM, the source size is of the order of $0.1\mu$m [240]. For sample-detector distances of around 5000 $\mu$m, this corresponds to an angular range of about 0.001 degrees ($2 \times 10^{-5}$ rad). As the width of the detector Kikuchi band features is of the order of several pixels of 55 $\mu$m in dimension (corresponding to an angular width of the order of 0.6 degrees for a sample-detector distances of around 5000 $\mu$m), in this case the influence of the source size which would otherwise lead to a blurring of the diffraction features can be still neglected.

To summarize, this approach provides an initial step towards a more accurate determination of the projection center of Kikuchi and other diffraction patterns, which will carry an inherent watermark of the projection center when measured with crystalline active-pixel detectors like Timepix or similar devices.

# Chapter 9

# Concluding discussion

To summarise, this thesis describes the instrument and techniques developed for advanced applications in the SEM. These exploited an energy filtering digital direct electron detector, Timepix, which had never used previously in the SEM. The latter was used to explore and evaluate a number of diffraction and imaging modes, such as EBSD, TKD, RHEED, STEM, SWR-ECCI and DDPs.

In the introductory part of the thesis, basic concepts of crystallography, quantum mechanics and electron imaging and diffraction modes have been described. Those were of fundamental importance for the understanding and interpretation of the experiments performed in this work. Attention was also given to the description of the dynamical theory of diffraction since it provides an understanding of how scattered electrons are generated within a crystal and how electron waves travel through the specimen.

Special attention was also given to energy filtering methods in diffraction experiments, as they may be used to differentiate between coherently elastically scattered, incoherently quasi-elastically scattered, and inelastically scattered electrons, all of which contribute to the diffraction pattern formation.

A description of the properties of CMOS hybrid pixel detectors was provided. The Timepix detector, its components, and its principle of operation were presented.

A novel method developed for the calibration of the energy threshold in the Timepix detector was discussed. The calibration procedure was necessary to quantify the energy filtering in diffraction experiments. It was shown that for diffraction experiments in the SEM, a convenient way to calibrate the Timepix's threshold is to use backscattered electrons rather than X-rays emitted by radioactive sources.

The digital direct acquisition of energy filtered EBSPs, TKD and TED patterns was described. This demonstrated the advantages of direct electron imaging with respect to the conventional indirect detectors, such as a reduced acquisition time, a decreased electron dose and the possibility for acquiring diffraction patterns using low energy electrons. Results from nitride semiconductors, silicon and diamond thin film samples were presented and used to illustrate the effect of energy filtering.

EBSD patterns show a strong increase in contrast and detail when only electrons having an energy close to the energy of the primary beam are collected. This effect was found to be particularly evident for the lightest, least dense materials, for example diamond. Additionally it was shown that there is a significant suppression of excess-deficiency lines in energy filtered EBSPs.

Transmission Kikuchi diffraction and the acquisition of transmission electron diffraction spot patterns were also discussed, showing that the acquisition of diffraction patterns in transmission geometry increases significantly the spatial resolution when compared to the EBSD technique. This is attributed to the smaller electron-specimen interaction volume when compared to conventional EBSD. It was also shown that, using an on-axis detector, pattens are strongly dominated by coherent Bragg diffraction if too thin a specimen is used and that an appropriate choice of the specimen thickness allows 'tuning' between Bragg, Kikuchi and inelastic diffraction.

The development of RHEED in the SEM was described. Here the experimental set up and the main features appearing in a RHEED pattern were described for both reflection and transmission geometry. Particular importance was given to the surface wave resonance effect, which resulted in the acquisition of RHEED patterns showing a strong increase in the detected intensities for specific diffraction conditions.

By combining RHEED and ECCI, preliminary results regarding the development of the SWR-ECCI technique were presented. This approach showed that by using SWR-ECCI crystalline defects such as surface steps, grain boundaries, dislocations and stacking faults can be imaged with a high level of surface sensitivity, extending furthermore the application of ECCI to non-flat surfaces, e.g. nano-structures.

The development of software which allows the Timepix detector to be used for mapping purposes was described. The software was used to acquire EBSD, TKD maps and STEM images from a range of materials, ranging from polycrystalline WC-Co, to AlGaN films, to ELO AlGaN/AlN/sapphire structures, demonstrating the acquisition of maps in both conventional and transmission modes. Experimental results were presented using the Timepix detector as a virtual forward scatter detector, illustrating the information which may be derived by processing data acquired from different areas of the detector.

A new method exploiting diffraction of the electrons in the Timepix's sensor was developed. It was used for determining the location of a point source relative to the detector. When a quasi-isotropic source of electrons is placed in front of the crystalline sensor, the so-called detector diffraction pattern (DDP) is observed. Comparison of the measured detector diffraction pattern with reference simulations makes it possible to determine the position of the electron beam on the sample relative to the detector. This provides an alternative procedure for the determination of the projection centre for accurate measurements of strain in materials.

In conclusion a number of experimental geometries were proven to be accessible in the SEM, by the exploitation of the Timepix detector.

The intrinsic energy discrimination capability of the detector makes it possible to use energy filtering without any additional hardware. This is a big advantage, considering that electrons which have lost significant energy during their interaction with the specimen do not provide useful information in diffraction experiments.

The compact size of the Timepix detector offered the possibility of positioning the detector in different geometries within the SEM chamber. This made possible the exploration of different diffraction geometries: backscattering, reflection and transmission. A number of conclusions were drawn.

The use of backscattering geometries allows the characterization of materials with very minimal surface preparation. EBSD and the use of virtual detectors make it possible to obtain crystallographic information from bulk materials. It allows the discrimination of grains having different crystallographic orientations or crystal types, and reveals grain boundaries and strain in materials. The use of virtual detectors can be used as an additional tool for obtaining information from the sample, by post-processing the acquired EBSD patterns. By using each pixel in the detector, or by clustering them so as to have virtual detectors, it is possible to obtain a variety of images, highlighting particular aspects of the micro-structure. These include Z-contrast, topography and orientation contrast images.

The spatial resolution in the backscattered geometry is predominantly limited by the electron-specimen interaction volume. The use of the Timepix detector, with its increased sensitivity, allows diffraction imaging using lower electron energies. This decreases significantly the electron interaction volumes making possible the extension of EBSD to the characterization of materials having a truly nano-metric microstructure, where conventional EBSD is limited. An improvement in the spatial resolution can be also achieved by exploiting a transmission diffraction geometry.

In this geometry the same crystallographic information can be obtained by exploiting TKD. The reduced electron-specimen interaction volume in transmission geometry is obtained by physically thinning down the thickness of the specimen. In general a much stronger electron intensity reaches the detector, reducing the acquisition time and dose necessary to obtain diffraction patterns. On the other hand the requirement of a thin specimen introduces non-trivial specimen preparation. An appropriate thickness of the specimen has also to be determined beforehand. Too thin a specimen can lead to diffraction patterns which are dominated by Bragg diffraction spots. This is a problem for TKD analysis, where the Kikuchi bands, similarly to EBSD, are used to extract the information from the diffraction pattern. When Bragg diffraction spots predominate, TKD analysis can be problematic and the Kikuchi bands are most likely to be identified incorrectly. Also when the thickness of the specimen is too large, absorption effects can reduce the intensity of the Kikuchi bands, leading to similar indexing problems. In specimens having a non-uniform thickness, for example in nanorods, the use of low energy EBSD rather than TKD would be advised.

When too thin a specimen is used the diffraction patterns can be effectively considered as transmission electron diffraction spot patterns. In this case the indexing procedures used in TEM can be used to extract the crystallographic information from the diffraction pattern. The other advantage is the possibility of using virtual detectors for obtaining bright and dark field images, which is not very common in the SEM.

By scanning the electron beam on the specimen, and by using virtual detectors, STEM-like images can be obtained in the SEM. This makes possible the acquisition of images showing mass-thickness, atomic number and crystalline defect contrasts. Virtual detectors can be used so as to collect particular scattering directions. This, effectively, is equivalent to having a virtual aperture through which electrons scattered through different solid angles can be collected. This can be used for implementing ADF and HAADF imaging. In general the use of a transmission diffraction geometry makes possible the transfer of a number of imaging modalities used in the TEM to the SEM.

The exploration of a reflection diffraction geometry was nonetheless fruitful. In reflection geometry, diffraction patterns from bulk materials are produced predominantly from the top-most region of the specimen, providing very good depth resolution. Although not fully explored, RHEED in the SEM revealed that the combination of RHEED spots and Kikuchi lines might be a valid alternative for determining the diffraction condition in diffraction experiments. Often the choice of a particular imaging condition can be problematic in the SEM, especially when the contrast in the image is dominated by a strong surface topography, or when the size of the surface is too small, making it difficult to acquire ECPs. This prevents the use of ECPs for the orientation of the sample to a particular diffraction condition. The use of RHEED spots not only allows diffraction conditions to be obtained when acquisition of ECPs is not possible, but also allows the local diffraction condition to be obtained, i.e for each point of the specimen, making possible, for example, the interpretation of crystalline defect contrast within grains.

In addition, the use of surface wave resonance effects in imaging applications allows the enhancement of defect contrast arising from crystalline defects. This could lead to more precise quantification of the material properties, especially of defects in ultra-thin films such as graphene for example.

Although only electron imaging has been addressed in this work, there is nothing to prevent the use of the Timepix detector for X-ray applications.

One can think about the application of X-ray imaging in the SEM. These include micro-computed tomography [241] and material decomposition methods [242] which may allow 3D reconstruction of materials and 3D compositional analysis.

Another possible application, particularly important for strain measurements in films, is Kossel diffraction in the SEM. Kossel diffraction [31] consists in the imaging of Kossel cones, which are produced by the X-rays in the same way as the diffraction cones are produced in Kikuchi diffraction. In contrast to scattered electrons, characteristic X-ray fluorescence lines have very defined emission energies, i.e. are monochromatic. They therefore produce very sharp edges on the detector screen. The advantage compared to EBSD for example, is that the strain sensitivity of Kossel diffraction is larger. This is, on the other hand, at the expense of the spatial resolution achievable with Kossel diffraction, which is of the order of 1 $\mu$m for the energies accessible in the SEM [31, 34, 243, 244].

Finally, the use of direct detectors provides an interesting fingerprint in the sensor material manifested in the form of detector diffraction patterns, which contain inherent information about the position of the electron source. The potential of DDPs will be further explored in future work. The same internal diffraction effect is expected to be produced by other sources of wave fields. This could be also useful for research fields beyond electron microscopy [230].

In general, there is scope to refine the proof of concept experiments described in this thesis by enhancing further the experimental configuration and enhancing the apparatus; it may be reasonably expected that in due course such refinements will realise the full potential of these new approaches. An improvement in the hardware is essential for fully exploiting the described techniques. For example sample and detector stages allowing precise positioning and orientation of the sample and detector are essential and are under development. The development of these techniques opens up new intriguing horizons which need be explored.

# References

[1] L. Barham and P. Mitchell, *The First Africans: African Archaeology from the Earliest Toolmakers to Most Recent Foragers.* Cambridge University Press, 2008.

[2] C. S. Henshilwood, F. d'Errico, R. Yates, Z. Jacobs, C. Tribolo, G. A. Duller, N. Mercier, J. C. Sealy, H. Valladas, I. Watts, *et al.*, "Emergence of modern human behavior: Middle Stone Age engravings from South Africa," *Science*, vol. 295, no. 5558, pp. 1278–1280, 2002.

[3] C. Kittel, *Introduction to Solid State Physics.* Wiley, 2005.

[4] M. De Graef, *Introduction to Conventional Transmission Electron Microscopy.* Cambridge University Press, 2003.

[5] S. K. Chatterjee, *Crystallography and the World of Symmetry*, vol. 113. Springer Science & Business Media, 2008.

[6] D. B. Williams and C. B. Carter, *The Transmission Electron Microscope.* Springer, 1996.

[7] A. J. Schwartz, M. Kumar, B. L. Adams, and D. P. Field, *Electron Backscatter Diffraction in Materials Science*, vol. 2. Springer, 2009.

[8] J. K. Mason and C. A. Schuh, "Representations of Texture," in *Electron Backscatter Diffraction in Materials Science*, pp. 35–51, Springer, 2009.

[9] L.-M. Peng, M. Whelan, and S. Dudarev, *High Energy Electron Diffraction and Microscopy.* Oxford University Press, 2011.

[10] J. M. Cowley and A. F. Moodie, "The scattering of electrons by atoms and crystals. I. A new theoretical approach," *Acta Crystallographica*, vol. 10, no. 10, pp. 609–619, 1957.

[11] P. B. Hirsch, A. Howie, and M. J. Whelan, "A kinematical theory of diffraction contrast of electron transmission microscope images of dislocations and other defects," *Philosophical Transactions of the Royal Society of London A: Mathematical, Physical and Engineering Sciences*, vol. 252, no. 1017, pp. 499–529, 1960.

[12] L. Allen and C. Rossouw, "Absorptive potentials due to ionization and thermal diffuse scattering by fast electrons in crystals," *Physical Review B*, vol. 42, no. 18, p. 11644, 1990.

[13] D. Bird and Q. King, "Absorptive form factors for high-energy electron diffraction," *Acta Crystallographica Section A: Foundations of Crystallography*, vol. 46, no. 3, pp. 202–208, 1990.

[14] A. Wilson and V. Geist, "International Tables for Crystallography. Volume C: Mathematical, Physical and Chemical Tables. Kluwer Academic Publishers, Dordrecht/Boston/London 1992 (published for the International Union of Crystallography), 883 Seiten, ISBN 0-792-3-16-38X," *Crystal Research and Technology*, vol. 28, no. 1, pp. 110–110, 1993.

[15] G. Smith and R. Burge, "The analytical representation of atomic scattering amplitudes for electrons," *Acta Crystallographica*, vol. 15, no. 3, pp. 182–186, 1962.

[16] P. Doyle and P. Turner, "Relativistic Hartree–Fock X-ray and electron scattering factors," *Acta Crystallographica Section A: Crystal Physics, Diffraction, Theoretical and General Crystallography*, vol. 24, no. 3, pp. 390–397, 1968.

[17] A. Weickenmeier and H. Kohl, "Computation of absorptive form factors for high-energy electron diffraction," *Acta Crystallographica Section A: Foundations of Crystallography*, vol. 47, no. 5, pp. 590–597, 1991.

[18] D. Rez, P. Rez, and I. Grant, "Dirac–Fock calculations of X-ray scattering factors and contributions to the mean inner potential for electron scattering," *Acta Crystallographica Section A: Foundations of Crystallography*, vol. 50, no. 4, pp. 481–497, 1994.

[19] P. Duhamel and M. Vetterli, "Fast fourier transforms: a tutorial review and a state of the art," *Signal Processing*, vol. 19, no. 4, pp. 259–299, 1990.

[20] P. Carr, D. Cruickshank, and M. Harding, "The determination of unit-cell parameters from Laue diffraction patterns using their gnomonic projections," *Journal of Applied Crystallography*, vol. 25, no. 2, pp. 294–308, 1992.

[21] S. Kikuchi, "Diffraction of cathode rays by mica," *Proceedings of the Imperial Academy*, vol. 4, no. 6, pp. 271–274, 1928.

[22] S. Nishikawa and S. Kikuchi, "The diffraction of cathode rays by calcite," *Proceedings of the Imperial Academy*, vol. 4, no. 8, pp. 475–477, 1928.

[23] K. Rice, R. Keller, and M. Stoykovich, “Specimen-thickness effects on transmission Kikuchi patterns in the scanning electron microscope,” *Journal of Microscopy*, vol. 254, no. 3, pp. 129–136, 2014.

[24] M. Gomoyunova, I. Pronin, N. Faradzhev, and D. Valdaitsev, “Kikuchi-band formation in medium-energy electron-diffraction patterns,” *Physics of the Solid State*, vol. 41, no. 3, pp. 369–374, 1999.

[25] M. Blackman and I. Khan, “The intensity of High Angle Kikuchi Bands,” *Proceedings of the Physical Society. Section A*, vol. 67, no. 6, p. 553, 1954.

[26] A. Winkelmann, G. Nolze, M. Vos, F. Salvat-Pujol, and W. Werner, “Physics-based simulation models for EBSD: advances and challenges,” in *IOP Conference Series: Materials Science and Engineering*, vol. 109, p. 012018, IOP Publishing, 2016.

[27] J. Goldstein, D. E. Newbury, D. C. Joy, C. E. Lyman, P. Echlin, E. Lifshin, L. Sawyer, and J. Michael, *Scanning Electron Microscopy and X-Ray Microanalysis*. Springer, third ed., 2003.

[28] L. Reimer, *Transmission Electron Microscopy: Physics of Image Formation and Microanalysis*, vol. 36. Springer, 2013.

[29] D. J. Dingley and S. Wright, “Phase identification through symmetry determination in EBSD patterns,” in *Electron Backscatter Diffraction in Materials Science*, pp. 97–107, Springer, 2009.

[30] W. Kossel, V. Loeck, and H. Voges, “Die Richtungsverteilung der in einem Kristall entstandenen charakteristischen Röntgenstrahlung,” *Zeitschrift für Physik*, vol. 94, no. 1-2, pp. 139–144, 1935.

[31] W. Kossel and H. Voges, “Röntgeninterferenzen an der Einkristallantikathode,” *Annalen der Physik*, vol. 415, no. 8, pp. 677–704, 1935.

[32] T. Gog, D. Bahr, and G. Materlik, “Kossel diffraction in perfect crystals: X-ray standing waves in reverse,” *Physical Review B*, vol. 51, no. 10, p. 6761, 1995.

[33] D. Bouscaud, A. Morawiec, R. Pesci, S. Berveiller, and E. Patoor, “Strain resolution of scanning electron microscopy based Kossel microdiffraction,” *Journal of Applied Crystallography*, vol. 47, no. 5, pp. 1699–1707, 2014.

[34] E. Langer, S. Däbritz, C. Schurig, and W. Hauffe, “Lattice constant determination from Kossel patterns observed by CCD camera,” *Applied Surface Science*, vol. 179, no. 1, pp. 45–48, 2001.

[35] C. Humphreys, “The scattering of fast electrons by crystals,” *Reports on Progress in Physics*, vol. 42, no. 11, p. 1825, 1979.

[36] A. Ichimiya, “Correction to Many-Beam Calculation of RHEED Intensities by the Multi-Slice Method,” *Japanese Journal of Applied Physics*, vol. 24, no. 10R, p. 1365, 1985.

[37] A. Howie and M. Whelan, “Diffraction contrast of electron microscope images of crystal lattice defects-II. the development of a dynamical theory,” in *Proceedings of the Royal Society of London A: Mathematical, Physical and Engineering Sciences*, vol. 263, pp. 217–237, The Royal Society, 1961.

[38] A. Howie and M. Whelan, “Diffraction contrast of electron microscope images of crystal lattice defects. III. Results and experimental confirmation of the dynamical theory of dislocation image contrast,” in *Proceedings of the Royal So-*

*ciety of London A: Mathematical, Physical and Engineering Sciences*, vol. 267, pp. 206–230, The Royal Society, 1962.

[39] A. Head, "The explicit solutions of the Howie-Whelan differential equations of electron microscopy," *Philosophical Magazine A*, vol. 44, no. 4, pp. 827–833, 1981.

[40] H. Bethe, "Theorie der Beugung von Elektronen an Kristallen," *Annalen der Physik*, vol. 392, no. 17, pp. 55–129, 1928.

[41] J. Zuo and J. Spence, *Electron Microdiffraction.* Springer Science & Business Media, 2013.

[42] A. Metherell, "Diffraction of electrons by perfect crystals," *Electron Microscopy in Materials Science*, vol. 2, pp. 397–552, 1973.

[43] S. Dudarev, P. Rez, and M. Whelan, "Theory of electron backscattering from crystals," *Physical Review B*, vol. 51, no. 6, p. 3397, 1995.

[44] R. Rüdenberg, "Origin and Background of the invention of the Electron Microscope," *Advances in Imaging and Electron Physics*, vol. 160, pp. 171–205, 2010.

[45] L. Reimer, "Electron diffraction methods in TEM, STEM and SEM," *Scanning*, vol. 2, no. 1, pp. 3–19, 1979.

[46] L. Reimer, "Scanning electron microscopy: physics of image formation and microanalysis," *Measurement Science and Technology*, vol. 11, no. 12, p. 1826, 2000.

[47] E. Rutherford, "LXXIX. The scattering of $\alpha$ and $\beta$ particles by matter and the structure of the atom," *The London, Edinburgh, and Dublin Philosophical Magazine and Journal of Science*, vol. 21, no. 125, pp. 669–688, 1911.

[48] H. Geiger and E. Marsden, "On a diffuse reflection of the $\alpha$-particles," *Proceedings of the Royal Society of London*, vol. 82, no. 557, pp. 495–500, 1909.

[49] J. J. Thomson, "XL. Cathode rays," *The London, Edinburgh, and Dublin Philosophical Magazine and Journal of Science*, vol. 44, no. 269, pp. 293–316, 1897.

[50] D. Hull and D. J. Bacon, *Introduction to Dislocations.* Butterworth-Heinemann, 2001.

[51] J. Steeds, "Convergent beam electron diffraction," in *Introduction to Analytical Electron Microscopy*, pp. 387–422, Springer, 1979.

[52] P. Liu and J. Skogsmo, "Space-group determination and structure model for $\kappa$-Al2O3 by convergent-beam electron diffraction (CBED)," *Acta Crystallographica Section B: Structural Science*, vol. 47, no. 4, pp. 425–433, 1991.

[53] R. T. Carpenter and J. Spence, "Three-dimensional strain-field information in convergent-beam electron diffraction patterns," *Acta Crystallographica Section A: Crystal Physics, Diffraction, Theoretical and General Crystallography*, vol. 38, no. 1, pp. 55–61, 1982.

[54] L. Reimer and M. Ross-Messemer, "Contrast in the electron spectroscopic imaging mode of a TEM," *Journal of Microscopy*, vol. 159, no. 2, pp. 143–160, 1990.

[55] C. C. Ahn, *Transmission Electron Energy Loss Spectrometry in Materials Science and the EELS Atlas.* John Wiley & Sons, 2006.

[56] F. Hofer, P. Warbichler, and W. Grogger, "Imaging of nanometer-sized precipitates in solids by electron spectroscopic imaging," *Ultramicroscopy*, vol. 59, no. 1-4, pp. 15–31, 1995.

[57] F. Hofer, W. Grogger, G. Kothleitner, and P. Warbichler, "Quantitative analysis of EFTEM elemental distribution images," *Ultramicroscopy*, vol. 67, no. 1-4, pp. 83–103, 1997.

[58] J. M. Cowley, *Diffraction Physics.* Elsevier, 1995.

[59] K. Kimoto, T. Asaka, T. Nagai, M. Saito, Y. Matsui, and K. Ishizuka, "Element-selective imaging of atomic columns in a crystal using STEM and EELS," *Nature*, vol. 450, no. 7170, pp. 702–704, 2007.

[60] J. E. Mahan, K. M. Geib, G. Robinson, and R. G. Long, "A review of the geometrical fundamentals of reflection high-energy electron diffraction with application to silicon surfaces," *Journal of Vacuum Science & Technology A*, vol. 8, no. 5, pp. 3692–3700, 1990.

[61] K. Tsuda and M. Tanaka, "Refinement of crystal structural parameters using two-dimensional energy-filtered CBED patterns," *Acta Crystallographica Section A: Foundations of Crystallography*, vol. 55, no. 5, pp. 939–954, 1999.

[62] Z. L. Wang, *Reflection Electron Microscopy and Spectroscopy for Surface Analysis.* Cambridge University Press, 2005.

[63] A. Scherer and B. Van der Gaag, "Characterization of nanostructures by reflection electron microscopy," *Applied Physics Letters*, vol. 56, no. 25, pp. 2566–2568, 1990.

[64] K. Yagi, "Reflection electron microscopy," *Journal of Applied Crystallography*, vol. 20, no. 3, pp. 147–160, 1987.

[65] J. M. Cowley, "Reflection electron microscopy," in *Surface and Interface Characterization by Electron Optical Methods*, pp. 127–158, Springer, 1988.

[66] P. Müller and J. Métois, "Low distortion reflection electron microscopy for surface studies," *Surface Science*, vol. 599, no. 1, pp. 187–195, 2005.

[67] P. Larsen and P. Dobson, *Reflection High-Energy Electron Diffraction and Reflection Electron Imaging of Surfaces*, vol. 188. Springer Science & Business Media, 2012.

[68] N. Ingle, A. Yuskauskas, R. Wicks, M. Paul, and S. Leung, "The structural analysis possibilities of reflection high energy electron diffraction," *Journal of Physics D: Applied Physics*, vol. 43, no. 13, p. 133001, 2010.

[69] A. Ichimiya and P. I. Cohen, *Reflection High-Energy Electron Diffraction.* Cambridge University Press, 2004.

[70] W. Braun, *Applied RHEED: Reflection High-Energy Electron Diffraction During Crystal Growth.* No. 154, Springer Science & Business Media, 1999.

[71] H. Banzhof and K. Herrmann, "Comparison of surface step images in reflection electron microscopy and scanning reflection electron microscopy," *Ultramicroscopy*, vol. 33, no. 1, pp. 23–26, 1990.

[72] H. Watanabe, N. Kuroda, H. Sunakawa, and A. Usui, “Scanning reflection electron microscopy study of surface defects in GaN films formed by epitaxial lateral overgrowth,” *Applied Physics Letters*, vol. 77, no. 12, pp. 1786–1788, 2000.

[73] N. Osakabe, K. Yagi, and G. Honjo, “Reflection electron microscope observations of dislocations and surface structure phase transition on clean (111) silicon surfaces,” *Japanese Journal of Applied Physics*, vol. 19, no. 6, p. L309, 1980.

[74] W. Braun, H. Möller, and Y.-H. Zhang, “Accurate growth rate determination on rotating substrates using electron diffraction dynamics,” *Applied Physics Letters*, vol. 74, no. 1, pp. 138–140, 1999.

[75] S. Ino, “Some new techniques in reflection high energy electron diffraction (RHEED) application to surface structure studies,” *Japanese Journal of Applied Physics*, vol. 16, no. 6, p. 891, 1977.

[76] D. Gall, “Electron mean free path in elemental metals,” *Journal of Applied Physics*, vol. 119, no. 8, p. 085101, 2016.

[77] E. H. Sondheimer, “The mean free path of electrons in metals,” *Advances in Physics*, vol. 1, no. 1, pp. 1–42, 1952.

[78] C. Wagner, L. Davis, and W. Riggs, “The energy dependence of the electron mean free path,” *Surface and Interface Analysis*, vol. 2, no. 2, pp. 53–55, 1980.

[79] H. Frohlich and N. Mott, “The mean free path of electrons in polar crystals,” in *Proceedings of the Royal Society of London A: Mathematical, Physical and Engineering Sciences*, vol. 171, pp. 496–504, The Royal Society, 1939.

[80] A. Ichimiya, “Many-beam calculation of reflection high energy electron diffraction (RHEED) intensities by the multi-slice method,” *Japanese Journal of Applied Physics*, vol. 22, no. 1R, p. 176, 1983.

[81] P. Maksym and J. L. Beeby, “A theory of RHEED,” *Surface Science*, vol. 110, no. 2, pp. 423–438, 1981.

[82] L. M. Peng and J. Cowley, “Dynamical diffraction calculations for RHEED and REM,” *Acta Crystallographica Section A: Foundations of Crystallography*, vol. 42, no. 6, pp. 545–552, 1986.

[83] H. Yang, H. Al-Brithen, A. R. Smith, J. Borchers, R. Cappelletti, and M. Vaudin, “Structural and magnetic properties of $\eta$-phase manganese nitride films grown by molecular-beam epitaxy,” *Applied Physics Letters*, vol. 78, no. 24, pp. 3860–3862, 2001.

[84] G. Whaley and P. Cohen, “The growth of strained InGaAs on GaAs: Kinetics versus energetics,” *Journal of Vacuum Science & Technology B*, vol. 6, no. 2, pp. 625–626, 1988.

[85] G. Whaley and P. Cohen, “Relaxation of strained InGaAs during molecular beam epitaxy,” *Applied Physics Letters*, vol. 57, no. 2, pp. 144–146, 1990.

[86] G. Whaley and P. Cohen, “Diffraction studies of the growth of strained epitaxial layers,” in *MRS Proceedings*, vol. 160, p. 35, Cambridge University Press, 1989.

[87] D. McMullan, “Scanning electron microscopy 1928–1965,” *Scanning*, vol. 17, no. 3, pp. 175–185, 1995.

[88] D. McMullan, "The early development of the scanning electron microscope," in *Biological Low-Voltage Scanning Electron Microscopy*, pp. 1–25, Springer, 2008.

[89] T. Klein, E. Buhr, and C. Georg Frase, "TSEM: A Review of Scanning Electron Microscopy in Transmission Mode and its Applications," *Advances in Imaging and Electron Physics*, vol. 171, p. 297, 2012.

[90] S. J. Pennycook, "A scan through the history of STEM," in *Scanning Transmission Electron Microscopy*, pp. 1–90, Springer, 2011.

[91] I. Müllerová and M. Lenc, "Some approaches to low-voltage scanning electron microscopy," *Ultramicroscopy*, vol. 41, no. 4, pp. 399–410, 1992.

[92] L. Frank, "Advances in scanning electron microscopy," *Advances in Imaging and Electron Physics*, vol. 123, pp. 327–373, 2002.

[93] M. T. Postek, K. S. Howard, A. H. Johnson, and K. L. McMichael, "The scanning electron microscope," *Handbook of Charged Particle Optics*, pp. 363–399, 1997.

[94] P. R. Edwards, L. K. Jagadamma, J. Bruckbauer, C. Liu, P. Shields, D. Allsopp, T. Wang, and R. W. Martin, "High-resolution cathodoluminescence hyperspectral imaging of nitride nanostructures," *Microscopy and Microanalysis*, vol. 18, no. 06, pp. 1212–1219, 2012.

[95] P. R. Edwards, R. W. Martin, K. P. O'Donnell, and I. M. Watson, "Simultaneous composition mapping and hyperspectral cathodoluminescence imaging of InGaN epilayers," *physica status solidi (c)*, no. 7, pp. 2474–2477, 2003.

[96] P. R. Edwards and R. W. Martin, “Cathodoluminescence nano-characterization of semiconductors,” *Semiconductor Science and Technology*, vol. 26, no. 6, p. 064005, 2011.

[97] R. W. Martin, P. R. Edwards, K. P. O’Donnell, M. D. Dawson, C.-W. Jeon, C. Liu, G. R. Rice, and I. M. Watson, “Cathodoluminescence spectral mapping of III-nitride structures,” *physica status solidi (a)*, vol. 201, no. 4, pp. 665–672, 2004.

[98] A. Wierschem, F.-J. Niedernostheide, A. Gorbatyuk, and H.-G. Purwins, “Observation of current-density filamentation in multilayer structures by EBIC measurements,” *Scanning*, vol. 17, no. 2, pp. 106–116, 1995.

[99] L. Pasemann, “Some remarks on the review ≪quantitative evaluation of the EBIC contrast of dislocations≫ by C. Donolato,” *Journal de Physique Lettres*, vol. 45, no. 3, pp. 133–136, 1984.

[100] S. Reyntjens and R. Puers, “A review of focused ion beam applications in microsystem technology,” *Journal of Micromechanics and Microengineering*, vol. 11, no. 4, p. 287, 2001.

[101] P. R. Edwards, S. A. Galloway, and K. Durose, “EBIC and luminescence mapping of CdTe/CdS solar cells,” *Thin Solid Films*, vol. 372, no. 1, pp. 284–291, 2000.

[102] E. Stefaniak, A. Buczynska, V. Novakovic, R. Kuduk, and R. Van Grieken, “Determination of chemical composition of individual airborne particles by SEM/EDX and micro-Raman spectrometry: a review,” in *Journal of Physics: Conference Series*, vol. 162, p. 012019, IOP Publishing, 2009.

[103] P. Velasquez, D. Leinen, J. Pascual, J. R. Ramos-Barrado, P. Grez, H. Gomez, R. Schrebler, R. Del Río, and R. Cordova, "A chemical, morphological, and electrochemical (XPS, SEM/EDX, CV, and EIS) analysis of electrochemically modified electrode surfaces of natural chalcopyrite ($CuFeS_2$) and pyrite ($FeS_2$) in alkaline solutions," *The Journal of Physical Chemistry B*, vol. 109, no. 11, pp. 4977–4988, 2005.

[104] R. S. White and A. D. Owens, "Automation of gunshot residue detection and analysis by scanning electron microscopy/energy dispersive X-ray analysis (SEM/EDX)," *Journal of Forensic Science*, vol. 32, no. 6, pp. 1595–1603, 1987.

[105] E. Silver, M. LeGros, N. Madden, J. Beeman, and E. Haller, "High-Resolution, Broad-Band Microcalorimeters for X-Ray Microanalysis," *X-Ray Spectrometry*, vol. 25, no. 3, pp. 115–122, 1996.

[106] R. Porat, A. Porst, J. Lohse, G. Matke, and M. Rebien, "The use of integrated Energy (EDX) and Wavelength (WDX) Dispersive X-ray system for defects root cause analysis in an advanced logic fab," in *Advanced Semiconductor Manufacturing Conference (ASMC), 2010 IEEE/SEMI*, pp. 123–128, IEEE, 2010.

[107] D. Shemesh, A. Boehm, O. Greenberg, and K. Dotan, "Advanced elemental analysis methods for sub 30nm defects in a defect review SEM," in *Advanced Semiconductor Manufacturing Conference (ASMC), 2011 22nd Annual IEEE/SEMI*, pp. 1–4, IEEE, 2011.

[108] D. Coates, "Kikuchi-like reflection patterns obtained with the scanning electron microscope," *Philosophical Magazine*, vol. 16, no. 144, pp. 1179–1184, 1967.

[109] O. C. Wells, “Comparison of different models for the generation of electron backscattering patterns in the scanning electron microscope,” *Scanning*, vol. 21, no. 6, pp. 368–371, 1999.

[110] E. Wolf and T. Everhart, “Electron beam channeling in single-crystal silicon by scanning electron microscopy,” *Applied Physics Letters*, vol. 14, no. 10, pp. 299–300, 1969.

[111] G. Booker, A. Shaw, M. Whelan, and P. Hirsch, “Some comments on the interpretation of the kikuchi-like reflection patterns observed by scanning electron microscopy,” *Philosophical Magazine*, vol. 16, no. 144, pp. 1185–1191, 1967.

[112] G. E. Lloyd, “Atomic number and crystallographic contrast images with the SEM: a review of backscattered electron techniques,” *Mineralogical Magazine*, vol. 51, no. 359, pp. 3–19, 1987.

[113] A. J. Wilkinson and P. B. Hirsch, “Electron diffraction based techniques in scanning electron microscopy of bulk materials,” *Micron*, vol. 28, no. 4, pp. 279–308, 1997.

[114] D. C. Joy, D. E. Newbury, and D. L. Davidson, “Electron channeling patterns in the scanning electron microscope,” *Journal of Applied Physics*, vol. 53, no. 8, pp. R81–R122, 1982.

[115] J. Ahmed, A. J. Wilkinson, and S. G. Roberts, “Characterizing dislocation structures in bulk fatigued copper single crystals using electron channelling contrast imaging (ECCI),” *Philosophical Magazine Letters*, vol. 76, no. 4, pp. 237–246, 1997.

[116] A. J. Wilkinson, G. R. Anstis, J. T. Czernuszka, N. J. Long, and P. B. Hirsch, “Electron channelling contrast imaging of interfacial defects in strained silicon-

germanium layers on silicon," *Philosophical Magazine A*, vol. 68, no. 1, pp. 59–80, 1993.

[117] A. Weidner, S. Martin, V. Klemm, U. Martin, and H. Biermann, "Stacking faults in high-alloyed metastable austenitic cast steel observed by electron channelling contrast imaging," *Scripta Materialia*, vol. 64, no. 6, pp. 513–516, 2011.

[118] S. Zaefferer and N.-N. Elhami, "Theory and application of electron channelling contrast imaging under controlled diffraction conditions," *Acta Materialia*, vol. 75, pp. 20–50, 2014.

[119] M. Crimp, B. Simkin, and B. Ng, "Demonstration of the g· bxu= 0 edge dislocation invisibility criterion for electron channelling contrast imaging," *Philosophical Magazine Letters*, vol. 81, no. 12, pp. 833–837, 2001.

[120] D. J. Prior, A. P. Boyle, F. Brenker, M. C. Cheadle, A. Day, G. Lopez, L. Peruzzo, G. J. Potts, S. Reddy, R. Spiess, *et al.*, "The application of electron backscatter diffraction and orientation contrast imaging in the SEM to textural problems in rocks," *American Mineralogist*, vol. 84, no. 11-12, pp. 1741–1759, 1999.

[121] C. Trager-Cowan, F. Sweeney, P. W. Trimby, A. P. Day, A. Gholinia, N.-H. Schmidt, P. J. Parbrook, A. J. Wilkinson, and I. M. Watson, "Electron backscatter diffraction and electron channeling contrast imaging of tilt and dislocations in nitride thin films," *Physical Review B*, vol. 75, no. 8, p. 085301, 2007.

[122] G. Naresh-Kumar, B. Hourahine, P. R. Edwards, A. P. Day, A. Winkelmann, A. J. Wilkinson, P. J. Parbrook, G. England, and C. Trager-Cowan, "Rapid

nondestructive analysis of threading dislocations in wurtzite materials using the scanning electron microscope," *Physical Review Letters*, vol. 108, no. 13, p. 135503, 2012.

[123] Y. Picard, M. Twigg, J. Caldwell, C. Eddy Jr, P. Neudeck, A. Trunek, and J. Powell, "Electron channeling contrast imaging of atomic steps and threading dislocations in 4 H-Si C," *Applied Physics Letters*, vol. 90, no. 23, p. 234101, 2007.

[124] M. A. Crimp, "Scanning electron microscopy imaging of dislocations in bulk materials, using electron channeling contrast," *Microscopy Research and Technique*, vol. 69, no. 5, pp. 374–381, 2006.

[125] K. Z. Baba-Kishi, "Review Electron backscatter Kikuchi diffraction in the scanning electron microscope for crystallographic analysis," *Journal of Materials Science*, vol. 37, no. 9, pp. 1715–1746, 2002.

[126] K. Z. Baba-Kishi, "Measurement of Crystal Parameters on Backscatter Kikuchi Diffraction Patterns," *Scanning*, vol. 20, no. 2, pp. 117–127, 1998.

[127] A. J. Wilkinson, "Measurement of elastic strains and small lattice rotations using electron back scatter diffraction," *Ultramicroscopy*, vol. 62, no. 4, pp. 237–247, 1996.

[128] A. J. Wilkinson, "Advances in SEM–based diffraction studies of defects and strains in semiconductors," *Journal of Electron Microscopy*, vol. 49, no. 2, pp. 299–310, 2000.

[129] A. J. Wilkinson, G. Meaden, and D. J. Dingley, "High-resolution elastic strain measurement from electron backscatter diffraction patterns: new levels of sensitivity," *Ultramicroscopy*, vol. 106, no. 4, pp. 307–313, 2006.

[130] A. J. Wilkinson, T. B. Britton, J. Jiang, and P. S. Karamched, “A review of advances and challenges in EBSD strain mapping,” in *IOP Conference Series: Materials Science and Engineering*, vol. 55, p. 012020, IOP Publishing, 2014.

[131] C. Maurice, J. H. Driver, and R. Fortunier, “On solving the orientation gradient dependency of high angular resolution EBSD,” *Ultramicroscopy*, vol. 113, pp. 171–181, 2012.

[132] S. Suzuki, “Features of transmission EBSD and its application,” *Jom*, vol. 65, no. 9, pp. 1254–1263, 2013.

[133] D. Dingley and D. Field, “Electron backscatter diffraction and orientation imaging microscopy,” *Materials Science and Technology*, vol. 13, no. 1, pp. 69–78, 1997.

[134] B. El-Dasher and A. Deal, “Application of electron backscatter diffraction to phase identification,” in *Electron Backscatter Diffraction in Materials Science*, pp. 81–95, Springer, 2009.

[135] S. Zaefferer and S. I. Wright, “Three-dimensional orientation microscopy by serial sectioning and EBSD-based orientation mapping in a FIB-SEM,” in *Electron Backscatter Diffraction in Materials Science*, pp. 109–122, Springer, 2009.

[136] M. A. Groeber, D. J. Rowenhorst, and M. D. Uchic, “Collection, processing, and analysis of three-dimensional EBSD data sets,” in *Electron Backscatter Diffraction in Materials Science*, pp. 123–137, Springer, 2009.

[137] S. D. Sintay, M. A. Groeber, and A. D. Rollett, “3D reconstruction of digital microstructures,” in *Electron Backscatter Diffraction in Materials Science*, pp. 139–153, Springer, 2009.

[138] R. Keller and R. Geiss, “Transmission EBSD from 10 nm domains in a scanning electron microscope,” *Journal of Microscopy*, vol. 245, no. 3, pp. 245–251, 2012.

[139] P. W. Trimby, “Orientation mapping of nanostructured materials using transmission Kikuchi diffraction in the scanning electron microscope,” *Ultramicroscopy*, vol. 120, pp. 16–24, 2012.

[140] M. Alam, M. Blackman, and D. Pashley, “High-angle Kikuchi patterns,” in *Proceedings of the Royal Society of London A: Mathematical, Physical and Engineering Sciences*, vol. 221, pp. 224–242, The Royal Society, 1954.

[141] J. Venables and C. Harland, “Electron back-scattering patterns-a new technique for obtaining crystallographic information in the scanning electron microscope,” *Philosophical Magazine*, vol. 27, no. 5, pp. 1193–1200, 1973.

[142] J. A. Venables and R. Bin-Jaya, “Accurate microcrystallography using electron back-scattering patterns,” *Philosophical Magazine*, vol. 35, no. 5, pp. 1317–1332, 1977.

[143] S. I. Wright, D. P. Field, and D. J. Dingley, “Advanced software capabilities for automated EBSD,” in *Electron Backscatter Diffraction in Materials Science*, pp. 141–152, Springer, 2000.

[144] B. L. Adams, S. I. Wright, and K. Kunze, “Orientation imaging: the emergence of a new microscopy,” *Metallurgical Transactions A*, vol. 24, no. 4, pp. 819–831, 1993.

[145] N. K. Lassen, D. J. Jensen, and K. Conradsen, “Image processing procedures for analysis of electron back scattering patterns,” *Scanning Microscopy*, vol. 6, no. 1, pp. 115–121, 1992.

[146] K. Lassen, “Automatic high-precision measurements of the location and width of Kikuchi bands in electron backscatter diffraction patterns,” *Journal of Microscopy*, vol. 190, no. 3, pp. 375–391, 1998.

[147] R. A. Schwarzer, D. P. Field, B. L. Adams, M. Kumar, and A. J. Schwartz, “Present state of electron backscatter diffraction and prospective developments,” in *Electron Backscatter Diffraction in Materials Science*, pp. 1–20, Springer, 2009.

[148] A. Winkelmann, K. Aizel, and M. Vos, “Electron energy loss and diffraction of backscattered electrons from silicon,” *New Journal of Physics*, vol. 12, no. 5, p. 053001, 2010.

[149] F. Yubero, N. Pauly, A. Dubus, and S. Tougaard, “Test of validity of the V-type approach for electron trajectories in reflection electron energy loss spectroscopy,” *Physical Review B*, vol. 77, no. 24, p. 245405, 2008.

[150] A. Winkelmann, C. Trager-Cowan, F. Sweeney, A. P. Day, and P. Parbrook, “Many-beam dynamical simulation of electron backscatter diffraction patterns,” *Ultramicroscopy*, vol. 107, no. 4, pp. 414–421, 2007.

[151] https://www.bruker.com/products/x-ray-diffraction-and-elemental-analysis/eds-wds-ebsd-sem-micro-xrf-and-sem-micro-ct/esprit-dynamics/overview.html, last accessed 26/02/2017.

[152] J. Illingworth and J. Kittler, “A survey of the Hough transform,” *Computer Vision, Graphics, and Image Processing*, vol. 44, no. 1, pp. 87–116, 1988.

[153] A. Winkelmann and G. Nolze, “Point-group sensitive orientation mapping of non-centrosymmetric crystals,” *Applied Physics Letters*, vol. 106, no. 7, p. 072101, 2015.

[154] A. Winkelmann and G. Nolze, “Chirality determination of quartz crystals using electron backscatter diffraction,” *Ultramicroscopy*, vol. 149, pp. 58–63, 2015.

[155] A. Winkelmann, “Principles of depth-resolved Kikuchi pattern simulation for electron backscatter diffraction,” *Journal of Microscopy*, vol. 239, no. 1, pp. 32–45, 2010.

[156] A. Winkelmann, “Dynamical simulation of electron backscatter diffraction patterns,” in *Electron Backscatter Diffraction in Materials Science*, pp. 21–33, Springer, 2009.

[157] A. Eades, A. Deal, A. Bhattacharyya, and T. Hooghan, “Energy filtering in EBSD,” in *Electron Backscatter Diffraction in Materials Science*, pp. 53–63, Springer, 2009.

[158] A. Deal, T. Hooghan, and A. Eades, “Energy-filtered electron backscatter diffraction,” *Ultramicroscopy*, vol. 108, no. 2, pp. 116–125, 2008.

[159] A. Oppelt, *Imaging Systems for Medical Diagnostics: Fundamentals, Technical Solutions and Applications for Systems Applying Ionizing Radiation, Nuclear Magnetic Resonance and Ultrasound*. John Wiley & Sons, 2011.

[160] M. Went, A. Winkelmann, and M. Vos, “Quantitative measurements of Kikuchi bands in diffraction patterns of backscattered electrons using an electrostatic analyzer,” *Ultramicroscopy*, vol. 109, no. 10, pp. 1211–1216, 2009.

[161] X. Llopart, R. Ballabriga, M. Campbell, L. Tlustos, and W. Wong, “Timepix, a 65k programmable pixel readout chip for arrival time, energy and/or photon counting measurements,” *Nuclear Instruments and Methods in Physics Research Section A: Accelerators, Spectrometers, Detectors and Associated Equipment*, vol. 581, no. 1, pp. 485–494, 2007.

[162] L. Allen and C. Rossouw, "Effects of thermal diffuse scattering and surface tilt on diffraction and channeling of fast electrons in CdTe," *Physical Review B*, vol. 39, no. 12, p. 8313, 1989.

[163] A. Winkelmann, "Dynamical effects of anisotropic inelastic scattering in electron backscatter diffraction," *Ultramicroscopy*, vol. 108, no. 12, pp. 1546–1550, 2008.

[164] https://www.fei.com/, last accessed 26/02/2017.

[165] http://www.adlinktech.com/, last accessed 26/02/2017.

[166] http://www.ftdichip.com/, last accessed 26/02/2017.

[167] V. Kraus, M. Holik, J. Jakubek, M. Kroupa, P. Soukup, and Z. Vykydal, "FITPix-fast interface for Timepix pixel detectors," *Journal of Instrumentation*, vol. 6, no. 01, p. C01079, 2011.

[168] https://www.bruker.com/products/x-ray-diffraction-and-elemental-analysis/eds-wds-ebsd-sem-micro-xrf-and-sem-micro-ct/esprit-dynamics/overview.html, last accessed 26/02/2017.

[169] https://msdn.microsoft.com/en-us/library/kx37x362.aspx, last accessed 26/02/2017.

[170] M. Williams, *Microsoft Visual C# (core reference)*. Microsoft Press, 2002.

[171] D. Turecek, T. Holy, J. Jakubek, S. Pospisil, and Z. Vykydal, "Pixelman: a multi-platform data acquisition and processing software package for Medipix2, Timepix and Medipix3 detectors," *Journal of Instrumentation*, vol. 6, no. 01, p. C01046, 2011.

[172] http://aladdin.utef.cvut.cz/ofat/others/Pixelman/Pixelman.html, last accessed 15/08/2016.

[173] https://www.continuum.io/anaconda-overview, last accessed 26/02/2017.

[174] G. Van Rossum *et al.*, "Python Programming Language.," in *USENIX Annual Technical Conference*, vol. 41, p. 36, 2007.

[175] https://www.python.org/, last accessed 26/02/2017.

[176] R. Gentleman, *R Programming for Bioinformatics*. CRC Press, 2008.

[177] https://www.r-project.org/about.html, last accessed 26/02/2017.

[178] https://imagej.net/Welcome, last accessed 26/02/2017.

[179] M. D. Abràmoff, P. J. Magalhães, and S. J. Ram, "Image processing with ImageJ," *Biophotonics International*, vol. 11, no. 7, pp. 36–42, 2004.

[180] T. J. Collins *et al.*, "ImageJ for microscopy," *Biotechniques*, vol. 43, no. 1 Suppl, pp. 25–30, 2007.

[181] G. Mueller, "The Czochralski Method-where we are 90 years after Jan Czochralskis invention," *Crystal Research and Technology*, vol. 42, no. 12, pp. 1150–1161, 2007.

[182] J. Achard, A. Tallaire, R. Sussmann, F. Silva, and A. Gicquel, "The control of growth parameters in the synthesis of high-quality single crystalline diamond by CVD," *Journal of Crystal Growth*, vol. 284, no. 3, pp. 396–405, 2005.

[183] R. Balmer, J. Brandon, S. Clewes, H. Dhillon, J. Dodson, I. Friel, P. Inglis, T. Madgwick, M. Markham, T. Mollart, *et al.*, "Chemical vapour deposition

synthetic diamond: materials, technology and applications," *Journal of Physics: Condensed Matter*, vol. 21, no. 36, p. 364221, 2009.

[184] P. Shields, M. Hugues, J. Zúñiga-Pérez, M. Cooke, M. Dineen, W. Wang, F. Causa, and D. Allsopp, "Fabrication and properties of etched GaN nanorods," *physica status solidi (c)*, vol. 9, no. 3-4, pp. 631–634, 2012.

[185] A. Knauer, V. Kueller, U. Zeimer, M. Weyers, C. Reich, and M. Kneissl, "AlGaN layer structures for deep UV emitters on laterally overgrown AlN/sapphire templates," *physica status solidi (a)*, vol. 210, no. 3, pp. 451–454, 2013.

[186] E. Richter, S. Fleischmann, D. Goran, S. Hagedorn, W. John, A. Mogilatenko, D. Prasai, U. Zeimer, M. Weyers, and G. Tränkle, "Hydride vapor-phase epitaxy of c-plane AlGaN layers on patterned sapphire substrates," *Journal of Electronic Materials*, vol. 43, no. 4, pp. 814–818, 2014.

[187] A. R. Faruqi and R. Henderson, "Electronic detectors for electron microscopy," *Current Opinion in Structural Biology*, vol. 17, no. 5, pp. 549–555, 2007.

[188] G. F. Knoll, *Radiation Detection and Measurement.* John Wiley & Sons, 2010.

[189] A. R. Faruqi and S. Subramaniam, "CCD detectors in high-resolution biological electron microscopy," *Quarterly Reviews of Biophysics*, vol. 33, no. 01, pp. 1–27, 2000.

[190] M. Bigas, E. Cabruja, J. Forest, and J. Salvi, "Review of CMOS image sensors," *Microelectronics Journal*, vol. 37, no. 5, pp. 433–451, 2006.

[191] http://medipix.web.cern.ch/medipix/, last accessed 26/02/2017.

[192] X. Llopart, M. Campbell, R. Dinapoli, D. San Segundo, and E. Pernigotti, "Medipix2: a 64-k pixel readout chip with 55-$\mu$m square elements working in

single photon counting mode," *Nuclear Science, IEEE Transactions on*, vol. 49, no. 5, pp. 2279–2283, 2002.

[193] G. McMullan, D. M. Cattermole, S. Chen, R. Henderson, X. Llopart, C. Summerfield, L. Tlustos, and A. R. Faruqi, "Electron imaging with Medipix2 hybrid pixel detector," *Ultramicroscopy*, vol. 107, no. 4, pp. 401–413, 2007.

[194] A. R. Faruqi, R. Henderson, and L. Tlustos, "Noiseless direct detection of electrons in Medipix2 for electron microscopy," *Nuclear Instruments and Methods in Physics Research Section A: Accelerators, Spectrometers, Detectors and Associated Equipment*, vol. 546, no. 1, pp. 160–163, 2005.

[195] A. R. Faruqi, H. N. Andrews, and R. Henderson, "A high sensitivity imaging detector for electron microscopy," *Nuclear Instruments and Methods in Physics Research Section A: Accelerators, Spectrometers, Detectors and Associated Equipment*, vol. 367, no. 1-3, pp. 408–412, 1995.

[196] G. McMullan, A. R. Faruqi, D. Clare, and R. Henderson, "Comparison of optimal performance at 300keV of three direct electron detectors for use in low dose electron microscopy," *Ultramicroscopy*, vol. 147, pp. 156–163, 2014.

[197] G. McMullan, A. T. Clark, R. Turchetta, and A. R. Faruqi, "Enhanced imaging in low dose electron microscopy using electron counting," *Ultramicroscopy*, vol. 109, no. 12, pp. 1411–1416, 2009.

[198] A. R. Faruqi, "Principles and prospects of direct high resolution electron image acquisition with CMOS detectors at low energies," *Journal of Physics: Condensed Matter*, vol. 21, no. 31, p. 314004, 2009.

[199] W. Snoeys, "CMOS monolithic active pixel sensors for high energy physics," *Nuclear Instruments and Methods in Physics Research Section A: Accelerators,*

*Spectrometers, Detectors and Associated Equipment*, vol. 765, pp. 167–171, 2014.

[200] M. H. Baker, "Method for forming solder bumps in semiconductor devices," Apr. 16 1996. US Patent 5,508,229.

[201] T. Hayashi, "An innovative bonding technique for optical chips using solder bumps that eliminate chip positioning adjustments," *IEEE Transactions on Components, Hybrids, and Manufacturing Technology*, vol. 15, no. 2, pp. 225–230, 1992.

[202] T. Holy, E. Heijne, J. Jakubek, S. Pospisil, J. Uher, and Z. Vykydal, "Pattern recognition of tracks induced by individual quanta of ionizing radiation in Medipix2 silicon detector," *Nuclear Instruments and Methods in Physics Research Section A: Accelerators, Spectrometers, Detectors and Associated Equipment*, vol. 591, no. 1, pp. 287–290, 2008.

[203] G. McMullan, S. Chen, R. Henderson, and A. R. Faruqi, "Detective quantum efficiency of electron area detectors in electron microscopy," *Ultramicroscopy*, vol. 109, no. 9, pp. 1126–1143, 2009.

[204] L. Tlustos, R. Ballabriga, M. Campbell, E. Heijne, K. Kincade, X. Llopart, and P. Stejskal, "Imaging properties of the Medipix2 system exploiting single and dual energy thresholds," *IEEE Transactions on Nuclear Science*, vol. 53, no. 1, pp. 367–372, 2006.

[205] M. Fiederle, D. Greiffenberg, J. Idárraga, J. Jakubek, V. Král, C. Lebel, C. Leroy, G. Lord, S. Pospíšil, V. Sochor, *et al.*, "Energy calibration measurements of MediPix2," *Nuclear Instruments and Methods in Physics Research*

*Section A: Accelerators, Spectrometers, Detectors and Associated Equipment*, vol. 591, no. 1, pp. 75–79, 2008.

[206] M.-M. Be, V. Chiste, C. Dulieu, X. Mougeot, V. Chechev, F. Kondev, A. Nichols, X. Huang, and B. Wang, "Table of Radionuclides (Comments on evaluation)," *Monographie BIPM-5*, vol. 7, 2004.

[207] L. Carramate, F. Nachtrab, M. Firsching, A. Silva, A. da Silva, J. Veloso, and N. Uhlmann, "Energy resolving CT systems using Medipix2 and MHSP detectors," *Journal of Instrumentation*, vol. 8, no. 03, p. C03022, 2013.

[208] S. Vespucci, A. Winkelmann, G. Naresh-Kumar, K. P. Mingard, D. Maneuski, P. R. Edwards, A. P. Day, V. O'Shea, and C. Trager-Cowan, "Digital direct electron imaging of energy-filtered electron backscatter diffraction patterns," *Physical Review B*, vol. 92, no. 20, p. 205301, 2015.

[209] A. J. Wilkinson, G. Moldovan, T. B. Britton, A. Bewick, R. Clough, and A. I. Kirkland, "Direct detection of electron backscatter diffraction patterns," *Physical Review Letters*, vol. 111, no. 6, p. 065506, 2013.

[210] A. Winkelmann, F. Salvat-Pujol, and W. Werner, "Monte Carlo Simulations for Applications in Electron Backscatter Diffraction," *Microscopy and Microanalysis*, vol. 19, no. S2, pp. 738–739, 2013.

[211] F. Ram, S. Zaefferer, and D. Raabe, "Kikuchi bandlet method for the accurate deconvolution and localization of Kikuchi bands in Kikuchi diffraction patterns," *Journal of Applied Crystallography*, vol. 47, no. 1, pp. 264–275, 2014.

[212] K. Akiba, P. Ronning, M. van Beuzekom, V. van Beveren, S. Borghi, H. Boterenbrood, J. Buytaert, P. Collins, A. D. Suárez, R. Dumps, *et al.*, "The Timepix

telescope for high performance particle tracking," *Nuclear Instruments and Methods in Physics Research Section A: Accelerators, Spectrometers, Detectors and Associated Equipment*, vol. 723, pp. 47–54, 2013.

[213] https://www.bruker.com/products/x-ray-diffraction-and-elemental-analysis/eds-wds-ebsd-sem-micro-xrf-and-sem-micro-ct/quantax-ebsd/hardware/transmission-kikuchi-diffraction-in-sem/optimus.html, last accessed 26/02/2017.

[214] Z. Zytkiewicz, "Laterally overgrown structures as substrates for lattice mismatched epitaxy," *Thin Solid Films*, vol. 412, no. 1, pp. 64–75, 2002.

[215] S. Vespucci, A. Winkelmann, K. Mingard, D. Maneuski, V. O'Shea, and C. Trager-Cowan, "Exploring transmission Kikuchi diffraction using a Timepix detector," *Journal of Instrumentation*, vol. 12, no. 02, p. C02075, 2017.

[216] G.-C. Wang and T.-M. Lu, "RHEED Transmission Mode and RHEED pole figure," in *RHEED Transmission Mode and Pole Figures*, pp. 73–106, Springer, 2014.

[217] S. Kikuchi and S. Nakagawa, "Die anomale Reflexion der schnellen Elektronen an die Einkristalloberflachen," *Scientific papers of the Institute of Physical and Chemical Research Tokyo*, vol. 21, pp. 256–65, 1933.

[218] K. Kohra, K. Molière, S. Nakano, and M. Ariyama, "Anomalous intensity of mirror reflection from the surface of a single crystal," *Journal of the Physical Society of Japan*, vol. 17, pp. 82–85, 1962.

[219] S. Miyake and K. Hayakawa, "Resonance effects in low and high energy electron diffraction by crystals," *Acta Crystallographica Section A: Crystal Physics,*

*Diffraction, Theoretical and General Crystallography*, vol. 26, no. 1, pp. 60–70, 1970.

[220] E. McRae and P. Jennings, "Surface-state resonances in low-energy electron diffraction," *Surface Science*, vol. 15, no. 2, pp. 345–348, 1969.

[221] K. Hirabayashi, "Resonance Effects in Diffraction of Low-Energy Electrons by Crystals," *Journal of the Physical Society of Japan*, vol. 25, no. 3, pp. 856–861, 1968.

[222] A. Ichimiya, K. Kambe, and G. Lehmpfuhl, "Observation of the surface state resonance effect by the convergent beam RHEED technique," *Journal of the Physical Society of Japan*, vol. 49, no. 2, pp. 684–688, 1980.

[223] H. Marten and G. Meyer-Ehmsen, "Resonance effects in RHEED from Pt (111)," *Surface Science*, vol. 151, no. 2-3, pp. 570–584, 1985.

[224] K. Baba-Kishi, "A study of directly recorded RHEED and BKD patterns in the SEM," *Ultramicroscopy*, vol. 34, no. 3, pp. 205–218, 1990.

[225] S. I. Wright, M. M. Nowell, R. de Kloe, P. Camus, and T. Rampton, "Electron imaging with an EBSD detector," *Ultramicroscopy*, vol. 148, pp. 132–145, 2015.

[226] A. Day and T. Quested, "A comparison of grain imaging and measurement using horizontal orientation and colour orientation contrast imaging, electron backscatter pattern and optical methods," *Journal of Microscopy*, vol. 195, no. 3, pp. 186–196, 1999.

[227] A. Winkelmann, G. Nolze, S. Vespucci, G. Naresh-Kumar, C. Trager-Cowan, A. Vilalta-Clemente, A. J. Wilkinson, and M. Vos, "Diffraction effects and in-

elastic electron transport in angle-resolved microscopic imaging applications," *Journal of Microscopy*, 2017.

[228] K. T. Mullen, "The contrast sensitivity of human colour vision to red-green and blue-yellow chromatic gratings.," *The Journal of Physiology*, vol. 359, no. 1, pp. 381–400, 1985.

[229] J. Demarest, K. Chanda, S. Klepeis, B. Redder, A. Shore, Y. Wang, C. Christiansen, and C. Rue, "Image Intensity Analysis for Defect Localization Utilizing SEM BSE Imaging," in *International Symposium for Testing and Failure Analysis*, vol. 32, p. 289, ASM International, 2006.

[230] S. Vespucci, G. Naresh-Kumar, C. Trager-Cowan, K. P. Mingard, D. Maneuski, V. O'Shea, and A. Winkelmann, "Diffractive triangulation of radiative point sources," *Applied Physics Letters*, vol. 110, no. 12, p. 124103, 2017.

[231] http://www.gel.usherbrooke.ca/casino, last accessed 18/03/2017.

[232] D. Drouin, A. R. Couture, D. Joly, X. Tastet, V. Aimez, and R. Gauvin, "CASINO V2. 42A Fast and Easy-to-use Modeling Tool for Scanning Electron Microscopy and Microanalysis Users," *Scanning*, vol. 29, no. 3, pp. 92–101, 2007.

[233] A. Morawiec, *Orientations and Rotations.* Springer, 2003.

[234] J. Lewis, "Fast normalized cross-correlation," in *Vision Interface*, vol. 10, pp. 120–123, 1995.

[235] K. Briechle and U. D. Hanebeck, "Template matching using fast normalized cross correlation," in *Aerospace/Defense Sensing, Simulation, and Controls*, pp. 95–102, International Society for Optics and Photonics, 2001.

[236] J. N. Sarvaiya, S. Patnaik, and S. Bombaywala, “Image registration by template matching using normalized cross-correlation,” in *2009 International Conference on Advances in Computing, Control, and Telecommunication Technologies*, pp. 819–822, IEEE, 2009.

[237] S. Villert, C. Maurice, C. Wyon, and R. Fortunier, “Accuracy assessment of elastic strain measurement by EBSD,” *Journal of Microscopy*, vol. 233, no. 2, pp. 290–301, 2009.

[238] C. Maurice, K. Dzieciol, and R. Fortunier, “A method for accurate localisation of EBSD pattern centres,” *Ultramicroscopy*, vol. 111, no. 2, pp. 140–148, 2011.

[239] T. B. Britton, C. Maurice, R. Fortunier, J. H. Driver, A. P. Day, G. Meaden, D. J. Dingley, K. Mingard, and A. J. Wilkinson, “Factors affecting the accuracy of high resolution electron backscatter diffraction when using simulated patterns,” *Ultramicroscopy*, vol. 110, no. 12, pp. 1443–1453, 2010.

[240] S. Zaefferer, “On the formation mechanisms, spatial resolution and intensity of backscatter Kikuchi patterns,” *Ultramicroscopy*, vol. 107, no. 2, pp. 254–266, 2007.

[241] E. L. Ritman, “Micro-computed tomography - current status and developments,” *Annu. Rev. Biomed. Eng.*, vol. 6, pp. 185–208, 2004.

[242] R. E. Alvarez and A. Macovski, “Energy-selective reconstructions in x-ray computerised tomography,” *Physics in Medicine and Biology*, vol. 21, no. 5, p. 733, 1976.

[243] C. Maurice and R. Fortunier, “A 3D Hough transform for indexing EBSD and Kossel patterns,” *Journal of Microscopy*, vol. 230, no. 3, pp. 520–529, 2008.

[244] V. Lider, “X-ray divergent-beam (Kossel) technique: A review,” *Crystallography Reports*, vol. 56, no. 2, pp. 169–189, 2011.